Title

Prediction and Mitigation of Airfoil Noise Using Large Eddy Simulations

Author

Kang, Dong Hun

Publication Date

2024

Prediction and Mitigation of Airfoil Noise Using Large Eddy Simulations

By

Dong Hun Kang
Dissertation

Submitted in partial satisfaction of the requirements for the degree of

Doctor of Philosophy

in

Mechanical and Aerospace Engineering

in the

Office of Graduate Studies

of the

University of California

Davis

Approved:

Seongkyu Lee, Chair

Cornelis van Dam

Stéphane Moreau

Committee in Charge

2024

ABSTRACT

This study aims to advance the fundamental flow physics of acoustic source generation, propagation, and mitigation using large-eddy simulations with specific emphasis on flows around an airfoil.

First, a wavelet-based recursive denoising algorithm is applied to airfoil flow field. The pressure field around the airfoil is decomposed into coherent contributions corresponding to denoised pressure and incoherent pressure corresponding to background noise. It is found that the denoised pressure represents physical phenomena associated with near-wall hydrodynamic wavy structures and sound propagation generated near the boundary-layer tripping region and trailing edge. On the other hand, the incoherent pressure or background noise exhibits a small and constant amplitude closely adhering to the Gaussian distribution.

Second, wavenumber-frequency decomposition and Amiet's theory are used to separate total pressure into two distinct components: hydrodynamic (incident) pressure and acoustic (scattered) pressure. The findings reveal that hydrodynamic pressure consists of turbulent coherent structures characterized by high-energy spectra but acts as non-propagating sources due to destructive interference within the streamwise correlation length. In contrast, acoustic pressure exhibits an in-phase nature that facilitates efficient sound propagation. Amiet's theory shows similarities in magnitude and directivity patterns, but the disparity between numerical and analytical studies exists, which is investigated in detail.

Third, this study delves into the detailed sound generation and propagation mechanisms associated with trailing-edge scattering and flow perturbations of boundary-layer tripping. Two distinct boundary-layer tripping techniques, namely a geometrically resolved stair strip and an artificially modeled trip using suction and blowing, are investigated. It is found that boundary-layer tripping notably leads to intricate, scenario-specific noise generation: there is an interaction between the laminar separation bubble and tripping for the stair strip case, whereas laminar boundary layer instability is evident for the suction and blowing scenario. Aerodynamic flow fields involving acoustic noise sources, their propagating natures near the wall, and far-field acoustics are cross-examined in detail.

Fourth, a cross-spectrum method is proposed to identify the origin of noise sources and understand sound production mechanisms. This novel method shows its potential by effectively detecting the acoustic source and propagation that are on par with or surpass those of dynamic mode decomposition and spectral proper orthogonal decomposition modes while simultaneously providing the spectral magnitude and phase topologies when applied to different flow transition mechanisms of an airfoil.

Fifth, the effect of misaligned flow on trailing-edge noise is studied to examine fundamental mechanisms governing noise mitigation. Flow misalignment observed in the swept airfoil is found to generate destructive interference, playing a crucial role in the noise reduction mechanism. Critical flow physics responsible for the noise source attenuation is discovered in the numerical simulations, which are cross-examined with Amiet's swept trailing-edge noise theory.

Sixth, the effects of trailing-edge morphing on aerodynamic and aeroacoustic performances are studied. Concave (M1) and convex (M2) shapes are imposed near the trailing edge of the airfoil. The M1 airfoil demonstrates enhanced performance in both aerodynamics and aeroacoustics, while the M2 airfoil shows deteriorated performances compared to the baseline airfoil. Flow features impacting the airfoil performances are examined in detail.

The dissertation is dedicated to my parents

for their heartening support throughout my academic career.

CONTENTS

List of Figures

List of Tables

ACKNOWLEDGMENTS

I sincerely express my gratitude to everyone who has been supportive in fulfilling this thesis work. First, I thank the PhD program advisor, Prof. Seongkyu Lee, who guided me in the field of aeroacoustics. His enthusiastic working attitude has inspired me to study harder. His invaluable advice has polished my research work and fostered my tenacity and research skills. I cherish these as invaluable assets. Secondly, I would like to thank Prof. Cornelis van Dam and Prof. Stéphane Moreau for their time and efforts in serving on my thesis committee.

Throughout my research career, I am profoundly obligated to convey my appreciation to Prof. Damiano Casalino, Dr. Julian Winkler, and Prof. Jung-Hee Seo.

This exciting but uphill journey would not have been possible without my colleagues in Davis and Korea sharing constructive talks, traveling, and playing sports together. I especially thank Rui, Deniz, Hyunjune, Jack, Huy, Jordon, Henry, Kevin, Jared, and Jagdeep.

I endlessly thank my parents, who always give me good words and powerful encouragement with their love and wisdom.

Finally, I would like to acknowledge the support from the Joseph L. Steger Fellowship and Stanford University Center for Turbulence Research 2022 Summer Program Fellowship.

List of Symbols

Nomenclature

Acronyms

APSD	Auto power spectral density
CPSD	Cross power spectral density
DMD	Dynamic mode decomposition
FFT	Fast Fourier transform
LES	Large-eddy simulation
LSB	Laminar separation bubble
OASPL	Overall sound pressure level
PDF	Probability density function
PSD	Power spectral density
RANS	Reynolds-averaged Navier-Stokes
SGS	Subgrid scale
SPL	Sound pressure level
SPOD	Spectral proper orthogonal decomposition
SPSL	Sound pressure spectrum level
SVD	Singular value decomposition
WPS	Wall-pressure spectrum

Greek Symbols

α	Angle of attack, deg

γ^2	Coherence
δ_{ij}	Kronecker symbol
δ	Boundary-layer thickness, m
δ^*	Displacement thickness, m
Δt	Physical time step, s
$\Delta x^+, \Delta z^+$	Streamwise and spanwise grid spacings in wall units, respectively
ϵ	Exponential convergence factor
θ	Momentum thickness, m
λ_k	k-th discrete-time DMD eigenvalue
$\mathbf{\Lambda_{f_k}}$	Modal energies for the k-th discrete frequencies
ν	Kinematic viscosity, m^2/s
ρ_∞	Ambient density, kg/m^3
σ_k	k-th growth rate of $\mathbf{X}$
τ_w	Tangential shear stress at the wall, Pa
τ^*	Non-dimensional time step
ϕ	Azimuthal angle, deg
Φ_{pp}	Cross spectrum in the pressure field, Pa^2/Hz
ψ	Sweep angle, deg
Ψ	Mother wavelet
ω	Angular frequency, rad/s
ω_k	Angular frequency of k-th DMD mode, rad/s
$\mathbf{\Omega}$	Vector form of ω_k

Roman Symbols

$\mathbf{A}$	Best-fit linear operator
b_k	Initial amplitude of k-th DMD mode
$\mathbf{b}$	Vector form of b_k
c	Physical chord length, m
c_o	Speed of sound, m/s
C_f	Skin friction coefficient
C_p	Surface pressure coefficient
e	Internal energy, $\mathrm{m}^2/\mathrm{s}^2$
E^*	Complex error function
f	Frequency, Hz
f_k	Frequency of k-th DMD mode, Hz
f_s	Sampling frequency, Hz
g_o, g_s	Incident and scattered wall pressures
h_{TE}	Trailing-edge thickness, m
h^+	Stair strip height in wall units
H_{12}	Shape factor
k_x,k_z	Chordwise and spanwise convective wavenumbers
k	Turbulence kinetic energy, $\mathrm{m}^2/\mathrm{s}^2$
$\bar{k}$	Acoustic wavenumber
$\dot{l}_r$	Rate of change of the surface pressure, $\mathrm{N}/(\mathrm{s}\cdot\mathrm{m})$
M_r	Mach number in the sound radiation direction

p_∞	Ambient pressure, Pa
p	Static pressure, Pa
$p_L^{'}$	Loading noise, Pa
$\sqrt{\overline{p'^2}}$	Root-mean-square pressure, Pa
$\mathbf{P_Y}$	Filtered Fourier coefficient
q_∞	Dynamic pressure, Pa
r	Distance between the acoustic source and observer, m
R_{pp}	Cross-correlation function between two pressure signals
St	Strouhal number
TI	Turbulence intensity
u_k	k-th continuous-time DMD eigenvalue
u_τ	Friction velocity, m/s
U_c	Turbulence convection, m/s
U_∞	Freestream velocity, m/s
w_j	Hamming window function
$\mathbf{X}$	Time-resolved snapshots of the pressure field
y^+	Distance from the first grid cell to the surface in wall units
$\hat{Y}$	Filtering coefficient

Other Symbols

$\mathcal{F}[:]$	Fourier transform
$\mathcal{F}^{-1}[:]$	Inverse Fourier transform
$\mathcal{L}_o$, $\mathcal{L}_s$	Incident and scattered aeroacoustic transfer functions

Chapter 1

Introduction

In conjunction with collective efforts to enhance aerodynamic performance in the aviation industry, noise reduction is increasingly being recognized as a critical factor in the development of future transportation systems. In this thesis, detailed investigations of the flow physics of airfoil noise and its reduction are performed using high-fidelity numerical simulations. This chapter provides a concise background of the thesis and outlines the motivation for each topic. It also includes a comprehensive literature review, the objectives of the research, and an overview of the thesis structure.

1.1 Background and Motivation

As air transportation applications like air taxis and drones are projected to be more widespread in residential areas [1], it becomes increasingly crucial to address noise-related concerns associated with their use. For instance, the noise generated by air taxis can surpass ambient background sounds, such as community or highway noise [2, 3]. A difference in noise levels between air taxis and helicopters is less than 15 dB, which is Uber's suggested noise guideline for air taxi [4]. The noise emitted by these vehicles can arise from mechanical vibrations or the interaction of surfaces with air, with the latter referred to as aerodynamic noise. Aerodynamic noise encompasses both tonal and broadband noise. For example, the rotating motion of blades creates tonal noise characterized by periodic and impulsive pressure fluctuations. However, airfoil-self broadband noise is generated by the interaction between an airfoil and laminar or turbulent flows, resulting in a wide range of noise magnitudes across the spectrum. As illustrated in Fig. 1.1, five fundamental mechanisms for airfoil-self noise have been identified: laminar and turbulent boundary-layer noise, trailing-edge bluntness noise, separation-stall noise, and tip vortex noise [5]. Of these various noise source mechanisms, turbulent boundary-layer trailing-edge noise has received the most attention due to its dominant noise contribution in many cases [6–9] (as reviewed comprehensively by Lee et al. [10]). In recent studies [11, 12], the significance of airfoil trailing-edge noise is also highlighted for air taxi operations. This dissertation advances the fundamental understanding of the flow and acoustic physics of airfoil broadband noise and its mitigation.

High-fidelity numerical simulations provide a better understanding of flow physics and mechanisms. It has been extended to aeroacoustic problems where the requirement on the acoustic grid scale is more stringent than the aerodynamic grid scale [14]. Specifically, large-eddy simulations (LES) or direct numerical simulations (DNS) have been employed to predict airfoil noise [15–22]. The seminal study [15] significantly influenced the direction of research in trailing-edge noise prediction using LES with an acoustic analogy of Ffowcs Williams and Hall [23]. Recently, the analysis of noise sources and relevant flow fields using LES has been getting much attention as it is utilized to give insights into noise generation mechanisms and to exploit noise mitigation devices, including suction flow control [24], boundary-layer bumps [25], bio-inspired shapes [18, 26–28], and porous materials [29, 30].

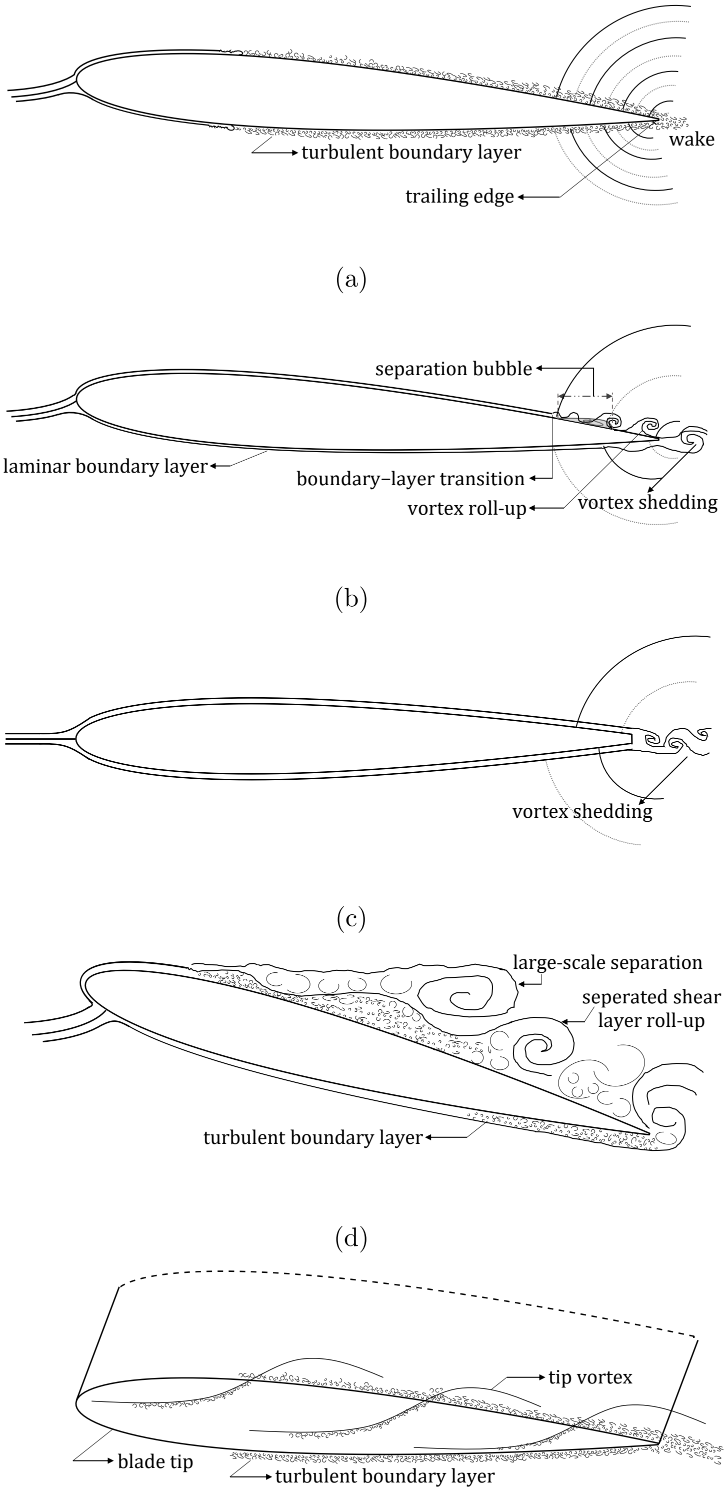

Figure 1.1: Airfoil noise generation and propagation [5, 13]: (a) turbulent-boundary-layer trailing-edge noise, (b) laminar-boundary-layer vortex-shedding noise, (c) trailing-edge bluntness vortex shedding noise, (d) separation-stall noise, and (e) tip vortex noise.

1.1.1 Challenges in Predicting and Understanding Airfoil Noise

One of the challenges in predicting airfoil noise is the fact that the numerical accuracy of these simulations relies on several factors, including grid resolution, time advancement, numerical scheme, and turbulence modeling [31, 32]. Insufficient grid resolution can result in unresolvable near-field noise sources, leading to the emergence of numerical spurious or background noise that may contaminate the physical noise in both near and far fields [33]. This obstructs the understanding of significant flow physics. The first motivation of the dissertation is to introduce the application of a novel approach, called wavelet-based decomposition, to a low-Mach number airfoil noise problem. The proposed method aims to identify and remove any background noise that may be present, whether it is of physical or numerical origin.

Although there have been significant strides in developing theories related to turbulent boundary-layer trailing-edge noise over several decades, with foundational works starting as early as the 1970s [6, 23, 34–36], it is challenging to separate pressure in compressible LES since the flow solutions inherently encompass both hydrodynamic pressure fluctuations and scattered acoustic pressures on the wall. Existing methodologies [37, 38] rest on exploring the difference in phase speeds associated with the hydrodynamic convection and the speed of sound of acoustic waves in the wavenumber-frequency domain. However, an enhanced understanding of the intricate contributions of hydrodynamic and acoustic pressures to far-field noise remains to be elucidated in the context of airfoil noise. The second part of the dissertation aims to bridge this gap through compressible LES, wavenumber-frequency Fourier filtering based on phase speed, and advanced time-frequency analysis methods.

Airfoil noise is influenced by the boundary-layer transition from laminar to turbulent flow, which is sensitive to various parameters, including pressure gradient, freestream turbulence, wall roughness, Mach number, wall suction or blowing, and wall heating or cooling [39]. These result in complex aeroacoustic mechanisms. Boundary-layer tripping is a classical approach to trigger the laminar-to-turbulent transition to match flow similarity between the scaled model and the full-scale model at different Reynolds numbers. Although far-field noise was reported to be sensitive to the types of tripping parameters [40], the lack of knowledge lies in the true origin of boundary-layer transition connecting with noise generation in turbulent boundary layer flows. In the third topic of the thesis, the effect of flow transition on airfoil noise for two different forced tripping methods with a natural transition case for comparison is given with detailed flow statistics associated with far-field acoustics at a non-zero angle of attack.

A visualization of flow and acoustic fields provides critical physical insights into understanding the generation and propagation of flow-induced noise sources. The conventional visualization methods, which will be surveyed in the next section, have strengths and limitations. In the fourth topic of the dissertation, a novel method for noise source identification and visualization is proposed using cross power spectral density. A thorough investigation of the new method is conducted by comparing it with conventional modal analysis methods, and its strengths and limitations are discussed. To deepen our understanding of noise generation and propagation mechanisms, this method is applied to the three distinct boundary-layer transition scenarios over an airfoil.

1.1.2 Strategies of Airfoil Noise Mitigation

Misaligned flow is observed in a variety of engineering and scientific applications, such as swept wings, saw-tooth shapes, and blades undergoing the Coriolis effect in rotational motion. Decades of research have demonstrated that turbofan engine noise [41–43] can be reduced through swept blade designs. Recently, the sweep angle has been adopted in the design of other engineering configurations to address high-frequency broadband noise [44–46]. Although previous works showed broadband noise reduction when the sweep angle was incorporated into the design criteria [45, 47], there has been little research on the fundamental flow physics to lead low efficiency of sound radiation of these configurations. The fifth topic is dedicated to focusing on misaligned flow physics to reveal noise reduction mechanisms through the modeling of an airfoil with a sweep angle.

The reduction of airfoil broadband noise through morphed strategies, often considered alongside their impact on aerodynamic performance, has been extensively studied through analytical [48, 49], numerical [50–52], and experimental approaches [53]. While the benefits of morphological shapes have catalyzed a plethora of studies in aerodynamics, aeroacoustics, and other multidisciplinary fields, there remains a notable gap in understanding the flow and acoustic interactions influenced by the morphed shape of an airfoil. Notably, much of the research on morphed airfoils has primarily focused on aerodynamics [53–55]. Motivated by the scarcity of comprehensive studies that address both the aerodynamic and aeroacoustic characteristics of morphed airfoils, the sixth topic of the dissertation seeks to explore the fundamental mechanisms through which the shape of morphed airfoils influences wall-bounded turbulent flows, sound propagation, and aerodynamic performance.

1.2 Literature Review

This section presents a literature review on six research topics related to airfoil noise prediction and mitigation, solidifying the motivation for each. The first four topics delineate previous works on predicting and understanding airfoil noise. The last two topics are dedicated to reducing airfoil noise through misaligned flow and trailing-edge morphing.

1.2.1 Wavelet-based Decomposition

The wavelet-based extraction method has been extensively utilized for the interpretation and analysis of turbulent flows [56–60]. This is because it can extract localized, nonlinear dynamical flow contributions involving shocks, flame fronts, and vortices from homogeneous, structureless, and uncorrelated components, thereby enabling the tracking of intrinsic structures in flows [61]. A coherent vortex extraction technique proposed by Farge et al. [62, 63] decomposes a vortical field into coherent vortices and Gaussian noise-like incoherent components. This algorithm consists of three procedures: decomposition, thresholding, and reconstruction. Significant findings from applying the wavelet-based denoising method to turbulent flows include the observation that only a few high-amplitude wavelet coefficients of coherent vortices can represent the energy-containing flow motions of turbulence, while the remaining incoherent parts are observed to possess the equipartition of energy in multiscale turbulence corresponding to white noise and can therefore be modeled statistically [56, 58, 63]. This wavelet-based denoising method generates denoised vortical flow fields and background noise. A collection of these early research papers [56, 58, 63–66] employing the wavelet-based denoising technique inspired us to seek a method to identify and eliminate background noise in airfoil noise simulations. The terminologies ‘coherent’ and ‘incoherent’ from these earlier papers will be adopted when discussing a similar wavelet decomposition algorithm. However, more precise wording for the context of airfoil noise application would be ‘denoised flow field’ and ‘background noise,’ respectively. These more precise terms will be introduced and justified later.

More recently, the wavelet-based separation method has been employed in the pressure field analysis of turbulent jet and landing gear subcomponent configurations [67–70]. In jet flows with Mach numbers of 0.6 and 0.9, the hypothesis for the decomposed components of the pressure field is that the coherent or hydrodynamic pressure, induced by localized coherent turbulent structures, dominates the low-frequency region of the spectrum. This consists of a few high-amplitude wavelet coefficients, while the incoherent or acoustic pressure, derived from the assumption of being Gaussian in nature, predominates at high frequencies [67, 71]. In these applications, the incoherent component, assumed to follow a Gaussian probability distribution, possesses physical acoustic characteristics in the pressure field and thus cannot be neglected or discarded as turbulent dissipation. This differs from earlier studies [56] that utilized a vorticity-based separation. Haczak et al. [68] applied wavelet separation techniques to the pressure field around a landing gear wheel modeled using the simplified geometry LAGOON [72] at a Mach number of 0.23. They found that the decomposed acoustic pressure, filtered through the wavelet-denoising method, shows different results from conventional Fourier-based filtering in the low-frequency region. The authors argued that the Gaussian probability assumption is insufficient for isolating acoustic pressure from hydrodynamic pressure. However, wavelet decompositions were applied to regions of low turbulence and non-uniform flow, where acoustic propagation is more prominent than turbulent hydrodynamic fluctuations. This makes the Fourier filtering, based on phase velocities, inaccurate or difficult to compare against wavelet-denoising filtering.

1.2.2 Pressure Decomposition into Hydrodynamic and Acoustic Components

Analytical understanding of acoustic scattering of turbulence isolated from the original pressure was studied by Ffowcs Willams and Hall [23]. The fundamental principle was integrating the rigid half-plane Green's function with volumetric sources that depict wake velocity statistics in Lighthill's equations [73]. Meng et al. [74] applied a finite-chord correction to Ffowcs Willams and Hall's theory, showing the improvement of far-field noise predictions compared to the experiment. Following this, there were augmentations to the model, accounting for both the finite chord length [75] and airfoil thickness [76]. With the incorporation of the finite-chord correction factor in Howe's model [75]—taking into account the multiple scattering events at the airfoil's leading and trailing edges—the precision of predictions for the far-field sound spectrum notably improved. Howe [36] further contributed with an asymptotic theory, wherein the scattering is characterized using the Wiener-Hopf method iteratively, with a dipole source defined by the wall pressure spectrum and spanwise correlation length. Parallelly, Amiet [6, 34, 35] derived an aeroacoustic transfer function, based on the Schwarzschild solution to handle the scattering effect. Amiet combined this aeroacoustic transfer function with acoustic sources near the trailing edge such as spanwise correlation length and wall pressure spectrum to determine the acoustic power spectral density. However, the theory rests on several assumptions, such as the exponential decay of incident pressure from the trailing edge to the leading edge, frozen turbulence [77], an infinitely long span, and a flat plate at zero incidence. Yet, despite such oversimplifications, the introduction of an advanced empirical wall pressure spectrum model [78] to Amiet's model has led to favorable outcomes for airfoil and rotor broadband noise predictions [79, 80]. This groundwork has facilitated successive refinements like factoring in leading-edge backscattering [81] and accounting for the airfoil camber and thickness [82]. While several researchers [83–86] as well as Amiet himself [35] have delved into examining the relative contributions of these pressures, the intricate physical dynamics underlying how each pressure distinctly contributes to the far-field noise warrants deeper exploration.

In numerical simulations, one can independently compute noise originating from both the incident and scattered pressures in conjunction with acoustic scattering solvers, such as the finite element method (FEM) or the boundary element method (BEM), along with an acoustic analogy. Oberai et al. [83] addressed the computation of trailing-edge noise through the variational formulation of Lighthill's acoustic analogies [73] using the FEM. They distinguished sound sources into incident and scattered fields. The incident field is either modeled as a basic quadrupole source or derived from Lighthill's turbulence tensor in free space. Conversely, the scattered field is computed by subtracting the incident contribution from the total pressure. Their observations revealed that the scattered component influences the directional attributes of the total pressure throughout the entire frequency spectrum. They noted that the resultant scattered sound retains a dipole pattern at low frequencies, corroborated by Curle's solution [87]. Moreover, the peak noise level in terms of directivity tends to lean upstream as the frequency increases. At high frequencies, additional lobes emerge in the dipole pattern due to scattering by wavelengths smaller than the airfoil chord length and the chord's finite nature. Consistent findings were reported by Martínez-Lera et al. [85, 86]. They used the FEM along with Lighthill's formulation, and their results indicated that the primary noise source emanating from the airfoil results from the scattering effect, with the incident field playing a minimal role. On another note, Khalighi et al. [84] used the BEM to solve Lighthill's equation in the presence of a body. Their most salient observation is the dominance of the scattering effect at high frequencies, contrasting it with sounds solely emanating from hydrodynamic sources on the wall.

1.2.3 Effect of Boundary-layer Tripping on Airfoil Noise

Boundary-layer tripping is used to ensure flow similarity between small-scale models and full-scale prototypes at varying Reynolds numbers [88, 89]. This is accomplished through forced boundary-layer transition, independent of local free-stream velocity [90]. For aerodynamic and aeroacoustic measurements in wind tunnel tests, several tripping methods are commonly employed, including trip wires [91], zigzags or serrations [92], surface roughness elements, and the more recently proposed sharkskin-like surface roughness [40, 93, 94]. These devices induce transition onset through high-intensity velocity fluctuations in the spanwise direction [92]. However, it has been reported that far-field noise is sensitive to the types of trips used: low-frequency noise increases due to the trip effects on trailing edge wall pressure fluctuations, while high-frequency noise increases because of noise generated by the trip itself [40]. Additionally, grid roughness elements were found to be less effective in promoting transition at speeds below the Reynolds number based on the distance of tripping from the leading edge of $\mathrm{Re}_{\mathrm{tr}} = 5.3 \times 10^4$ compared to zigzag types, with an underpredicted intermittency factor near the wake. This directly impacts far-field noise measurement, resulting in a maximum discrepancy of 3 dB between the two trip types [92]. Consequently, obtaining consistent data is challenging due to uncertain boundary-layer tripping parameters and varying flow conditions.

In numerical approaches, there was an attempt to employ stochastic sand grain roughness to simulate a realistic tripping configuration [95]. However, artificial tripping is more often employed to circumvent the complexities associated with randomly distributed surface grit or geometrically resolved ones. Examples of such techniques include suction and blowing [17, 96] and high-frequency unsteady tangential reverse blowing [18, 97]. Wolf and Lele [17, 96] applied the suction and blowing method on the suction side of a NACA 0012 airfoil, successfully predicting far-field acoustic pressure spectra with good agreement to experimental measurements [5]. Concurrently, Bodling and Sharma [97] investigated two different tripping models using compressible LES for a NACA 0012 airfoil, which included a geometrically resolved trip and an artificially modeled tangential reverse blowing trip. They found that the trip wire generated extraneous high-frequency noise when the permeable data surface encompassed the wave propagation from the trip wire. The reverse blowing method, however, produced minimal noise from the trip region [97]. More recently, Winkler et al. [98] conducted a comprehensive examination of tripping models both experimentally and numerically to explore wall-pressure evolution and acoustic predictions for a NACA 6512-63 airfoil at zero incidence. The wall-pressure spectra revealed that the serrated trip effectively modeled the tripping effect, showing broadband humps at specific frequencies consistent with experimental data. Furthermore, they discovered that the thickness effect of the boundary-layer trip led to a gradual decrease in broadband far-field noise, making the magnitude of trailing-edge broadband noise dependent on both trip thickness and trip models.

1.2.4 Visualization of Acoustic Source and Propagation

A visualization of flow and acoustic fields deepens our understanding of the generation and propagation of flow-induced noise sources. Three approaches are often employed to identify and visualize noise generation and propagation. The first method utilizes the dilatation parameter, which associates pressure perturbation with the divergence of velocity [99]. This allows for the detection of sound propagation originating from noise sources. However, the shortcoming of this method arises when time-domain pressure fluctuations are primarily dominated by strong acoustic waves like low-frequency tonal noise. This causes high-frequency, low-amplitude perturbations to be often masked by those dominant waves. Thus, the acoustic waveforms across a broad frequency range can make it challenging to interpret the acoustics related to a specific frequency range of interest.

The second approach involves using the Fourier transform for either band-pass filtering of the time-domain pressure field or calculating pressure spectra. For the band-pass filtered pressure field, Fourier coefficients of pressure within the desired frequency range are filtered and then transformed back to the time domain. This effectively highlights the dominant sound waves that emerge from specific flow structures at certain frequencies. One distinct advantage of this method is its simplicity in data processing such that it does not require manipulating massive data matrices. Turner and Kim [19] applied this approach to observe the multiple generations of noise produced by the separated shear flows at mid-frequency and the formation and subsequent breakdown of Kelvin-Helmholtz vortices at high frequencies. While the band-pass filtered pressure can illustrate the propagation and interaction of acoustic waves, acquiring detailed information regarding the spectral magnitude of both hydrodynamic sources and acoustic waves can prove challenging. Jones et al. [100] converted the pressure field from the time domain to the Fourier domain using one-third-octave averaging centered on frequencies of interest. They visualized the propagation pattern through contours of auto power spectral densities or the real part of the acoustic pressure around the airfoil. However, this approach limits the identification of both hydrodynamic convection and acoustic propagation, as the spectral energies of the hydrodynamic component are significantly higher than those of the acoustic component. Therefore, hydrodynamic pressure, dominated by turbulent flows near the wall, was simply hidden from the flow snapshots to emphasize the acoustic propagation [100].

The third approach for identifying noise sources and propagation is rooted in modal analysis. This method is often referred to as a data-driven approach. These methods can distill physically important flow structures related to the problem of interest [101]. An overview of several such data-driven techniques is listed in Ref. [102]. Among them, modal analyses incorporating spectral proper orthogonal decomposition (SPOD) [103–105] and dynamic mode decomposition (DMD) [106–108] have been frequently used as the initial step in investigating a variety of engineering problems. Sano et al. [109] employed SPOD modes on the pressure field to examine the turbulent boundary-layer trailing-edge noise, revealing the relationship between the large-scale flow structures, the high-energy frequency content of the flow, and the sound propagation of turbulent coherent structures. Similarly, Hu et al. [110] illuminated the effect of serration on noise reduction in airfoil configurations using DMD modes, showcasing the spanwise incoherence in the serrated case at peak energy frequencies. This demonstrates the diverse ways in which the DMD method can be adapted to enhance our understanding of airfoil noise. While these data-based approaches are specialized in isolating essential coherent structures linked to physically important flows, some difficulties are faced when dealing with high-dimensional data. It often faces prohibitive memory requirements, especially for visualizing high-dimensional spaces such as the handling of data matrices with the billion order of magnitude in the full-scale aircraft configuration [111]. This remains a challenge despite the ongoing efforts to develop new data-driven methodologies [112].

1.2.5 Airfoil Noise Mitigation through Misaligned Flow

While the use of sweep angle has been widespread for turbofan engine noise reduction over several decades [41–43], it has also been adopted in fan, propeller, and open rotors where the high-frequency broadband noise is significant [44–46]. The application of the sweep angle to Amiet's theories on broadband noise has been recently explored by Giez et al. [113] and Grasso et al. [45, 47], respectively. These studies incorporated the sweep angle into the radiation integral, taking into account both streamwise and spanwise wavenumbers. For trailing-edge scattering by the swept airfoil, the generalized Corcos' model [114] was used to consider the effect of spanwise wavenumbers on the correlation length. However, the trailing-edge pressure spectrum was obtained from the empirical modeling, neglecting the sweep angle effect. Amiet's leading-edge noise model, modified to include the sweep angle, was found to align with measurements [113], consistently showing reduced sound spectra across the entire frequency range. Zarri et al. [115] employed these leading-edge and trailing-edge analytical formulations in conjunction with steady-state numerical simulation to develop multi-fidelity fan-broadband noise prediction models. The authors emphasized the importance of considering sweep-angle effects for accurate noise predictions. In the meantime, an example of using high-fidelity simulations of swept fan blades is found in Ref. [46], where the Lattice Boltzmann Method (LBM) [116] is employed to study the effect of sweep angle on axial-fan noise. Notable findings were the noise reduction at low-frequency subharmonics with the forward-swept blade, which efficiently alleviated tip flows, aligning with previous observations [117]. An experimental study for the swept fan blade showcased a noticeable reduction in sound spectra compared to the straight fan blade [44, 117]. Nevertheless, a comprehensive understanding of the favorable impact of the sweep angle on sound radiation is still lacking.

1.2.6 Airfoil Noise Mitigation through Trailing-edge Morphing

Over the decades, constant efforts have been made to reduce noise through morphed strategies [48–52]. Morphological adaptations may involve not only adjustments in chord, span, and sweep angle but also out-of-plane transformations characterized by bending and twisting [118, 119]. In this work, morphing specifically refers to adjustments in airfoil profiles [118]. Furthermore, our focus is on the analysis of rigid-static morphed airfoil profiles without considering dynamic motion or structural deformation.

Trailing-edge noise is significantly influenced by the shape of the airfoil near the trailing edge, including the wedge angle. Recently, Spiropoulos et al. [49] presented a study on far-field sound reduction using wedge angles, employing a combined analytical modeling approach that incorporates scattering effects [34] and vortex sound sources with vorticity spectrum [120]. Their study showed that the wide wedge angle reduces noise. However, their results did not consider the flow field, which might induce periodic shedding as noise sources—a limitation acknowledged by the authors [49]. In a related approach, the concept of a wedge angle was incorporated into airfoil parameterization as a boat-tail angle, as proposed by Lim [121]. Building on this idea, Liu and Lee [122] integrated this airfoil parameterization method with low-fidelity tools such as XFOIL [123] and a semi-empirical wall-pressure spectrum model [78], alongside Howe's diffraction theory [124], to address trailing-edge noise. Their findings suggested that employing a negative boat-tail angle, which results in a concave airfoil shape, holds promise for reducing overall sound pressure levels while simultaneously improving lift and lift-to-drag ratios. However, the potential noise reduction benefits were not extensively explored in all observer directions, and the authors noted that prediction accuracy is particularly sensitive and uncertain in conditions of highly separated flows.

1.3 Research Objective

The primary objective of the thesis is to predict airfoil noise and advance our understanding of noise generation and propagation mechanisms using high-fidelity large-eddy simulations and physics-informed analytical theories. Another purpose is to mitigate airfoil noise and reveal the noise reduction mechanism. Thus, the specific goals of the thesis are delineated within the two frameworks.

1.3.1 Airfoil Noise Prediction

- Identify and eliminate numerical or background noise using the wavelet denoising algorithm to keep track of the true physics of noise source and propagation.
- Decompose the pressure into hydrodynamic (incident) and acoustic (scattered) components to delineate the complexity of trailing-edge noise generation and propagation.
- Analyze the aerodynamic and aeroacoustic effects of flow transition on airfoil noise with different boundary-layer tripping models.
- Propose a novel method based on cross power spectral density to visualize sound generation and propagation.

1.3.2 Airfoil Noise Mitigation

- Deepen our understanding of the noise reduction mechanism of swept airfoil, focusing on misaligned flow physics.
- Investigate the aerodynamic and aeroacoustic performances of morphed airfoils.

1.4 Outline of the Dissertation

The thesis is structured with seven chapters, which are outlined as follows:

- Chapter 1 presents the research background and motivation for airfoil noise prediction and mitigation. The literature review entails the previous works relevant to airfoil noise prediction and mitigation. Lastly, the research objective of the thesis is described.
- Chapter 2 details the computational methodology, encompassing large-eddy simulations, aeroacoustic analogy, pressure decomposition, modal analysis, and cross-spectrum method. The validation results of flow and acoustic codes are subsequently provided.
- Chapter 3 presents the results of pressure decomposition, which are subdivided into two sections. Section 3.1 describes the wavelet-based pressure decomposition, while Section 3.2 discusses the Fourier-based pressure decomposition.
- Chapter 4 addresses the effect of boundary-layer tripping on airfoil noise.
- Chapter 5 proposes the cross-spectrum method and assesses its ability for acoustic source identification and visualization.
- Chapter 6 entails the research results of airfoil noise mitigation, which are subdivided into two sections. Section 6.1 displays the results of the sweep angle effect with misaligned flow, whereas Section 6.2 gives the results of the trailing-edge morphing effect.
- Chapter 7 concludes the thesis with summaries of the six independent research works, contributions, recommendations for future work, and a list of publications.

Chapter 2

Computational Methodology

2.1 Large-Eddy Simulations

2.1.1 Governing Equations and Numerical Methods

The equations governing the large-scale motions of compressible flows can be formulated using Favre-filtered quantities, as outlined in previous studies [125–127]. In the following, the operator symbols $\bar{\cdot}$ and $\tilde{\cdot}$ are employed to denote the Reynolds and Favre averages, respectively, following the notation introduced by Favre [128]. These equations encompass the continuity, momentum, and total energy equations, which are expressed as follows:

$$\frac{\partial \bar{\rho}}{\partial t} + \frac{\partial}{\partial x_j}(\bar{\rho}\tilde{v}_j) = 0, \tag{2.1}$$

$$\frac{\partial \bar{\rho}\tilde{v}_i}{\partial t} + \frac{\partial}{\partial x_j}(\bar{\rho}\tilde{v}_j\tilde{v}_i) = -\frac{\partial \bar{p}}{\partial x_i} + \frac{\partial \tilde{\sigma}_{ij}}{\partial x_j} - \frac{\partial \tau_{ij}^{sgs}}{\partial x_j}, \tag{2.2}$$

$$\frac{\partial \bar{\rho}\tilde{E}}{\partial t} + \frac{\partial}{\partial x_j}(\bar{\rho}\tilde{v}_j\tilde{H}) = \frac{\partial}{\partial x_j}\left(\tilde{v}_i\tilde{\sigma}_{ij}\right) + \frac{\partial}{\partial x_j}\left(\tilde{k}\frac{\partial \tilde{T}}{\partial x_j}\right) - \frac{\partial}{\partial x_j}\left(\tilde{v}_i\tau_{ij}^{sgs}\right) - \frac{\partial q_j^{sgs}}{\partial x_j}, \tag{2.3}$$

where $\bar{\rho}$, $\tilde{v}_i$, $\tilde{E}$, $\tilde{H}$, $\tilde{T}$, $\tilde{k}$ are the filtered density, filtered velocity components in the i-th direction, filtered total energy $\tilde{e} + \tilde{v}_k \cdot \tilde{v}_k/2$, filtered total enthalpy $\tilde{E} + \bar{p}/\bar{\rho}$, filtered temperature, and filtered thermal conductivity. Here, $\tilde{e}$, $\bar{p}$ are the filtered internal energy and filtered pressure, respectively. τ_{ij}^{sgs} is the Favre-averaged subgrid-scale (SGS) stress tensor denoted as $\bar{\rho}(\widetilde{v_i v_j} - \tilde{v}_i \tilde{v}_j)$ while q_j^{sgs} is the SGS heat flux denoted as $\bar{\rho}(\widetilde{e v_j} - \tilde{e}\tilde{v}_j)$. $\tilde{S}_{ij}$ denotes the rate of strain tensor of the resolved flow field, which is defined as

$$\tilde{S}_{ij} = \frac{1}{2}\left(\frac{\partial \tilde{v}_i}{\partial x_j} + \frac{\partial \tilde{v}_j}{\partial x_i}\right). \tag{2.4}$$

$\tilde{\sigma}_{ij}$ is the shear-stress tensor of the resolved flow field, which is defined as

$$\tilde{\sigma}_{ij} = 2\tilde{\mu}\left(\tilde{S}_{ij} - \frac{1}{3}\tilde{S}_{kk}\delta_{ij}\right), \tag{2.5}$$

where $\tilde{\mu}$, δ_{ij} are the filtered dynamic viscosity and Kronecker symbol, respectively. Both SGS components, τ_{ij}^{sgs} and q_j^{sgs}, must be modeled, the former being determined based on the deviatoric stress tensor for the eddy viscosity assumption:

$$\tau_{ij}^{sgs} - \frac{1}{3}\tau_{kk}^{sgs}\delta_{ij} = -2\bar{\rho}\nu_T\left(\tilde{S}_{ij} - \frac{1}{3}\tilde{S}_{kk}\delta_{ij}\right), \tag{2.6}$$

where ν_T stands for the turbulent eddy viscosity. This relates the SGS stress tensor to the turbulent eddy viscosity and the rate of strain tensor. Likewise, the SGS heat flux q_j^{sgs} can be associated with the turbulent eddy viscosity as $q_j^{sgs} = -\frac{\bar{\rho}\nu_T C_p}{\mathrm{Pr}_t}\frac{\partial \tilde{T}}{\partial x_j}$ where C_p is the specific heat at constant pressure, and Pr_t is the SGS turbulent Prandtl number equal to 0.85, which is the ratio of the turbulent eddy viscosity to the thermal diffusivity, thus being determined by calculating ν_T [125]. In this thesis, the turbulent eddy viscosity ν_T is determined by the wall-adapting local eddy-viscosity (WALE) [129] model defined as

$$\nu_T = (C_w\Delta)^2 \frac{\left(S_{ij}^d S_{ij}^d\right)^{3/2}}{\left(\tilde{S}_{ij}\tilde{S}_{ij}\right)^{5/2} + \left(S_{ij}^d S_{ij}^d\right)^{5/4}}, \tag{2.7}$$

where C_w is specified as 0.325, Δ is the filter width defined as $(\Delta_x, \Delta_y, \Delta_z)^{1/3}$, and S_{ij}^d is defined as

$$S_{ij}^d = \frac{1}{2}\left(\left(\frac{\partial \tilde{v}_i}{\partial x_j}\right)^2 + \left(\frac{\partial \tilde{v}_j}{\partial x_i}\right)^2\right) - \frac{1}{3}\delta_{ij}\left(\frac{\partial \tilde{v}_k}{\partial x_k}\right)^2. \tag{2.8}$$

In the simulations of compressible turbulent flows, the rhoPimpleFoam solver is employed, which represents a density-based PIMPLE (Pressure Implicit with the Splitting of Operator combined with Semi-Implicit Method for Pressure-Linked Equations) algorithm [130]. The computational domain is discretized using the finite volume method. Spatial variables are discretized with second-order accuracy, utilizing the Gauss linear scheme, while temporal variables are discretized using the backward-differencing scheme. The initial flow field for LES is derived from a steady-state Reynolds-averaged Navier-Stokes (RANS) simulation. In this RANS simulation, the $k - \omega$ shear stress transport model proposed by Menter [131] is employed as a closure model. To ensure temporal accuracy, time-accurate simulations are conducted with a non-dimensional time step denoted as τ^*, which is selected as 1.133×10^{-3} and expressed as $\Delta t c_o / l$. Here, Δt, c_o, and l represent the physical time step, speed of sound, and characteristic length, respectively. The simulations progress in time while maintaining a Courant-Friedrichs-Lewy (CFL) number of less than 0.9. The total duration of the LES corresponds to 20 airfoil flow-through times (FTT). Spectral analyses are conducted using numerical data collected at intervals of 1/3000 FTT during the final 10 FTT, where flow statistics have reached convergence.

2.1.2 Boundary Conditions and Grid Topology

The computational domain and boundary conditions surrounding a NACA 0012 airfoil with a blunt trailing edge configuration are illustrated in Fig. 2.1. An angle of attack α varies on the $x-y$ plane. To implement the swept airfoil, the freestream is rotated by a sweep angle ψ on the $x-z$ plane. This methodology aligns with numerical modeling strategies used to study dynamic stall in swept airfoils [132]. The trailing-edge bluntness, denoted as h_{TE}/δ^* and defined as the ratio of the trailing-edge thickness (h_{TE}) to the displacement thickness (δ^*) calculated at $x/c \approx 0.99$, is determined to be 0.5. An O-type two-dimensional computational domain with a radius of $8.0c$ is modeled, where c represents the airfoil chord length. This domain extends by $0.1c$ in the spanwise direction, and periodic boundary conditions are applied to the two O-type planes to facilitate three-dimensional simulations. This spanwise size showed the rapid decay of spanwise coherence in a statistical sense, which suffices to simulate the noise sources [96]. The airfoil itself is equipped with a no-slip wall boundary condition,

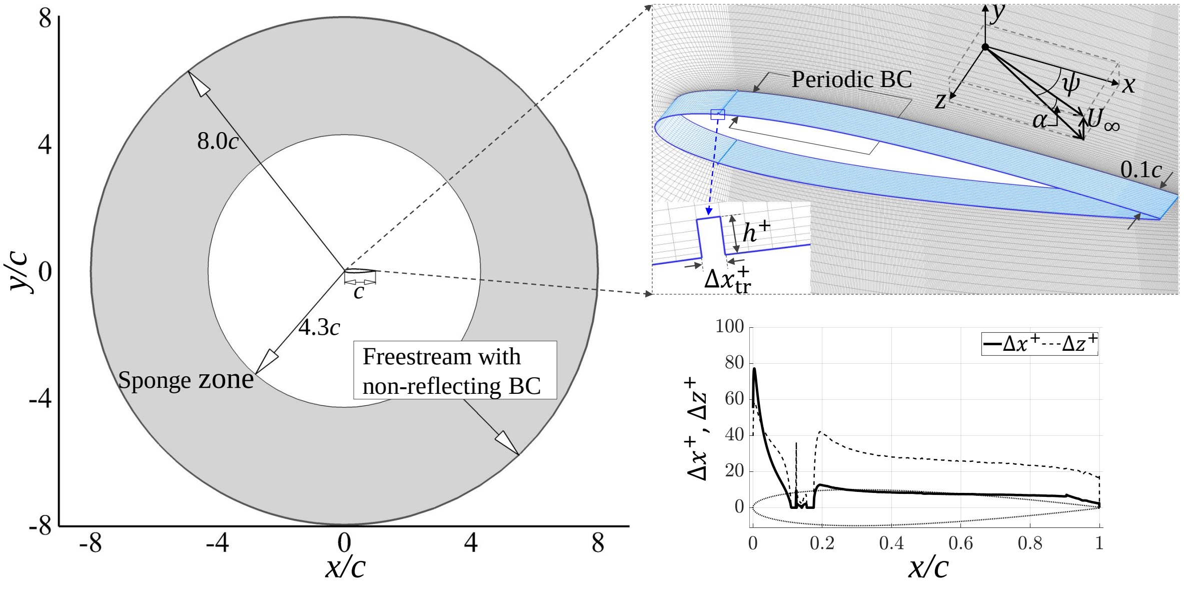

Figure 2.1: Boundary conditions over the computational domain.

while the freestream boundary encompasses the outer edge of the computational domain. To mitigate acoustic perturbations within the finite computational domain, a non-reflecting boundary condition is implemented alongside the freestream boundary [133]. Additionally, a sponge zone is introduced, consisting of a concentric circle with a radius spanning from $4.3c$ to $8.0c$. The acoustic damping source term is added to the compressible momentum equation as follows:

$$S_m = -F_D \mathbf{u}, \tag{2.9}$$

where $\mathbf{u}$ is the reference velocity field and F_D is the damping coefficient defined as

$$F_D = wfF_B, \tag{2.10}$$

where w, f, F_B are the stencil width equal to 20, frequency, and blending factor, respectively. The blending factor creates a profile for the damping zone with a smooth transition between $4.3c$ to $8.0c$ using the trigonometric function:

$$F_B = 1 - \cos\left(\pi\left(\frac{r - r_1}{r_2 - r_1}\right)\right), \tag{2.11}$$

where r_1 and r_2 are $4.3c$ to $8.0c$, respectively. This sponge zone is designed to dampen acoustic disturbances. To induce turbulent flows downstream, a boundary layer is tripped using a squared trip dot positioned at 12.5% of the airfoil's leading edge on both sides. The width and height of tripping consisting of multiple grid points are $\Delta x_{\mathrm{tr}}^{+} \approx 42.45$ and $h^{+} \approx 70.75$ in wall units where $\Delta x_{\mathrm{tr}}^{+} = \Delta x_{\mathrm{tr}} u_\tau/\nu$ and $h^{+} = h u_\tau/\nu$. Here, u_τ represents the friction velocity, and ν denotes the kinematic viscosity. This grid sizing corresponds to numerical modeling used in Chapter 6.1. The tripping sizes and flow conditions in each chapter are summarized in Table 2.1.

Table 2.1: Tripping sizes and flow conditions in each chapter.

Chapter	$\Delta x_{\mathrm{tr}}/c$	h/c	Re	M	$\alpha(^\circ)$	$\psi(^\circ)$
3.1 & 3.2	0.0015	0.0015	4×10^5	0.058	0	0
4 & 5	0.0015	0.0015	4×10^5	0.058	6.25	0
6.1	0.0018	0.003	4×10^5	0.058	0	0, 30 & 45
6.2	0.0018	0.0022	6×10^5	0.088	0 & 4	0

This tripping size is found to be enough to transition from laminar to turbulent flows, which will be shown in the flow field later. An overview of the grid topology within the computational domain is also provided in Fig. 2.1. The structured meshes are visible near the airfoil and on the wall. The grid dimensions are specified as $N_x \times N_y \times N_z = 4538 \times 323 \times 65$ in the streamwise, normal, and spanwise directions, respectively, resulting in an approximate total cell count of 90 million. Notably, the grid resolution on the upper side is the same as that on the lower side of the airfoil. Mesh refinement is evident near the trailing edge, a crucial aspect for accurately resolving acoustic sources and scattering at this location. To quantify the grid size, it is depicted as grid spacing normalized by the viscous length scale, denoted as $\Delta x^+ = \Delta x u_\tau/\nu$ and $\Delta z^+ = \Delta z u_\tau/\nu$. The results indicate that Δx^+ remains below 20, while Δz^+ is less than 40 around the stair strip, where the laminar-to-turbulent transition initiates. Additionally, the average value of the first cell height y^+ along the airfoil surface is less than 0.5. Therefore, the current grid resolution aligns with the criteria for grid size in wall-resolved LES as outlined by Georgiadis et al. [134].

2.2 Aeroacoustic Analogy

2.2.1 Ffowcs Williams and Hawkings Acoustic Analogy

The calculation of sound radiation is carried out using Farassat's Formulation 1A [135], which involves solving the integral formulation of the Ffowcs Williams-Hawkings (FW-H) equation [136]. This computational process is implemented in the PSU-WOPWOP code [137, 138]. Pressure fluctuations occurring on the surface of the airfoil are extracted to calculate the loading noise. In the case of low-speed Mach numbers, the analysis excludes considerations for thickness noise and the quadrupole source term within the FW-H equation. The sets of equations representing Farassat's Formulation 1A for thickness noise and loading noise are as follows:

$$p'(\mathbf{x},t) = p'_T(\mathbf{x},t) + p'_L(\mathbf{x},t), \tag{2.12}$$

$$4\pi p'_T(\mathbf{x},t) = \int_{f=0} \left[\frac{\rho_\infty(\dot{v}_n + v_{\dot{n}})}{r|1-M_r|^2}\right]_{\mathrm{ret}} \mathrm{d}S + \int_{f=0} \left[\frac{\rho_\infty v_n(r\dot{M}_r + c(M_r - M^2))}{r^2|1-M_r|^3}\right]_{\mathrm{ret}} \mathrm{d}S, \tag{2.13}$$

$$\begin{aligned} 4\pi p'_L(\mathbf{x},t) = {} & \frac{1}{c}\int_{f=0} \left[\frac{\dot{l}_r}{r|1-M_r|^2}\right]_{\mathrm{ret}} \mathrm{d}S + \int_{f=0} \left[\frac{l_r - l_M}{r^2|1-M_r|^2}\right]_{\mathrm{ret}} \mathrm{d}S \\ & + \frac{1}{c}\int_{f=0} \left[\frac{l_r(r\dot{M}_r + c(M_r - M^2))}{r^2|1-M_r|^3}\right]_{\mathrm{ret}} \mathrm{d}S, \end{aligned} \tag{2.14}$$

where ρ_∞, v_n, M_r, $1/|1-M_r|$, r, $\dot{l}_r$, $f=0$ are the freestream density, velocity in the surface normal direction, source Mach number in the sound radiation direction, Doppler amplification factor, relative distance between the source and an observer, rate of change of the surface pressure, and acoustic data surface, respectively. The thickness noise is not considered since the magnitude is negligible in the present low-speed flow condition. It is important to note that the receivers move at the same speed as the airfoil within a stationary medium. This scenario can be likened to an acoustic field in a wind tunnel, where both the airfoil and observers remain stationary in a medium that is in motion.

2.2.2 Amiet's Trailing-edge Noise Theory with a Sweep Angle

Amiet [6, 34, 35] developed a model for trailing-edge noise in uniform flow, U_∞, considering a flat plate or a thin airfoil within a source coordinate system (X, Y, Z). Each axis coordinate is normalized by b, which is half the chord length, such that $X = x/b$, $Y = y/b$, and $Z = z/b$, oriented in the streamwise, lateral, and wall-normal directions as shown in Fig. 2.2. Grasso et al. [45] introduced the sweep angle, ψ, to the convective wave equation, which is reformulated in the normalized transformed source coordinate, $(X^{'}, Y^{'}, Z)$ where $X^{'} = x^{'}/b$, $Y^{'} = y^{'}\beta_x/b$, $Z = z\beta_x/b$, $\beta_x = \sqrt{1 - M_x^2}$, and $M_x = M\cos(\psi)$ with $M = U_\infty/c_o$. Here, c_o is the speed of sound. The schematic of the swept airfoil's source and observer coordinate systems is displayed in Fig. 2.2. In the figure, the airfoil streamwise extends from $-2b$ to 0, and the origin of the source coordinate is at the trailing edge and midspan. As the swept airfoil has the shape of a parallelogram, the integral along the transposed source coordinate can be performed in the non-Cartesian reference frame (ξ, η) as $x^{'} = \xi\cos(\psi)$ and $y^{'} = \eta + \xi\sin(\psi)$. The incident pressure field upstream of the trailing edge in the frequency domain is represented as follows:

$$g_o(\bar{k}_x^{'}, X^{'}, Y^{'}) = \mathrm{e}^{-\mathrm{i}(\alpha\bar{k}_x^{'}X^{'} + \bar{K}_2Y^{'}) + \epsilon\alpha\bar{K}X^{'}}, \tag{2.15}$$

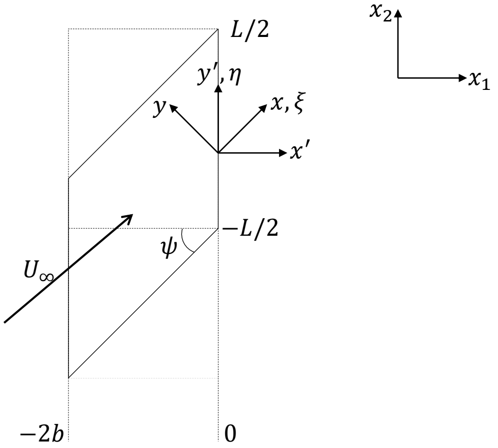

Figure 2.2: Source and observer coordinate systems for the swept airfoil [45].

where $\alpha = U_c/U_\infty$, $\bar{k}_x' = b\omega/U_\infty \cos(\psi)$, and $\bar{K}_2 = b\omega y'/(c_o S_0)$. Here, S_0 is defined as

$$S_0 = \sqrt{\beta_y^2 x_1^2 + \beta_x^2 x_2^2 + \beta_0^2 x_3^2}, \tag{2.16}$$

where $\alpha = U_c/U_\infty$, $\bar{k}_x' = b\omega/U_\infty \cos(\psi)$, and $\bar{K}_2 = b\omega y'/(c_o S_0)$. Here, S_0 is $\sqrt{\beta_y^2 x_1^2 + \beta_x^2 x_2^2 + \beta_0^2 x_3^2}$ for the observer located at (x_1, x_2, x_3), $\beta_0^2 = 1 - M^2$, $\beta_y^2 = 1 - M_y^2$, $M_y = M\sin(\psi)$, and ω is the angular frequency. The parameter U_c is the turbulence convection velocity, approximately $0.8U_\infty$. $\bar{K}_2 = 0$ because noise is computed at midspan. The parameter ϵ is used as an exponential convergence factor, designed to maintain the incident pressure at the trailing edge while causing it to exponentially diminish towards the leading edge [35, 139]. In this context, the value of the exponential convergence factor ϵ is set to 0.01 [140]. Importantly, the ultimate solution produced by Amiet's model is not significantly affected by the specific choice of this value. The scattered pressure is determined using Schwarzschild's solution, which satisfies the Kutta condition, and it is expressed as follows:

$$g_s(\bar{k}_x', \bar{k}_y', X') = \mathrm{e}^{-\mathrm{i}\alpha\bar{k}_x' X'}[(1+\mathrm{i})E^*(-[\alpha\bar{k}_x' + \bar{\kappa} + M\bar{\mu}]X') - 1], \tag{2.17}$$

where E^* is the complex error function defined as:

$$E^*(x) = \int_0^x \frac{\mathrm{e}^{-\mathrm{i}t}}{\sqrt{2\pi t}}\mathrm{d}t = C_2(x) - \mathrm{i}S_2(x). \tag{2.18}$$

In this equation, C_2 and S_2 are Fresnel integrals [141]. Here, $\bar{\kappa}^2 = \bar{\mu}^2 - \frac{\bar{k}_y'^2}{\beta_x^2}$ with $\bar{\mu} = \bar{k}_x' M_x/\beta_x^2$ and $\bar{k}_y' = \sin(\psi)k_x b$.

2.2.2.1 Aeroacoustic Transfer Functions

The aeroacoustic transfer function is derived by integrating the incident pressure and the scattered pressure from the leading edge to the trailing edge, utilizing the following equation:

$$\mathcal{L}(\bar{k}_x', \bar{k}_y', \vec{x}) = \int_{-2}^{0} g(\bar{k}_x', \bar{k}_y', \bar{\xi})\mathrm{e}^{-\mathrm{i}\bar{\mu}\left(C-\alpha\bar{k}_x'\right)\bar{\xi}\cos(\psi)}\,\mathrm{d}\bar{\xi}, \tag{2.19}$$

where $\vec{x}$ denotes the vector of the observer coordinate system.

The aeroacoustic transfer function for the incident pressure is given by

$$\mathcal{L}_o(\bar{k}_x', \bar{k}_y', \vec{x}) = -\frac{1}{4\mathrm{i}C\cos(\psi)}, \tag{2.20}$$

where

$$C = \alpha\bar{k}_x' + \bar{k}_y'\tan(\psi) - \frac{\bar{k}}{\cos(\psi)\beta_0^2}\left(\frac{\beta_y^2 x_1\cos(\psi)}{S_0} + \frac{\beta_x^2 x_2\sin(\psi)}{S_0} - M\right) \text{with}\,\bar{k} = b\omega/c_o.$$

The exact solution of the aeroacoustic transfer function for the scattered pressure can be obtained as

$$\mathcal{L}_s(\bar{k}_x', \bar{k}_y', \vec{x}) = -\frac{\mathrm{e}^{2\mathrm{i}C}}{\mathrm{i}C\cos(\psi)}\left((1+\mathrm{i})\mathrm{e}^{-2\mathrm{i}C}\sqrt{\frac{B}{B-C}}E^*[2(B-C)] - (1+\mathrm{i})E^*[2B] + 1 - \mathrm{e}^{-2\mathrm{i}C}\right), \tag{2.21}$$

where $B = \alpha\bar{k}_x' + M_x\bar{\mu} + \bar{\kappa}$.

2.2.2.2 Far-field Acoustic Spectrum

The computation of the far-field acoustic spectrum radiated by the sound source is accomplished through the cross spectrum of Curle's acoustic analogy [87], which relates it to the surface pressure fields. The far-field spectrum at the observer location is expressed as follows:

$$S_{pp}(\vec{x},\omega) = 4\left(\frac{\omega x_3 b\cos(\psi)}{2\pi c_o S_0^2}\right)^2 \frac{L}{2}|\mathcal{L}_o(\bar{k}_x^{'},\bar{k}_y^{'},\vec{x}) + \mathcal{L}_s(\bar{k}_x^{'},\bar{k}_y^{'},\vec{x})|^2 l_y(\omega,k_y^{'})S_{qq}(\omega), \tag{2.22}$$

where L stands for the airfoil span and S_{qq} is the wall-pressure spectrum near the trailing edge, which is directly obtained from the LES to account for the crossflow effect. The parameter l_y is spanwise correlation length. Grasso et al. [45] incorporated the sweep angle effect into the generalized Corcos' model proposed by Caiazzo and Desmet [114] as follows

$$l_y(\omega,k_y^{'}) = \pi\int_{-\infty}^{\infty}\frac{\frac{n\sin(\pi/2n)}{\pi\alpha_\omega}}{1+\left(\frac{k_x^{'}\cos(\psi)+k_y^{'}\sin(\psi)-K_c}{\alpha_\omega}\right)^{2n}}\frac{\frac{m\sin(\pi/2m)}{\pi\beta_\omega}}{1+\left(\frac{-k_x^{'}\sin(\psi)+k_y^{'}\cos(\psi)}{\beta_\omega}\right)^{2m}}\mathrm{d}k_x^{'}, \tag{2.23}$$

where $\alpha_\omega = \alpha_x\omega/U_c$, $\beta_\omega = \alpha_y\omega/U_c$, $n = m = 1$, $\alpha_x = 0.1$, and $\alpha_y = 0.77$. It is worth noting that Eq. (2.22) yields a magnitude that is four times that of Amiet's original model [34]. This is because the scattering taking place on one side of an airfoil affects both sides [81, 142]. However, it is important to recognize that the incident field should not be influenced by the trailing-edge boundary condition or the Kutta condition. To address this, Li and Lee [143] introduced a correction to Eq. (2.20), dividing it by a factor of four. In the analysis, this modified equation is utilized. Normalized wavenumbers ($\bar{k}_x^{'}$,$\bar{k}_y^{'}$) appearing in the aeroacoustic transfer functions and spanwise correlation length in Eq. (2.22) must be replaced by $\bar{K}_c^{'}$ and $\bar{K}_y^{'}$ through the dispersion relation and treatment of sine cardinal squared function [45], respectively, which can be represented

$$S_{pp}(\vec{x},\omega) = 4\left(\frac{\omega x_3 b\cos(\psi)}{2\pi c_o S_0^2}\right)^2 \frac{L}{2}|\mathcal{L}_o(\bar{K}_c^{'}, \bar{K}_y^{'}, \vec{x}) + \mathcal{L}_s(\bar{K}_c^{'}, \bar{K}_y^{'}, \vec{x})|^2 l_y(\omega, \bar{K}_y^{'}) S_{qq}(\omega), \tag{2.24}$$

where $\bar{K}_y^{'} = \frac{\bar{k}}{\beta_0^2}\left(\frac{\beta_x^2 x_2}{S_0} - M_y\right)$ and $\bar{K}_c^{'} = \frac{\omega}{U_c\cos(\psi)} - \bar{K}_y^{'}\tan(\psi)$. Ultimately, the right-hand side in Eq. (2.24) becomes the function of the angular frequency and the observer coordinate system. When the flow is aligned with the trailing edge of an airfoil (i.e., $\psi = 0°$), all the formulations derived above can readily revert to the original form of Amiet's model [6, 34, 35]. The original form of Amiet's model is listed in Appendix A.

2.3 Pressure Decomposition

2.3.1 Wavelet Decomposition

The continuous wavelet transform (CWT) of pressure fluctuations in the time domain $p(t)$ consists of a projection over a basis of either compact or non-compact support functions obtained by dilations and translations of the mother wavelet $\Psi(t)$ [144]. The mother wavelet is localized in both the time and frequency domains. The resulting wavelet coefficient is a function of time t and of the scale s, the latter being inversely proportional to frequency. According to Meneveau [145], Camussi and Guj [146], and Grizzi and Camussi [147], the CWT in the time domain is defined as follows:

$$w(s,t) = C_\Psi^{-1/2} s^{-1/2} \int_{-\infty}^{\infty} \Psi^*\left(\frac{t-\tau}{s}\right) p(\tau)\,\mathrm{d}\tau, \tag{2.25}$$

where $\Psi^*((t-\tau)/s)$ is the complex conjugate of the dilated and translated from $\Psi(t)$, and $C_\Psi^{-1/2}$ is obtained by satisfying the admissibility condition

$$C_\Psi = \int_{-\infty}^{\infty} |\omega|^{-1} |\hat{\Psi}(\omega)|^2\,\mathrm{d}\omega < \infty. \tag{2.26}$$

Here, $\hat{\Psi}(\omega)$ is the Fourier transform of $\Psi(t)$,

$$\hat{\Psi}(\omega) = \int_{-\infty}^{\infty} \Psi(t) \mathrm{e}^{-\mathrm{i}\omega t} \, \mathrm{d}t, \tag{2.27}$$

where $\mathrm{i} = \sqrt{-1}$.

A random pressure fluctuation can also be decomposed by a discrete wavelet transform (DWT) for practical applications in a one-dimensional case [145]. The discrete wavelet coefficients are given by

$$w_p^{(s)}(n) = \sum_{k=-\infty}^{+\infty} \Psi^{(s)}(n - 2^s k) p(k), \tag{2.28}$$

where s denotes the discretized scale and $p(k)$ is an arbitrary function, which is a pressure signal in this work. The wavelet function $\Psi^{(s)}(n - 2^s k)$ is the discretized version of $\Psi^{(s)} = 2^{-\frac{s}{2}} \Psi \left(t/2^s \right)$ [146]. The wavelet kernel used is the Daubechies-12 type, which was also used for the pressure decomposition using wavelet transform by Mancinelli *et al.* [67].

The wavelet coefficients obtained from DWT are used in a wavelet filtering based on the recursive denoising algorithm [148] with a nonlinear threshold motivated by the denoising theory [149]. Originally, based on statistical reasoning, an initial threshold [67, 69] is guessed by

$$T_o = \sqrt{2 \langle p'^2 \rangle \log_2 N_s}, \tag{2.29}$$

where $\langle p'^2 \rangle$ is the variance of the pressure signal and N_s is the number of samples, equal to 1.5×10^5. Starting from the initial guess above, the threshold is updated at each iteration in loop. The threshold at n-th iteration can be written as

$$T_n = \sqrt{2 \langle p_i'^2 \rangle |_n \log_2 N_s}, \tag{2.30}$$

where $\langle p_i'^2 \rangle |_n$ indicates the variance of the incoherent pressure in time at n-th iteration. The flowchart of wavelet-based pressure decomposition based on the recursive denoising

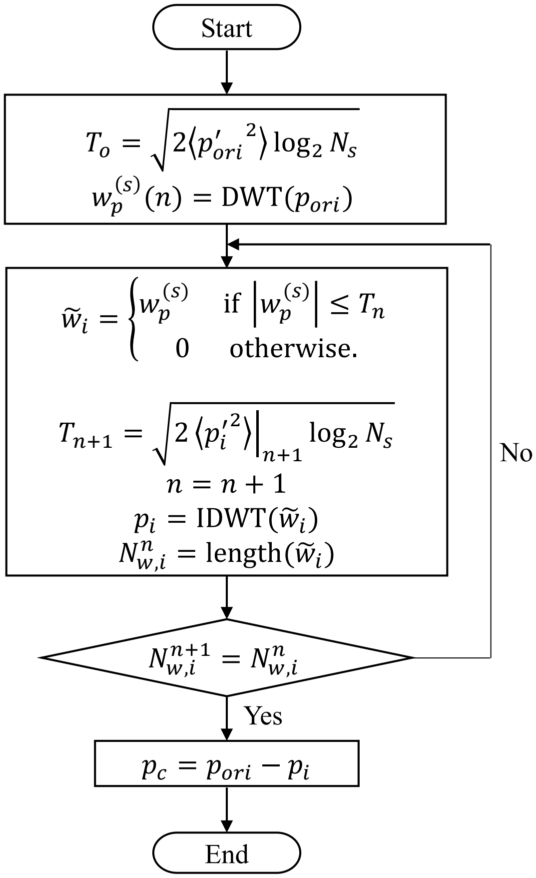

Figure 2.3: Flowchart of the wavelet-based decomposition algorithm.

algorithm [148] is presented in Fig. 2.3. The wavelet coefficients with magnitude less than the threshold in loop are referred to as incoherent wavelet coefficients. These are reverted in the time domain by the inverse discrete wavelet transform (IDWT), which is called the incoherent pressure p_i. The coherent pressure p_c is what remains after subtracting the incoherent pressure from the original pressure p_{ori}. It is iteratively filtered until the number of incoherent samples at n-th iteration is the same as that at $n+1$-th iteration.

2.3.2 Wavenumber-frequency Decomposition

The wavenumber-frequency analysis is represented in the form of a multi-dimensional Fourier transform. This multi-dimensional spectrum can be expressed as follows:

$$\mathbf{P}(f,k) = \int_{-\infty}^{\infty}\int_{-\infty}^{\infty} p(t,x)\mathrm{e}^{-\mathrm{i}(2\pi f t - kx)}\,\mathrm{d}t\mathrm{d}x, \tag{2.31}$$

where k represents the wavenumber, f denotes the frequency, and t stands for time. Specifically, only the streamwise wavenumber is considered, simplifying the identification of various wave modes based on their propagation direction and speed. This approach enables the isolation of specific wave modes through a filtering process, allowing for the detection of a single-mode wave [150]. Time-accurate pressure data is collected from probes distributed evenly on both the upper and lower sides of the airfoil. The wavenumber resolution, denoted as Δk, is determined as $\Delta k = 3.33\mathrm{m}^{-1}$, which is calculated using the formula $\Delta k = 1/(N\mathrm{d}x)$, where N represents the number of probes, and $\mathrm{d}x$ is the distance between neighboring probes. Wavenumber, in this context, is defined as the number of complete waves within a unit distance, with units of m^{-1}. Fourier coefficients in the wavenumber-frequency domain are subjected to filtering using the following relationship:

$$\mathbf{P}_{\mathbf{Y}}(f,k) = \mathbf{P}(f,k)\hat{Y}(f,k), \tag{2.32}$$

$$\hat{Y}(f,k) = \begin{cases} 1 & f_{\text{lower band}} \leq f \leq f_{\text{upper band}} \\ 0 & f < f_{\text{upper band}} \\ 0 & f > f_{\text{lower band}}, \end{cases} \tag{2.33}$$

where $\mathbf{P_Y}(f,k)$ represents the filtered Fourier coefficient, while $\hat{Y}(f,k)$ stands for the filtering coefficient, taking values of either 0 or 1. The lower and upper bands of the filtering coefficient delineate the threshold range, which is determined by the phase velocities of convective velocity $U_c \approx 0.8U_\infty$ and the speed of sound c_o. The acoustic-wave mode can be further decomposed into downstream and upstream waves, resulting in the identification of three distinct pressure waves upon decomposition. These are as follows: hydrodynamic pressure (p_{hy}), which travels along the wall at the convective velocity U_c, downstream acoustic pressure (p_{ac}^{+}), propagating at a speed of approximately $U_c + c_o$, and upstream acoustic pressure (p_{ac}^{-}), propagating in the opposite direction to the freestream, approximately at $U_c - c_o$. The filtered pressure spectra are then transformed back to the time domain by applying the inverse Fourier transform denoted as $\mathcal{F}^{-1}[:]$,

$$p_Y(t,x) = \mathcal{F}^{-1}[\mathbf{P_Y}(f,k)]. \tag{2.34}$$

The filtering process is repeated until three wave modes of the pressure are obtained:

$$p_Y(t,x) = p_{hy} + p_{ac}^{+} + p_{ac}^{-}. \tag{2.35}$$

2.4 Modal Analysis

2.4.1 Dynamic Mode Decomposition

DMD is a data-driven technique that facilitates the extraction of spatiotemporal coherent patterns from complex systems [108]. Inherent in DMD is the conjunction of principal component analysis in volume space and Fourier transform in time, enabling the isolated examination of dominant coherent patterns at specific frequencies. The core principle revolves around the derivation of dynamic information from time-resolved snapshots. Schmid [106] initially introduced the concept of DMD and its application to fluid dynamics, showcasing its potential to derive physical insights from high-dimensional flow data. The most contemporary definition of the DMD algorithm was provided in Refs. [107, 108]. Consequently, this study adheres to the definition and algorithm of DMD as established by Tu et al. [107]. The time-resolved snapshots of the pressure field from the LES are compiled into an n by m matrix, denoted as $\mathbf{X}$:

$$\begin{bmatrix} | & | & & | \\ \mathbf{x_1} & \mathbf{x_2} & \ldots & \mathbf{x_m} \\ | & | & & | \end{bmatrix}, \tag{2.36}$$

where n is the number of spatial points saved per time snapshot and m is the number of snapshots taken. With two dynamical sets of data comprised of $\mathbf{x_1}$ to $\mathbf{x_{m\text{-}1}}$ and $\mathbf{x_2}$ to $\mathbf{x_m}$, denoted as $\mathbf{X_1}$ and $\mathbf{X_2}$, respectively, the discrete linear dynamical system is written in the following form:

$$\mathbf{X_2} \approx \mathbf{A}\mathbf{X_1}, \tag{2.37}$$

where $\mathbf{A}$ is a best-fit linear operator solved by minimizing the Frobenius norm of the equation $||\mathbf{X}_2 - \mathbf{A}\mathbf{X}_1||_F$. SVD and eigen decomposition are applied to the matrix $\mathbf{A}$ consequently in order to calculate the eigenvalues and eigenvectors. Further details of DMD algorithm are referred to in Refs. [107, 108]. The discrete-time DMD eigenvalues are $\lambda_k = \Re(\lambda_k) + \Im(\lambda_k)\mathrm{i}$, which are also called Ritz values. The growth rate is measured by its magnitude such that the mode grows if $|\lambda_k| > 1$ and decays otherwise. The continuous-time DMD eigenvalues that represent the stability of eigenmodes are obtained from logarithmic mapping as follows:

$$u_k = \frac{\ln(\lambda_k)}{\Delta t} = \sigma_k + \omega_k \mathrm{i}, \tag{2.38}$$

where σ_k denotes the growth rate of u_k, and ω_k is the angular frequency of the k-th DMD mode. The frequency of the k-th DMD mode is defined as $f_k = \omega_k/(2\pi)$. The pressure field $\mathbf{x}(t)$ can be constructed as a linear combination of the eigenvectors of the $\mathbf{A}$ matrix ($\mathbf{\Phi}$), or the DMD modes, as follows:

$$\mathbf{x}(t) \approx \sum_{k=1}^{r} \Phi_k \exp(\omega_k t) b_k = \mathbf{\Phi} \exp(\mathbf{\Omega} t)\mathbf{b}, \tag{2.39}$$

where b_k is the initial amplitude of each mode. $\mathbf{b}$ and $\mathbf{\Omega}$ indicate the vector form of b_k and ω_k. The vector $\mathbf{b}$ is calculated by the Moore-Penrose pseudo inverse in the relation of $\mathbf{x_1} = \mathbf{\Phi b}$ where $\mathbf{x_1}$ is the initial snapshot. r denotes the rank of SVD. Flow snapshots $m = 3000$ from the final FTT are stored for the DMD analysis with the sampling frequency of 20 kHz, $f_s = 1/(50\Delta t)$. To examine the DMD modes at low-to-high frequencies, all singular values are kept without truncation, retaining the corresponding eigenvalues. This implies that the rank of the SVD is equal to one less than the number of flow snapshots, $m - 1$ or $r = 2999$. The stored data matrices of the pressure field are extracted in midspan of the computational domain.

2.4.2 Spectral Proper Orthogonal Decomposition

For stationary data originating from stochastic processes, SPOD combines the benefits of DMD—primarily the representation of temporal correlation amongst resultant structures—with the optimality inherent to Proper Orthogonal Decomposition (POD) [105]. The definition and procedure for calculating SPOD modes are derived from Refs. [103, 105]. The data matrix comprising the number of spatial points, n, saved per time snapshot and the time-resolved snapshots, m, is partitioned into the number of sub-blocks $N_{\text{blk}} = 22$ in this work. Each block $\mathbf{X}$ can be articulated as follows:

$$\begin{bmatrix} \\ | & | & & | \\ \mathbf{x_1^{(p)}} & \mathbf{x_2^{(p)}} & ... & \mathbf{x_{N_{FFT}}^{(p)}} \\ | & | & & | \\ \\ \end{bmatrix}, \tag{2.40}$$

where $p = 1, ..., n$, and N_{FFT} is 2^8 in this study. The Welch periodogram method is applied to each block, which constructs an ensemble of realizations of the temporal Fourier transform. Each block has partial time-resolved snapshots that amounts to N_{FFT} and 50% overlaps with the next block. Next, the discrete Fourier transform is computed for each block, and then the resulting matrix $\hat{\mathbf{X}}$ can be written as:

$$\begin{bmatrix} \\ | & | & & | \\ \hat{\mathbf{x}}_\mathbf{1}^{\mathbf{(p)}} & \hat{\mathbf{x}}_\mathbf{2}^{\mathbf{(p)}} & ... & \hat{\mathbf{x}}_\mathbf{N_{FFT}}^{\mathbf{(p)}} \\ | & | & & | \\ \\ \end{bmatrix}, \tag{2.41}$$

where

$$\hat{\mathbf{x}}_\mathbf{k}^{\mathbf{(p)}} = \sum_{j=1}^{N_{\text{FFT}}} w_j \mathbf{x_j} \text{exp}(-\text{i}2\pi(k-1)[(j-1)/N_{\text{FFT}}]) \tag{2.42}$$

for $k = 1, ..., N_{\mathrm{FFT}}$. The scalar weights w_j are used as a Hamming window function to reduce spectral leakage due to non-periodicity of the data in each block. Then, a matrix is assembled with Fourier realizations from k-th column of $\hat{\mathbf{X}}$ in every block: $\hat{\mathbf{X}}_{\mathbf{f_k}} \longleftarrow [\hat{\mathbf{x}}_{\mathbf{k}}^{(\mathbf{1})}, \hat{\mathbf{x}}_{\mathbf{k}}^{(\mathbf{2})}, ..., \hat{\mathbf{x}}_{\mathbf{k}}^{(\mathbf{N}_{\mathrm{blk}})}]$. Then, the matrix of sampled cross spectral density (CSD) at each frequency can be calculated:

$$\mathbf{C}_{\mathbf{f_k}} = \hat{\mathbf{X}}_{\mathbf{f_k}}^{\mathbf{H}} \hat{\mathbf{X}}_{\mathbf{f_k}}, \tag{2.43}$$

where the superscript $\mathbf{H}$ is the Hermitian. The eigenvalues and eigenvectors of $\mathbf{C}_{\mathbf{f_k}}$ can be obtained as $\boldsymbol{\Theta}_{\mathbf{f_k}}$ and $\boldsymbol{\Lambda}_{\mathbf{f_k}}$ after the eigenvalue decomposition so the SPOD mode is retrieved as $\boldsymbol{\Psi}_{\mathbf{f_k}} = \hat{\mathbf{X}}_{\mathbf{f_k}} \boldsymbol{\Theta}_{\mathbf{f_k}} \boldsymbol{\Lambda}_{\mathbf{f_k}}^{-\mathbf{1/2}}$ with modal energies $\boldsymbol{\Lambda}_{\mathbf{f_k}}$ for the k-th discrete frequencies.

2.5 Cross-spectrum Method

A Fourier-based cross-spectrum method is presented in this section. The determination of either the auto power spectral density (APSD), denoted as S_{xx}, or the cross power spectral density (CPSD), represented as S_{xy}, depends on whether the reference probe y is identical to the arbitrary probe x or not. The CPSD function is defined as

$$S_{xy} = S(x, y, f) = \lim_{T \to \infty} \frac{\hat{P}(x, f) \hat{P}^{*}(y, f)}{T} = |S_{xy}| \mathrm{exp}(\mathrm{i}\phi_{xy}), \tag{2.44}$$

where T is the finite period of time, the asterisk, $'*'$, on the superscript stands for the complex conjugate, and $\hat{P}(x, f)$ is the Fourier transform of temporal signal, $p(x, t)$, which can be denoted as

$$\hat{P}(x, f) = \int_{-T}^{T} p(x, t) \mathrm{exp}(\mathrm{i}2\pi f t) \, \mathrm{d}t. \tag{2.45}$$

A phase angle, ϕ_{xy}, due to the occurrence of phase difference between two signals, can be represented as

$$\phi_{xy} = \Im(S_{xy})/\Re(S_{xy}), \tag{2.46}$$

where it varies from -π to π. The core principle of the cross-spectrum method is the utilization of phase angle ϕ_{xy}, through which three variants can be formulated. The first formulation is the multiplication of APSD and the complex exponential of the phase angle denoted as $S_{xx}\mathrm{exp}(\mathrm{i}\phi_{xy})$. The second one is representative of the CPSD, S_{xy}. The last one is the subtraction of the APSD from CPSD, which can denoted as $S_{xy} - S_{xx}$. Since the three formulations are basically complex numbers, the real or imaginary part can be taken to plot on a linear scale. Furthermore, each formulation can be represented as the sound pressure spectrum level (SPSL) with the following

$$\begin{aligned} \mathrm{SPSL_{xx}} &= 10\mathrm{log}_{10}\frac{|S_{xx}\mathrm{exp}(\mathrm{i}\phi_{xy})|\Delta f_{\mathrm{ref}}}{P_{\mathrm{ref}}^2} \\ &= 10\mathrm{log}_{10}\frac{|S_{xx}|\Delta f_{\mathrm{ref}}}{P_{\mathrm{ref}}^2}, \end{aligned} \tag{2.47}$$

$$\mathrm{SPSL_{xy}} = 10\mathrm{log}_{10}\frac{|S_{xy}|\Delta f_{\mathrm{ref}}}{P_{\mathrm{ref}}^2}, \tag{2.48}$$

$$\mathrm{SPSL_{xy-xx}} = 10\mathrm{log}_{10}\frac{|S_{xy} - S_{xx}|\Delta f_{\mathrm{ref}}}{P_{\mathrm{ref}}^2}, \tag{2.49}$$

where $\Delta f_{\mathrm{ref}} = 1/T = 6.66$ Hz, and $P_{\mathrm{ref}} = 20$ μPa. When calculating either S_{xx} or S_{xy}, samples are subdivided into 10 segments with a Hanning window and an overlap of 50%. Using the SPSL formulation shifts the metric from a linear scale to a logarithmic scale, thereby aiding in the quantitative assessment of noise strength. This conversion enables the evaluation of the inherent characteristics of each cross-spectrum method in both linear and logarithmic scales. Notably, the first formulation represents the characteristics of the APSD in the logarithmic scale. This suggests that the first formulation is independent of the choice of reference point on the logarithmic scale, a concept that will be further elucidated in the following section. Since the spectral processing between two pressure signals is performed independently, parallel computation can be easily implemented to accelerate the overall computations of the cross-spectrum method without handling large datasets. This easy parallelization would be difficult in SPOD and DMD since they require handling large datasets and complex mathematical or matrix operations that are inherently more sequential in nature.

The reference point y is selected at three different locations as depicted in Fig. 2.4: (1) near the trailing edge ($x/c = 0.99$, $y/c = 0.002$) marked as P1, (2) the boundary-layer tripping region ($x/c = 0.15$, $y/c = 0.06$) marked as P2, and (3) half chord away from the trailing edge in the positive wall-normal direction ($x/c = 0.99$, $y/c = 0.5$) marked as P3. The first two reference points, P1 and P2, are strategically located in areas where turbulent hydrodynamic flows are anticipated to interact with the wall. Conversely, the point at P3 is situated in a region with low turbulence, making it an ideal location for observing more pronounced acoustic wave propagation.

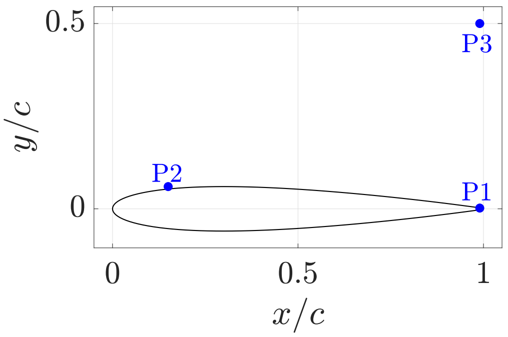

Figure 2.4: Diagram of three reference points around the airfoil for the cross-spectrum method.

2.6 Validation of Flow and Acoustic Codes

Flow quantities and acoustic sources are validated against an experimental campaign conducted by Garcia-Sagrado and Hynes [91], which includes the pressure coefficient, skin friction coefficient, boundary layer velocity profile, turbulence intensity, and wall pressure spectra at a chord-based Reynolds number, $Re = 4 \times 10^5$, and Mach number, $M = 0.058$. The far-field acoustics are validated against experimental data obtained by Brooks *et al.* [5] at a chord-based Reynolds number, $Re = 3.2 \times 10^5$, and Mach number, $M = 0.093$. Both cases are at zero angle of attack.

The time-averaged predicted negative pressure coefficient $-C_p$ and the skin friction coefficient C_f compared to midspan experimental results are presented in Fig. 2.5. The nearly identical magnitude in both quantities between the upper and lower sides of the airfoil confirms that the airfoil is symmetric and simulated at a zero incidence angle. The pressure curve shows that the predicted abrupt suction peak due to the enforced tripping is similar to the measurement. The simulation results exhibit fairly good agreement with the experiments. Boundary layer velocity profiles on the airfoil suction side and wake region at

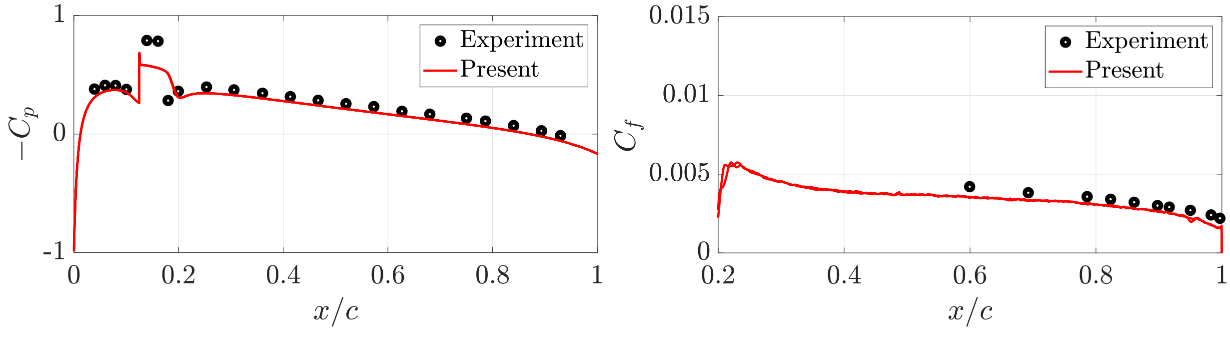

(a) (b)

Figure 2.5: Time-averaged distributions in midspan against experimental data [91]: (a) $-C_p$ and (b) C_f.

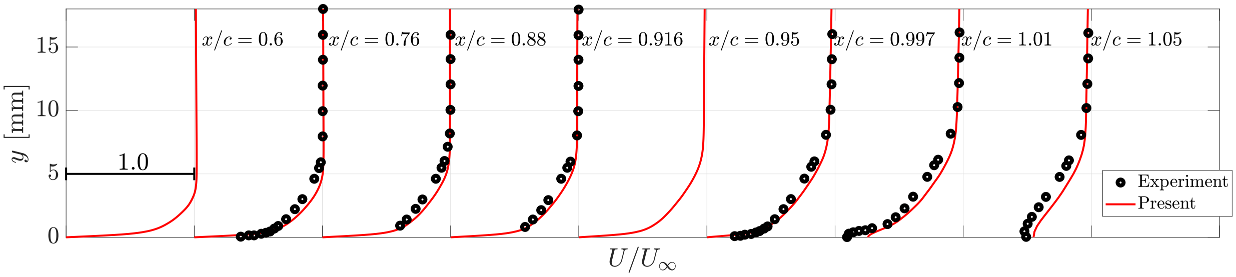

Figure 2.6: Time-averaged boundary layer velocity profiles in midspan on the suction side of airfoil and two wake regions in the streamwise direction against experimental data [91].

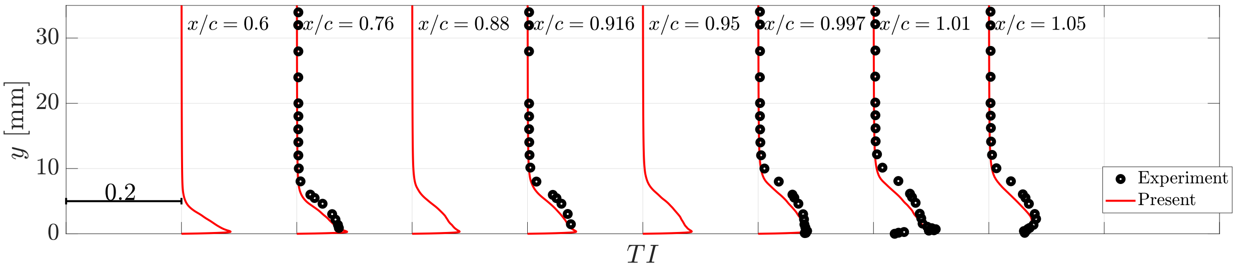

Figure 2.7: Turbulence intensity profiles on the suction side of airfoil and two wake regions in the streamwise direction against experimental data [91].

several stations are depicted in Fig. 2.6. One can observe that the boundary layer thickness increases in the streamwise direction as the adverse pressure gradient increases. A slight discrepancy is observed in the wake region at $x/c = 1.05$, but the overall velocity profiles in the LES match well with the experiments. The boundary layer turbulence intensity profiles, defined as $TI = \sqrt{2/3k}/U_\infty$ where k is the turbulent kinetic energy, are computed at several streamwise locations on the airfoil suction side and wake regions, as shown in Fig. 2.7. It is observed that turbulence production occurs near the wall, but it expands further away from the wall in the wake regions. The maximum turbulence intensity is around values of 0.1, which is similar to experimental results [151], demonstrating favorable agreement with the measurements. The predicted wall pressure spectra in midspan, compared with experiments, are given in Fig. 2.8. Spectral computations are performed with samples corresponding to the last 10 FTT, which are divided into 28 segments with a Hanning window of 50% overlap.

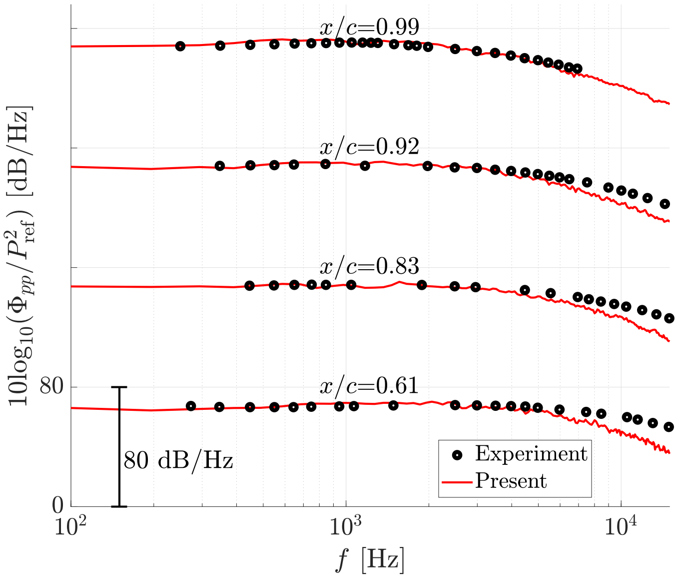

Figure 2.8: Wall pressure spectra referenced to $P_{\text{ref}} = 20\,\mu$Pa on the suction side of the airfoil at various streamwise locations in comparison with experiments [91].

At $x/c = 0.61$ and 0.83, the predicted spectra show discrepancies at high frequencies, but spectral distributions close to the trailing edge exhibit fairly good agreement with available experimental data. The discrepancy of the spectra between LES predictions and experiments, especially at upstream locations, is thought to be attributed to the modeling of the transition using a stair strip, which differs from the experimental setup.

Figure 2.9 illustrates the time-averaged streamlines colored with the streamwise velocity component, along with the dilatation field in the background, localized in the tripping and trailing edge regions at a chord-based Reynolds number, $Re = 4 \times 10^5$. In the tripping region near the leading edge, the separated-flow transition [39] is clearly visible behind the recirculation flow due to the boundary-layer tripping, resulting in hydrodynamic coherent pressure perturbations that advect in the streamwise direction. Figure 2.10 illustrates the iso-surface of the normalized Q-criterion colored by the mean velocity magnitude at a chord-based Reynolds number, $Re = 4 \times 10^5$. Q-criterion is defined [152]:

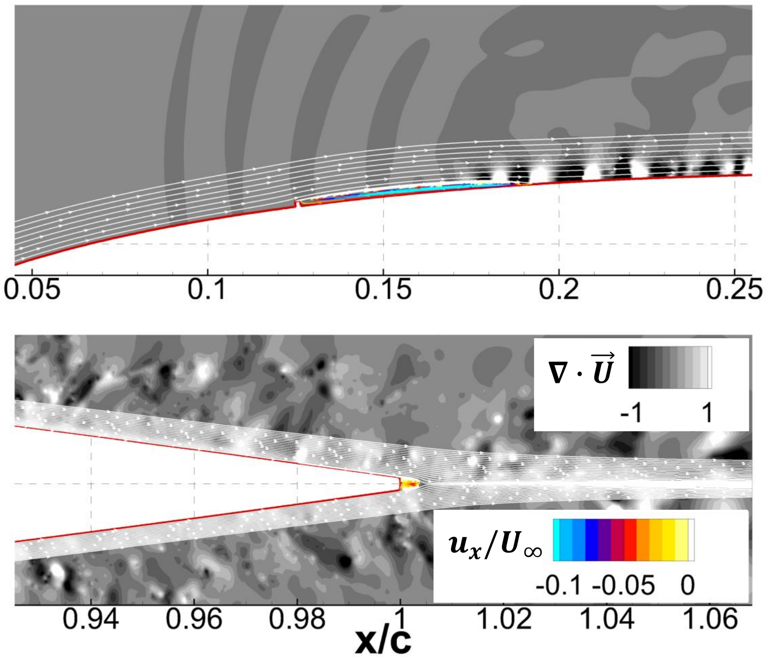

Figure 2.9: Time-averaged streamlines colored with the streamwise velocity normalized by U_∞ and the instantaneous dilatation field in the background close to the leading edge (top) and trailing edge (bottom). The color scale range highlights the recirculation flow.

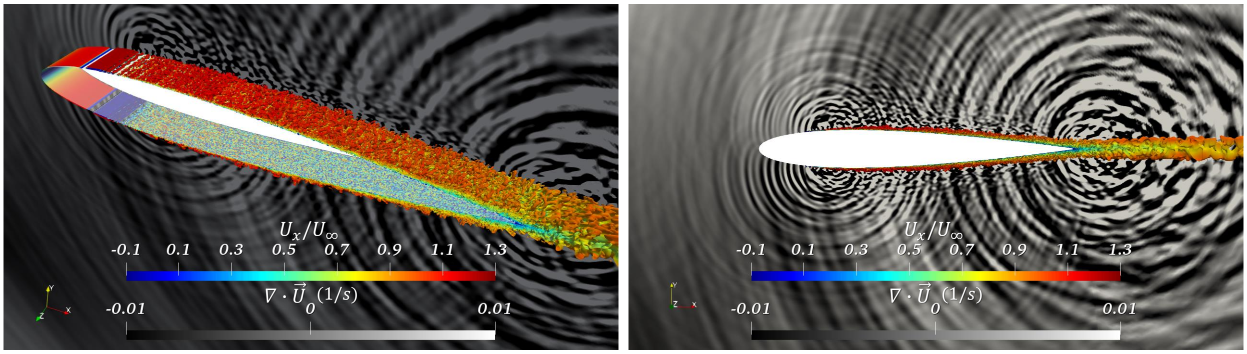

(a)

(b)

Figure 2.10: Normalized Q-criterion ($Qc^2/U^2 = 10$) colored by the mean velocity magnitude with the dilatation field in the background: (a) isometric view and (b) plane view.

$$Q = \frac{1}{2}\left(\|\Omega\|^2 - \|S\|^2\right), \tag{2.50}$$

where Ω is the rate of vorticity tensor and S was defined in Eq. (2.4). The operator $\|\cdot\|$ denotes Frobenius norm of tensor.

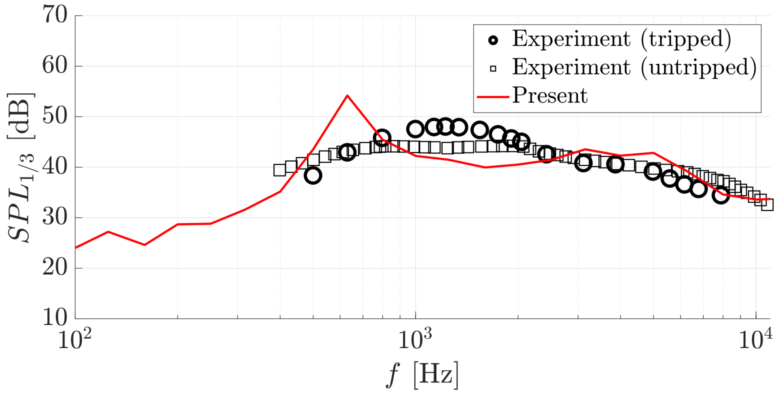

Figure 2.11: Sound pressure level at an observer location x=c, y=8.0c, and z=midspan compared with tripped and untripped experiments [5].

The transition to turbulence involving Tollmien-Schlichting (T-S) waves [39], spanwise vorticity, and three-dimensional vortex breakdown, evolving into turbulent flows behind the tripping, is clearly shown along the suction and pressure sides near the tripping region. The dilatation field indicates that the acoustic wave propagates from the tripping region at $x/c = 0.125$, as similarly observed in simulations by Bodling and Sharma [18]. Acoustic scattering is also evident around the trailing edge in the plane view of Fig. 2.10(b).

The sound pressure level (SPL) at a microphone positioned at $x = c$, $y = 8.0c$, and z =midspan, predicted at a chord-based Reynolds number, $Re = 3.2 \times 10^5$, is presented in Fig. 2.11 comparing with untripped and tripped experiments [5]. The narrow-band SPL was first obtained using ensemble averaging. Then, the one-third octave band SPL was calculated and is shown in Fig. 2.11. Kato's correction [153] is applied to account for the difference in the spanwise length between the experiment and simulation, as the experimental airfoil's spanwise length is 20 times longer than that of the simulation. In the tripped experiment, turbulent boundary layers develop on both the suction and pressure sides due to the forced tripping mechanism, while the natural boundary-layer transition occurs on both sides for the untripped experiment. The stair-striped tripping is modeled on 20 percent of the chord from the leading edge in the numerical simulation to mimic the random distribution of grit in strips in experimental conditions [5]. The low-frequency tonal tone around 0.63 kHz may be attributed to the trailing-edge-bluntness-vortex-shedding noise emanating from the recirculation flow at the blunt trailing edge, as shown in Fig. 2.9, where the test case is in a similar flow regime. This observation is consistent with the literature, in which the trailing-edge bluntness induces a low-frequency peak [154]. The origin of the tonal peak will be further supported by the DMD modes of the original and denoised pressure later, which demonstrates the propagation of acoustic waves emanating from the trailing edge at this low frequency. However, the experiments do not show this peak since a sharp trailing edge is designed [5]. Despite the boundary-layer tripping by the stair strip, the onset of fully turbulent flows might not be abrupt but undergo some natural transition processes, as similarly observed in Fig. 2.10, although the test case is slightly different. Consequently, such retardation of the laminar-to-turbulent transition behind the stair strip might yield numerical results comparable to the untripped experimental condition between 1 and 2 kHz. Beyond 2 kHz, however, the broadband spectral shape and its magnitude show good agreement with the tripped experimental data.

Chapter 3

Pressure Decomposition

This chapter stems from the unified research theme of pressure decomposition but encompasses two independent research topics: wavelet-based pressure decomposition and Fourier-based pressure decomposition. Both research topics utilize the same LES results, specified at a chord-based Reynolds number, $Re = 4 \times 10^5$, Mach number, $M = 0.058$, and a zero incidence angle over a NACA 0012 airfoil configuration.

In Sec. 3.1, the pressure field is split into coherent (denoised) pressure and incoherent pressure (background noise) using the wavelet-based pressure decomposition. The section entails the physical interpretation focused on predicting and better understanding the true physics of airfoil noise in the numerical domain.

In Sec. 3.2, the wall pressure is decomposed into hydrodynamic (incident) and acoustic (scattered) pressure using the Fourier-based pressure filtering and Amiet's trailing-edge noise theory. This section scrutinizes the role of the decomposed pressures on fundamental mechanisms governing trailing-edge noise generation and propagation within turbulent boundary layer flows.

3.1 Wavelet-based Pressure Decomposition

3.1.1 Assessment of Wavelet Algorithm

The wavelet decomposition of the pressure field is carried out without downsampling for the last 10 FTT in the LES. Figure 3.1 presents the convergence trend of the decomposition algorithm with respect to the ratio of the number of incoherent wavelet coefficients to the total number of wavelet coefficients and the threshold level at three selected streamwise positions on the suction side. It is observed that the incoherent portion plateaus in magnitude at approximately 0.96 to 0.97, indicating that the coherent turbulent structure is represented by a few large amplitude coefficients, while most of the coefficients signify incoherent flows [59]. The converged threshold level in the separation algorithm is obtained when the decomposed incoherent pressure reaches a statistically convergent state, indicating a constant amplitude in pressure fluctuations. This value converges to nearly zero, which means that the magnitude of the incoherent pressure is much smaller than the coherent part. This point will be discussed in more detail later. The separation algorithm terminates after reaching the constant threshold value within fewer than 20 iterations, a convergence similar to that obtained in jet noise studies [67]. Different wavelet kernels are also tested and investigated for the effect of the choice of wavelet kernels on the convergence behavior. The details can be found in Appendix B.

The converged values of the ratio of the number of incoherent wavelet coefficients to the total number of wavelet coefficients and the threshold level are plotted along the suction side in midspan in Fig. 3.2. Upstream of the boundary-layer trip position, where the flow is stable and laminar, the coherent component constitutes a relatively larger portion as compared to the downstream of the stair strip. One can observe that the incoherent portion

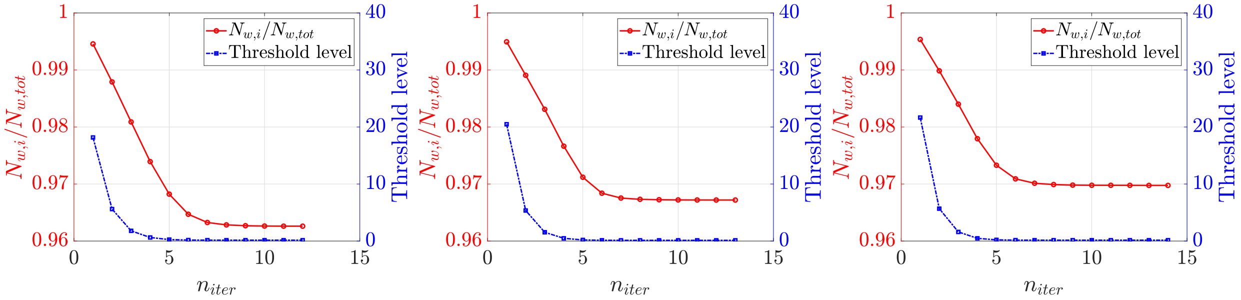

(a)

(b)

(c)

Figure 3.1: Convergence of the ratio of the number of incoherent wavelet coefficients to the total number of the wavelet coefficients and the threshold level measured on the suction side of the airfoil at x/c: (a) 0.83, (b) 0.97, and (c) 0.99.

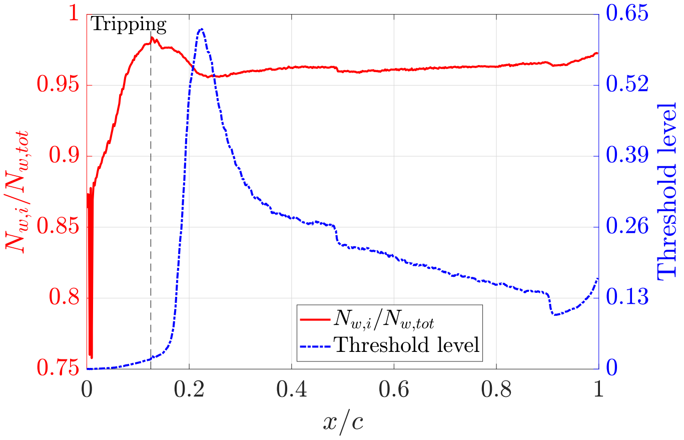

Figure 3.2: Ratio of the number of incoherent wavelet coefficients to the total number of wavelet coefficients and threshold level from the leading edge to the trailing edge on the suction side.

is at its maximum right after the tripping, where the flow is perturbed, as is evident in the contour level in Fig. 3.3(a). For the threshold level, however, the maximum peak is slightly downstream from the boundary-layer trip at around $x/c = 0.2$, where turbulent flow is established after the forced boundary-layer transition by the stair strip, as shown in Figs. 2.9 and 2.10. This pattern is clearly visible in the contours of the threshold level in Fig. 3.3(b). The maximum in the threshold level seems to indicate the full transition to turbulent flow, which was also confirmed in the study of the onset of transition in Kelvin-Helmholtz

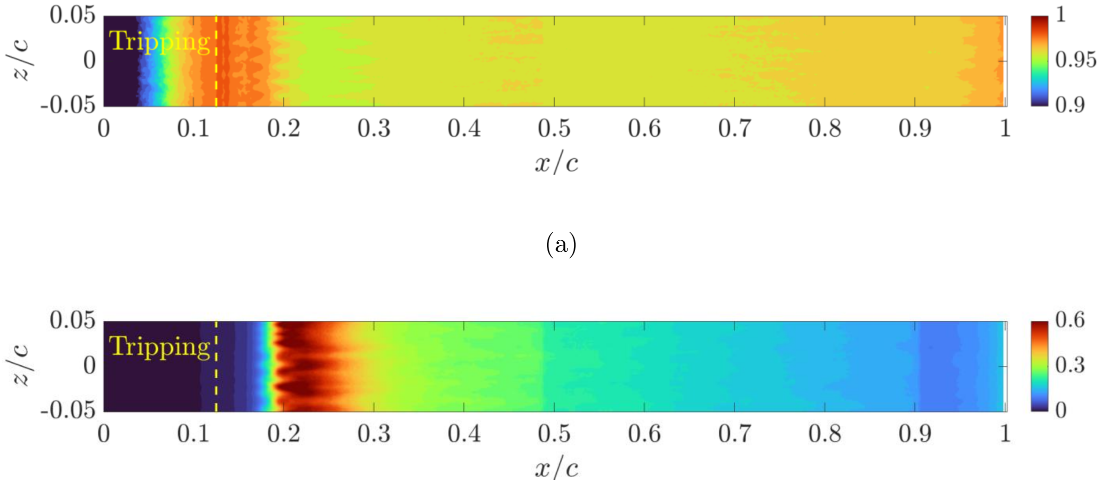

(a)

(b)

Figure 3.3: Converged contours on the suction side: (a) ratio of the number of incoherent wavelet coefficients to the total number of wavelet coefficients and (b) threshold level.

unstable plasma flows [155]. After that, the incoherent portion slowly increases towards the trailing edge, while the threshold level decays. The decay of the threshold level could be a sign of weakening coherent vortices. It is observed that the two parameters vary unevenly around $x/c = 0.5$ and 0.9, where the grid refinement level of Δx^+ changes abruptly, as shown in Fig. 2.1. This suggests that wavelet filtering can be affected by both the degree of flow perturbations and the grid resolution.

Figure 3.4 illustrates the spatial distributions of the ratio of the number of incoherent wavelet coefficients to the total number of wavelet coefficients and the threshold level. In Fig. 3.4(a), a thin green layer colored at the level of 0.94 to 0.96 for the incoherent portion develops in the boundary layer along the wall behind the tripping. Above that, more intensified incoherent portions are spatially identified as oval shapes centered around the tripping and wake regions, respectively. The filtered incoherent pressure is prominent inside these oval shapes, which will be discussed further in the next section. In Fig. 3.4(b), similar oval shapes

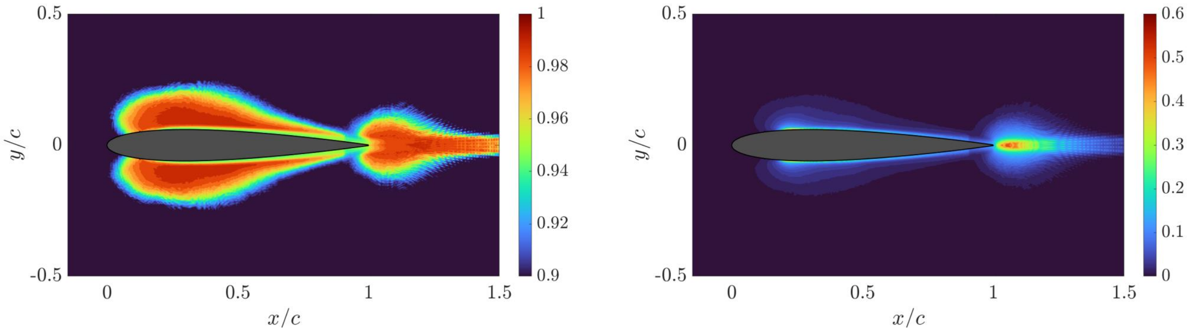

(a)

(b)

Figure 3.4: Converged contours around the airfoil cut in midspan: (a) the ratio of the number of incoherent wavelet coefficients to the total number of wavelet coefficients and (b) the threshold level.

are observed for the threshold level, providing information on the strength of the incoherent wavelet coefficients. The tripping region exhibits higher strength where flows begin to be tripped, evolving into unsteady turbulent flows, consistent with Fig. 3.3(b). Moreover, a region with higher strength appears right behind the trailing edge or wake region, where recirculation flows are generated, as presented in Fig. 2.9. This implies that the incoherent pressure has a high amplitude in these regions, which might be due to insufficient grid resolution along the blunt trailing edge with high curvature. The slight increase in both parameters on the surface around $x/c = 0.9$, as shown in Fig. 3.2, is associated with the influence of the oval shape patterns near the trailing edge. Based on the denoising threshold criteria, diffusive and homogeneous turbulent flows [64], which can be statistically modeled, remain in the incoherent pressure and are exhibited in oval shapes. Another reason for these oval shapes might be due to insufficient grid refinement for the small stair strip geometry and wake flows. However, it is unclear whether the diffusive and homogeneous flows or background noise are more dominant in the incoherent pressure. Overall, the flow perturbations and their strength on the surface or in space can be detected by the converged parameters of the separation algorithm.

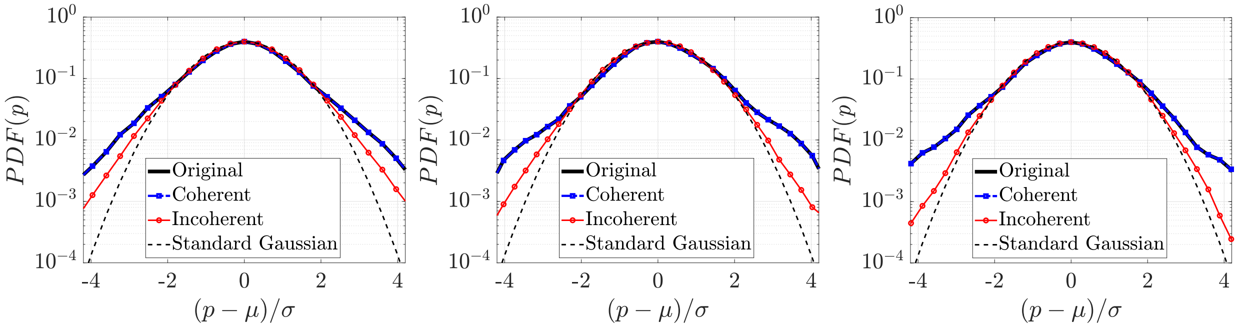

(a)

(b)

(c)

Figure 3.5: Polar evolution of PDFs for the original, coherent, and incoherent pressures with the standard Gaussian distribution at x/c: (a) 0.83, (b) 0.97, and (c) 0.99.

In a statistical test, polar evolutions of probability density functions (PDFs) for the original, coherent, and incoherent pressures are shown in Fig. 3.5. The predicted PDFs are compared to a standard Gaussian distribution, with μ and σ on the x-axis representing the mean and standard deviation of the pressure signal, respectively. The PDF of the incoherent pressure closely follows the Gaussian distribution, indicating statistical convergence. However, it slightly deviates from the Gaussian distribution when far from the mean at the selected streamwise locations. This observation aligns with previous studies that found the PDF of the incoherent part of vortices, filtered using the same wavelet-filtering algorithm, closely followed the Gaussian fit despite slight deviations far from the mean [62–64].

The PDF of the incoherent pressure tends to be closer to the Gaussian distribution across the entire range of $(p-\mu)/\sigma$ as it approaches the trailing edge, where the incoherent portion of wavelet coefficients is high, as shown in Fig. 3.2. This observation may be attributed to the effect of grid size on resolving the diffusive and homogeneous characteristics of turbulence, leading to a more distinct Gaussian distribution where the grid is finer, such as at the trailing edge, rather than downstream positions. Another possible explanation might stem from the Gaussian white noise characteristics due to insufficient grid resolution in discretizing the highly curved geometry of the trailing edge, as shown in Fig. 3.4(b). Both factors might contribute to these observations. On the other hand, the PDF of the coherent pressure exhibits higher tails. This observation has been reported in jet experiments [67, 147], where the tails of the coherent pressure are associated with turbulence development and generation of intermittent peaks of vorticity related to large pressure drops. A similar physical perspective can be speculated for the present airfoil problem in low Mach number flows, suggesting that the coherent pressure near the wall is influenced by the interaction of turbulent boundary layer flows with the surface, contributing to the higher tails in the PDF of the coherent pressure.

Figure 3.6 depicts the spectral magnitude of the original and decomposed pressures on the suction side of the airfoil wall. It is evident that the coherent pressure has a high energy spectrum at low-to-mid frequencies, while the incoherent pressure predominates at high frequencies at the selected streamwise locations. The near-uniform amplitude of the inco-

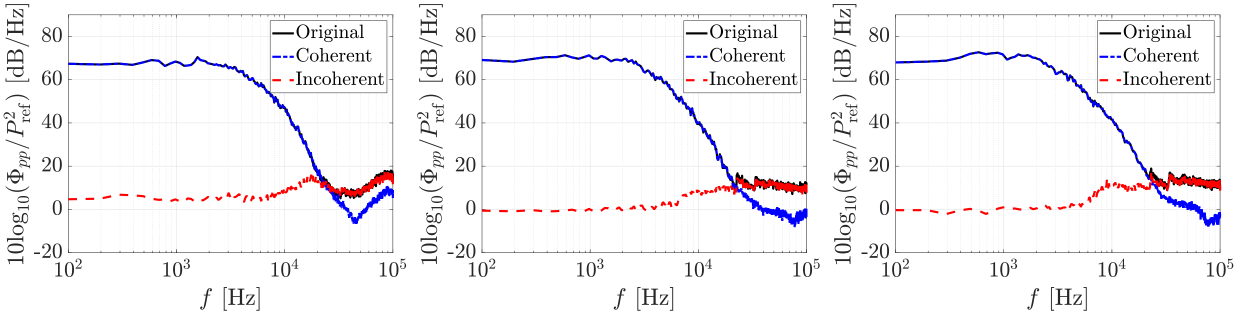

(a) (b) (c)

Figure 3.6: Wall pressure spectra of the original, coherent, and incoherent pressures calculated from the wavelet-based decomposition at x/c: (a) 0.83, (b) 0.97, and (c) 0.99.

herent pressure in the high-frequency domain is characteristic of white background noise. Furthermore, one can observe that the transition of energy spectral contribution between the coherent and incoherent pressures occurs at frequencies between 21 kHz and 22 kHz, where the power spectral slope shifts. This shift in the power spectral slope and the transition from coherent to incoherent pressure contribution have also been observed in jet flows [67]. However, the fact that the coherent pressure represents most of the energy in fluid flows while the incoherent pressure contributes only a small portion of the energy at low-Mach flow regimes differs from observations in high Mach number jet flows, where the acoustic pressure accounts for a large portion of the energy in the near field [67, 147]. This suggests that the physical meaning of the coherent and incoherent pressures in airfoil noise at low Mach numbers may be different from jet noise at high Mach numbers. To find the connection between the decomposed pressures and hydrodynamic/acoustic pressures, a wavenumber-frequency decomposition was performed and compared with the wavelet-based decomposed pressures. Detailed filtering procedures are described in Sec. 2.3.2, and wavenumber resolution associated with virtual probe arrays are reported in detail in Refs. [150, 156].

Figure 3.7 displays the wavenumber-frequency spectrum of the pressure on the suction side of the airfoil. It can be observed that the wide-band convective ridge along the U_c line has a high spectral magnitude due to the hydrodynamic turbulent flow interacting with the wall. The two other phase speeds—downstream sound propagation ($+c_\infty$) and upstream sound propagation ($-c_\infty$)—both superimposed with the convective speed, exhibit a smaller spectral magnitude than the hydrodynamic convection in the present low Mach number flow. Figure 3.8 presents the hydrodynamic and acoustic pressures obtained from the wavenumber-frequency filtering process. Most of the pressure spectrum is found to be

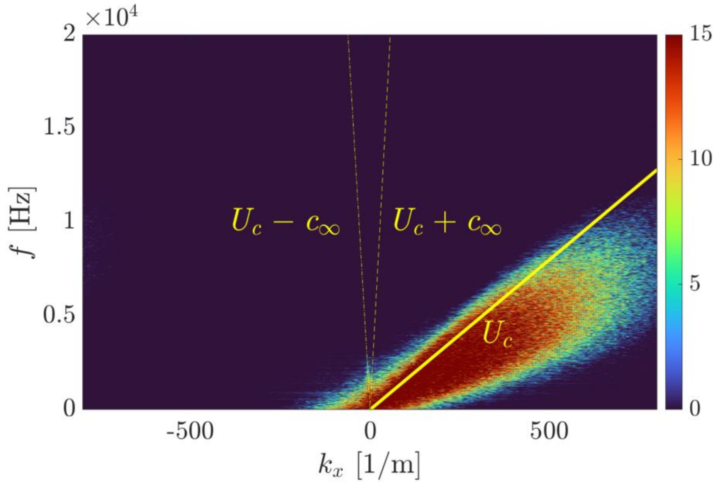

Figure 3.7: Wavenumber-frequency spectrum, $10\log_{10}\left(\mathbf{P}(f,k)\mathbf{P}^*(f,k)/P_{\mathrm{ref}}^2\right)$, referenced to $P_{\mathrm{ref}} = 20\mu$Pa on the suction side of the airfoil from $x/c = 0.49$ to 0.99. An asterisk superscript denotes the complex conjugate of a scalar. The spectrum has the unit of dB/(Hz^{2}m^{-2}).

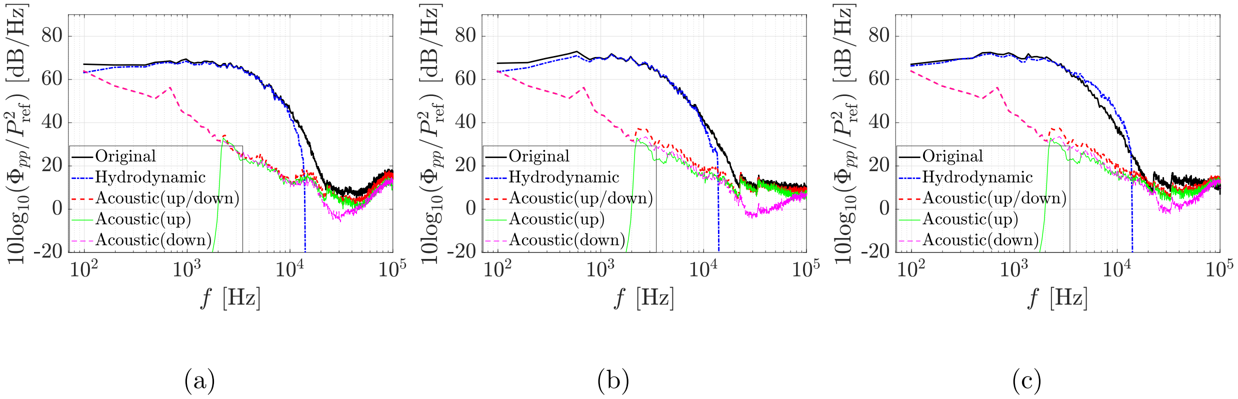

Figure 3.8: Wall pressure spectra of the original, hydrodynamic, and acoustic pressures calculated from the wavenumber-frequency decomposition at x/c: (a) 0.83, (b) 0.97, and (c) 0.99.

represented by the hydrodynamic pressure, as was the case for the coherent pressure in Fig. 3.6. Moreover, the transition of contribution from coherent to incoherent pressure or from hydrodynamic to acoustic pressure occurs in a similar frequency range of about 10-20 kHz. However, the acoustic pressure is composed of the incoherent pressure shown beyond 10-20 kHz and the high amplitude at low frequencies, including a quasi-tonal peak around 0.7-0.8 kHz. This implies that the acoustic pressure in wall-bounded flow cannot be generalized by the Gaussian statistical assumption, which was the case for high-speed jet noise [67, 69, 70].

It has been observed that the ratio of incoherent wavelet coefficients to the total number of wavelet coefficients and the threshold levels are influenced by grid resolution parameters, perturbed flows induced by boundary-layer tripping, and unsteady wake flows, as presented in Figs. 2.1, 3.2, 3.3, and 3.4. Additionally, the incoherent pressure exhibits Gaussian and white noise characteristics, with the incoherent portion remaining high near the establishment of turbulent flow and the trailing edge, respectively. Furthermore, the amplitude of the incoherent pressure spectra is negligible compared to that of the coherent component. Based on these observations, it is postulated that the coherent pressure represents the hydrodynamic pressure near or on the surface. Conversely, the incoherent pressure displays Gaussian noise-like characteristics such as disorganized, homogeneous, or background noise [62, 63]. Henceforth, the coherent and incoherent pressures are referred to as denoised pressure and background noise, respectively. This intermediate conclusion aligns with the original motivation of this paper, as described in the introduction, which is to identify and eliminate background noise. Further investigation will involve the concrete characteristics of denoised pressure and background noise using spectral analyses and DMD near the surface and the contribution of each decomposed component to the far-field noise in the subsequent section.

3.1.2 Spectral Analyses of Decomposed Pressures on Wall and around Airfoil

In the previous section, the convergence trend and properties of the wavelet denoising algorithm were examined, along with the statistical characteristics of the decomposed pressures. Since numerical simulations offer the flexibility to virtually place probes within the computational domain, investigating underlying flow physics in specific areas of interest can be accomplished by coupling the wavelet-based decomposition with a series of spectral processing and data-driven techniques. This section explores the decomposed pressures using a continuous wavelet transform, phase distribution on the surface, velocity-pressure coherence, sound pressure spectrum near the wall, and dynamic mode decomposition around the airfoil.

3.1.2.1 Continuous Wavelet Transform

The CWT-based pressure fluctuations represent the energy level in the time-frequency domain simultaneously, thus allowing for the assessment of where the high energy is located and revealing the properties of the decomposed pressure signals. In Fig. 3.9, the energy distributions of the original and the two decomposed pressures based on the wavelet filtering are illustrated by the magnitude scalogram of continuous wavelet coefficients, $|w(s,t)|$ [144, 157], on the suction side of the airfoil at $x/c = 0.3$ and 0.99 using the CWT. Morse wavelet [157] is employed for analyzing modulated signals with time-varying amplitude and frequency. This wavelet function is a Gaussian envelope modulated by a complex-valued carrier wave, which is implemented in MATLAB®'s wavelet toolbox. Detailed theory and further applications are listed in Refs. [157–159]. Several tests were conducted on different wavelet kernels and determined that the results presented in this paper are independent of the choice of wavelet kernels. Further details can be found in Appendix B. It is evident that various energy levels are identified from 0.5 to 10 kHz, and intermittent high-energy spots are excited in the 0.5 to 4 kHz range on the suction side of the airfoil due to localized turbulent boundary layer flows on the wall. This confirms that the coherent pressure is characterized by a few, but strong amplitude wavelet coefficients [59, 63, 67]. However, a relatively even energy band is

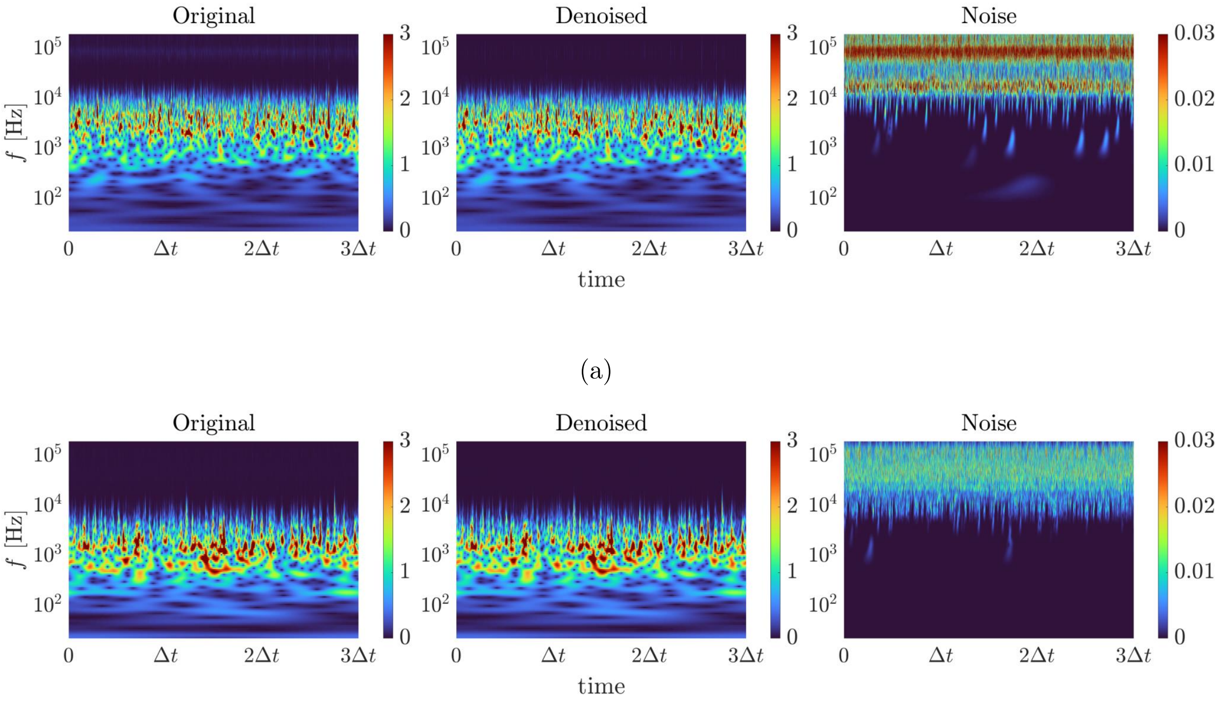

(a)

(b)

Figure 3.9: Magnitude scalogram of continuous wavelet coefficients, $|w(s,t)|$, for the original and decomposed pressures in the time-frequency domain using CWT on the suction side at (a) $x/c = 0.3$ and (b) $x/c = 0.99$.

shown beyond 10 kHz in the incoherent pressure or background noise, displaying a similar trend to the polar evolutions of PDF in terms of statistical convergence, as shown in Fig. 3.5. At $x/c = 0.3$, the high magnitude of the continuous energy band is more distinct in the background noise compared to $x/c = 0.99$, which might result from boundary-layer tripping and the associated intense pressure perturbations of the turbulent flows. Note that the color levels of the background noise are two orders of magnitude lower than those of the denoised pressure.

3.1.2.2 Phase Distributions on Wall

In Fig. 3.10, the phase distributions on the suction side of the airfoil are presented at four different frequencies using the cosine function of the pressure phase, given by $\cos(\phi) = \mathrm{Re}(\boldsymbol{Pss})/|\boldsymbol{Pss}|$, where $\boldsymbol{P_{ss}}$ is the Fourier transform of the pressure fluctuations on the suction side. In the denoised pressure at 1 kHz, unstable two-dimensional TS waves, the formation of

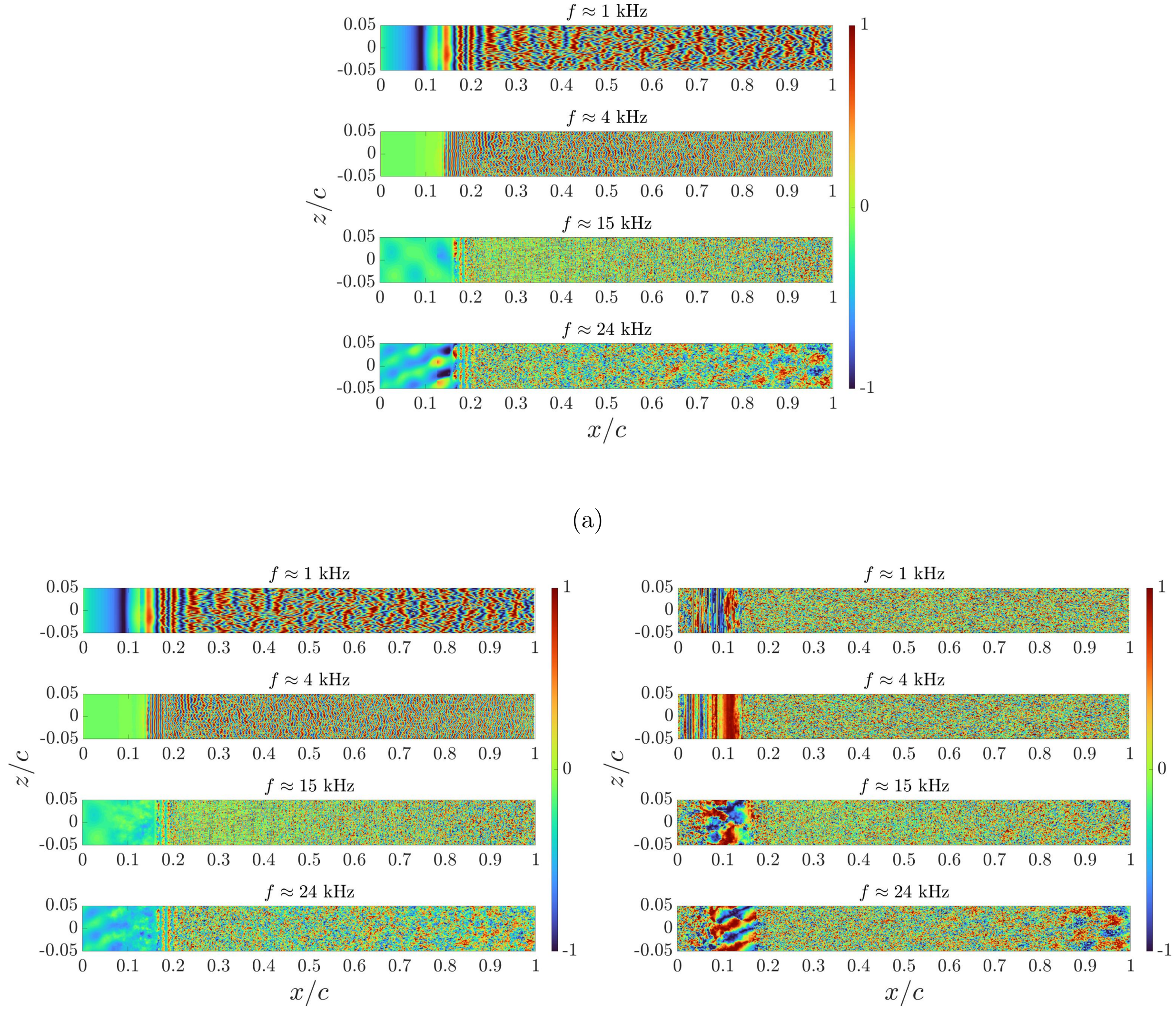

(a)

(b)

(c)

Figure 3.10: Phase distributions based on wall pressure fluctuations at four different frequencies: (a) the original pressure, (b) the denoised pressure, and (c) the background noise.

spanwise vorticity, and three-dimensional vortex breakdown occur near the tripping region, as shown in Fig. 2.10. Following this, the fully turbulent flow is convected downstream. Such a coherent wavy structure in the streamwise direction is still observed up to 4 kHz but becomes difficult to discern from 15 kHz onwards. On the other hand, the background noise exhibits disorganized and structureless phase distributions. At high frequencies of 15 and 24 kHz, the phase displays chordwise-coherent characteristics near the tripping region and the trailing edge, where the incoherent pressure or background noise was found to be high, as shown in Figs. 3.1.and 3.2.

3.1.2.3 Near-wall Velocity-Pressure Coherence and Sound Pressure Spectrum

The velocity-pressure coherence is calculated as follows:

$$\gamma^2_{Vp} = \frac{|S_{Vp}|^2}{|S_{VV}||S_{pp}|}, \tag{3.1}$$

where S_{Vp} is the cross-spectral density function. The operator $|\cdot|$ denotes the absolute value. Here, V and p subscripts denote the velocity and the wall pressure, respectively. The cross-spectral density function [160] can be obtained by Fourier transforming the raw cross-correlation function R_{Vp}:

$$S_{Vp}(f) = \int_{-\infty}^{\infty} R_{Vp}(\tau)\mathrm{e}^{-\mathrm{i}2\pi f\tau}\,\mathrm{d}\tau, \tag{3.2}$$

where R_{Vp} is defined:

$$R_{Vp}(\tau) = \int_{-\infty}^{\infty} V(t)p(t+\tau)\,\mathrm{d}\tau, \tag{3.3}$$

where $V(t)$ and $p(t)$ are the velocity magnitude and pressure signals in the time domain, respectively.

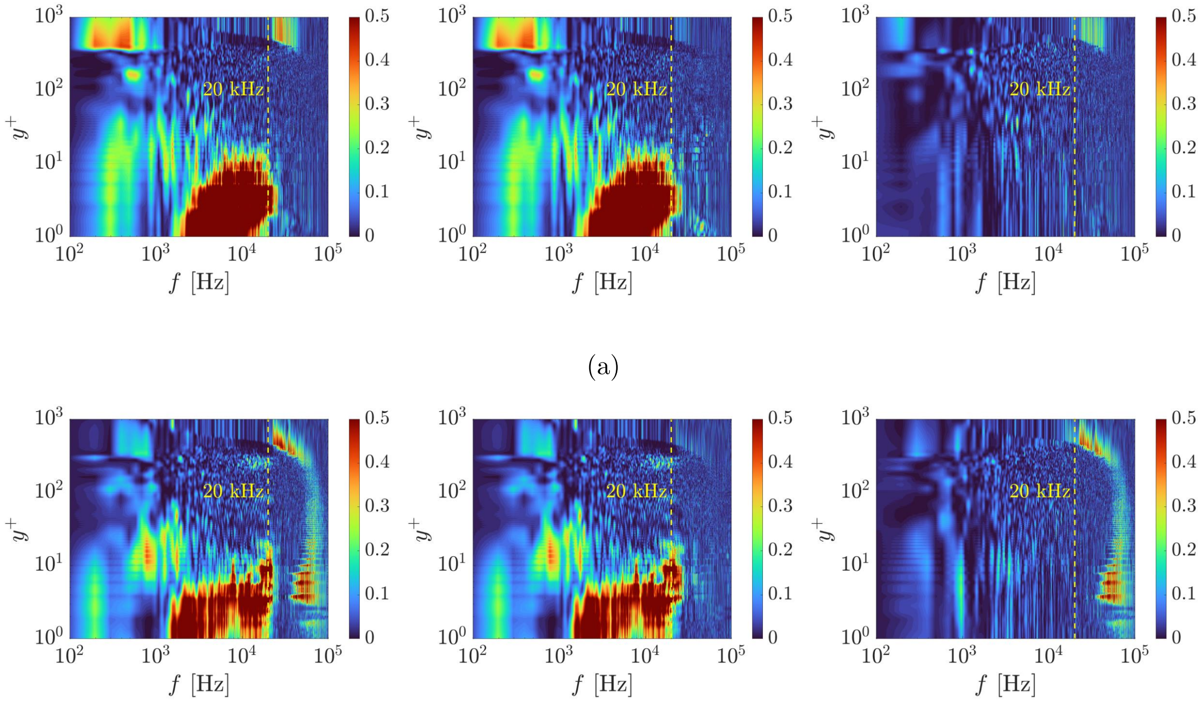

(a)

(b)

Figure 3.11: Velocity-pressure coherence, γ^2_{Vp}, of the original pressure (left), the denoised pressure (mid) and the background noise (right) at x/c: (a) 0.83 and (b) 0.99.

Figure 3.11 presents the velocity-surface pressure coherence to determine the relative contribution of the original and decomposed spectral components in the boundary layer region at various streamwise locations. The left, middle, and right columns represent the original pressure, denoised pressure, and background noise, respectively. It is evident that the denoised pressure is highly correlated with the velocity at low-to-mid frequencies up to $y^+ \approx 1000$. Localized high coherence stretches from 2 to 20 kHz within the viscous sublayer and buffer layer, $y^+ < 10$, at the selected streamwise locations. These velocity-pressure-based coherent sources are characterized experimentally by Szoke et al. [161] in turbulent boundary layers over a flat plate. This demonstrates that the coherent or denoised pressure is primarily influenced by the interaction of the turbulent boundary layer flows with the wall.

The velocity-background noise coherence appears strong along the wall-normal distance at $x/c = 0.99$, which is consistent with the observation that the incoherent portion is found to be noticeable as oval shapes near the trailing edge, as shown in Fig. 3.4(a).

The sound pressure spectrum level (SPSL) [67] is defined as:

$$\mathrm{SPSL} = 10\log_{10}\frac{\mathrm{PSD}\Delta f_{\mathrm{ref}}}{P_{\mathrm{ref}}^2}, \tag{3.4}$$

where PSD is the power spectral density of the pressure, $\Delta f_{\mathrm{ref}} = 6.66$ Hz, and $P_{\mathrm{ref}} = 20$ μPa.

SPSLs for the denoised pressure, background noise, and the original pressure are plotted in Fig. 3.12. As seen in the case of the wall pressure spectra in Fig. 3.6 and the velocity-pressure coherence in Fig. 3.11, the denoised pressure dominates most of the pressure spectra in the viscous boundary layers. The background noise has less than 20 dB at frequencies above 20 kHz, which can be considered negligible when compared to the denoised spectral amplitude.

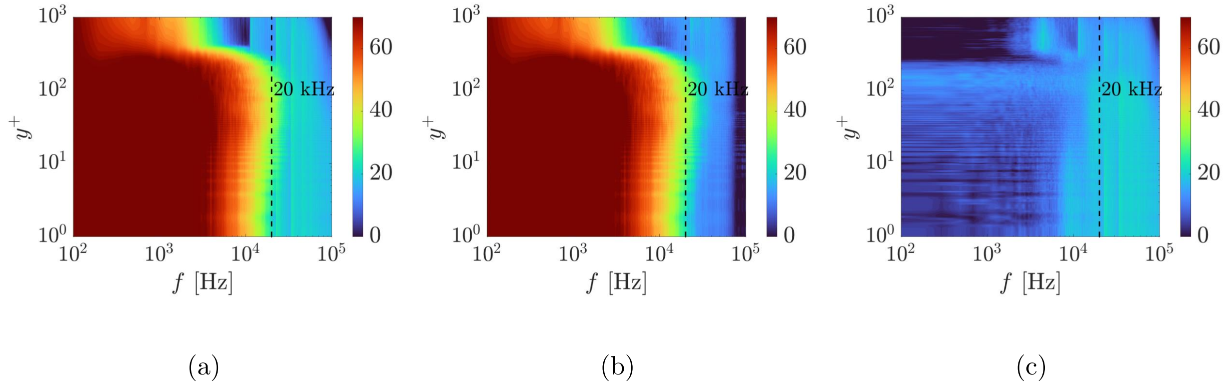

(a)

(b)

(c)

Figure 3.12: SPSLs at $x/c = 0.99$: (a) original pressure, (b) denoised pressure, and (c) background noise.

3.1.2.4 Dilatation and Dynamic Mode Decomposition around Airfoil

Figures 3.13(a) to 3.13(c) display the dilatation fields of the original and decomposed pressures. In Fig. 3.13(b), the denoised pressure captures both the physical flow and acoustic features: the near-wall flow structures involving coherent hydrodynamic convection and the far-field sound propagation. Moreover, the tripping region is a significant source of background noise, which is denoised as shown in Fig. 3.4(b). However, the denoised and original pressures are found to be similar close to the trailing edge due to the dominant physical flow phenomena accompanied by acoustic perturbations of non-Gaussian and non-diffusive coherent pressure, even though the background noise is denoised. Compared to the con-

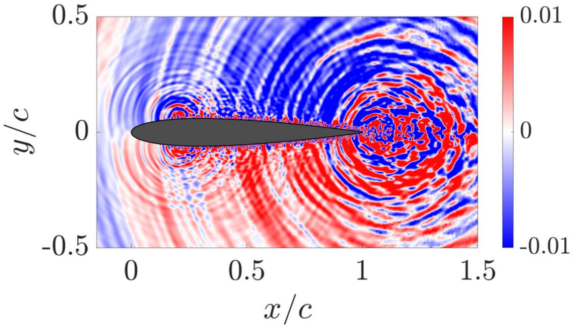

(a)

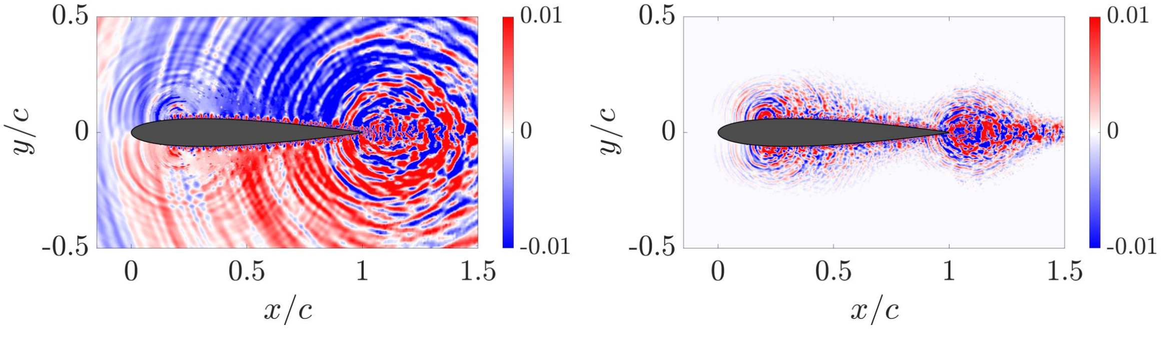

(b) (c)

Figure 3.13: Dilatation fields cut in midspan for (a) the original pressure, (b) the denoised pressure, and (c) the background noise.

verged incoherent portion in Fig. 3.4(a), the denoised pressure field demonstrates that it is representative of the original pressure with a few but high wavelet coefficients. This is consistent with observations in previous works when denoising-based wavelet filtering is applied to homogeneous isotropic turbulent flow [62, 63], inhomogeneous vortex bursting [59], and jet flows [67]. In Fig. 3.13(c), the topology of the background noise exhibits disorganized and random characteristics in the pressure field. It is not surprising that the background noise field resembles the spatial distributions of the converged incoherent portion, as shown in Fig. 3.4(a), since the background noise is generated from the incoherent wavelet coefficients. As discussed in Fig. 3.4, it is found that the background noise is dominant where acoustic waves are generated near the tripping, as demonstrated by Bodling and Sharma [18], and trailing-edge regions. This might be due to the diffusive, homogeneous, and random motion characteristics of turbulence filtered from turbulent flows [64] or insufficient grid resolution in these regions. However, It cannot be determined which factor is more dominant from the denoising algorithm. Note that the background noise is primarily distributed around the airfoil and does not propagate significantly to the far field, so it cannot be solely characterized as acoustic pressure propagating with the speed of sound in wall-bounded turbulent flows at a low Mach number.

Global pressure structures at particular frequencies of interest are calculated using DMD. All the discrete-time eigenvalues and five eigenvalues of interest are plotted on a red-dashed unit circle in Fig. 3.14. The zero real part of the eigenvalue, i.e., $f = 0$, denotes the stationary mode, indicating that the flow field is neither growing nor decaying in time [162]. To verify that the sampled flow field of DMD is in statistical equilibrium, the stationary DMD mode is compared with the time-averaged pressure field, as shown in Fig. 3.15. The

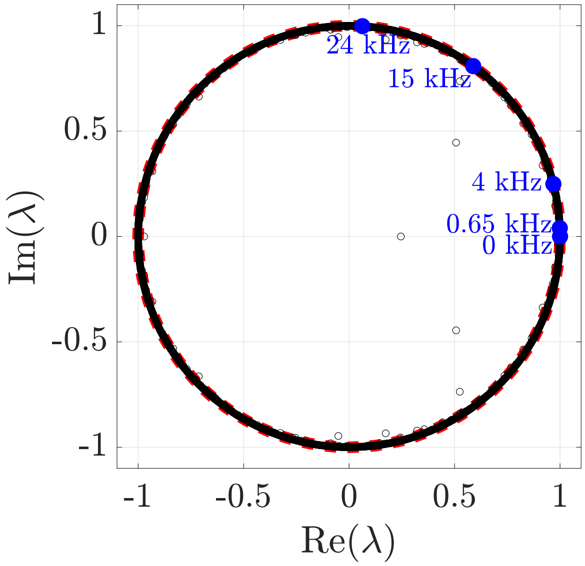

Figure 3.14: All eigenvalues of DMD modes highlighting five eigenvalues of interest with a red-dashed unit circle.

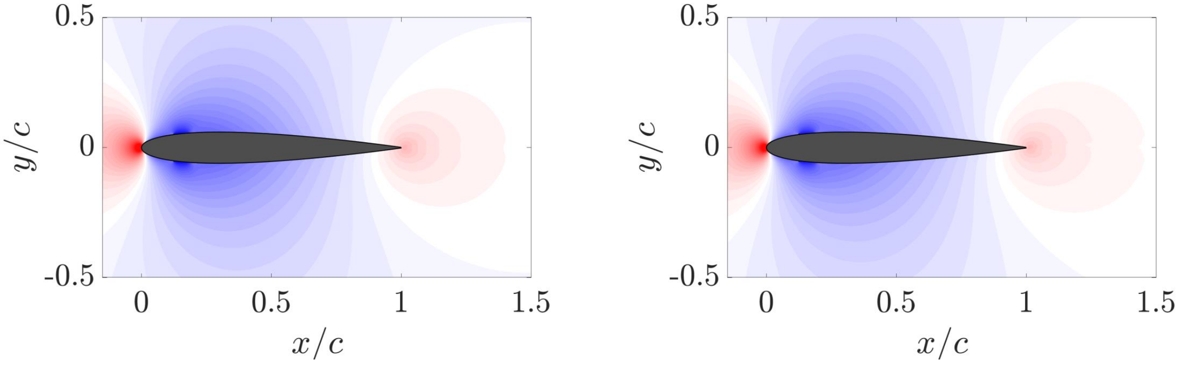

(a)

(b)

Figure 3.15: (a) Time-averaged pressure field and (b) stationary DMD mode, f=0. The blue and red colors denote the lower and higher values, respectively.

pressure field of the stationary mode is represented by the eigenvector, which is a different quantity from the time-averaged pressure profile. Therefore, color scales are omitted for qualitative comparison. It is demonstrated that the time-averaged pressure field is similar to the pressure field captured by DMD, which serves as a simple validation of the statistical equilibrium of the present flow snapshots for the DMD analysis [162].

Four extracted DMD modes are visible in Figs. 3.16(a) to 3.16(d) for the original pressure,

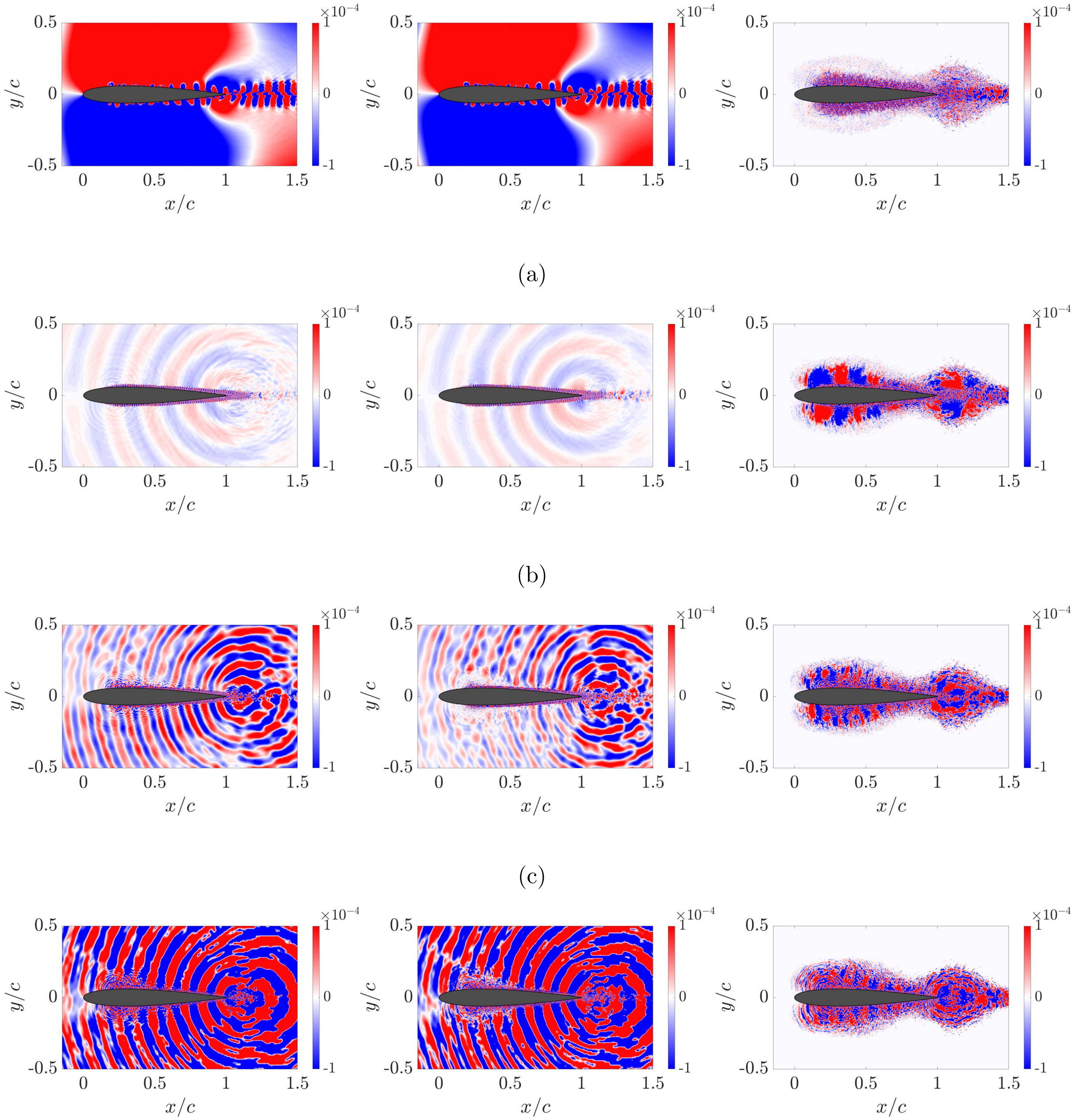

(a)

(b)

(c)

(d)

Figure 3.16: DMD modes for the original pressure (left), the denoised pressure (mid) and the background noise (right) at about (a): 0.65 kHz, (b): 4 kHz, (c): 15 kHz, and (d): 24 kHz.

denoised pressure, and background noise. The denoised pressure exhibits localized wavy structures near the wall, advecting along both sides of the airfoil at frequencies from 0.65 to

4 kHz. However, these structures increasingly vanish at high frequencies, which is associated with the decay of the wall pressure spectra at high frequencies. The denoised pressure also shows edge scattering of the coherent near-wall pressure fluctuations, a typical trailing-edge noise generation in the form of antisymmetric waves between the suction and pressure sides, which was also confirmed by the spectral proper orthogonal decomposition technique [109]. This antisymmetric waveform is known to intensify the scattered sound [6]; however, it is not observed at high frequencies where in-phase waves propagate. It is found that denoising is primarily significant at high frequencies, as shown for the denoised pressures at 15 and 24 kHz in Figs. 3.16(c) and 3.16(d). This observation is consistent with the wall pressure spectra of background noise starting to contribute to the original pressure at these frequencies, as presented in Figs. 3.6 and 3.12. In contrast, the topology of the background noise exhibits decorrelated and disorganized random structures. Although the background noise propagates in the near-wall region at high frequencies, such propagation is limited only to the area near the wall and hardly extends to the far field, unlike the behavior of denoised or physical acoustic waves.

3.1.3 Sound Pressure Level at Far Field

The far-field pressure spectra are computed for the original and decomposed components using the FW-H acoustic analogy, which is presented in Fig. 3.17. KATO's correction [153] is not applied in this simulation, as our goal is to compare the contributions from the original and decomposed pressures. As seen in the wall pressure spectra in Fig. 3.6, the denoised pressure primarily contributes to the far-field acoustics, while the background

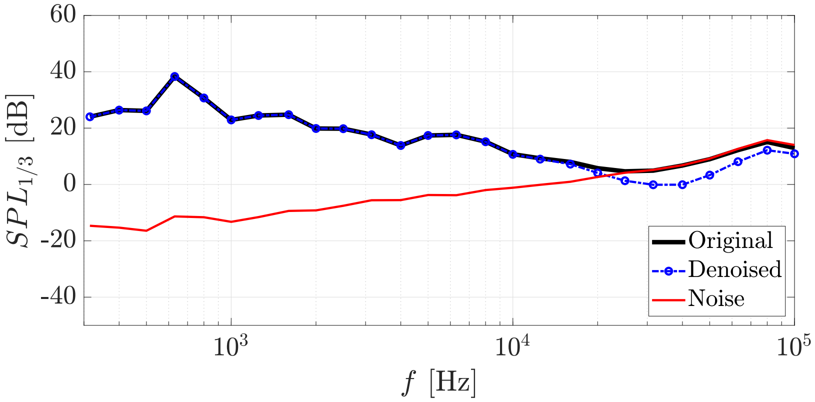

Figure 3.17: Sound pressure level at an observer location $x/c = 1.0$, $y/c = 4.06$, z/c =midspan for the original and decomposed pressures.

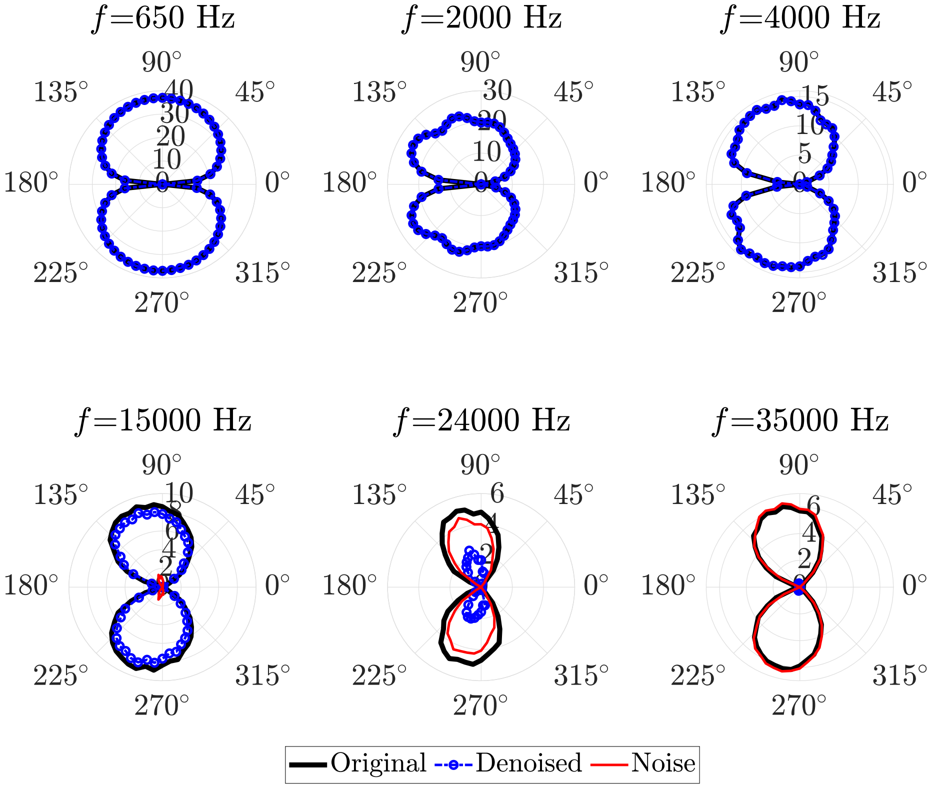

Figure 3.18: Directivity of sound pressure levels at several frequencies at the radius of $4.06c$ on the origin of the trailing edge in midspan for the original and decomposed pressures.

noise becomes dominant beyond 20 kHz. This observation further confirms that the far-field acoustic pressure is not explained by the incoherent component of pressure. The sound directivity is plotted at several frequencies in Fig. 3.18. A compact dipole behavior is observed at 0.65 kHz, and cardioid shapes are evident from 2 to 4 kHz, which is associated

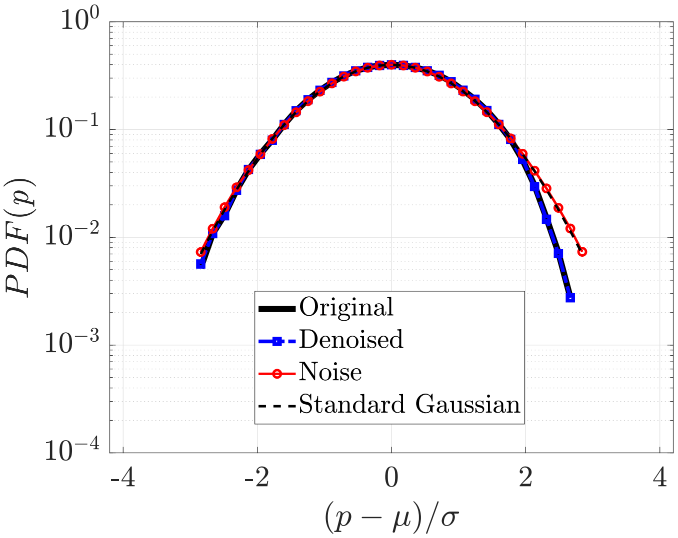

Figure 3.19: Polar evolution of PDFs for the original and decomposed pressures at an observer location $x/c = 1.0$, $y/c = 4.06$, $z/c =$midspan.

with trailing-edge noise [23]. This physical acoustic spectrum has the highest contribution from the denoised pressure at these frequencies, suggesting that airfoil noise is represented by the denoised pressure. On the other hand, the background noise exhibits a simple dipolar pattern, with its contribution becoming more prominent beyond 24 kHz, although the sound amplitude is negligible. The tonal acoustic peak at about 0.65 kHz is due to the trailing-edge bluntness noise. This is supported by the DMD modes of the original and denoised pressure in Fig. 3.16 depicting the acoustic propagation emanated from the trailing edge. The acoustic tonal peak observed in Fig. 2.11 can be speculated as the same noise characteristics although the simulation case is different, but the two flows are in similar Reynolds numbers and Mach numbers.

Figure 3.19 shows the PDFs of the original and decomposed pressures. The PDF of the background noise is identical to a standard Gaussian distribution. However, the denoised pressure is off the Gaussian distribution in the positive tail, which is in contrast to the quasi-Gaussian distribution of acoustic pressure in high-Mach jet flows [67, 147]. This indicates that the assumption of Gaussian distribution cannot be solely relied upon for filtering the acoustic pressure in wall-bounded flows at low Mach numbers. In addition, airfoil noise consists of both tonal and broadband acoustic waves at low to high frequencies [10], which makes it challenging to extract the acoustic component.

Overall, when the wavelet filtering technique is employed for airfoil noise in a low Mach number flow, it can effectively separate the acoustic and pseudo-acoustic components, which are represented by the denoised pressure and background noise, respectively. As a result, this approach provides useful information on where to truncate the frequency in the far-field noise spectrum to interpret the physical noise.

3.1.4 Summary

This section decomposed the pressure field around a NACA 0012 airfoil in low Mach number flows using a wavelet filtering based on the recursive denoising algorithm. The filtered pressures were split into coherent and incoherent pressure, designated as denoised pressure and background noise, respectively. This was supported by comparing the wavelet-based decomposed pressures to the conventional wavenumber-frequency decomposition method.

Various spectral analyses were performed on the original and decomposed pressures on the wall and around the airfoil. The results showed that the denoised pressure has a few but high wavelet coefficients and represented physical phenomena such as hydrodynamic wavy structures advecting along the wall and sound scattering mechanisms near the tripping region and trailing edge. On the other hand, the contribution of the background noise to the original pressure was found to be primarily dominant at high frequencies, with lower wavelet coefficients or sound spectrum levels compared to the denoised pressure. These findings were consistent with previous works that applied the wavelet-denoising algorithm to homogeneous isotropic turbulent flow, inhomogeneous vortex bursting, and jet flows. The effect of denoising was found to be noticeable near the tripping and trailing-edge regions where background noise was mostly produced. The underlying reasons for this effect may be due to the diffusive, homogeneous, and random motion characteristics of turbulence filtered from turbulent flows, or insufficient grid resolution. However, it is difficult to determine which factor was more dominant. It was shown at the far-field acoustic spectra that the background noise is dominant at high frequencies, despite having a negligible sound amplitude. The PDF shape of denoised pressure was off the Gaussian distribution in the positive tail, which contrasted with acoustic pressure in high-Mach jet flows, whose PDF shape was closer to the quasi-Gaussian distribution. This confirmed that the acoustic pressure on wall-bounded flows at a low Mach number could not be solely filtered with the Gaussian assumption.

3.2 Fourier-based Pressure Decomposition

3.2.1 Behaviors of Hydrodynamic and Acoustic Pressures on The Wall

This section delves into the wall pressure data derived from LES conducted at a chord-based Reynolds number, $Re = 4 \times 10^5$, and Mach number, $M = 0.058$. Our objective is to decompose this wall pressure into its hydrodynamic and acoustic components. It is crucial to highlight that the key factor enabling this decomposition is the difference in phase speed between these two pressure components. This decomposition process is achieved through wavenumber-frequency decomposition, as detailed in Sec. 2.3.2. Special emphasis is placed on understanding the characteristics and nature of these decomposed pressure components acting on the wall.

Figure 3.20 provides an illustration of the spanwise-averaged wavenumber-frequency spectrum on the upper side of the airfoil. In the plot, a wide-band ridge is prominently visible aligned with the freestream velocity U_∞. It is noted that the hydrodynamic pressure is characterized by turbulent convection, displaying high-energy spectra within the convective speed range of U_c. Another noteworthy observation emerges from the spectra along the boundaries of two sound speeds: upstream $U_c - c_o$ and downstream $U_c + c_o$. The upstream acoustic pressure is likely associated with the trailing-edge scattering of coherent structures. In contrast, the downstream acoustic pressure could be attributed to the influence of vortex shedding from trailing-edge bluntness and leading-edge noise sources due to boundary-layer tripping. These aspects will be further explored in subsequent analyses.

Figure 3.21 presents space-time contour maps for three decomposed pressures in addition to the original pressure. The time scale is normalized using the phase speed of each de-

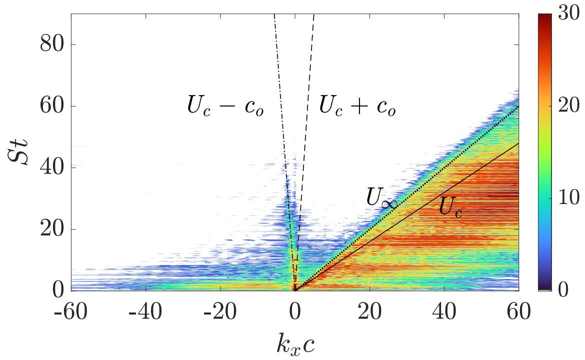

Figure 3.20: Spanwise-averaged wavenumber-frequency spectrum on the upper side of the airfoil from the leading edge to trailing edge.

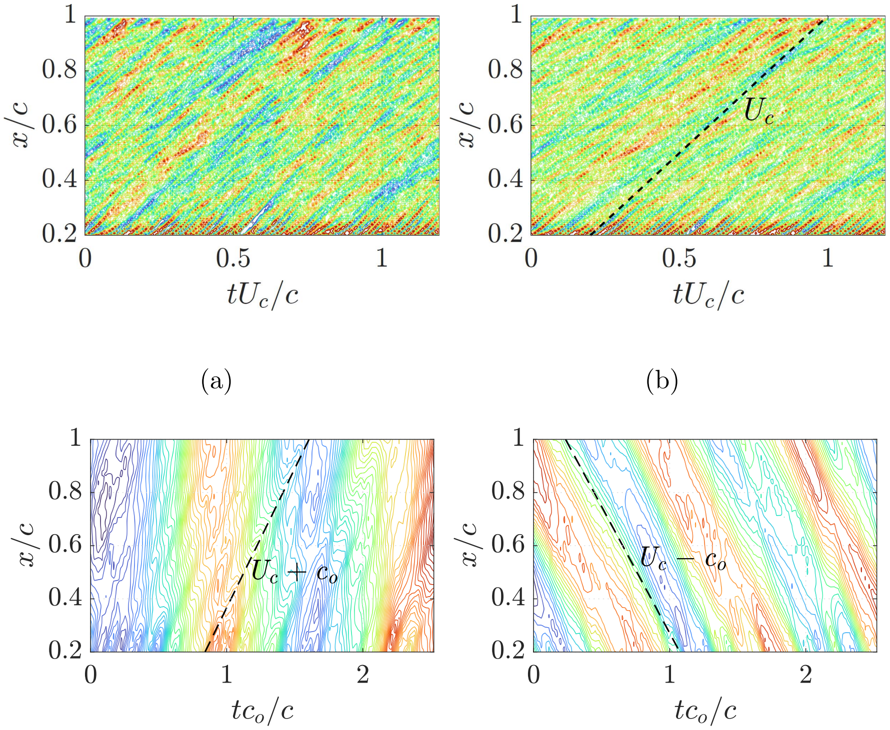

Figure 3.21: Space-time map of original and decomposed pressures: (a) original pressure, (b) hydrodynamic pressure, (c) acoustic pressure in the downstream direction, and (d) acoustic pressure in the upstream direction. The time scale on the x-axis for the original and hydrodynamic pressures is normalized by the convective velocity, whereas the time scale for the upstream and downstream acoustic pressures is normalized by the speed of sound, c_o. The lines of phase velocity are shown on each decomposed pressure.

composed pressure to emphasize the propagation effect. The time duration for the original and hydrodynamic pressures spans 1 airfoil FTT, while the duration for the acoustic pressure is 0.1 FTT. As depicted in the plot, the hydrodynamic pressure closely resembles the original pressure, indicating that near-wall pressure fluctuations are primarily governed by high-energy turbulent streaks, as observed in Refs. [163, 164]. The plot effectively captures the intense pressure fluctuations in the flow tripped after $x/c \approx 0.2$ and their time-accurate convection. In Fig. 3.21(c), the presence of wrinkles represented by contour lines signifies downstream propagation from the leading edge to the trailing edge. On the other hand, in Fig. 3.21(d), the upstream propagation aligns well with its phase speed, indicating that the wavenumber-frequency decomposition along the airfoil chord effectively separates the acoustic components from the hydrodynamic pressure disturbances. This representation provides valuable insights into the spatiotemporal dynamics of flow and acoustic components.

Given that both upstream and downstream acoustic pressures exhibit similar phase speeds, these two components are combined into a single acoustic pressure for a comprehensive examination of their source and propagation characteristics in comparison to the hydrodynamic component. Figure 3.22 illustrates the spanwise-averaged temporal fluctuations for the original, hydrodynamic, and acoustic pressures, measured at a reference point located at $x/c = 0.99$ from the leading edge. It is worth noting that the magnitude of the hydrodynamic pressure closely resembles that of the original pressure, while the acoustic pressure exhibits weaker fluctuations. This observation aligns with the common understanding that acoustic energy is a byproduct of noise-producing flow fluctuations [15, 165]. These findings from the wall will further be cross-examined with the decomposed far-field pressure perturbations in the subsequent section.

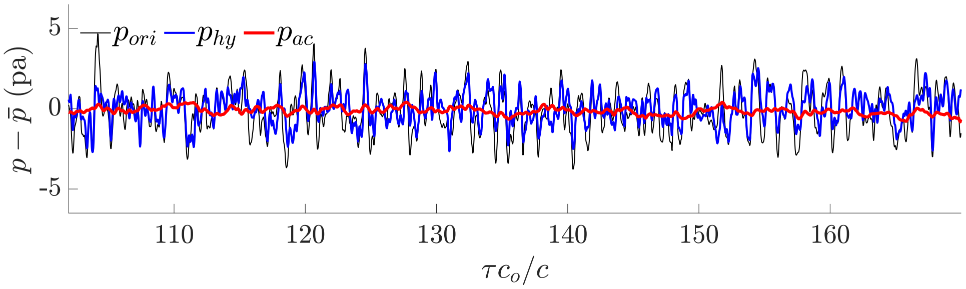

Figure 3.22: Spanwise-averaged decomposed wall pressure fluctuations at $x/c \approx 0.99$.

The fundamental characteristics of the decomposed wall pressures are subjected to statistical assessment through the calculation of their coherence and phase. To begin, a spanwise pressure coherence [160, 166] is defined as follows:

$$\gamma^2(z, \Delta z, f) = \frac{|\phi_{pp}(z, \Delta z, f)|^2}{|\phi_{pp}(z, 0, f)||\phi_{pp}(z + \Delta z, 0, f)|}, \tag{3.5}$$

where the cross power spectrum density (CPSD) Φ_{pp} is the Fourier transform of the space-time cross-correlation function:

$$\phi_{pp}(z, \Delta z, f) = \int_{-\infty}^{\infty} \left\langle p(z,t)p(z + \Delta z, t + \tau) \right\rangle \mathrm{e}^{-\mathrm{i}f\tau} \, \mathrm{d}\tau, \tag{3.6}$$

where $\mathrm{i} = \sqrt{-1}$, and the operator $\langle \cdot \rangle$ denotes the ensemble average over the spanwise separation distance, Δz.

Figure 3.23 presents the variation of coherence with respect to the non-dimensional separation distance $\Delta z/c$ and Strouhal number for both the hydrodynamic and acoustic pressures. The coherence pattern of the original pressure, which closely resembles that of the hydrodynamic pressure, has been excluded from the plot for clarity. An evident observation is the incoherent nature of the hydrodynamic pressure, whereas the acoustic pressure exhibits strong coherence along the spanwise direction. This observation confirms that the spanwise coherent structure of acoustic pressure disturbances is associated with trailing-edge noise [109, 167]. Notably, the spanwise coherence is particularly pronounced at low frequencies around $St \approx 10$, which can be attributed to the source of vortex shedding noise due to trailing-edge bluntness.

Next, the streamwise pressure coherence is computed based on the spanwise-averaged wall pressure. A fixed reference pressure, denoted as p_{ref} and located at $x/c = 0.99$, is used to assess the coherence between the trailing-edge noise source and other sources along the airfoil side. This calculation does not require the ensemble averaging process. Figure 3.24 illustrates the streamwise coherence distribution along the upper side of the airfoil for all Strouhal numbers. It is worth noting that the hydrodynamic pressure exhibits only a small region of coherence near the trailing edge, corresponding to the size of coherent turbulent eddies. As one moves further away from the trailing edge, the coherence rapidly diminishes, resulting in an incoherent pattern. In contrast, the acoustic pressure displays significant coherence spanning the entire chord length, particularly in the Strouhal number range of 15 to 30. At Strouhal numbers less than 10, the straight, uniform coherence lines indicate a compact noise source with a wavelength longer than the acoustic chord length. As the Strouhal numbers increase, the appearance of wavy lines signifies non-compact noise sources associated with acoustic scattering. It is essential to note that this coherence measure does not consider the spectral magnitude but provides some insights into the correlation between the point source at the trailing edge and pressure disturbances at other regions.

To gain insights into sound propagation characteristics, including constructive and destructive wave interferences, the phase of the acoustic pressure along the streamwise direction is analyzed. The phase difference between two points is computed as $\Re(\exp(\mathrm{i}\phi_{xy}))$, where ϕ_{xy} represents the phase of the CPSD. The subscript x refers to an arbitrary point on the upper side of the airfoil, while the subscript y denotes the fixed reference point at $x/c \approx 0.99$, as

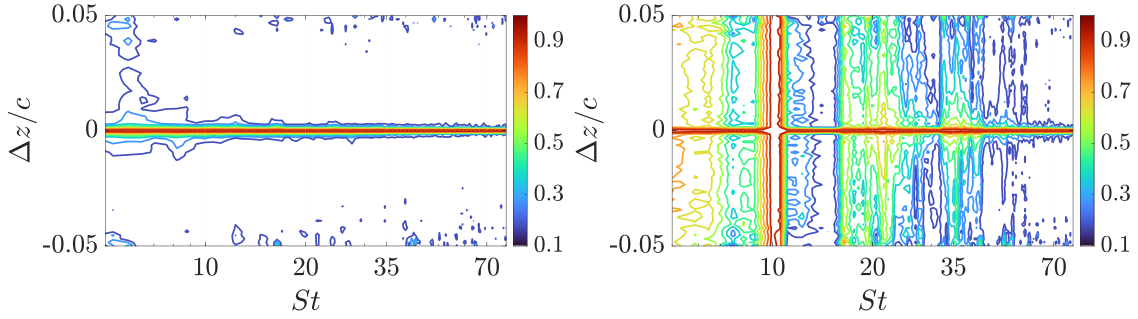

(a)

(b)

Figure 3.23: Contours of spanwise coherence, γ^2_{pp}, at $x/c = 0.99$: (a) hydrodynamic pressure and (b) acoustic pressure.

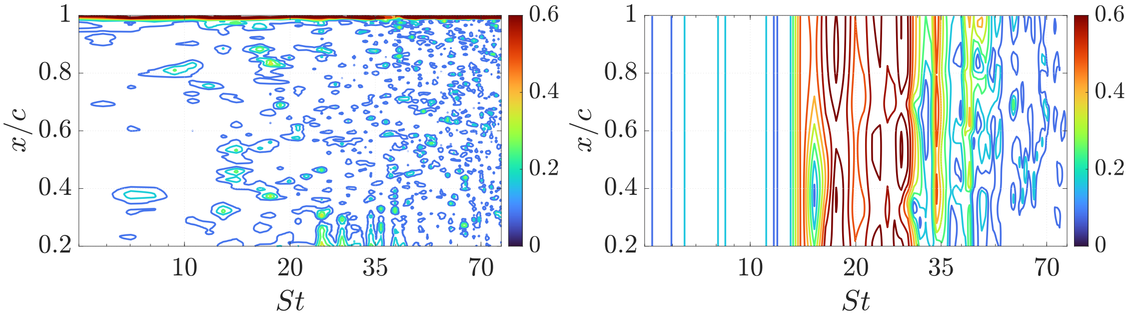

(a)

(b)

Figure 3.24: Contours of streamwise coherence, $\gamma^2_{pp_{\text{ref}}}$. The reference pressure is the original pressure located at $x/c \approx 0.99$: (a) hydrodynamic pressure and (b) acoustic pressure.

used for streamwise and spanwise coherences. It is important to note that the original pressure is used as the reference pressure at a fixed position. Additionally, to observe this phase interference within the local coherent structure for non-frozen gust [168], the streamwise correlation length is employed:

$$l_x^*(f) = \int_{\xi_1}^{\xi_2} \gamma(\xi, 0, f)\mathrm{d}\xi, \tag{3.7}$$

where ξ represents the streamwise separation distance normalized by the chord length, and the integration spans from $0.2c$ to x, where turbulent flows are established. Constructive or destructive wave interferences are only meaningful within this streamwise correlation length for the non-frozen gust case [168]. In this analysis, x is placed at the trailing edge, which means that the correlation length is computed at the trailing edge. Equation (3.7) is validated by comparing it with the empirical model [169], which is provided in Appendix C. Figure 3.25 illustrates the streamwise-phase distribution along the airfoil streamwise direction on the upper side. A black dashed line indicates the streamwise correlation length, starting from the trailing edge at $St \approx$10, 20, and 35. The phase values close to 1 indicate that the two wall-pressure signals are in-phase, while values close to -1 signify an out-of-phase relationship [166]. The hydrodynamic pressure exhibits high oscillations between neighboring sources across a range of Strouhal numbers, suggesting that destructive interference is a characteristic feature of hydrodynamic pressure, likely associated with the streaky structure in streamwise direction among turbulence structures [109, 167], as observed in Fig. 3.21(a). In contrast, the acoustic pressure shows a much longer waveform. At around $St \approx 10$, there is a constant in-phase relationship due to the longer wavelength at this frequency, which aligns with the observation of streamwise coherence (Fig. 3.24(b)). As the Strouhal number increases, it transitions to a shorter waveform associated with a non-compact source. The waveforms are observed to have one or two periods for the acoustic pressure for the entire airfoil length; however, the phase interference is only effective within the local turbulent coherent structure since the phase interference operates independently at each correlation interval. In this context, the phase alteration for the acoustic pressure within the streamwise correlation length is found to be in phase, making it efficient for sound propagation. These results suggest that the hydrodynamic pressure is ineffective in terms of sound generation due to strong destructive interference, while the acoustic pressure is effective for far-field sound

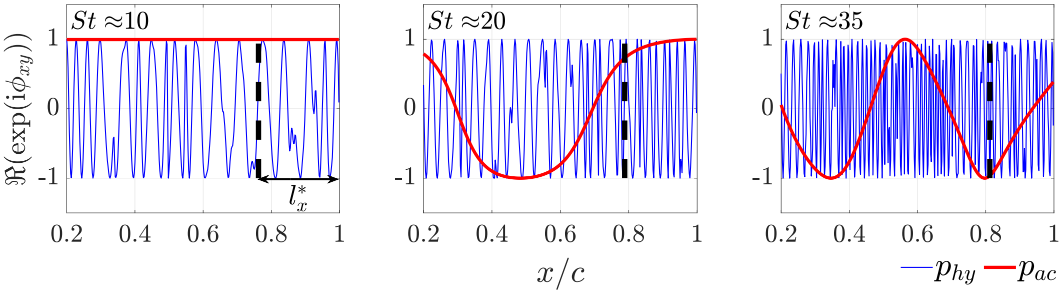

Figure 3.25: Spanwise-averaged phase distributions for the hydrodynamic and acoustic pressures along with the streamwise correlation length at the trailing edge at $St \approx$ 10, 20, and 35.

propagation due to constructive interference. This observation will be further supported with more detailed far-field noise analyses and in comparison with analytical models in the subsequent sections.

3.2.2 Evaluation of Hydrodynamic and Acoustic Pressures at Near and Far Fields

In this section, the decomposed wall pressures are radiated through the FW-H acoustic analogy to examine the propagating nature of each component at near and far fields. Thus, the far-field pressure fluctuations in each decomposed component are either solely scrutinized or cross-correlated with near-field pressures. Figure 3.26 plots the contribution from the decomposed wall pressures to the far-field pressure at a receiver, located 10.0c away normal to the origin of the trailing edge in midspan. In contrast to the decomposed wall pressures, as shown in Fig. 3.22, the far-field pressure is significantly affected by the acoustic pressure on the wall, while the hydrodynamic component is negligible. The non-propagating nature of the hydrodynamic pressure is related to the destructive interference of incoherent turbulent structures in the streamwise direction, as presented in Fig. 3.25. This characteristic, marked by convecting turbulent streaks (Fig. 3.21(b)), aligns with the observation that

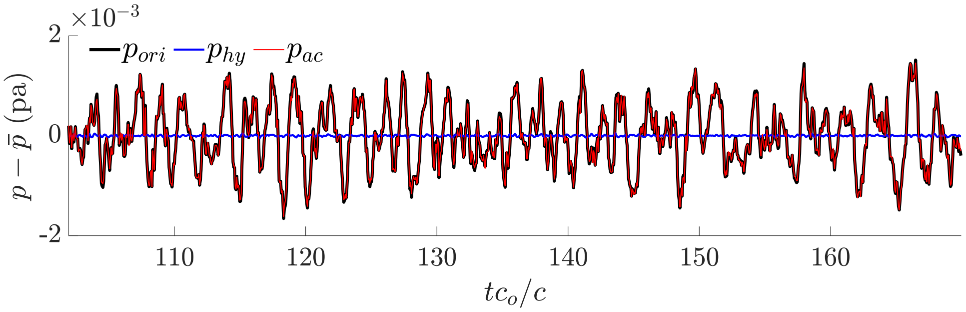

Figure 3.26: Radiated pressure fluctuations at an observer location $x/c = 1.0$, $y/c = 10.0$, and z/c=midspan. The far-field pressure is computed from the original or the decomposed pressure on the wall through FW-H equation.

the predominant streaky structures in the turbulent boundary layer have minimal effect on trailing-edge noise [109], whereas the efficiency of sound radiation is more likely related to the spanwise-coherent structure [167, 170].

The temporal signals of the propagation from surface hydrodynamic and acoustic pressures, as shown in Fig. 3.26, are statistically evaluated through the PDF. Figure 3.27 presents PDFs of the original and decomposed pressures. Neither hydrodynamic nor acoustic pressure follows a Gaussian distribution, as indicated by the deviation of one of the tails on the curve from the standard Gaussian shape. This suggests that the original pressure cannot be separated based on the hypothesis that the acoustic pressure follows a Gaussian assumption. This is different from previous observations where the Gaussian assumption was used to separate acoustic pressure from near-field pressure in jet flows at a Mach number of 0.9 using wavelet transform [67]. This observation is consistent with the finding of Kang and Lee [140].

Visual assessment of sound propagation and dominance near the airfoil for each decomposed pressure is performed by correlating the noise recorded at the far field with the near-field pressure field. The spatial domain pressures are averaged in the spanwise direc-

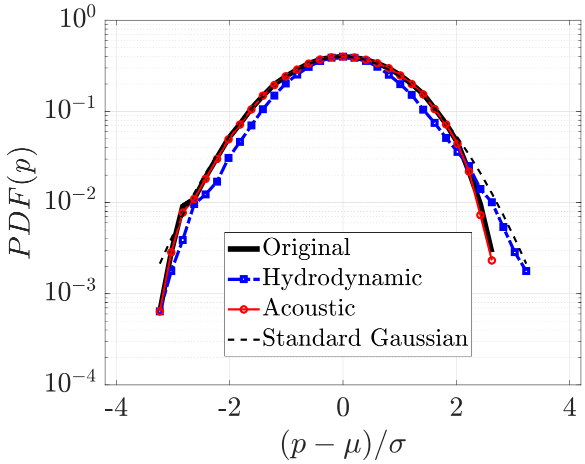

Figure 3.27: Polar evolution of PDFs for the far-field pressure that is obtained from the original, hydrodynamic, and acoustic wall pressures with the standard Gaussian distribution at the observer position of $x/c = 1.0$, $x/c = 10.0$, $z/c =$ midspan.

tion. Two statistical variables are employed: the phase of CPSD, $\Re(\exp(\mathrm{i}\phi_{xy}))$, as was used for the previous section, and the normalized spatial correlations when the temporal lag is equal to zero, denoted as $R_{\tilde{p}\tilde{p},\tau=0}$, which is a special case of the general definition of cross correlation [29, 160, 171] as follows:

$$R_{\tilde{p}\tilde{p}}(\mathbf{x_1}, \mathbf{x_2}, \tau) = \frac{E\left[\tilde{p}(\mathbf{x_1}, t)\tilde{p}(\mathbf{x_2}, t+\tau)\right]}{E\left[\tilde{p}^2(\mathbf{x_1}, t)\right]^{1/2} E\left[\tilde{p}^2(\mathbf{x_2}, t)\right]^{1/2}}, \tag{3.8}$$

where the operator $\tilde{\cdot}$ stands for the band-pass filter applied to the pressure signal, operator $E[\cdot]$ denotes the expected value of the signal, and τ is the temporal lag between two signals at point $\mathbf{x_1}$ and point $\mathbf{x_2}$. The threshold for filtering of interest ranged from $9 < St < 35$, which was found to be the best range from a series of numerical experiments to highlight the physical property of decomposed pressures. The point $\mathbf{x_1}$ is the arbitrary point near the airfoil at which the original pressure is used for the computation of spatial correlation. The reference pressure signal at point $\mathbf{x_2}$ is the far-field pressure propagated from either the hydrodynamic or the acoustic wall pressure measured at the observer location $x/c = 1.0$, $y/c = 10.0$, and $z/c =$ midspan. Figure 3.28 provides two contours of filtered normalized

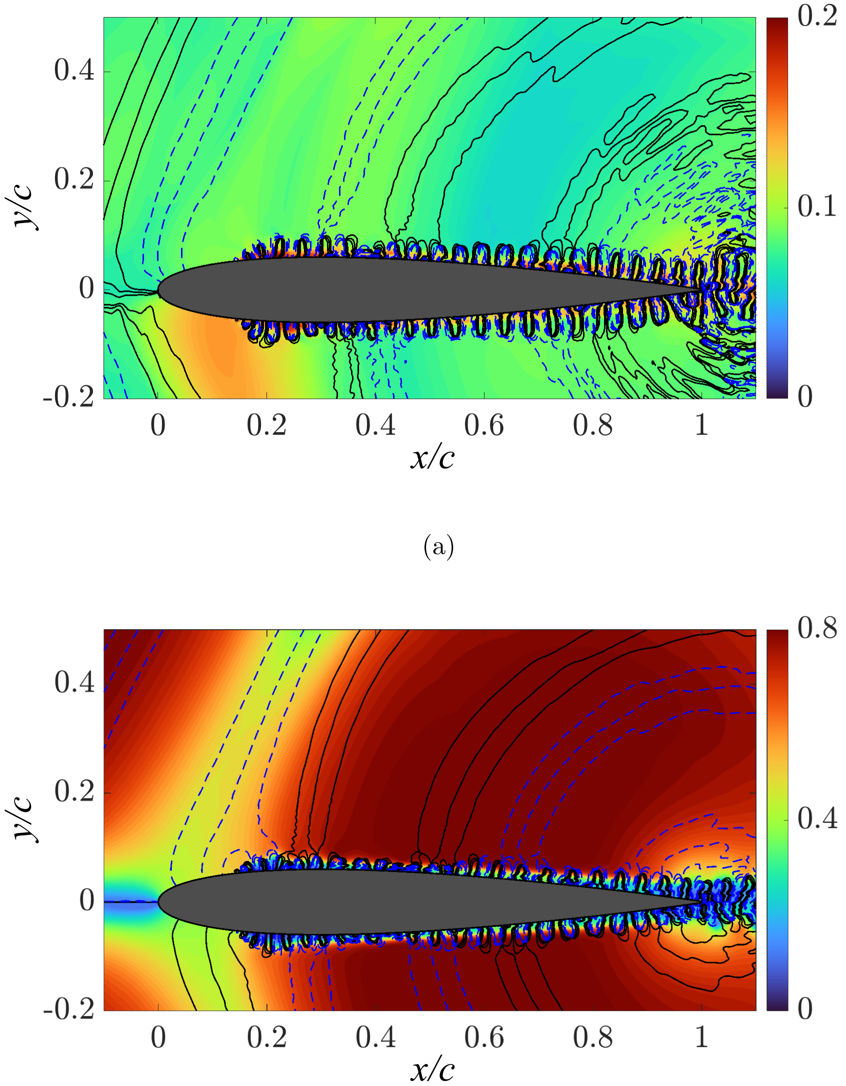

(a)

(b)

Figure 3.28: Normalized spatial correlations filtered at $9 < St < 35$ overlapped with line phase at $St \approx 20$ varying -1 (blue-dashed line) to 1 (black-solid line): (a) $R_{\tilde{p}_{ori}\tilde{p}_{hy,far},\tau=0}$ with $\Re(\exp(\mathrm{i}\phi_{p_{ori},p_{hy,far}}))$ and (b) $R_{\tilde{p}_{ori}\tilde{p}_{ac,far},\tau=0}$ with $\Re(\exp(\mathrm{i}\phi_{p_{ori},p_{ac,far}}))$.

spatial correlations: one between the filtered hydrodynamic pressure contribution at the far field and the original pressure in the spatial domain (Fig. 3.28(a)), and the other between the filtered acoustic pressure contribution at the far field and the original pressure in the spatial domain (Fig. 3.28(b)). Additionally, a line phase contour extracted at $St \approx 20$ is added to the plot to represent the nature of the sound propagation. The contour plots reveal coherent turbulent structures on both pressure components. These structures exhibit an out-of-phase behavior along the chord as shown in the phase plots (see Fig. 3.25). Sound generation from the trailing-edge scattering is evident in both plots. It means that the driving mechanism for far-field sound propagation concerns trailing-edge scattering for both two pressures, regardless of their noise strengths. The filtered normalized spatial correlations between the far-field hydrodynamic pressure contribution and near-field pressures show a relatively high correlation underneath the coherent structure. However, their distributions of coherent structures along the wall are out-of-phase with each other, leading to a dissipative or evanescent wave toward the far field. Thus, its contribution to the far field is negligible compared to the total acoustic pressure. On the other hand, the filtered normalized spatial correlations between far-field acoustic pressure contribution and near-field pressures are shown to be significantly high away from coherent turbulent structures. This indicates the efficient propagation of sound waves at speeds comparable to the speed of sound from the trailing edge. This sound source propagation phenomenon is related to the presence of in-phase within the turbulent length scale, as observed in Fig. 3.25.

Our findings revealed that the phase behavior, rather than the source magnitude, has a crucial impact on the differentiation between the roles of hydrodynamic and acoustic pressures, whether they function as actual sound or pseudo-sound sources. Subsequent analysis

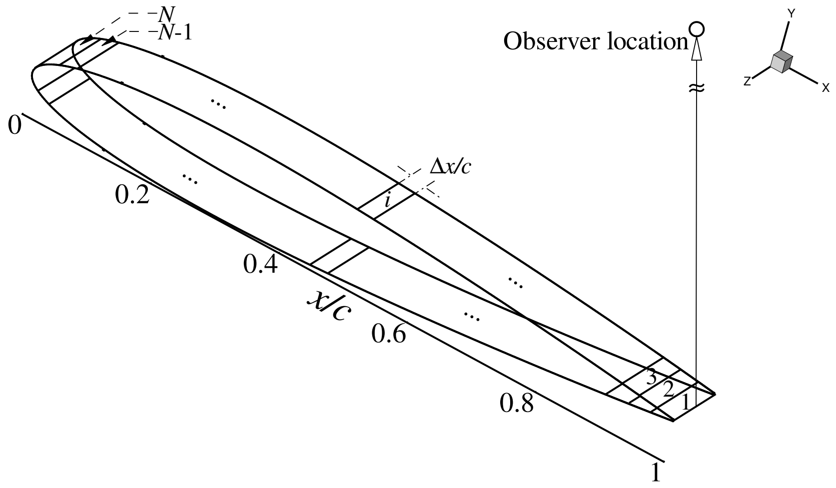

Figure 3.29: Schematic of sectional noise analysis. The index starts from the trailing edge. The observer is located at $x/c = 1.0$, $x/c = 10.0$, $z/c =$ midspan.

entails partitioning the airfoil into strips to emphasize the significance of phase variation. Figure 3.29 illustrates the schematic for the sectional noise analysis. The airfoil surface is evenly divided into strips with a width of $\Delta x/c = 0.011$. The wavelength corresponding to this strip size is the order of 10^3 of Strouhal number, which is considered small enough to treat the single strip as a point source independent of phase relation among neighboring strips. Two different pressures are to be evaluated; one corresponds to the sectional noise radiated from each strip, and the other is derived by gradually accumulating noise from the trailing-edge strip. This allows for a comprehensive analysis of decomposed noises with and without phase effects. All the analyses consider both sides of the airfoil, and the strip is marked from the trailing edge, increasing towards the leading edge. Noise radiated by the FW-H acoustic analogy from each strip is measured at the observer positioned $x/c = 1.0$, $y/c = 10.0$, and $z/c =$midpsan.

Figure 3.30 displays the octave band SPLs of the original and two decomposed sectional noises emitted from an array of strips on the airfoil surface. In this analysis, the impact

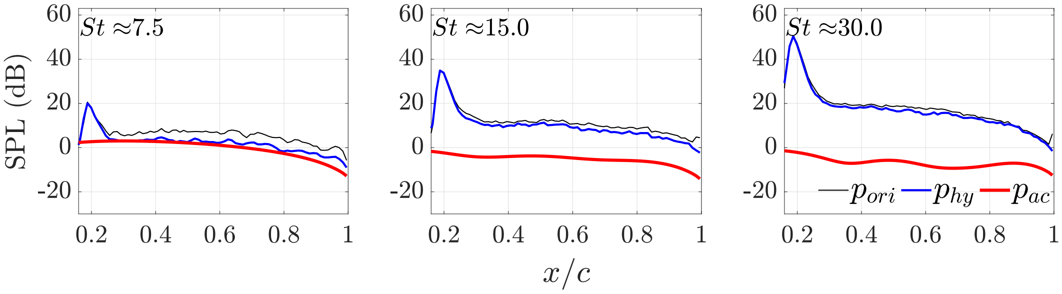

Figure 3.30: Octave band SPLs radiated from each strip arranged from the leading-edge region to the trailing edge on both sides of airfoil at $St \approx 7.5$, 15, and 30.

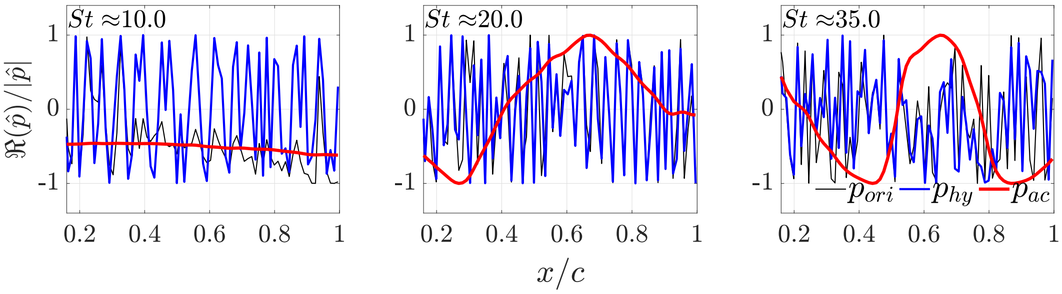

Figure 3.31: Phases of airfoil noise radiated from each strip arranged from the leading-edge region to the trailing edge on both sides of airfoil at $St \approx 10$, 20, and 35.

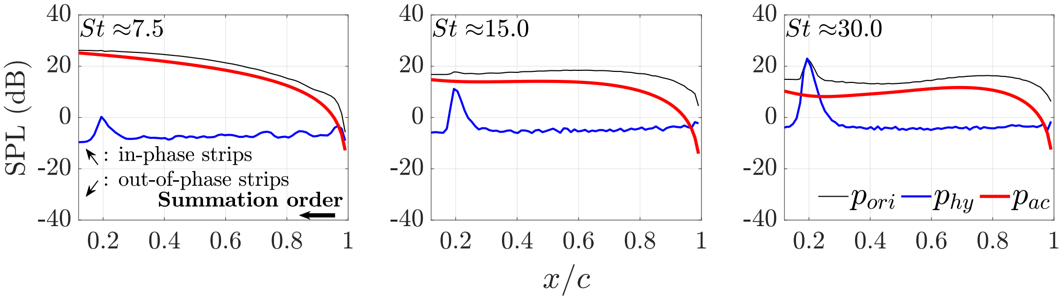

Figure 3.32: Cumulative octave band SPLs radiated from each strip arranged from the leading-edge region to the trailing edge on both sides of airfoil at $St \approx 7.5$, 15, and 30.

of phase interference among neighboring strips is excluded. Remarkably, the influence of the wall-associated hydrodynamic pressure on the far-field acoustics is evident across the entire airfoil, spanning from low to high Strouhal numbers. This effect is attributed to the high turbulent energy levels, which act as a self-noise point source beneath the coherent structure, as indicated in Fig. 3.28(a). When considering phase effects, the contribution of hydrodynamic pressure to the total pressure shows a substantial similarity between the wall and the far field. However, the opposite trend applies to the acoustic pressure, with the fluctuations of the acoustic pressure becoming lower than the hydrodynamic component [15, 165], which is similar to Fig. 3.22.

Figure 3.31 displays the phase distributions of the far-field pressure obtained from the original and decomposed pressures, calculated using the real part of the Fourier-transformed pressure of each strip divided by its absolute value. The phase of the hydrodynamic pressure contribution exhibits a pronounced oscillatory pattern across all Strouhal numbers, mirroring the out-of-phase feature of the coherent structure observed on the wall, as shown in Fig. 3.25. In contrast, the acoustic pressure contribution demonstrates an in-phase nature akin to what is observed on the wall. Shorter wavelengths at higher Strouhal numbers are thought to still exhibit in-phase characteristics when compared to the streamwise correlation length (see Fig. 3.25). This observation highlights that hydrodynamic pressure displays out-of-phase attributes among neighboring turbulent sources, providing crucial evidence that the far-field pressure from the hydrodynamic component is significantly lower than that from the acoustic component.

The cumulative pressure $p_i^{'}$ is calculated by gradually integrating the sectional pressures emitted from each strip as follows:

$$p_i^{'} = \sum_{k=1}^{i} p_k, \tag{3.9}$$

where p_k stands for the radiated noise from the trailing-edge strip to the k^{th} airfoil strip, and the subscript $k = 1$ denotes the trailing-edge strip. This incorporates the phase interference with strips being accumulated. Figure 3.32 provides a quantitative assessment of the two decomposed pressure contributions in comparison to the total pressure with respect to the octave band SPLs. In the figure, the upward and downward arrows represent in-phase and out-of-phase strips, respectively, while the summation order indicates the direction of the accumulation of strips. One can observe nearly uniform sound strength in the cumulative noise originating from hydrodynamic wall pressure. This consistent sound level across the airfoil underscores the typical phenomenon of destructive interference caused by streamwise incoherent turbulent eddies or streamwise turbulent streaks [163, 164]. There is a sudden increase in sound near the tripping region due to a local perturbation induced by the trip, but this spike is subsequently mitigated as a result of interactions between upward and downward scattering around the trip. Despite this cancellation, leading-edge noise near the tripped region contributes slightly to the overall sound at higher frequencies. Conversely, cumulative noise generated by acoustic wall pressure exhibits a progressive increase as strips are integrated. This can be attributed to constructive, in-phase relationships with neighboring sources. This in-phase nature is particularly notable at lower Strouhal numbers, where the corresponding wavelength exceeds the airfoil chord length. Another significant observation is the abrupt increase in noise from the trailing edge to approximately $x/c \approx 0.8$, coinciding with the region where edge scattering has a substantial impact. This region closely aligns

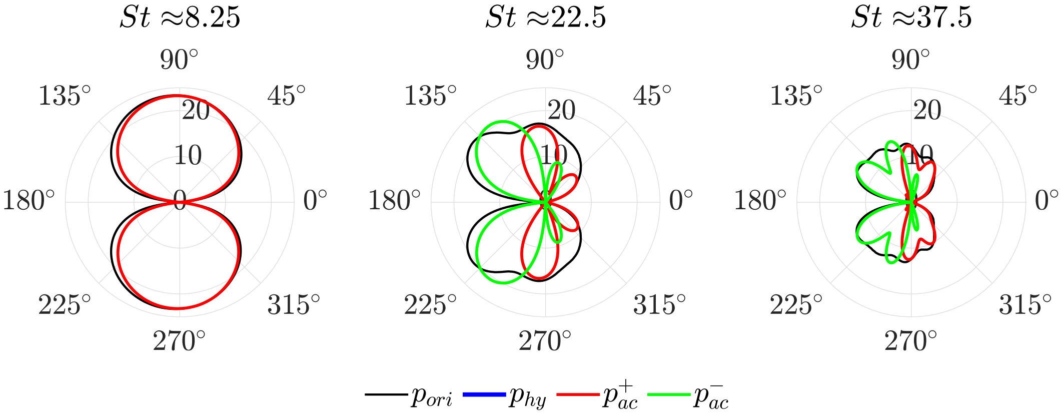

Figure 3.33: Directivity of the far-field pressures obtained from the original and decomposed wall pressures at the radius of 10.0c from the trailing-edge origin.

with the streamwise correlation length, as illustrated in Fig. 3.25. The width of approximately $x/c \approx 0.2$ suggests efficient scattering within the streamwise correlation length, which is shorter than the phase period of the acoustic wave. It is important to distinguish this local region of efficient scattering from the entire chord length, where the cancellation effect is presumed to occur. When compared to the sectional noises in Fig. 3.30, it demonstrates the non-propagating characteristic of hydrodynamic pressure when integrated, even though the sound spectra of point sources are similar to those of the total pressure. This non-propagating behavior arises from the out-of-phase relationships between neighboring strips, leading to rapid dissipation as evanescent waves. In contrast, noise radiation is found to be efficient for edge-scattered acoustic pressure.

Figure 3.33 presents the directivity patterns for the far-field sound spectra obtained from the original and decomposed pressures at three specific Strouhal numbers, highlighting two distinct propagating directions for acoustic pressure. The downstream-traveling acoustic pressure is denoted as p_{ac}^{+}, while the upstream-propagating acoustic pressure is denoted as p_{ac}^{-}. At $St \approx 8.25$, one can observe that the downstream-traveling acoustic pressure forms a compact dipolar pattern, which corresponds to a shorter acoustic source length or the chord length than the wavelength. This sound source is likely associated with vortex shedding caused by trailing-edge bluntness [140, 154]. When the noise source is nearly non-compact, the upstream-propagating pressure dominates, creating the forward cardioid pattern. The rearward lobes spanning more than 90° are contributed by the downstream-traveling acoustic pressure. While decomposed pressures, p_{ac}^{-} dominated by trailing-edge scattering and p_{ac}^{+} dominated by diffraction from leading-edge tripping installation, shows the distinct lobes at $St \approx 37.5$, the lobe pattern is alleviated for the total pressure. This results from the interaction of those multiple noise sources, although the strength of p_{ac}^{+} is much smaller than that of p_{ac}^{-} in the upstream direction. In contrast, the magnitude of hydrodynamic pressure is negligible due to destructive interference among coherent turbulent structures. This result contradicts the findings presented in Ref. [86], where hydrodynamic pressure was identified as the dominant noise source at the compact-dipolar frequency. However, as will be shown later, the directivity trend observed in the current numerical results aligns with the conclusions derived from the analytical approach. Although the magnitude of hydrodynamic pressure is minimal, its nonlinear interaction with varying wavenumbers in the streamwise and spanwise directions under large-to-small turbulent flows may alter the phase relationship between acoustic and total pressures [172]. These alterations can lead to an imperfect overlap of the total and acoustic pressure directivity patterns and their magnitudes, as similarly observed in Figs. 3.30 and 3.32.

3.2.3 Incident and Scattered Pressures in Amiet's Trailing-edge Noise Theory

The previous sections have explored the inherent characteristics of hydrodynamic and acoustic pressures, which were separated through wavenumber-frequency filtering within the numerical framework. This section pivots to evaluating the role of incident and scattered pressures on the wall and in the far field in the framework of analytical solution of Amiet's model. These pressures are derived based on assumptions stemming from flat plate geometry and the frozen turbulence hypothesis [77], as detailed in Sec. 2.2.2. Finally, this section concludes with a comparative analysis of far-field sound spectra obtained from numerical and analytical approaches.

Figure 3.34 presents the magnitudes of the incident and scattered pressures, as well as their cumulative values, across various Strouhal numbers. These wall pressures are calculated using Eqs. (2.15) and (2.17), respectively. The incident pressure exhibits exponential decay at all Strouhal numbers, with the rate of decay controlled by the parameter ϵ in Eq. (2.15). On the other hand, the scattered pressure reaches its maximum magnitude at the trailing edge and then rapidly decays from the trailing edge to the leading edge. This behavior is consistent with the idea that edge scattering is most significant near the trailing edge. It is important to note that while the magnitudes of the incident and scattered pressures are equal at the trailing edge, their cumulative value or total pressure is not simply the algebraic sum of the two pressures. Additionally, the combined pressure exhibits a distinct and highly oscillatory pattern, which will be examined in the subsequent phase analysis.

The phase variation along the airfoil chord is effectively represented by the real part of the wall pressure divided by its own magnitude, as demonstrated in Fig. 3.31. Figure 3.35 plots

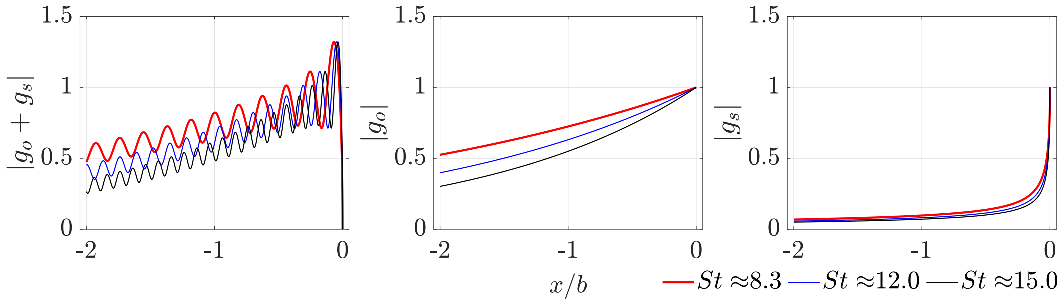

Figure 3.34: Magnitude of summation of incident (g_o) and scattered (g_s) wall pressures and each separate component side by side for three Strouhal numbers.

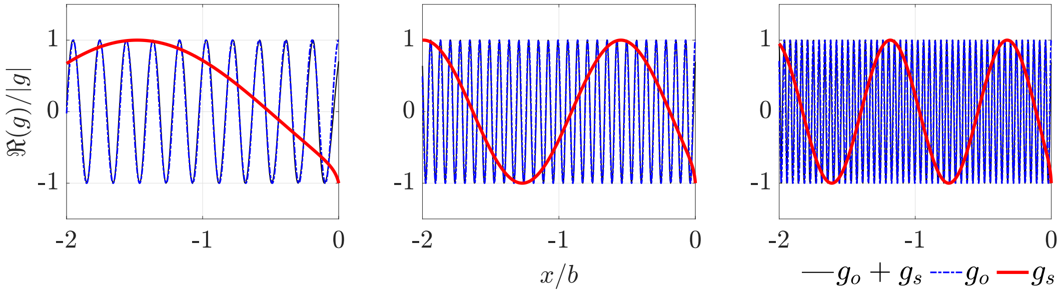

Figure 3.35: Phase of summation of incident (g_o) and scattered (g_s) wall pressures and each component side by side. Strouhal numbers are 8.3, 22.5, and 37.5 from left to right.

the phase topology along the chord for the total, incident, and scattered pressures. Notably, the incident pressure exhibits highly oscillatory phases, while the phase of the scattered pressure transitions from monotonic to sinusoidal waves as the Strouhal number increases. The phase of the total pressure is mainly influenced by the incident pressure, given its higher amplitude than the scattered pressure, as evident in Fig. 3.34. It should be noted that these phase dynamics observed in the incident and scattered pressures are compared with those of hydrodynamic and acoustic pressures in numerical simulations, although pairs of pressures are derived from different principles of decomposition.

Figure 3.36 displays the normalized incident, scattered, and total aeroacoustic transfer functions, which are a pivotal component in the computation of the radiated sound spectra as per Amiet's theory (Eq. (2.22)). These are obtained through the integration of the wall

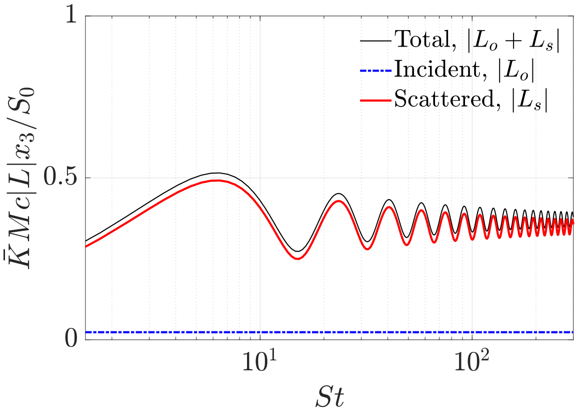

Figure 3.36: Normalized aeroacoustic transfer functions of the summation of incident and scattered components along with each separate component at a microphone position of $x/c = 1.0$, $x/c = 10.0$, $z/c =$ midspan.

pressures using the analytical formulations provided in Eqs. (2.15) and (2.17), respectively. The scattered pressure is found to exhibit higher magnitudes than the incident pressure across the entire frequency range. This contrasts with the observation in Fig. 3.34, where the magnitude of the incident wall pressure surpasses that of the scattered pressure. However, this is a consistent observation with Fig. 3.26, where the acoustic pressure significantly contributes to the total pressure. The non-propagating physics of incident pressure is a direct result of the destructive interference, as evidenced by the highly oscillatory pattern depicted in Fig. 3.35.

Figure 3.37 provides the directivity patterns of incident, scattered, and total pressures across a range of Strouhal numbers. A dominant compact dipole pattern is evident at $St \approx 8.25$, resulting in significant noise in all directions. The multi-lobed pattern emerges at higher Strouhal numbers, primarily derived from the scattered pressure. This aligns with the typical directional characteristics of trailing-edge noise [17, 173]. The consistent dominance of scattered pressure over the entire range of Strouhal numbers in contributing to the total pressure further supports its role as the primary actual sound source for the far-field

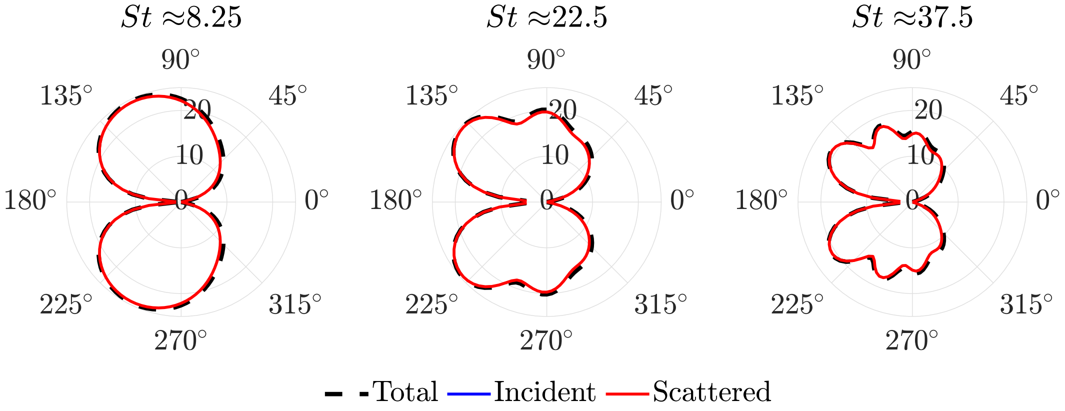

Figure 3.37: Directivity of the one-third octave band SPLs for the summation of the incident and scattered parts and each separate component at the radius of $10.0c$ from the trailing-edge origin.

acoustic pressure, as established in the preceding numerical approach, involving the cardioid directivity pattern ranging from 22.5 to 37.5 in Strouhal numbers. It is worth noting that the dominance of hydrodynamic pressure at the low-frequency compact dipole range reported in Ref. [86] differs from the current two approaches. It is crucial to note that the hydrodynamic pressure, as per the numerical approach, exhibits limited far-field radiation, aligning with the observations presented in Fig. 3.33 and corroborated by Oberai et al. [83]. Amiet's theory reveals that the magnitudes and directional shapes of scattered and total pressures are much closer than those of total and acoustic pressures in the numerical approach. One potential explanation is that Amiet's theory was developed under assumptions involving frozen turbulence [77] and infinitely long spans with a flat plate configuration. Consequently, the role of the incident pressure might have a lesser influence on the interaction between total and scattered pressures, resulting in similar magnitude levels between the two pressures. This aligns with the indirect demonstration by Tiomkin and Jaworski [172], where the relaxation of frozen turbulence gust by a linearly varying wavenumber significantly alters the total acoustics due to its impact on the incident pressure. A pivotal realization from Amiet's ana-

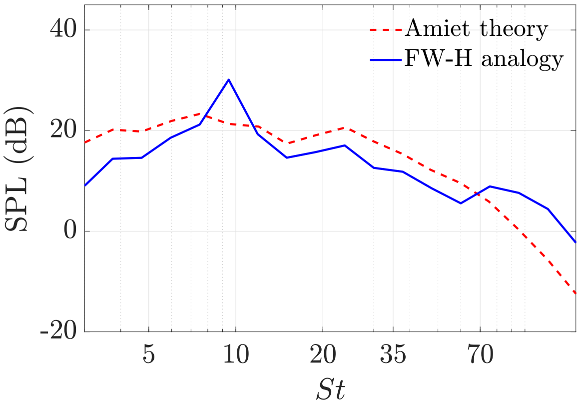

Figure 3.38: One-third octave band SPLs computed from Amiet's theory and FW-H analogy at a microphone position of $x/c = 1.0$, $x/c = 10.0$, $z/c =$ midspan.

lytical approach relating to the numerical approach is that the scattered or acoustic pressure exhibits an in-phase nature, contributing to the far-field sound. On the other hand, the incident or hydrodynamic pressure demonstrates a pseudo-sound nature due to destructive interference with the oscillatory phase along the chord, even though the magnitude of wall pressure is higher than that of the scattered or acoustic pressure.

Figure 3.38 displays the one-third octave band SPLs derived from Amiet's theory and the FW-H acoustic analogy using the LES data, presented in parallel. The microphone is positioned at $10.0c$ away from the trailing edge in midspan. The relevant formulations of the two approaches can be found in Eqs. (2.14) and (2.22), respectively. The results show that both the numerical and analytical frameworks produce comparable acoustic spectra in the broadband range of $15 < St < 70$. This indicates that the simplified geometry and frozen turbulence gust assumptions [77] made in Amiet's model [6, 34, 35] suffice to predict broadband noise effectively. However, subtle discrepancies in sound spectra between the two approaches are evident at a low-frequency tonal peak of $St \approx 9$ and a high-frequency weak hump higher than $St \approx 70$. These deviations may be attributed to the fact that Amiet's theory only takes the wall pressure spectrum near the trailing edge obtained from the

LES and multiplies it by the aeroacoustic transfer functions integrated from the normalized incident and scattered pressures. In contrast, the FW-H acoustic analogy accounts for all noise sources, encompassing trailing-edge scattering and leading-edge noise developed under various scenarios of turbulent structures in the turbulent boundary-layer flows [163, 164, 167]. Although the hydrodynamic pressure is characterized by a non-propagating nature, its impact on the phase interference between the total and acoustic pressures might be a non-negligible contribution to acoustic spectra in the FW-H solutions, but this is not observed in the analytical approach.

3.2.4 Summary

In this section, an in-depth examination of the fundamental characteristics of hydrodynamic (incident) and acoustic (scattered) pressures was conducted, providing insights into the complexities of sound propagation within turbulent boundary layer flows, with a specific emphasis on trailing-edge noise. Spectral analyses were performed on wall pressures, which were decomposed into hydrodynamic and acoustic components through wavenumber-frequency filtering within the numerical framework. Additionally, incident and scattered pressures were analyzed based on Amiet's theory and analytical formulations. Subsequently, these decomposed wall pressures were cross-examined with the far field using the FW-H equation and Amiet's theory.

This section first uncovered distinctive characteristics of hydrodynamic pressure. This pressure source arises from streamwise turbulent streaks along the wall, with phase velocities close to the convective speed, U_c. These spatiotemporal structures exhibit incoherence between adjacent turbulent eddies, resulting in highly oscillatory phase variations, which give rise to non-propagating or evanescent waves. Consequently, the far-field noise radiated from the hydrodynamic pressure remained significantly lower than that of the decomposed acoustic component. Despite acting as inherently pseudo-sound sources, hydrodynamic pressure played a crucial role in generating acoustic pressure, primarily through interactions with spanwise-coherent turbulent structures near the trailing edge. Furthermore, the presence of hydrodynamic pressure, as resolved by LES, was identified as a contributing factor to the differences in magnitude and directional characteristics between total and acoustic pressures. This was attributed to the non-linear interactions among multiple incoherent turbulent sources in the streamwise and spanwise directions. This phenomenon was proposed as a potential explanation for the disparities between numerical and analytical sound spectra. The latter is derived from flows assuming frozen turbulence gust conditions in Amiet's theory. The finding also demonstrated the physical properties of incident pressure in the analytical approach align with those derived from the decomposed hydrodynamic pressure on the wall and at the far field.

Secondly, the acoustic pressure revealed efficient propagation at nearly the speed of sound, with its spectral characteristics primarily associated with the effects of spanwise turbulent coherent structures. Despite the significantly lower magnitude of acoustic pressure source on the wall than that of the hydrodynamic pressure, it played a predominant role in shaping far-field sound spectra. This predominance could be attributed to the in-phase behavior of the acoustic pressure, which was particularly pronounced in the case of compact dipolar sources at lower Strouhal numbers. Even at higher Strouhal numbers, the in-phase tendencies persisted within the streamwise correlation length, facilitating efficient sound propagation across the entire frequency range. It is worth noting that non-compact noise sources or the streamwise correlation length near the trailing edge covered approximately 20% of the trailing edge. These areas were identified as regions of proficient trailing-edge scattering, contributing to the formation of the cardioid directional pattern observed at these specific Strouhal numbers. This behavior was further exemplified by the upstream-propagating acoustic pressure. Moreover, the downstream-traveling acoustic pressure exhibited characteristics akin to low-frequency compact dipolar sources and downward-cardioid shapes. These underlying noise sources were associated with the influence of vortex shedding from the trailing-edge bluntness and leading-edge scattering caused by boundary-layer tripping. In contrast, when comparing Amiet's theory with acoustic pressure, subtle disparities in their physical properties emerged. Sound spectra and directivity patterns derived from the FW-H acoustic analogy underscored the presence of trailing-edge bluntness vortex shedding noise at low Strouhal numbers and broadband humps resulting from the diffraction of incident waves due to boundary-layer tripping at higher Strouhal numbers. However, Amiet's theory did not account for these acoustic sources or the potential non-linear interactions of incoherent turbulent eddies. It relied solely on the wall-pressure spectrum in close proximity to the trailing edge, incorporating phase information from the integration of turbulent flows governed by the frozen turbulent gust assumption. Additionally, it is crucial to note that both radiated hydrodynamic and acoustic pressures exhibited non-Gaussian distributions. Consequently, statistical assumptions typically used in pressure decomposition models, which rely on Gaussian distributions, are not applicable to wall-bounded flows with edge scattering.

Chapter 4

Effect of Boundary-layer Tripping on Airfoil Noise

The chapter studies two distinct boundary-layer tripping methods, namely a geometrically resolved stair strip and an artificially modeled trip using suction and blowing, against the natural boundary-layer transition as a baseline scenario. Flow is specified at a chord-based Reynolds number of 4×10^5, a Mach number of 0.058, and a non-zero angle of attack of 6.25° over a NACA 0012 airfoil configuration. Detailed sound generation and propagation mechanisms associated with tripping-induced flow perturbations and trailing-edge scattering are discussed.

4.1 Modeling of Two Different Tripping Methods

The computational domain's size and boundary conditions are illustrated in Fig. 4.1. For this study, a NACA 0012 airfoil with a blunt trailing edge is chosen, which has a physical chord length (c) of 0.3 m, mirroring the experimental setup described by Garcia-Sagrado and Hynes [91]. The trailing-edge bluntness, h_{TE}/δ^*, defined as the ratio of the trailing-edge thickness (h_{TE}) to the displacement thickness (δ^*) computed at $x/c \approx 0.99$, is found to be

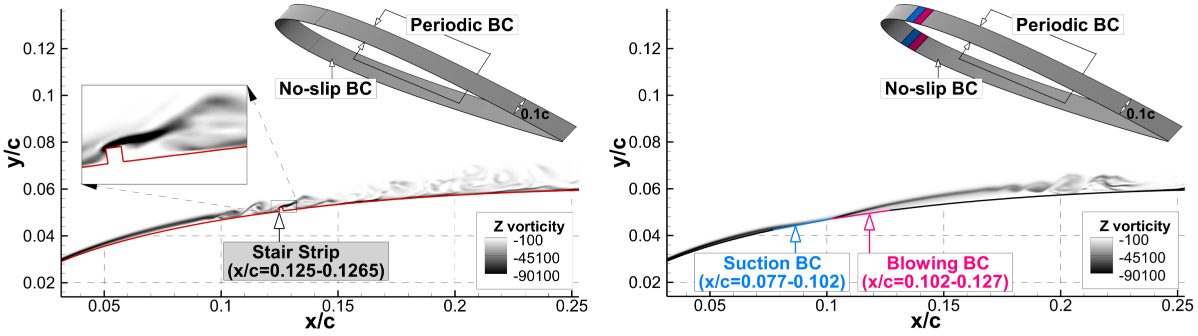

(a) (b)

Figure 4.1: Computational domain and boundary conditions (BCs): (a) O-type domain over the airfoil, and shear layers colored by spanwise vortices on the airfoil suction side for (b) stair strip and (c) suction and blowing.

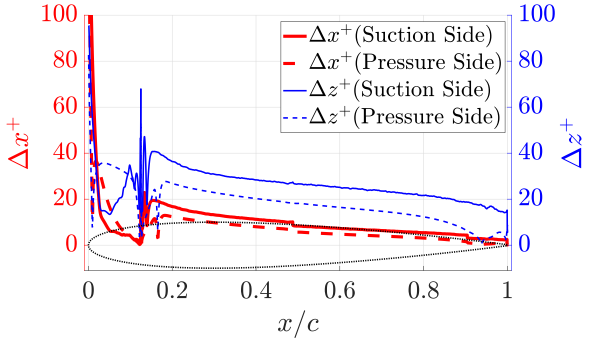

Figure 4.2: Grid spacing in wall units along both airfoil sides for the stair strip case.

0.21 − 0.25 on the suction side and 0.47 − 0.58 on the pressure side for all the cases in this work. The installation of two forced tripping approaches and their respective tripping mechanisms are detailed in Figs. 4.1(a) and 4.1(b). In Fig. 4.1(a), a square tripdot, with a size equivalent to 0.15% of the chord length, is placed approximately 12.5% of the chord from the leading edge on both sides of the airfoil. This placement induces a flapping shear layer behind the stair strip, perturbing the flows to transition into turbulence. The height of stair strip is chosen from numerical experimentation, while its location is the same as one in the experimental study [91] for the validation purpose of aerodynamic and wall-pressure spectral quantities.

In Fig. 4.1(b), the suction boundary condition is applied from 7.7% to 10.2% of the chord from the leading edge, and the blowing boundary condition ranges from 10.2% to 12.7% on both sides of the airfoil. A steady momentum with a magnitude equal to 3% of the freestream velocity is imposed on both the suction and blowing boundaries. The modeling of suction and blowing—both in terms of its duration and momentum strength—was benchmarked against other numerical studies [17, 96]. These studies similarly employed the same strategy to induce flow transitions in comparable flow regimes. However, there is a difference in the spanwise distribution of suction and blowing. This study implements it over the entire span, while Wolf et al. [17, 96] restricted it to $0.01 < z/c < 0.09$. Figure 4.2 shows the mesh topology of the stair-strip case and the grid spacing in wall units, serving as a representative example among the three simulation cases. The structured mesh size is $N_x \times N_y \times N_z = 4308 \times 323 \times 65$ in the streamwise, wall-normal, and spanwise directions, respectively, and is symmetrically distributed on both sides of the airfoil. The non-dimensional stair-strip height h^+ spans 60 viscous wall unit lengths, which is enough to perturb viscous flows up to the log-law region within the boundary layer. Here, $h^+ = hu_\tau/\nu$ where u_τ and ν are the friction velocity and kinematic viscosity, respectively. For all three simulation cases, approximately 120 grid points are situated within the boundary layer near the trailing edge. Figure 4.2 illustrates the asymmetric grid spacing in wall units on the airfoil's suction and pressure sides, a result of the non-zero incidence. The streamwise grid spacing Δx^+ is less than 20, and the spanwise grid spacing Δz^+ is less than 40, excluding a local spike behind the tripping region. Here, $\Delta x^+ = \Delta x u_\tau/\nu$, and $\Delta z^+ = \Delta z u_\tau/\nu$. This grid spacing is sufficient to perform wall-resolved LES with the current grid refinements, according to Georgiadis et al. [134].

4.2 Flow Quantities and Acoustic Fields

Figure 4.3 displays the time-averaged negative pressure coefficient $-C_p$ and friction coefficient C_f for the three cases simulated, compared to midspan experimental measurements. The experimental data used in this paper were collected under forced tripped conditions using a trip wire [91]. In Fig. 4.3(a), the predicted pressure distributions align reasonably well with the experiment. Friction coefficients on the airfoil suction side are presented in Fig. 4.3(b), showcasing a close correlation with the measured data in the aft region. It is worth noting the appearance of negative skin friction coefficients around $x/c = 0.04$ to 0.12 for the stair strip and natural transition. A plateau of negative quantities for the two aerodynamic coefficients from $x/c = 0.04$ to 0.08 signifies the existence of LSB [174]. For the suction and blowing, the LSB is approximately located from $x/c = 0.10$ to 0.18. Contrarily, on the airfoil pressure side, local separated flows near the trailing edge are observed in all the cases at larger than $x/c = 0.93$, as depicted in Fig. 4.3(c).

Figure 4.4 shows the quantification of flow-induced perturbations, measured by the root-mean-square (RMS) values of the wall pressure. The RMS quantities are normalized by the dynamic pressure q_∞, defined as $1/2\rho_\infty U_\infty^2$. An abrupt increase in RMS value can be seen at $x/c \approx 0.1$, marking the termination of the LSB for the stair strip and natural transition. However, for the suction and blowing case, the transition is delayed, and the LSB extends to $x/c \approx 0.2$. For the stair strip, there is an additional spike due to the tripping mechanism itself, which may contribute to additional noise, as will be shown later. Remarkably, minimal perturbations are observed on the airfoil pressure side for the stair strip and natural transition. In contrast, for the suction and blowing case, perturbations

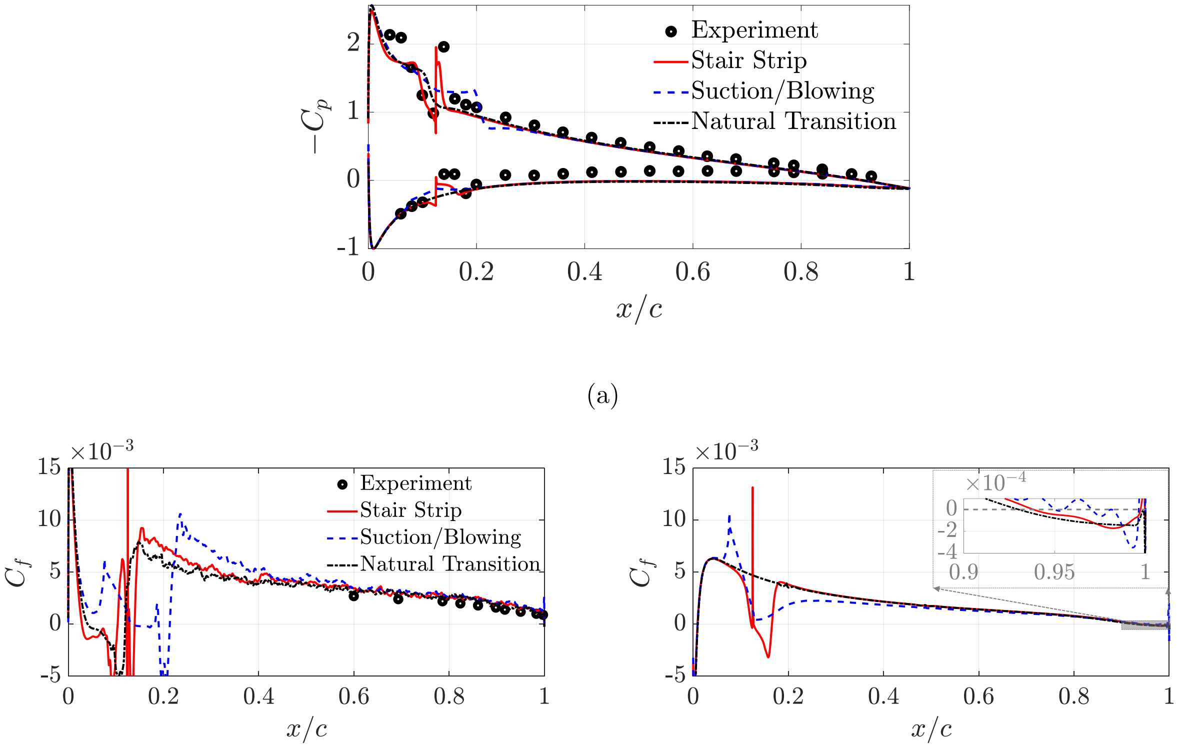

(a)

(b)

(c)

Figure 4.3: Time-averaged distributions for the three simulated cases against the available tripped experiment in midspan [91]: (a) $-C_p$, (b) C_f on the suction side, and (c) C_f on the pressure side.

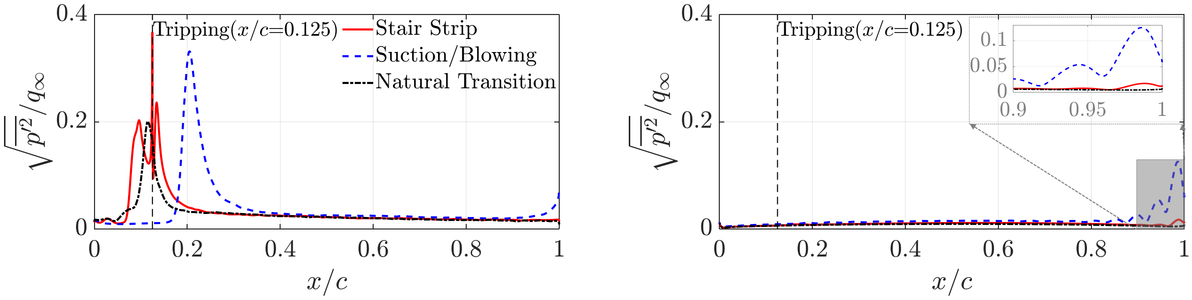

(a)

(b)

Figure 4.4: RMS pressure normalized by q_∞: (a) suction side and (b) pressure side.

grow from $x/c = 0.85$ towards the trailing edge on the airfoil pressure side. The dynamics of these oscillating disturbances, related to acoustics, will be further clarified through visual flow fields and frequency domain analysis.

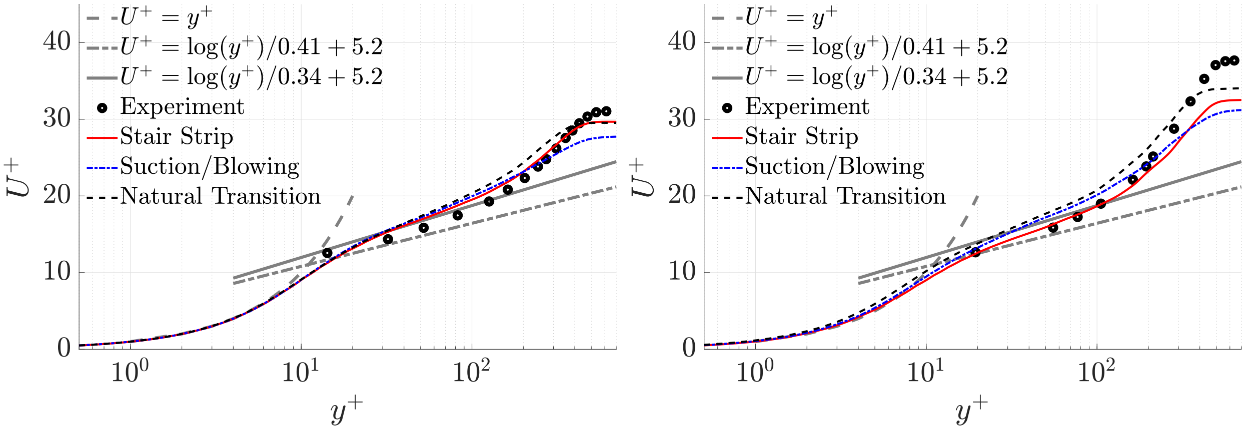

(a)

(b)

Figure 4.5: Time-averaged velocity profiles normalized by friction velocity along the wall units against the available tripped experiment [91] at (a) $x/c = 0.76$ and (b) $x/c = 0.916$.

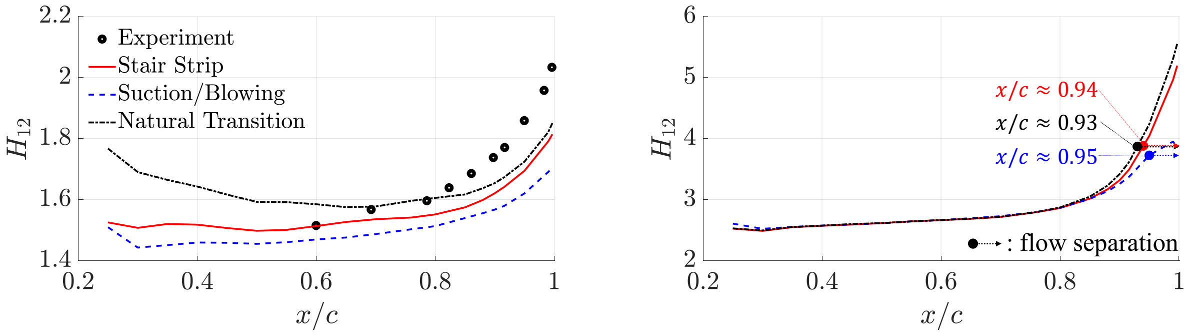

(a)

(b)

Figure 4.6: Variations of shape factor in the streamwise direction against the available tripped experiment [91] on (a) suction side and (b) pressure side.

Figure 4.5 depicts the boundary layer profiles in wall units to highlight the near-wall behavior within turbulent boundary layers on the suction side of the airfoil. The profiles, displayed at two separate streamwise locations ($x/c = 0.76$ and 0.916), exhibit similarities between the predictive simulations and actual experiments within the inner region. At $x/c = 0.916$, boundary layers are spatially thickening in the outer region, as compared to the ones at $x/c = 0.76$ due to the downstream APG flows. Discrepancies noted in the outer region could arise from slight flow modifications caused by variations in tripping geometry or wind tunnel installation.

Figure 4.6 depicts the shape factor (H_{12}) on both sides of the airfoil, which is the ratio of displacement thickness (δ^*) to momentum thickness (θ). The displacement thickness and the momentum thickness are calculated through integration from the wall to the boundary layer thickness. All of the relations can be written as follows:

$$H_{12} = \delta^*/\theta, \quad \delta^* = \int_0^\delta \left(1 - \frac{U}{U_\infty}\right) \mathrm{d}y, \quad \theta = \int_0^\delta \frac{U}{U_\infty}\left(1 - \frac{U}{U_\infty}\right) \mathrm{d}y. \tag{4.1}$$

Here, the boundary layer thickness is estimated using the local-reconstruction method developed by Griffin et al. [175]. Figure 4.6(a) displays the evolution of shape factor on the airfoil suction side for three tripping approaches with available experimental data [91]. While the trends are similar, the natural transition shows a relatively higher magnitude than the others. This difference evidences the effect of tripping installation, causing a deficit in the mass and momentum fluxes within the boundary layer. Though the natural transition's shape factor behavior slightly deviates from the two forced tripping models near the leading edge, its progression remains consistently flat downstream. One can observe a rapid increase in shape factor near the trailing edge. This suggests the velocity profiles are significantly affected by APG flows, and this tendency matches the tripped experiment [91]. The discrepancy in magnitude against the experiment might be due to an analogous speculation when described in Fig. 4.5. On the pressure side in Fig. 4.6(b), the variation of shape factor for all the transition cases is flat across the chord, while all three simulated cases show a sharply increasing rate near the trailing edge, being associated with flow separation caused by the APG flows. The separation points of each case are denoted on the curve based on the skin friction coefficient in Fig. 4.3(c).

Boundary layer turbulence intensities (TI), defined by $TI = \sqrt{2/3k}/U_\infty$, where k is the turbulence kinetic energy, are presented for both airfoil sides in Fig. 4.7. On the airfoil suction side, the degree of turbulence intensifies off the wall in the streamwise direction, aligning reasonably with the tripped experiment. Both forced tripping approaches exhibit stronger turbulence intensities than the natural transition at heights greater than $y/c > 0.02$, up to $x/c = 0.95$. This could be due to enhanced turbulence mixing induced by tripping installations, particularly noticeable near the tripping region around $x/c = 0.4$. Conversely, on the airfoil pressure side, spatial disturbances are considerably low, suggesting a stable laminar flow for the stair strip and natural transition. Exceptions include areas near the trailing edge, which show weak turbulent intensity. However, in the case of suction and blowing, local disturbances seem to gradually increase from $x/c = 0.88$ to the trailing edge.

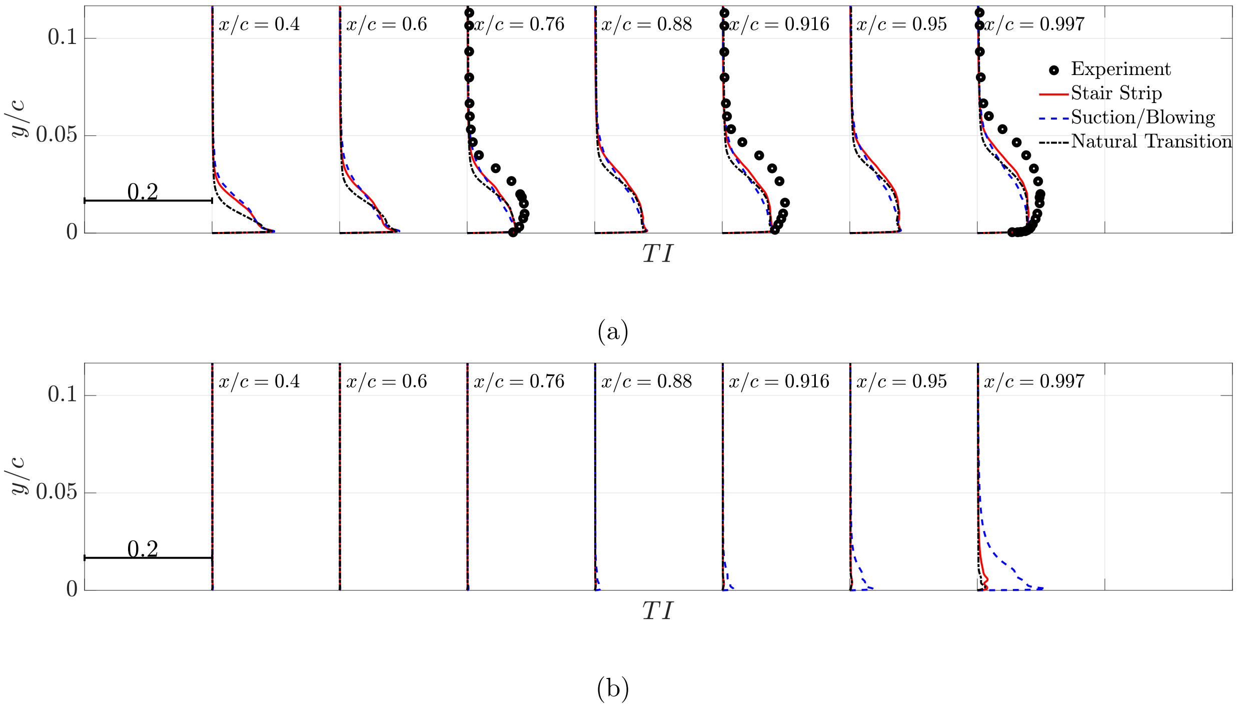

Figure 4.7: Turbulence intensities against the available tripped experiment [91]: (a) suction side and (b) pressure side.

While these turbulent fluctuations up to $x/c = 0.95$ are notably smaller than those on the suction side, they surpass them at $x/c = 0.997$. Considering the minimal turbulent disturbances upstream on the airfoil pressure side for suction and blowing, along with similar disturbance growth patterns observed in RMS flow quantities (Fig. 4.4), it is plausible that the stable boundary-layer flow on the pressure side undergoes a laminar-to-turbulent transition. This transition could involve the initial stages of unstable laminar boundary layer instabilities, known as T-S waves, near the trailing edge [176, 177]. Detailed examinations of flow structures and related acoustic fields will follow to further validate this boundary-layer transition process.

Local transient flows and acoustic perturbations near the boundary-layer tripping region and the trailing edge are visualized in Fig. 4.8. This figure presents time-averaged velocity streamlines, colored with the streamwise velocity (normalized by freestream velocity), u_x/U_∞, with the instantaneous dilatation field, $\nabla \cdot \vec{U}$, in the background. In all three simulated cases, the formation of LSB is indicated by the streamlines, where the acoustic perturbations are amplified. Though the onset of LSB for the suction and blowing case is positioned more rearward due to the blowing boundary, all cases exhibit non-equilibrium turbulent flows developed under APG flows. A separation bubble near the trailing edge on the pressure side is observed for the stair strip and the natural transition, while coherent acoustic waves are seen to travel in the streamwise direction for the suction and blowing case. The former is due to locally developed APG flows, a consistent observation in Fig. 4.6(b) where the shape factor shows an increasing rate. The latter results from the initiation of flow transition involving the T-S waves, where the flow perturbations were observed to enhance in the streamwise direction, as evidenced in the RMS quantities (Fig. 4.4) and turbulence

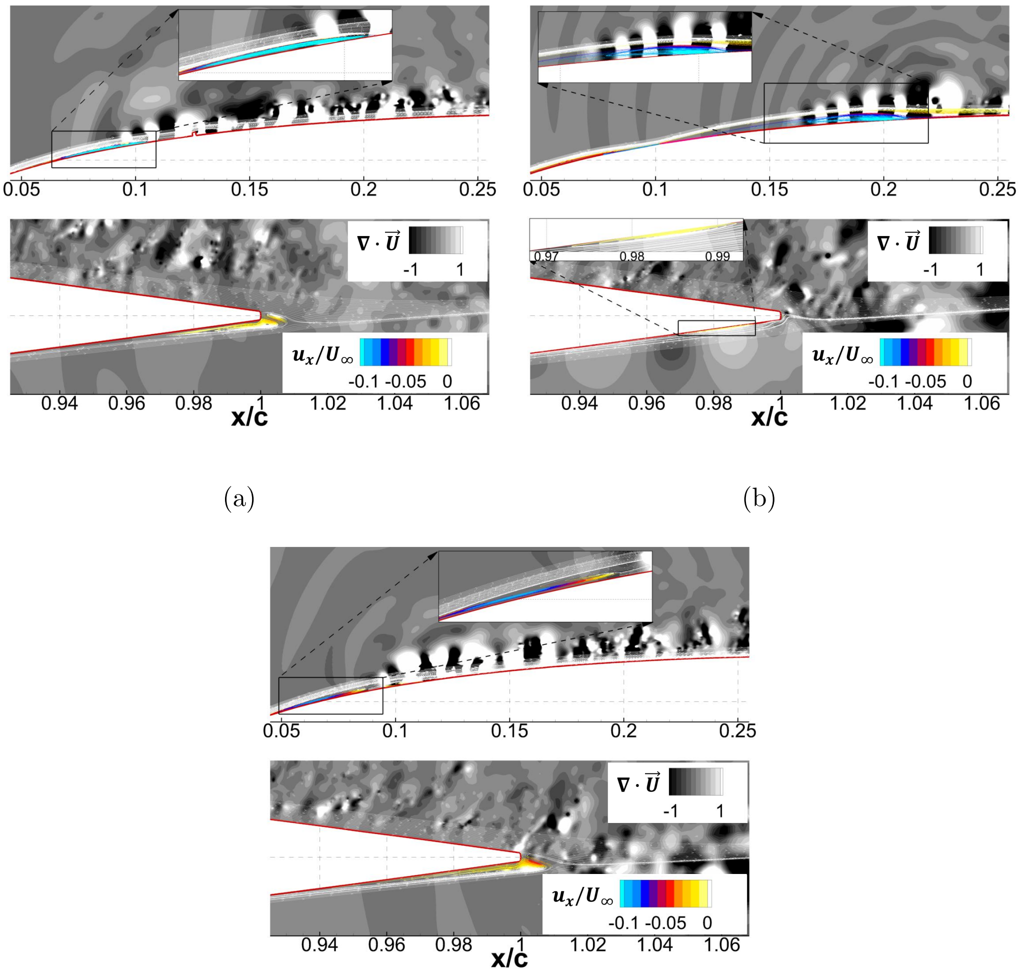

(a)

(b)

(c)

Figure 4.8: Time-averaged streamlines colored with the streamwise velocity normalized by U_∞ with the instantaneous dilatation field in background: (a) stair strip, (b) suction and blowing, and (c) natural transition. The color scale range of u_x/U_∞ highlights the formation of LSB.

intensity profiles (Fig. 4.7(b)). The streamlines in Fig. 4.8(b) reveal localized, separated, and reattached flows, forming a separation bubble that extends from $x/c = 0.97$ to 0.99 on the airfoil pressure side. Therefore, for the suction and blowing, the separated-flow transition occurs on the pressure side near the trailing edge, skipping several natural transition processes such as vortex breakdown and turbulent spots, but involving laminar instability waves and the subsequent separation bubble [39]. This transition represents a somewhat different flow topology from the stair strip and the natural transition. As depicted in Figs. 4.8(a) and 4.8(c), recirculated flows are identified as the source of vortex shedding, as corroborated under similar flow conditions [96].

Boundary-layer fluctuations and acoustic sources near the wall are further examined by

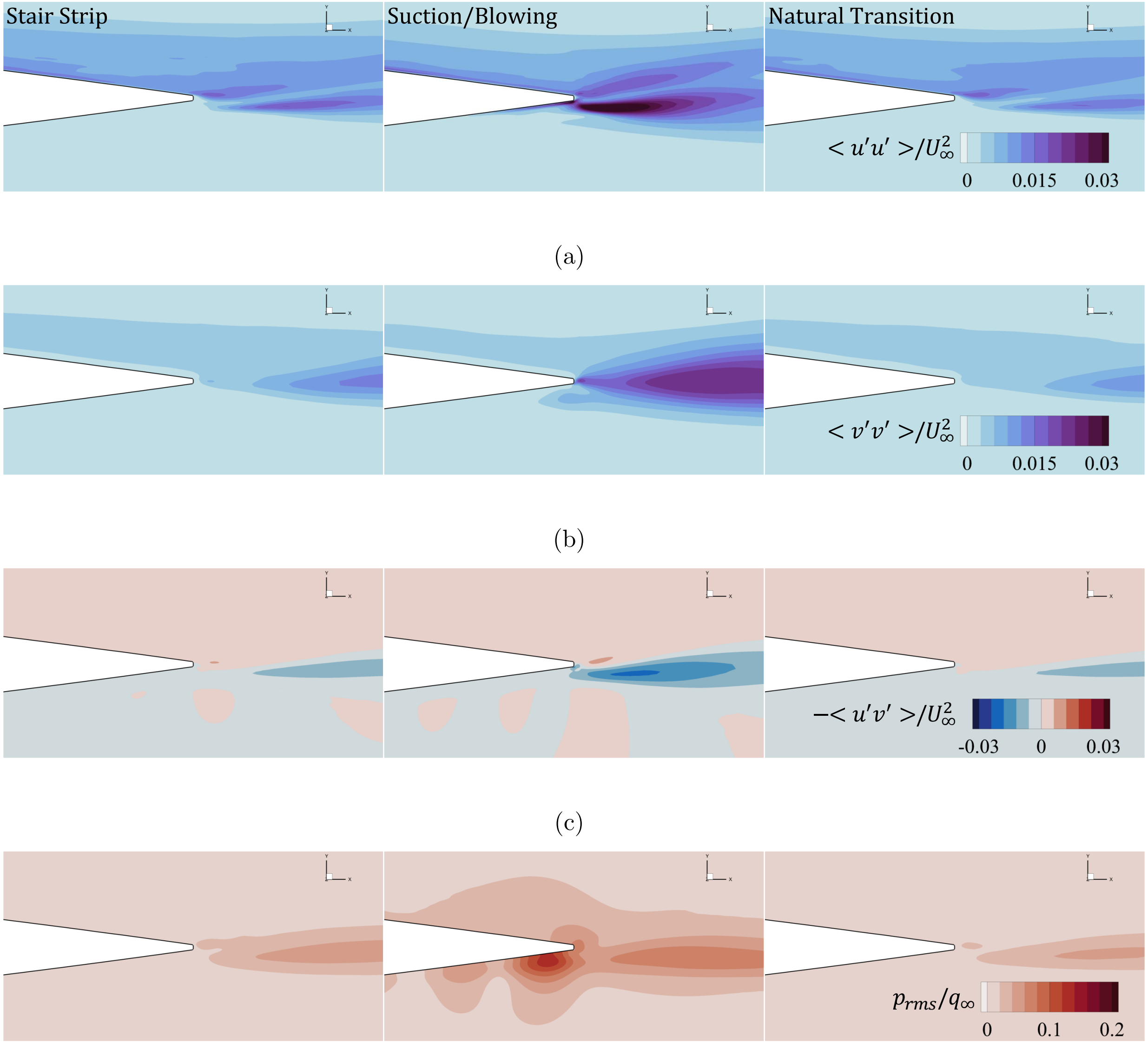

(a)

(b)

(c)

(d)

Figure 4.9: Spatial distributions of Reynolds stress tensors and RMS pressure normalized by U_∞^2 and q_∞ for three transition scenarios: (a) $< u^{'}u^{'} > /U_\infty^2$, (b) $< v^{'}v^{'} > /U_\infty^2$, (c) $- < u^{'}v^{'} > /U_\infty^2$, and (d) p_{rms}/q_∞.

plotting the Reynolds stresses, and RMS pressure are provided for three transition cases, which are plotted in Fig. 4.9. In Fig. 4.9(a), the dimensionless streamwise Reynolds stress tensor $< u'u' > /U_\infty^2$ is notably intense on the suction side near the trailing edge in each scenario, attributable to turbulent flows. This is a common phenomenon associated with trailing-edge noise sources [10]. However, for the suction and blowing case, the intense streamwise Reynolds stress tensor is distributed near the pressure-side wall close to the trailing edge, exceeding the strength found on the airfoil suction side, as observed in Fig. 4.7(b). This region encompasses both the trailing edge and the separation bubble that spans from $x/c = 0.97$ to 0.99, as indicated in Fig. 4.8(b). This supports the postulated mechanism of tonal noise generation; initial disturbances from the T-S waves get amplified when interacting with the separation bubble, producing significant velocity perturbations near the wake [178–180]. This can further be observed in spatial distributions of the dimensionless shear stress tensor $- < u'v' > /U_\infty^2$ and the dimensionless wall-normal Reynolds stress tensor $< v'v' > /U_\infty^2$. Particular attention is given to the intense magnitudes of $- < u'v' > /U_\infty^2$ and $< v'v' > /U_\infty^2$ off the pressure-side wall for the suction and blowing scenario. In particular, the wall-normal stress component accounts for the large portion of turbulence kinetic energy, corresponding to $y/c \approx 0.01$, as seen in Fig. 4.7(b). It is also shown that the coherent acoustic waves traveling along with the T-S waves become amplified when passing through the separation bubble, shedding into the wake regions. For the suction and blowing, it is transparent that acoustic noise sources are found to appear on the airfoil pressure side close to the trailing edge due to the T-S waves and the separation bubble developed during the separated-flow transition [39], which remains to be further investigated to relate those acoustic sources to laminar boundary layer vortex shedding noise [5]. However, bear in mind that these observations are in the same context as conclusions of earlier studies that the interaction of strong oscillatory motion with the trailing edge is the dominant tone generation process [13, 181]. Meanwhile, for the stair strip and natural transition, velocity and pressure perturbations above the airfoil pressure side are left quiescent.

Global views of flow and acoustic fields around the airfoil are provided in Fig. 4.10,

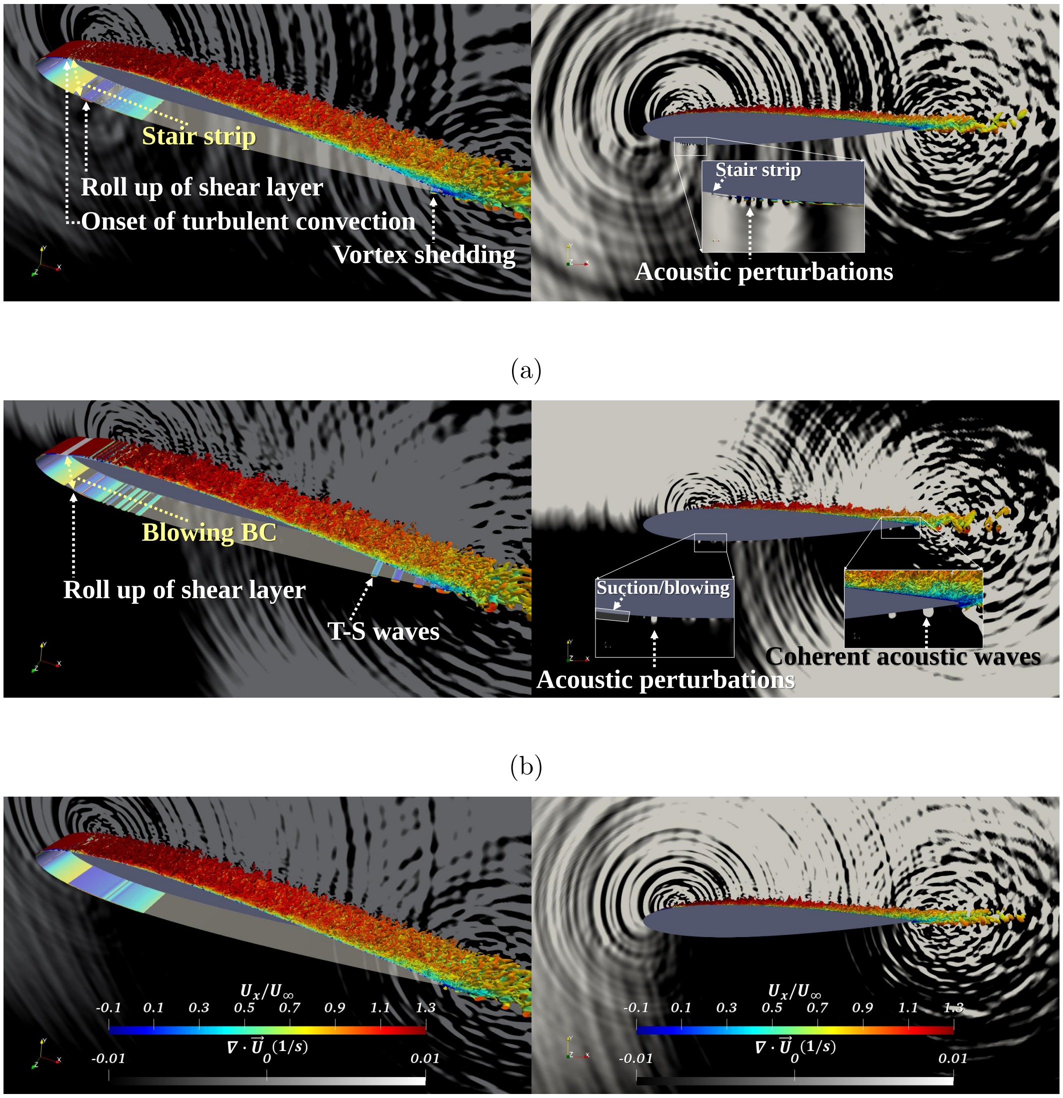

(a)

(b)

(c)

Figure 4.10: Normalized Q-criterion ($Qc^2/U_\infty^2 = 100$) colored by the normalized streamwise velocity component (u_x/U_∞) with the dilatation field ($\nabla \cdot \vec{U}$) in background: (a) stair strip, (b) suction and blowing, and (c) natural transition.

being visualized by the iso-surface of the normalized Q-criterion colored with the normalized streamwise velocity component. This is set against the backdrop of the dilatation field. For the stair strip and natural transition cases, non-equilibrium turbulent flows are observed following the separated-flow transition, a result of APG. This transition occurs particularly ahead of the stair-strip position. For the suction and blowing case in the vicinity of the tripping, the free shear layer rolls up two-dimensional vortical structures. These structures become unstable, breaking down into fully three-dimensional fluctuations before evolving into turbulent flows. This flow transition can also be classified as a separated-flow transition [39], given that the boundary-layer transition begins after the LSB formed under the free shear layer, as shown in Fig. 4.8(b). While the three cases can be grouped under the same transition scenario, the fully turbulent flows in the suction and blowing case are enriched through a series of natural transition processes, unlike the other two cases. This difference is linked to the augmented momentum flux provided by the blowing boundary, which delays the boundary-layer transition and the subsequent flow separation due to APG flows. The findings reveal that APG flows trigger the boundary-layer transition for the stair strip and natural transition simulation cases at a non-zero angle. In contrast, the wall suction and blowing boundary significantly impacts the flow transition on the suction side. On the airfoil pressure side, the shear layers rolled up near the leading edge appear to reattach, maintaining a stable laminar flow at least to the mid-chord for all three simulated cases. For the two forced tripping approaches, local acoustic perturbations near the free shear layers on the pressure side can be considered negligible compared to those on the airfoil suction side when viewed in a 2-D plane.

In the stair strip and natural transition scenarios, flow near the trailing edge on the pressure side separates, forming a localized laminar bubble as shown in Figs. 4.8(a) and 4.8(c). However, only in the case of the stair strip does a spanwise-coherent vortex originating from recirculating flows shed into the wakefield, as illustrated in Fig. 4.10(a). For the suction and blowing scenario, the two-dimensional T-S waves advect downstream along the airfoil pressure side, shedding into the wakefield, as shown in Fig. 4.10(b). Simultaneously, coherent acoustic waves propagate along the T-S waves, as already noted in Fig. 4.8(b). Considering that the two-dimensional flows are the governing mechanism of generating noise [173], and these flow structures maintain significant strength and coherence [13], it is reasonable to hypothesize that the vortex shedding and T-S waves contribute to the generation of far-field sound. The extent of this acoustic source's contribution to the radiated noise will be demonstrated later in this study. For all three simulated cases, the acoustic waves near the wake emanate in a dipolar nature, typical of trailing-edge noise at low frequencies [140, 173]. It is also crucial to underscore the importance of acoustic perturbations induced by the LSB near the leading edge, as they constitute a significant source of leading-edge sound [182, 183]. These perturbations have a comparable impact on far-field noise as does the trailing-edge noise, emphasizing their role in overall acoustic dynamics.

4.3 Spectral Analysis on Wall and Near-Wall Pressures

The surface wall-pressure spectrum plays a pivotal role in the generation of airfoil noise, especially in the context of trailing-edge noise [78, 79]. This spectrum captures the pressure fluctuations on the airfoil surface, which in turn becomes a primary source for aerodynamic sound radiation. As turbulent structures interact with the trailing edge, they produce pressure variations that propagate as sound waves into the surrounding medium. By analyzing the wall-pressure spectrum, one can gain insights into the characteristics and frequencies of these pressure fluctuations, allowing for a more comprehensive understanding of the aerodynamic noise mechanisms and potential mitigation strategies. Pressure fields are analyzed in the Fourier domain by means of several post-processing and data-driven methods, both at the wall and near-wall. Spectra were computed using 6,000 samples, subdividing them into 10 segments with a Hanning window and an overlap of 50%. For the spanwise coherence, the samples are subdivided into 22 segments with the Hanning window and overlap of 50%. The frequency is represented by a Strouhal number, $St = fc/U_\infty$. Figure 4.11 displays

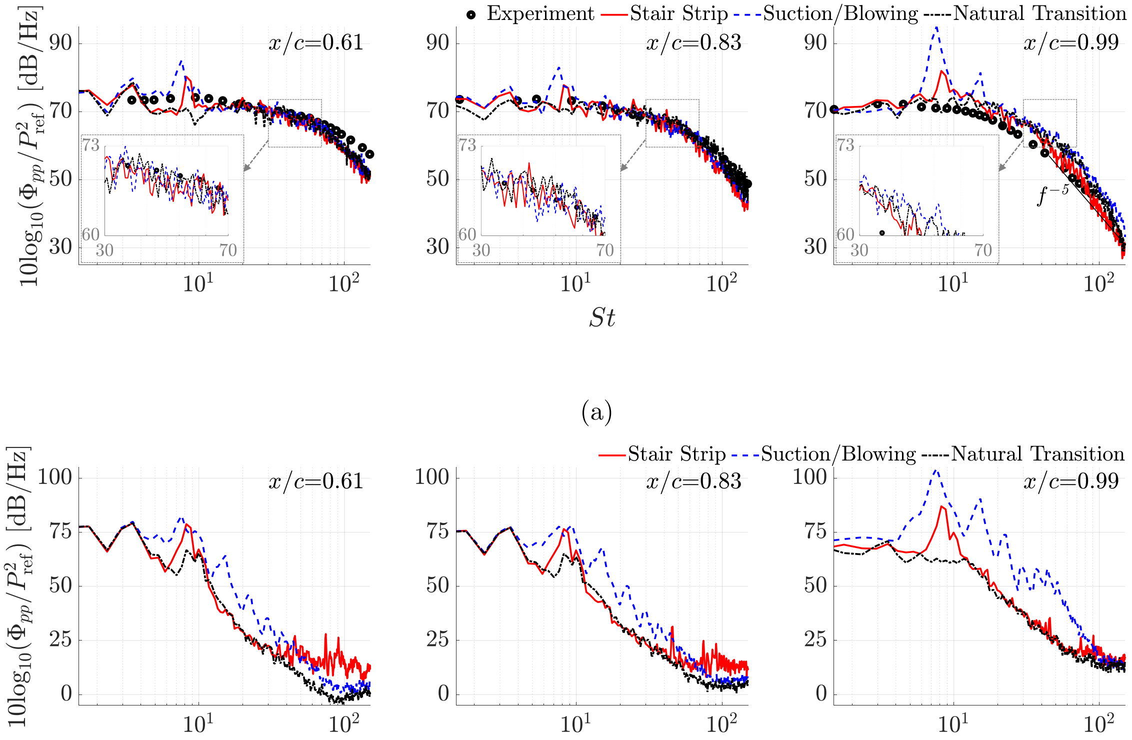

(a)

(b)

Figure 4.11: Wall-pressure spectra referenced to $P_{\rm ref} = 20\mu$Pa against the available tripped experiment [91] at different streamwise locations: (a) suction side and (b) pressure side.

the predicted wall-pressure spectra at various streamwise locations on both the suction and pressure sides of the airfoil, contrasted against the tripped experiment. It is shown that the spectra on the airfoil suction side for the suction and blowing as well as natural transition scenarios are slightly higher than for the stair strip scenario. This finding aligns with previously identified variations in the displacement thickness as shown in Fig. 4.6; the stair strip installation induces greater momentum losses, thereby resulting in increased energy dissipation in the turbulence spectra. Two spectral peaks are of particular interest; a primary low-frequency spectral peak around $St = 7.5$ associated with vortex shedding near the wake is observed in the two forced tripping scenarios, and a distinct secondary peak is notable only for the suction and blowing scenario, particularly at $x/c = 0.99$. Moreover, fifth-power law scaling in the frequency range of $St = 50 - 120$ is evident on the airfoil's suction side, where turbulent boundary layers develop and persist along the chord. The results demonstrate an excellent agreement between predictions and measurements, especially near the trailing edge. On the pressure side, as illustrated in Fig. 4.11(b), the energy spectra are quite low in the high-frequency range, a characteristic of equilibrium flows or the early stages of flow transition. This is despite the forced tripping applied around the leading edge. Furthermore, discrete high-frequency tones around $St = 40 - 100$ on the broadband spectra are unique to the stair strip scenario. These sound sources might predominantly be attributed to the tripping itself or the interaction between the LSB and the tripping occurring around the leading edge on the airfoil's suction side influencing on the pressure side. Excluding these tripping-induced sound sources and the low-frequency hump, the broadband shape of the acoustic spectra for the stair strip closely resembles that of the natural transition scenario. However, the pressure spectra for the suction and blowing scenario are considerably higher than the other two cases. The amplification of the spectra at $x/c = 0.99$ for the suction and blowing can be attributed to the sequence of laminar boundary-layer instabilities and the subsequent separation bubble on the pressure side, a phenomenon validated in the previous section.

The high-amplitude pressure spectra near the trailing edge for the suction and blowing scenario are further explored using a continuous wavelet transform (CWT). Morse wavelet [157] is employed for analyzing modulated signals with time-varying amplitude and frequency. This wavelet function is a Gaussian envelope modulated by a complex-valued carrier wave, which is implemented in MATLAB®'s wavelet toolbox. Detailed theory and further applications are listed in Refs. [157–159]. Figure 4.12 displays the square root of the magnitude scalogram of pressure fluctuations on both sides of the airfoil at $x/c = 0.99$. Energy distributions are typically depicted by a squared magnitude scalogram, but the square root is taken here to highlight the energy distribution at high frequencies. On the airfoil's suction

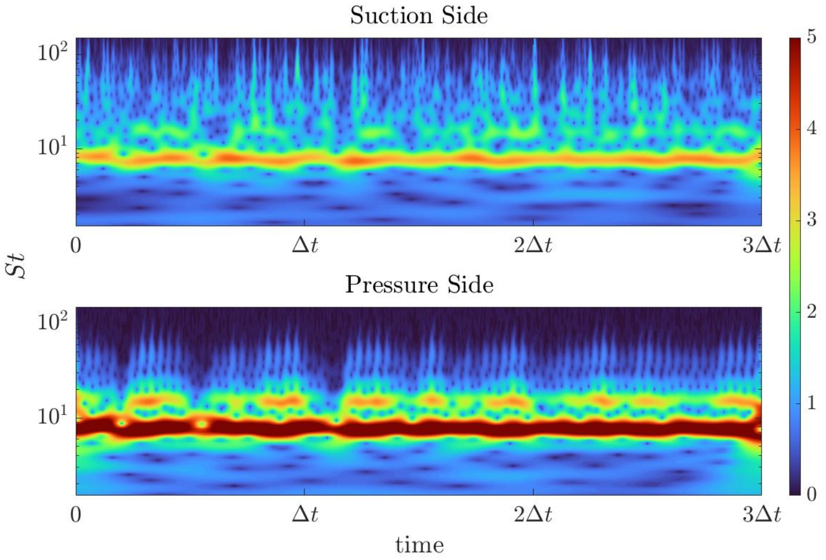

Figure 4.12: Square root of magnitude scalogram for the suction and blowing in the time-frequency domain using CWT at $x/c = 0.99$.

side, there is a clear transfer of energy to smaller scales or higher frequencies, indicating the presence of incoherent turbulent eddies across a broad frequency range. The vortex-shedding frequency is clear near the narrowband of $St = 7.5$, which evolves in time on both airfoil sides but has higher energies on the airfoil pressure side. Strongly periodic pressure fluctuations are shedding from the separation bubble close to the trailing edge on the airfoil pressure side. This nature in addition to the strong spanwise coherence as already observed in Fig. 4.10(b) satisfies the necessary condition of emitting spectral tones [13]. This is applicable to the stair strip case where the spectral tone is distinct at about $St = 7.5$, and the spanwise-coherent vortex is shedding to the wakefield from the separation bubble close to the trailing edge on the pressure side as shown in Figs. 4.10(a) and 4.11, respectively. On the pressure side, however, intermittent spots near $St = 15$ are attributed to the periodic convection of T-S waves indicating the energy transfer to high frequency. It remains to be further clarified for the acoustic feedback loop mechanism in which the part of diffraction from the acoustic dipolar source near the wake gives rise to the T-S instability waves and the subsequent generation of separation bubble [173, 184]. This intermittent behavior in scalogram is similarly observed in Ricciardi et al. [185], which addressed the mechanism of acoustic feedback loop in detail. In addition, the frequency range of intermittent behavior aligns with secondary and territory tones on wall-pressure spectrum for the suction and blowing in Fig. 4.11(b), and this similar observation can be found in Ricciardi and Wolf [186]. Note that the presence of a separation bubble plays a role in the laminar boundary layer vortex shedding noise [173, 178, 181, 187], as resolved in streamlines depicted in Fig. 4.8(b). Thus, it is apparent that the existence of the separation bubble and the interaction with laminar-boundary instability waves contribute to multiple humps along the broadband spectral range on the pressure side presented

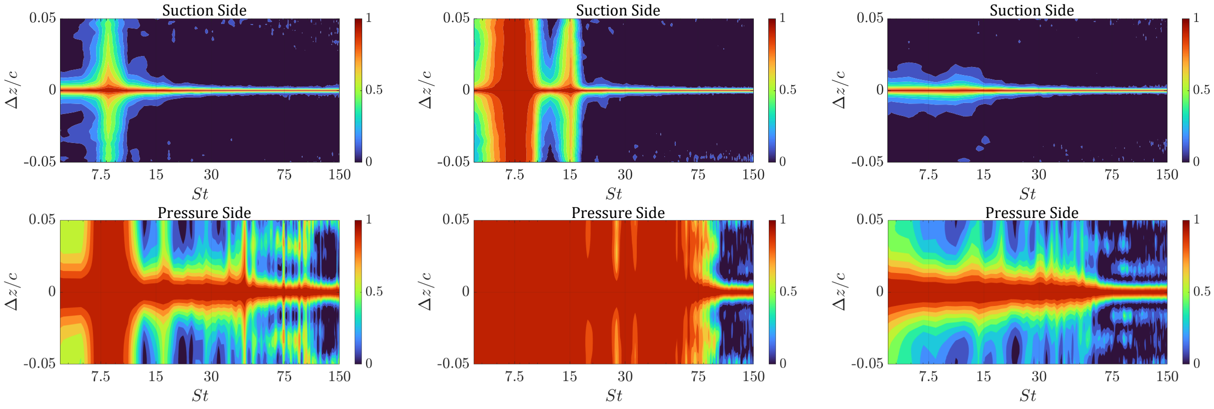

(a) (b) (c)

Figure 4.13: Spanwise coherence contours at $x/c = 0.99$: (a) stair strip, (b) suction and blowing, and (c) natural transition.

in Fig. 4.11(b). Readers can find the other recent work about the acoustic feedback loop mechanism, which focuses on amplitude modulation taking place on the suction side [188].

Spanwise coherence is defined as

$$\gamma^2(z, \Delta z, f) = \frac{|\Phi_{pp}(z, \Delta z, f)|^2}{|\Phi_{pp}(z, 0, f)||\Phi_{pp}(z + \Delta z, 0, f)|}, \tag{4.2}$$

where the cross-spectrum Φ_{pp} is the Fourier transform of the space-time cross-correlation function:

$$\Phi_{pp}(z, \Delta z, f) = \int_{-\infty}^{\infty} \big\langle p(z, t)p(z + \Delta z, t + \tau)\big\rangle\, \mathrm{e}^{-\mathrm{i}f\tau}\, \mathrm{d}\tau, \tag{4.3}$$

where $\mathrm{i} = \sqrt{-1}$, and the operator $\langle\cdot\rangle$ denotes the ensemble average over the spanwise separation distance, Δz.

The spanwise coherence represents the size of the source region that radiates noise independently from neighboring sources, in a statistical sense [96, 189]. Figure 4.13 depicts the contour of the spanwise coherence as a function of Strouhal number and spanwise separation distance normalized by the chord length $\Delta z/c$ on both sides of the airfoil at $x/c = 0.99$ for the three transition cases. Note the rapid decline on the airfoil's suction side for all cases at frequencies higher than $St = 15$, indicating the spanwise size of the computational domain is sufficient to simulate noise sources produced by incoherent turbulent eddies of various scales and intensities. Conversely, a strong spanwise correlation is observed on the airfoil's pressure side at several Strouhal numbers for the three simulated cases. For the stair strip in Fig. 4.13(a), strong coherence in the spanwise direction is observed around $St = 7.5$ and $St = 45 - 90$. These two narrowband ranges correspond to the vortex-shedding frequency and the frequency related to the tripping itself or LSB-tripping interaction, respectively. For the suction and blowing in Fig. 4.13(b), the strong spanwise coherence spans the low-to-high frequency range, corresponding with acoustic perturbations traveling on the pressure side such as two-dimensional T-S waves, and overall increase of energy spectra on the airfoil pressure side, as shown in Figs. 4.8(b), 4.9, 4.10(b), and 4.11(b). It is worth noting that high spanwise coherence at $St = 7.5$ and 15 remains on the suction side, influenced by the acoustic sources on the pressure side. However, for the natural transition in Fig. 4.13(c), the spanwise coherence is somewhat less pronounced than for the other two forced transition approaches, particularly for the vortex-shedding frequency around $St = 7.5$, but it presents a harmonically varying spanwise coherent pattern with increasing frequency, attributed to a self-excited LSB mechanism. As the governing mechanism of quasi-tones stems from a two-dimensional nature like the high spanwise coherence [13, 173], the primary acoustic noise sources for the two tripping approaches can be collectively described with preceding flow structures depicted in Figs. 4.8, 4.9, and 4.10: (1) the vortex shedding and the tripping itself or the LSB-tripping interaction for the stair strip and (2) the vortex shedding with multiple peaks originating from the laminar boundary-layer instability waves and the separation bubble for the suction and blowing. These spectral peaks were observed to contain higher energy spectra than the pure scattering of turbulent boundary layers past the trailing edge on the suction side as shown in Fig. 4.11(b), as it approaches the trailing edge.

To investigate the propagating direction of acoustic waves as well as the phase speed near the wall, the wavenumber-frequency spectrum is computed utilizing an array of probes parallel to the airfoil surface, distributed from $x/c = 0.365$ to 1.0. The wavenumber-frequency spectrum taken to the pressure field $p(t, x)$ can be written as follows:

$$\hat{\mathbf{P}}(f, k) = \int_{-\infty}^{\infty} \int_{-\infty}^{\infty} p(t, x) \mathrm{e}^{-\mathrm{i}(2\pi f t - kx)} \, \mathrm{d}t\mathrm{d}x, \tag{4.4}$$

where k is the wavenumber, f is the frequency, t is the time, and x is the coordinate in chordwise direction. The wavenumber resolution, defined by $\Delta k = 1/(N dx)$ where N is the number of probes and dx is the distance between neighboring probes. Δk is equal to $5.25\mathrm{m}^{-1}$. The wavenumber, representing the number of complete waves in a unit dis-

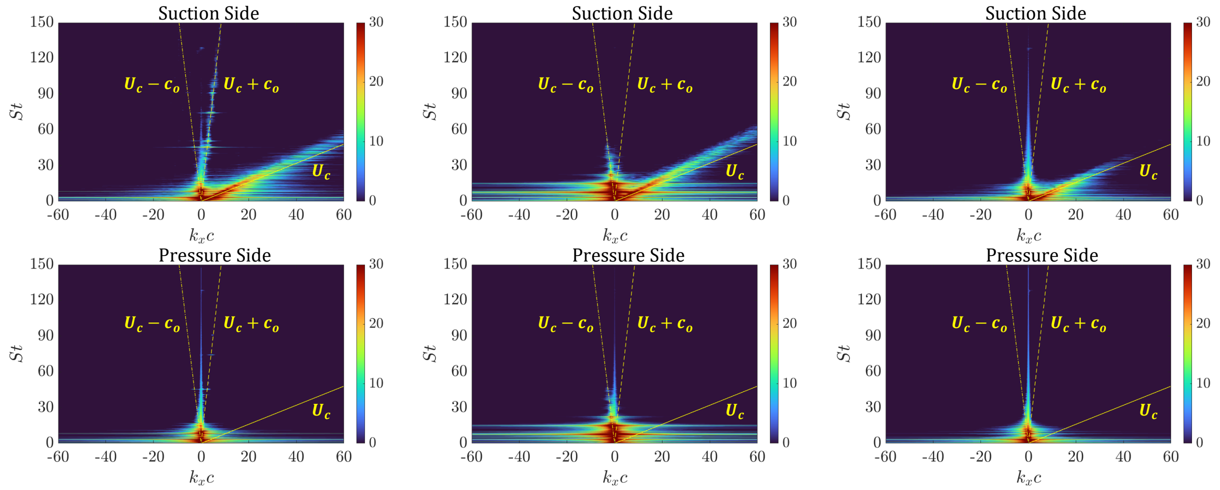

(a)

(b)

(c)

Figure 4.14: Wavenumber-frequency spectra, $10\log_{10}\left(\hat{\mathbf{P}}(f, k)\hat{\mathbf{P}}^{*}(f, k)/P_{\mathrm{ref}}^{2}\right)$, referenced to $P_{\mathrm{ref}} = 20\mu\mathrm{Pa}$, from $x/c = 0.365$ to the trailing edge: (a) stair strip, (b) suction and blowing, and (c) natural transition. An asterisk superscript denotes the complex conjugate. The spectrum has the unit of $\mathrm{dB}/(\mathrm{Hz}^2\mathrm{m}^{-2})$.

tance, has the unit of m^{-1}. The probe arrays are positioned off the wall at approximately $y/c = 0.05$ on both the suction and pressure sides. Figure 4.14 illustrates the near-wall pressure wavenumber-frequency spectra, $10\log_{10}\left(\hat{\mathbf{P}}(f,k)\hat{\mathbf{P}}^{*}(f,k)/P_{\mathrm{ref}}^{2}\right)$, on both sides of the airfoil. Here, an asterisk superscript denotes the complex conjugate. The spectrum has the unit of $\mathrm{dB}/(\mathrm{Hz}^{2}\mathrm{m}^{-2})$. The broad ridge of turbulent convection U_c along the near-wall is prominently visible above the airfoil suction side, as demonstrated in Figs. 4.14(a) to 4.14(c), with $U_c = 0.8U_\infty$. For the suction and blowing case, higher convection speed compared to the other two cases is a consequence of increased momentum transfer by the blowing boundary. For the stair strip, the tripping-induced sources are distinct at $St = 30 - 90$ with enhanced energy spectra along the acoustic ridge on the airfoil suction side, but it is scarcely visible on the airfoil pressure side since equilibrium flows are developed without turbulence mixing. Notably, this LSB-tripping interaction is one of the acoustic noise sources propagating downstream, $U_c + c_o$, over a broad spectral range, but propagates upstream $U_c - c_o$ at $St = 45$. The spectral peak of vortex shedding, observed near the frequency of $St = 7.5$ for all cases, aligns with both hydrodynamic and acoustic phase speeds. As confirmed in the wall-pressure spectra in Fig. 4.11 for the case of suction and blowing, distinct additional discrete-frequency peaks around $St = 15 - 50$ are evident, represented as upstream propagation on both airfoil sides in Fig. 4.14(b). This upstream propagation implies intense acoustic noise sources along the T-S waves and subsequent separation bubble. Meanwhile, the spectra of turbulent convection are scarcely detected above the airfoil pressure side, suggesting flows are again predominantly in an equilibrium state, except near the trailing edge, as validated by the turbulence intensities in Fig. 4.7. For the stair strip scenario, it is noted that the spectra responsible for upstream propagation resemble those for the natural transition scenario.

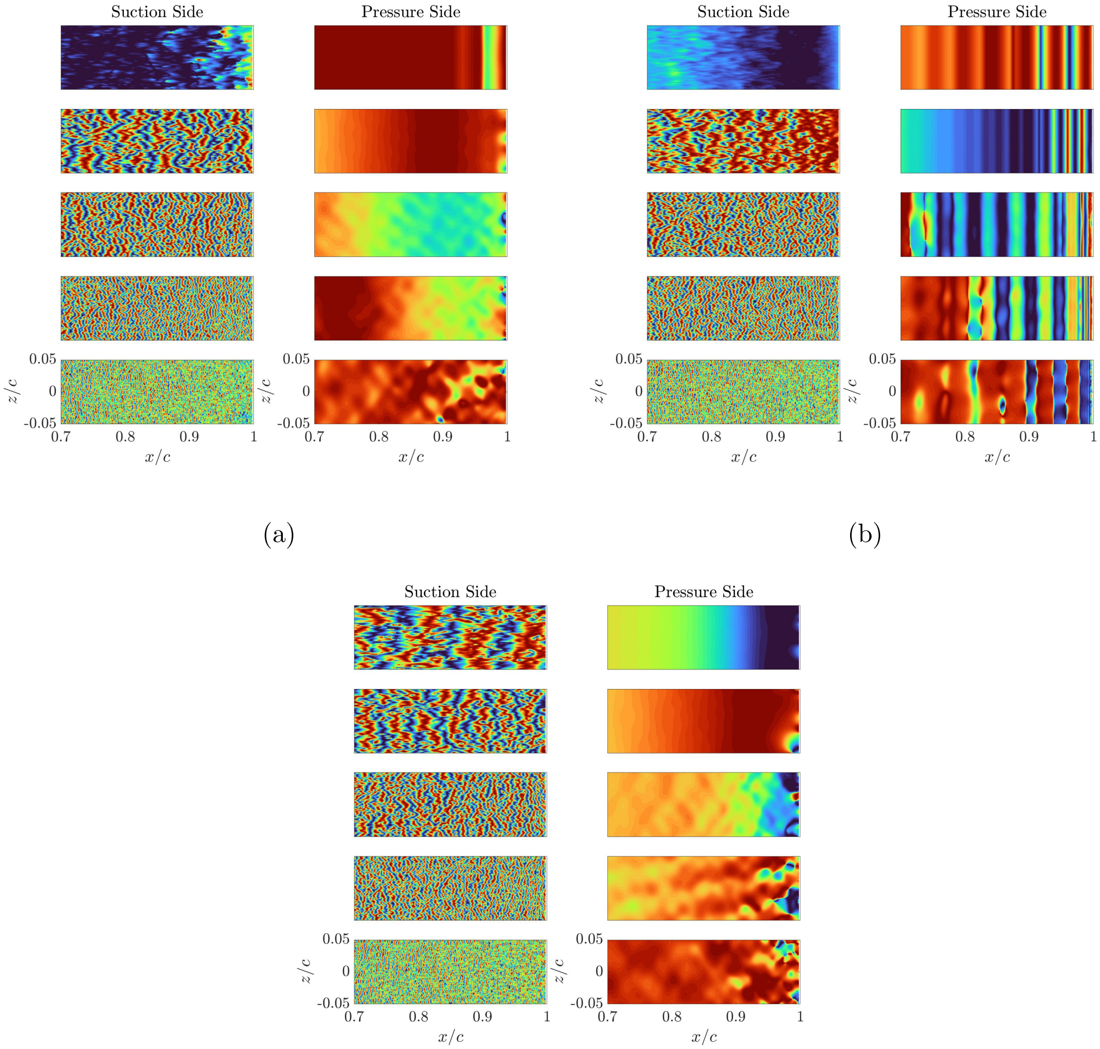

(a)

(b)

(c)

Figure 4.15: Phase distributions based on wall pressure fluctuations at $St \approx 7.5, 15, 30, 45,$ and 60 from top to bottom: (a) stair strip, (b) suction and blowing, and (c) natural transition. Phase varies from -1 (blue) to 1 (red).

Figure 4.15 presents phase distributions along both airfoil sides from $x/c = 0.7$ to 1.0 at five different frequencies, computed using the cosine function of the phase given by $\cos(\phi) = \mathrm{Re}(\hat{p})/|\hat{p}|$, where $\hat{p}$ represents the Fourier transform of the pressure fluctuation. For the two forced tripping approaches, the out-of-phase near the trailing edge is distinct on the airfoil pressure side at about $St \approx 7.5$, a feature of a two-dimensional vortex shedding.

However, at the same location and Strouhal number, the natural transition does not display any two-dimensional phase but instead depicts a gradual change like a long waveform. For the case of suction and blowing, a periodically traveling waveform of the spanwise-coherent phase is distributed in the streamwise direction on the airfoil pressure side at all selected Strouhal numbers. This type of two-dimensional phase structure arises from the hydrodynamic instability of T-S waves as the disturbance grows due to APG flows. This essentially contributes to high-amplitude spectra as shown in Fig. 4.11(b). Meanwhile, a strong phase variation is depicted on the pressure side at Strouhal numbers higher than $St \approx 15$ for the stair strip and natural transition, illustrating trailing-edge scattering. This scattering mechanism is more pronounced for the natural transition than for the stair strip. On the other hand, the spanwise-coherent phases and the intense phase variation adjacent to the trailing edge observed on the airfoil pressure side are rarely seen on the suction side for all cases. This is due to masking by non-equilibrium turbulent boundary layers whose pressure fluctuations are much higher than acoustic perturbations. This is particularly at Strouhal numbers higher than 15 where turbulent pressure structures are visible as the chordwise out-of-phase along the chord. However, at the vortex-shedding frequency at $St \approx 7.5$, the vortex-shedding phase masks the hydrodynamic turbulent phase for both the stair strip and suction and blowing scenarios. The intermediate conclusions drawn from the wall or near-wall spectra emphasize the importance of examining pressure statistics on the pressure side in addition to the suction side. This is because local non-equilibrium flows involving the disturbance and its amplification along the T-S waves contribute to the acoustic source in airfoil noise at a non-zero angle of attack.

It is known that the hydrodynamic pressure field develops on the wall with low-to-high

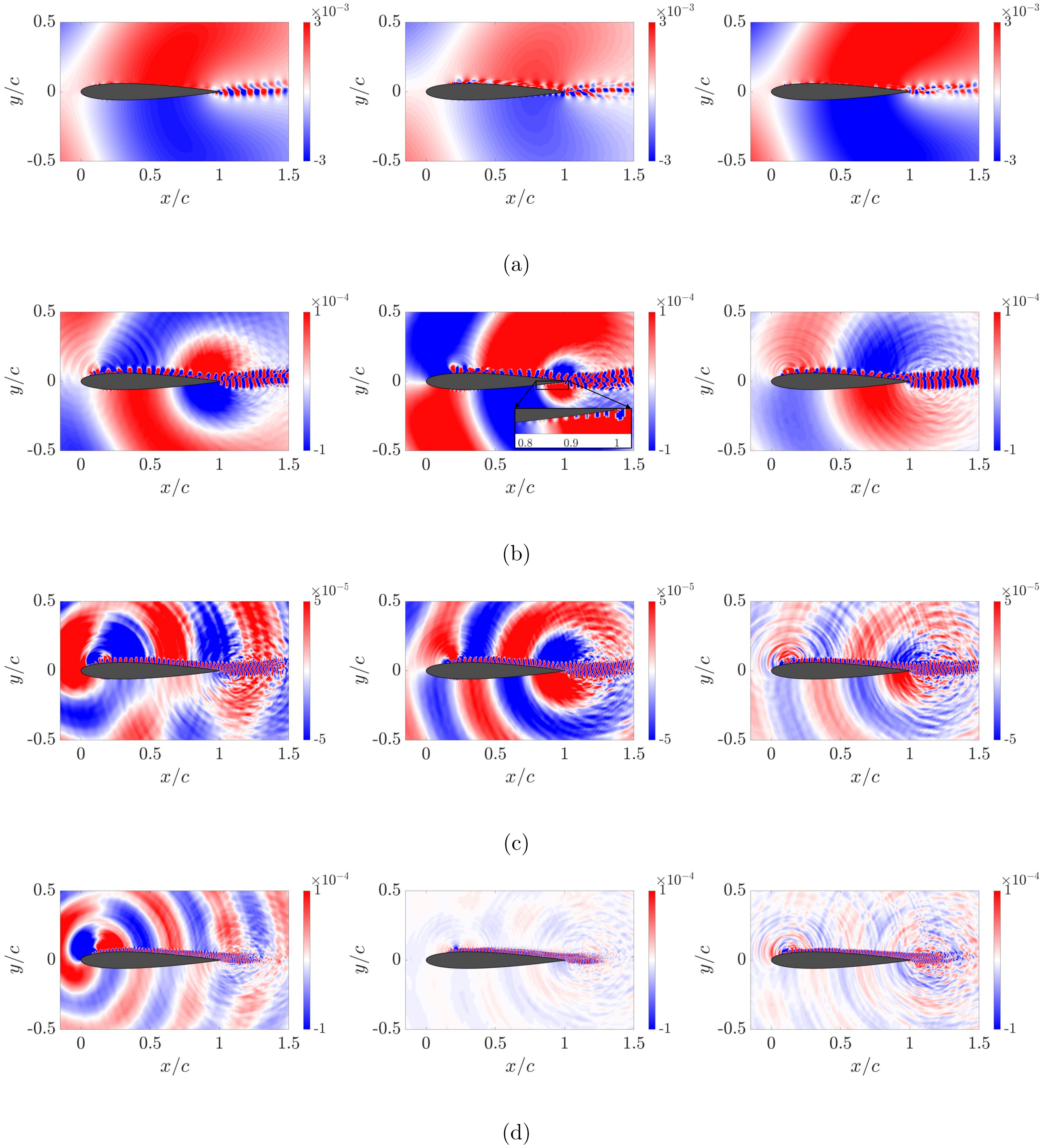

Figure 4.16: DMD modes for stair strip (left), suction and blowing (mid) and natural transition (right) in midspan: (a) $St \approx 8.4$, (b) $St \approx 15$, (c) $St \approx 30$, and (d) $St \approx 45$.

turbulent scales convecting through the wall, while the acoustic perturbation and its propagation dominate off the wall to the far field [190]. Pressure-based DMD analyses can represent both the hydrodynamic coherent structure near the wall and the acoustic propagation off the wall at a specific frequency [191]. Thus, each mode illuminates the dynamics of the system, defining its spatiotemporal characteristics at a specific frequency. Nonetheless, multiple waveforms can coexist at a single frequency due to different phase speeds in flow and acoustics, as was depicted in the pressure spectra on the wavenumber-frequency domain in Fig. 4.14. An accompanying DMD spectrum and the validation of the statistical equilibrium of selected flow snapshots for the three cases are enlisted in Appendix D. Figure 4.16 illustrates four different DMD modes around the airfoil cut in midspan for the three simulated cases. It becomes clear at $St \approx 7.5$ that the coherent structure near the wake is related to the vortex shedding, whose acoustic wavelength appears longer than the chord length. Note that some hydrodynamic coherent structures along the turbulent convection, shown at Strouhal numbers higher than 7.5, seem to be masked by the perturbed acoustic wave at $St \approx 7.5$. A similar long acoustic waveform with vortex shedding structure is found in the natural transition because DMD modes are sliced in midspan, not quantified by spanwise coherence. At Strouhal numbers higher than 7.5, the coherent wavy structures from the leading edge are clearly shown to advect along the airfoil suction side and scatter in all directions, taking the form of antisymmetric dipole behavior for the three simulated cases. The sound propagation is found to originate from the acoustic dipolar source located in the wake as a short waveform, which is considered as trailing-edge noise [173]. Meanwhile, noticeable acoustic perturbations emitted from the LSB-tripping interaction are seen for the stair strip scenario at $St \approx 30$ and 45. For the suction and blowing scenario, depicted in Fig. 4.16(b), the coherent pressure structures perceived as the T-S waves are traveling downstream along the airfoil pressure side close to the trailing edge. In conclusion of this section, while the sound generation and propagation mechanisms associated with trailing-edge noise predictions are similar for the three simulated cases, the effect of boundary-layer tripping makes each case substantially different in fluid-induced noise generations: the LSB-tripping interaction for the stair strip, and the laminar boundary-layer instability flows for the suction and blowing in the present non-zero angle of attack.

4.4 Far-field Acoustics

In line with our previous investigations into flow configurations and associated sound generation mechanisms in relation to wall and near-wall hydrodynamic sources, this section presents a quantitative analysis of far-field acoustic levels using the FW-H computations. Figure 4.17 depicts the narrowband sound pressure levels (SPLs) and the one-third octave band SPLs measured from the entire airfoil surface at a microphone position specified by $x/c = 1.0$, $y/c = 10.0$, and $z/c = 0.05$. For both forced tripping strategies, the previously observed vortex-shedding spectral peak at $St = 7.5$ is confirmed to be a radiated noise source, indicating a tonal peak at the same Strouhal number. It is also worth noting the equidistant harmonics starting from the main peak, $St \approx 7.5$. This tone noise is associated with the strong spanwise-coherent flow patterns, as shown in Figs. 4.15(a) and 4.15(b) on the pressure side for the stair strip and suction and blowing. The natural transition, on the other hand, exhibits a lower magnitude due to its relatively weak spanwise-coherent nature, and it indicates the weak tone at $St \approx 7.5$ as shown in Fig. 4.17(a).

In the case of suction and blowing, the secondary and tertiary quasi-tonal peaks at $St = 15$ and 22 remarkably mirror the wall-pressure spectra on the pressure side (Fig. 4.11(b)). This phenomenon results from the two-dimensional T-S instability waves and the

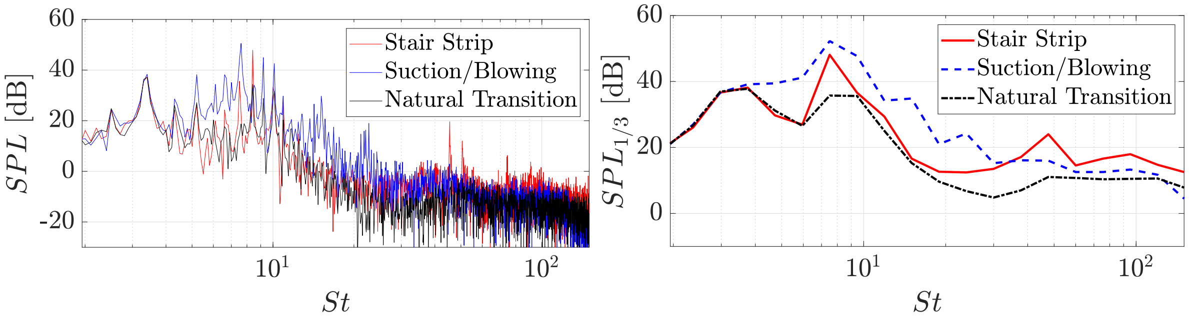

(a) (b)

Figure 4.17: Acoustic spectra at an observer location $x/c = 1.0$, $y/c = 10.0$, and $z/c = 0.05$: (a) narrowband SPL and (b) one-third octave band SPL.

subsequent separation bubble, which amplifies the noise compared to the other two scenarios, as outlined by Nash et al. [180]. These observations reinforce the conclusion that the noise generated in the suction and blowing scenario is largely due to laminar boundary layer instability. For the stair strip, however, one can observe a general increase in the acoustic level at Strouhal numbers higher than 15, forming a broadband hump with a peak embedded at $St = 45$. This characteristic differentiates it from the other two cases and aligns with the near-wall pressure spectra, as seen in Fig. 4.11(b). Even in the natural transition scenario, a distinct weak broadband hump appears near $St = 45$. This is associated with LSB-self excitation under non-equilibrium flows due to APG flows. Overall, by comparing the wall-pressure spectra on the airfoil pressure side in Fig. 4.11(b) and the far-field acoustic levels in Fig. 4.17, one can identify similar acoustic dynamics across the two forced tripping approaches. These include the vortex shedding peak around $St = 7.5$, a broadband hump with a peak at $St = 45$ for the stair strip scenario, and additional humps at $St = 15 - 30$ for suction and blowing scenario. As previously mentioned in the intermediate summaries, these findings suggest that the pressure field on the airfoil pressure side plays a critical role in understanding sound source generation and propagation mechanisms in the current non-zero angle flow conditions. Although the narrowband spectra provide clear acoustic tones, the follow-up results are plotted with one-third octave band SPL because it highlights the unique noise spectrum of each transition scenario and facilitates their comparison along the entire range of Strouhal numbers.

Analyzing the far-field acoustics originating from sectional components on the airfoil helps clarify the relative contribution of near-wall noise sources to the far-field sound spectra. The schematic for this sectional noise analysis is identical, as depicted in Fig. 3.29. The index of each segmented component, or airfoil strip, is marked, beginning from the trailing edge and moving in the upstream direction. Each strip's streamwise width normalized by the airfoil chord, $\Delta x/c$, is 0.011. The sound radiated from each strip is computed on both sides of the airfoil at observer position coordinates $x/c = 1.0$, $y/c = 10.0$, and $z/c = 0.05$ using

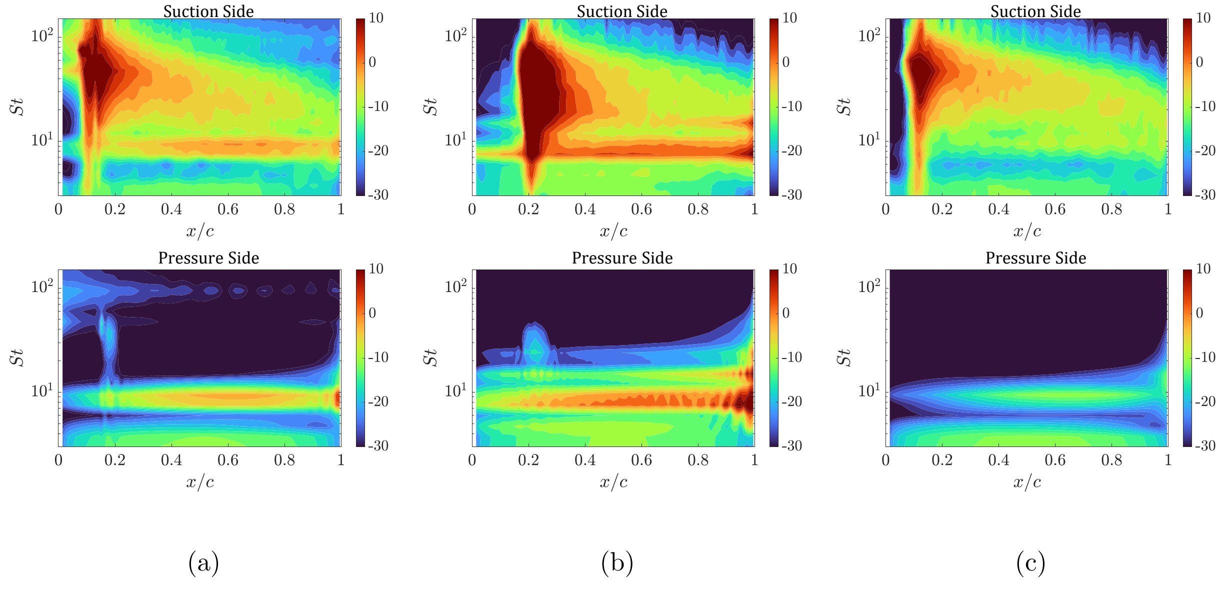

(a)

(b)

(c)

Figure 4.18: Sectional noise contours of the one-third octave band SPLs at an observer location $x/c = 1.0$, $y/c = 10.0$, and $z/c = 0.05$: (a) stair strip, (b) suction and blowing, and (c) natural transition.

the FW-H acoustic analogy. First, the sound waves radiated from each strip on the airfoil are examined. This approach concentrates on identifying the relative contribution of local acoustic sources across the airfoil, thus minimizing the phase of neighboring sources. Figure 4.18 presents the resulting sectional noise on both sides of the airfoil as one-third octave band SPLs in contour levels. Both forced tripping scenarios in Figs. 4.18(a) and 4.18(b) feature the primary vortex-shedding noise that encompasses the entire airfoil at $St = 7.5$. For the case of stair strip, the high intensity of the leading-edge noise is particularly noticeable due to the LSB-tripping interaction, which is distinct at Strouhal numbers above $St = 15$. For the suction and blowing scenario, stronger leading-edge noise is evident behind the blowing boundary ($x/c \approx 0.2$). However, most of this noise source will be proved to be a non-radiating component due to the phase cancellation between neighboring point sources later. For the suction and blowing scenario, the noise oscillation evolves and amplifies on the pressure side near the trailing edge where the separation bubble was observed, particularly around $St = 7.5$ and 15. This pattern strikingly mirrors previous observations of RMS wall pressure in Fig. 4.4(b), the coherent acoustic pattern in Fig. 4.9(d), and the convection of T-S waves in Fig. 4.10(b). Based on these observations involving the propagation of spanwise coherent instability waves traveling along the wall and the sound amplification mechanism in the presence of a separation bubble, it can be concluded that the suction and blowing scenario emits laminar boundary layer vortex shedding noise [5, 13, 173, 180]. In the case of natural transition (Fig. 4.18(c)), the leading-edge noise due to the LSB-self excitation is observed on the suction side though the boundary-layer tripping is absent. In conjunction with the flow-acoustic interactions discussed in the previous sections, it is important to emphasize the significance of the design and installation of boundary-layer tripping. This factor directly

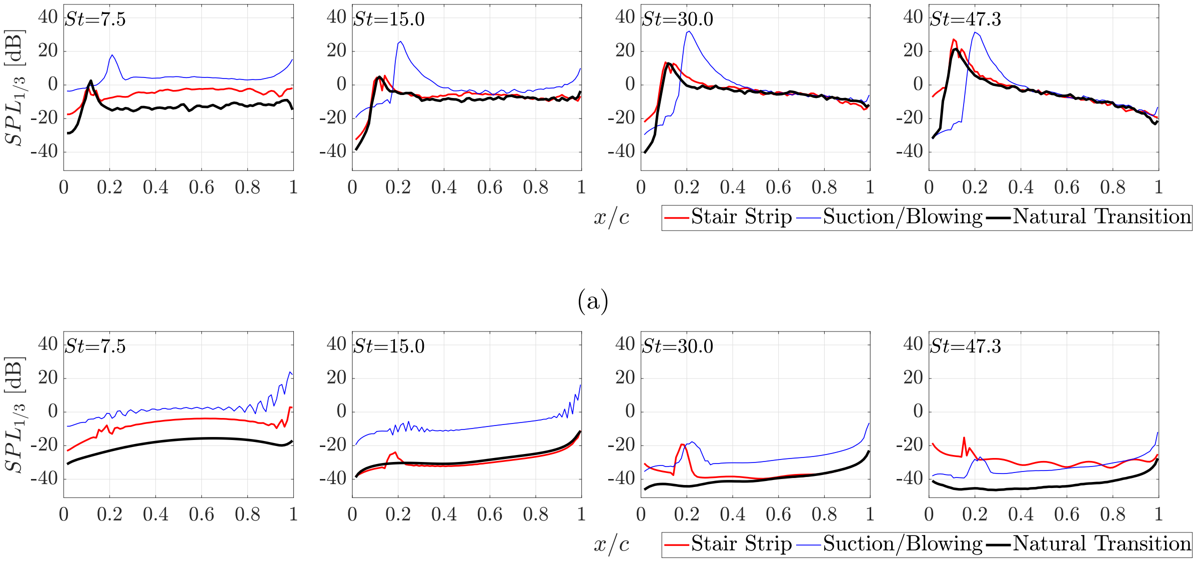

(a)

(b)

Figure 4.19: Sectional noises of the one-third octave band SPLs from the leading edge to the trailing edge at particular Strouhal numbers: (a) suction side and (b) pressure side.

influences the acoustic dynamics in both single and multiple airfoil noise mechanisms.

The quantitative comparison of the three scenarios at four selected frequencies is presented in Fig. 4.19. Three scenarios showcase the noise spike after the separated-flow transition on the suction side, which is an extremely similar behavior to the RMS quantity in Fig. 4.4. For the suction and blowing scenario, the oscillating amplification driven by laminar boundary layer instability and the local separation bubble results in a higher acoustic level than the other two scenarios from $St = 7.5$ to 15 on the pressure side. This local increase in noise gradient at the trailing edge implies the scattering mechanism, which is shown to interact with the acoustic source on the suction side. Notably, leading-edge noise is observed from $St = 30$ to 47.3 on the suction side around $0.2c$ to $0.4c$, but it dissipates like in the other two scenarios from the mid-chord onwards. For the stair strip scenario, an oscillation similar to that in the suction and blowing scenario is developing on the pressure side, but its strength is weak and confined only to $St = 7.5$.

As the final stage of the sectional noise analysis, the cumulative pressure is computed by integrating from the trailing-edge strip (the 1st strip) to the i-th strip of the airfoil as follows:

$$p_i^{'} = \sum_{k=1}^{i} p_k, \tag{4.5}$$

where p_k is the sectional far-field pressure radiated from the k-th strip, and $p_i^{'}$ is the cumulative far-field pressure derived from the integration on the right-hand side. It should be noted that this cumulative pressure accounts for the phase relation between neighboring strips within the partial integration. The one-third octave band SPLs of this cumulative pressure for the three transition scenarios are depicted in Fig. 4.20. In the figure, the positive and negative gradients correlate to in-phase and out-of-phase relations in neighboring strips, respectively. A consistent increase is observed at $St = 7.5$ for all cases, indicating

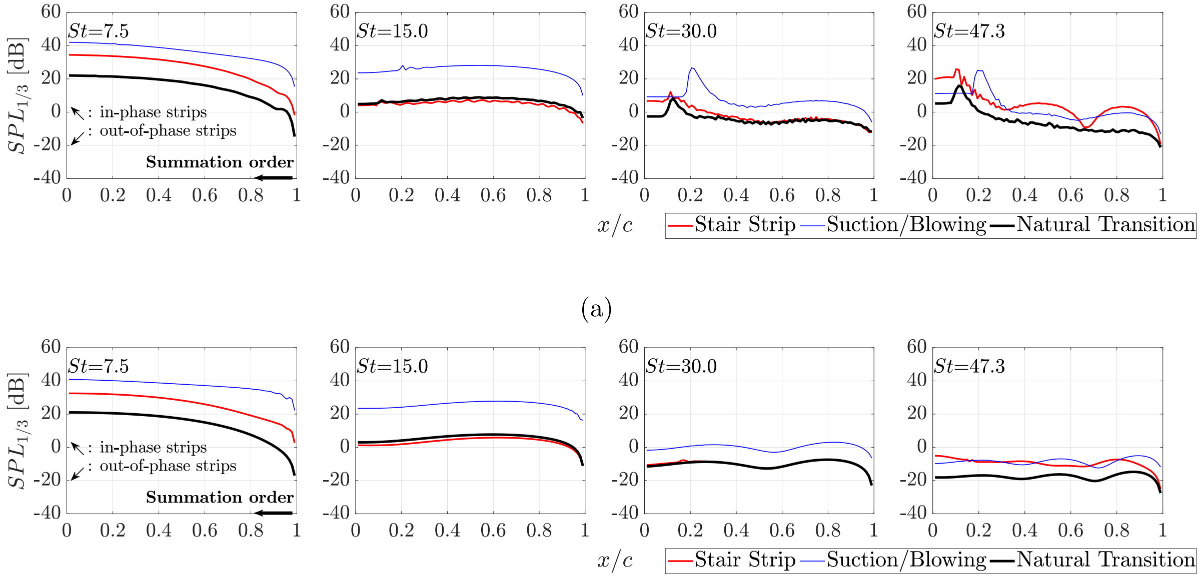

(a)

(b)

Figure 4.20: Cumulative noises of the one-third octave band SPLs from the leading edge to the trailing edge at particular Strouhal numbers: (a) suction side and (b) pressure side.

in-phase characteristics. The higher noise of two forced tripping approaches than the natural transition is due to the spanwise-coherent vortex shedding on the pressure side as observed earlier. For the stair strip scenario, one can observe the valley curve around $x/c \approx 0.65$ on the suction side at $St = 47.3$. As presented earlier, this frequency is dominated by the strong LSB-tripping interaction around the leading edge while the scattering of hydrodynamic coherent structure is prominent around the trailing edge. The significant interaction of two acoustic sources from the leading- and trailing- edge of airfoil is attributed to such a nonlinear curve [165]. For the suction and blowing scenario, the cumulative noise remains constant on the suction side at $St = 15$ as it integrates towards the leading edge, despite the presence of local intense acoustic sources, as presented in Figs. 4.18 and 4.19. This supports the previous assertion that the destructive interference between neighboring noise sources leads to evanescent waves. Such destructive interference is also evident from $x/c = 0.4$ to 0.8 in the frequency range from $St = 30$ to 47.3, whereas noise slightly decreases or remains the same. Furthermore, the tiny noise oscillations in the streamwise direction only observed on the suction side are related to consecutive constructive and destructive interferences due to turbulent fluctuations similar to Fig. 4.15 for three scenarios. The stair strip scenario illustrates a slight increase in gradient at $St = 30$ or a gradual increase at $St = 47.3$ near the leading edge, with both being influenced by the LSB-tripping interaction to generate noise. Significant trailing-edge scattering is observed around 90% of the chord length from the trailing edge, which shows a rapid increase at all frequencies for all scenarios. One can further observe that the cumulative noise magnitude between both airfoil sides is fairly approximate when compared to the sectional noise magnitude between both airfoil sides in Fig. 4.19. This implies that although the turbulent hydrodynamic pressure has a high energy spectrum, the nature of chordwise phase cancellation involving the tripping region makes this pressure component a pseudo-sound source unless the scattering or diffraction is not considered. The other thing to note is an abrupt decrease in cumulative noise near the leading edge on the suction side as shown in Fig. 4.19(a). This local decrease is due to significant phase cancellation between acoustic sources fore and aft of the flow transition, which is notably observed at higher frequencies. This is likely due to the non-compactness of shorter wavelengths of acoustic sources. In general, the segment-based (sectional) and cumulative noises provide valuable insights into the relationship between acoustic sources and highlight the propagating natures of noise sources on the airfoil and far-field noise.

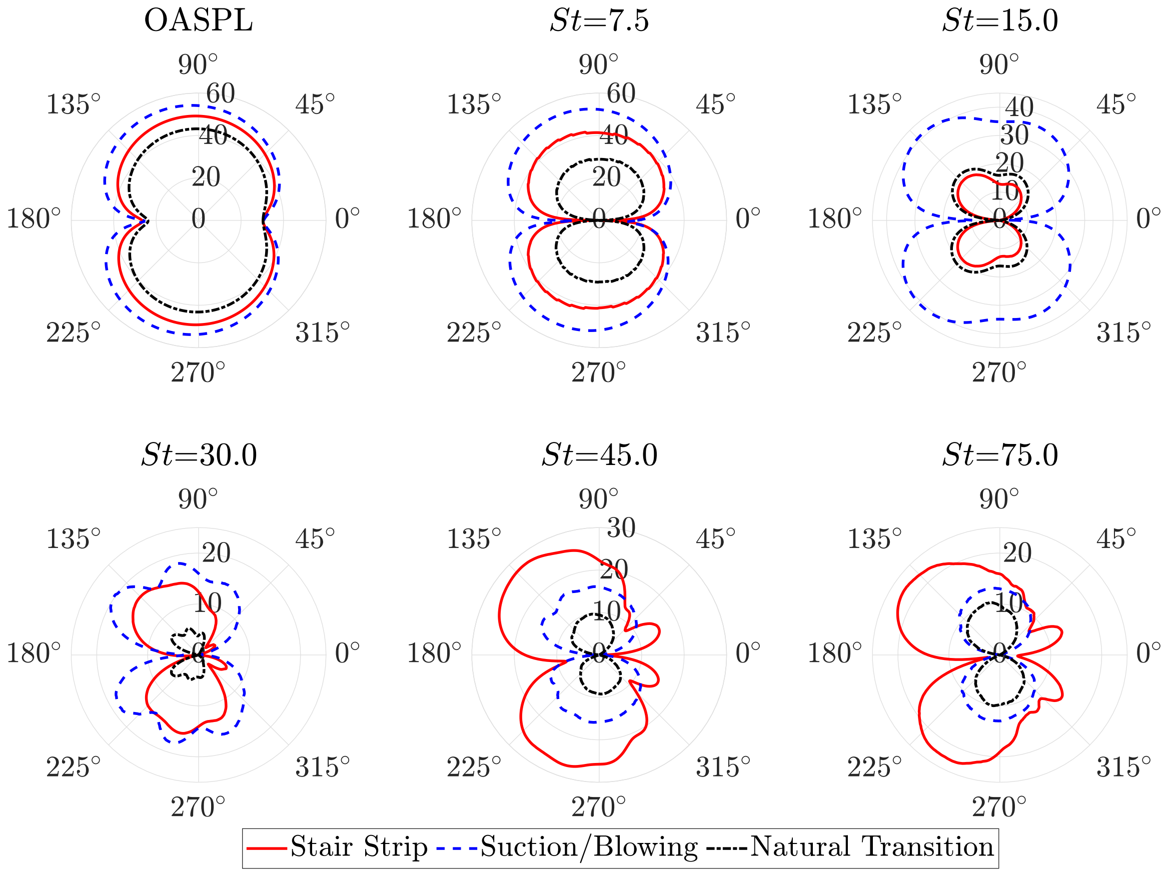

OASPL

St=7.5

St=15.0

St=30.0

St=45.0

St=75.0

Figure 4.21: Directivity of OASPL and one-third octave band SPLs at particular Strouhal numbers computed at the radius of 10.0c from the origin at trailing edge.

Finally, the directivity pattern is derived from the pressure fluctuations along the entire airfoil. The microphone arrays are positioned mid-span with a radius of $10.0c$ from the origin at the trailing edge. The overall sound pressure level (OASPL) and one-third octave band SPLs at five different frequencies are presented in Fig. 4.21. For the microphone at $\theta = 90^\circ$, the OASPL for the stair strip and suction and blowing is 2.76 dB and 6 dB higher than for the natural transition, respectively. At the vortex-shedding frequency at $St = 7.5$, the two forced-tripping approaches display a greater dipole source strength than the natural transition. At a Strouhal number of 15, high SPLs are observed in all azimuthal directions for the suction and blowing scenario, where the driving mechanism is the hydrodynamic instability and the existence of the separation bubble. As the Strouhal number increases, multiple lobes are added to the simple dipole pattern, forming the cardioid shape typically associated with the non-compactness of trailing-edge noise [23, 192]. As shown at $St = 30$, the cardioid shape is clearly displayed for the case of suction and blowing, as well as the natural transition. This aligns with the significant contribution from the trailing-edge component when partially integrated from the trailing-edge strip as displayed in Fig. 4.20. For the stair strip, however, a simpler cardioid directivity along with a small oval shape near $\theta = 0^\circ$ is observed. This small oval shape primarily might arise from the tripping effect. The LSB-tripping interaction noise peaks at $St = 45$ for the case of stair strip and remains dominant at higher Strouhal numbers over the other two cases.

4.5 Summary

This chapter investigated the impact of boundary-layer tripping on airfoil noise at a Reynolds number of 4×10^5, a Mach number of 0.058, and an angle of attack of 6.25°. Two distinct forced tripping methods were considered: a geometrically resolved stair strip and artificially imposed suction and blowing. The untripped case, reflecting the natural transition of boundary layers, was scrutinized as a comparative baseline. The transition of flow into non-equilibrium turbulent states and the generation of acoustic sources were observed to vary between the different boundary-layer tripping methods. To interrogate this, the aerodynamic flow fields were quantified, and spectral and modal analyses of both near-wall and far-field pressures were conducted. The primary outcomes of this chapter are as follows:

1) The suction and blowing case exhibited a delayed transition on the airfoil suction side compared to the other two cases. This delay was attributed to the increased momentum flux generated by the blowing boundary. While the transition position in both the stair trip scenario and natural transition scenario is comparable, there are pronounced differences between the two. For instance, the stair trip case introduces a more intricate leading-edge sound scattering phenomenon due to the interaction between flow and/or acoustic waves at the stair-strip location. Near the trailing edge, a separation bubble was observed for all cases. This phenomenon was identified through various pieces of evidence including visual flow fields, spatial variation of skin friction, and a sudden increase in the shape factor. In the suction and blowing case, the convection of two-dimensional T-S instability waves was identified as the unique noise source that distinguished this scenario from the other two.

2) As turbulent boundary layers developed on the suction side following the flow transi-

tion, the primary acoustic source in all cases was the scattering of the hydrodynamic coherent structure by the trailing edge. This noise was detected as an antisymmetric wave and multi-lobe pattern at frequencies between $St = 15$ and 30, particularly intense within 10% of the airfoil chord near the trailing edge. The installation of tripping mechanisms introduced additional acoustic source phenomena. A common feature of tripping installations was the tonal peak around $St = 7.5$ due to vortex shedding. This far-field noise correlated with the spanwise coherent phase on the wall, meeting the necessary condition for tonal noise emission. Moreover, distinct noise mechanisms were discovered in the stair strip and the suction and blowing scenarios. In the stair strip scenario, the interaction between LSB and tripping amplified LSB broadband noise, with a high-frequency quasi-tonal peak. This noise amplification occurred in all azimuthal directions and peaked at $St = 45$, with a distinct additional oval shape in the downstream direction. In contrast, in the suction and blowing scenario, the spanwise coherent T-S waves and the presence of a separation bubble disrupted both velocity and pressure fields near the trailing edge on the airfoil pressure side. The acoustic radiation was characterized by a dipolar directivity pattern and an overall increase in SPL in a harmonic manner, being called laminar boundary layer vortex shedding noise. It is summarized that the suction and blowing can introduce an added noise source on the pressure side. This becomes particularly apparent when the favorable pressure gradient is strong enough to keep the perturbed flow behind the tripping stable and laminar. Yet, it is essential to stress that both methods, suction and blowing and stair strip, have effectively tripped the boundary-layer flow on the suction side.

Chapter 5

Cross-spectrum Method for Acoustic Source Identification and Visualization

This chapter proposes a novel approach, the cross-spectrum method, based on cross power spectral density, for identifying acoustic sources and visualization of sound propagation. The numerical data on the three different transition mechanisms over a NACA 0012 airfoil studied in Chapter 4 are utilized in this chapter to examine and evaluate cross-spectrum formulations. From the far-field sound spectra of the stair strip, suction and blowing, natural transition scenarios, as shown in Fig. 4.17, it was observed that the primary noise sources are broadband trailing-edge scattering of turbulent flows and T-S instability waves as well as tripping-induced leading-edge noise, corresponding to frequencies of 1 kHz ($St = 15$) and 3 kHz ($St = 45$), respectively. Thus, this section focuses on these frequency domains (1 kHz and 3 kHz) for further exploration of the cross-spectrum method.

5.1 Assessment of Magnitude, Phase, and Time Dynamics of Cross-spectrum Formulation

This section delves into the magnitude, phase, and time dynamics of the first cross-spectrum formulation $S_{xx}\exp(\mathrm{i}\phi_{xy})$ for the stair-strip case. This formulation basically includes intrinsic properties that characterize the cross-spectrum method through the phase angle, ϕ_{xy}, although APSD or S_{xx} is involved. Figure 5.1 shows snapshots of S_{xx}, real part of complex exponential of phase angle using the reference point of P1 (see Fig. 2.4), and multiplication of S_{xx} and phase fields at 1 kHz. These snapshots were computed based on data matrices of $n_x = 500$ and $n_y = 400$, spanning the spatial domain in the streamwise (x) direction from $-0.5c$ to $2.0c$ and in the normal (y) direction from $-0.5c$ to $0.5c$, cut at midspan. The minimum and maximum values of the color scale are statistically determined, corresponding to $\mu \mp 4\sigma$, where μ and σ represent the mean and standard deviation of each quantity collected from $x/c \in [0, 1.5]$ and $y/c = 0.5$. The sampling position is strategically placed in areas where acoustic wavefronts are most significant. The APSD, or S_{xx}, effectively illustrates the sound field's strength, while the phase field reveals the relative phase differences between spatial points and the reference point or the sound propagation characteristics. At 1 kHz, significant noise emission from the trailing edge is observed, as well as the high intensity of the spectrum and the acoustic phase discontinuity on both sides of the airfoil, as depicted in Figs. 5.1(a) and 5.1(b). However, each of these measurements provides limited information about the other. For example, the hydrodynamic coherent structures and sound propagation patterns evident in the phase field are not discernible in the APSD, and conversely, the magnitude of the sound cannot be ascertained from the phase field alone. Yet, when these two

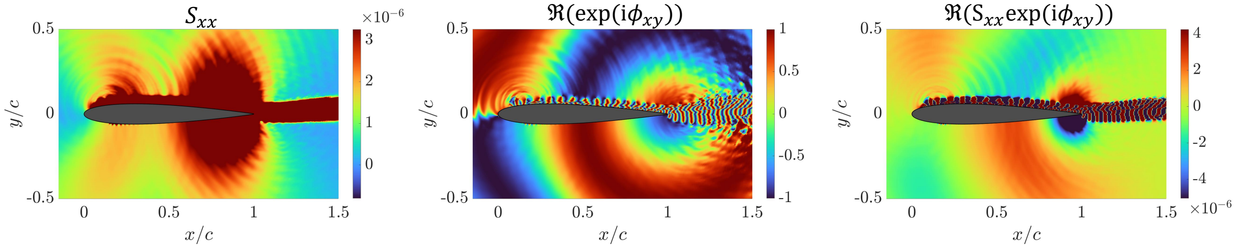

(a) (b) (c)

Figure 5.1: (a) APSD S_{xx}, (b) real part of complex exponential of phase angle $\Re(\exp(\mathrm{i}\phi_{xy}))$, and (c) multiplication of APSD and real part of complex exponential of phase angle $\Re(S_{xx}\exp(\mathrm{i}\phi_{xy}))$ for the reference point of P1 at 1 kHz.

measurements are superimposed, as shown in Fig. 5.1(c), the near-wall coherent structures in the hydrodynamic pressure field and the sound propagation in the acoustic pressure field become distinctly visible. This principle is similarly applied to the pressure field at 3 kHz, as presented in Fig. 5.2. In Fig. 5.2(a), the interaction between the LSB and tripping at the leading edge is identified as the primary driver of sound generation at this frequency. Figures 5.2(b) and 5.2(c) highlight the sound propagation from the leading edge and the near-wall wavy structures, as well as the combined visual representation of the spectral magnitude and phase topology. This combination effectively illustrates the wavefronts of leading-edge noise propagation. It is crucial to understand that despite the reference point being situated near the trailing edge, the dominant noise originating from the leading edge is still effectively captured at this specific frequency. This highlights that the chosen reference point does not dictate the identification of the noise source's origin in this approach. The effect of the reference point is investigated later.

Figure 5.3 illustrates the temporal variation of the formulation $\Re(S_{xx}\exp(\mathrm{i}\phi_{xy}))$ using the reference position of P1, focusing on frequencies at 1 kHz and 3 kHz. The phase angle is represented by the real part of the complex exponential, or a cosine function. It is shown

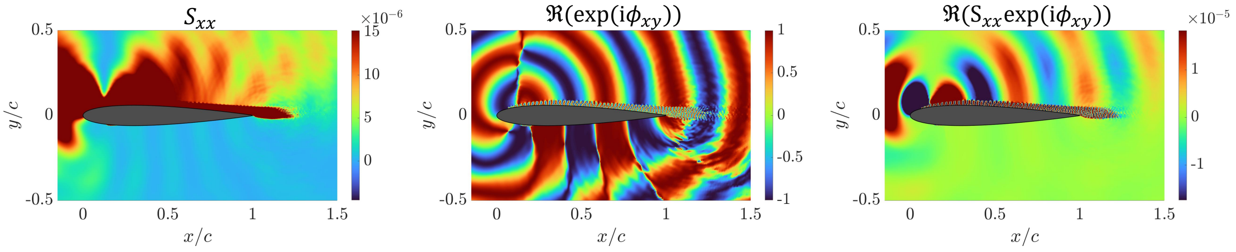

(a) (b) (c)

Figure 5.2: (a) APSD S_{xx}, (b) real part of complex exponential of phase angle $\Re(\exp(\mathrm{i}\phi_{xy}))$, and (c) multiplication of APSD and real part of complex exponential of phase angle $\Re(S_{xx}\exp(\mathrm{i}\phi_{xy}))$ for the reference point of P1 at 3 kHz.

that the magnitude of this quantity at 1 kHz is significantly greater than that observed at 3 kHz. This method can be applied to any frequency of interest. Furthermore, by extending this approach spatially from a single point to multiple points across a plane, as shown in Figs. 5.1 and 5.2, it becomes possible to visualize the dynamic motions of principal flow structures and acoustic propagation. These dynamic motions include turbulent convection, trailing-edge scattering, and the interaction of the LSB with tripping at specific frequencies. It is important to note that while future state predictions in time can also be accomplished using DMD [108] and SPOD [105], the cross-spectrum method uniquely enables the quantification of sound magnitude, as shown in Fig. 5.3. This aspect and its implications will be discussed in further detail later in the paper.

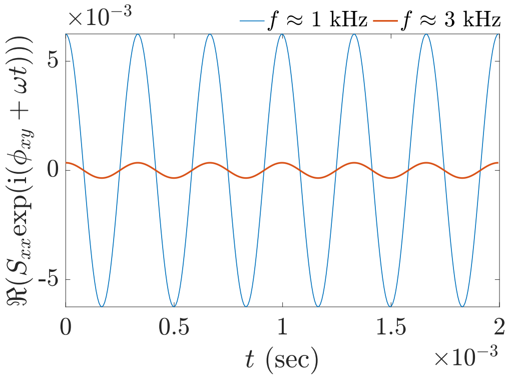

Figure 5.3: Time dynamics of $\Re(S_{xx}\exp(\mathrm{i}(\phi_{xy}+\omega t)))$ at 1 kHz and 3 kHz.

5.2 Comparison of Three Cross-spectrum Methods and Effect of the Choice of the Reference Point

While the previous section separately examined or combined the spectral magnitudes and phase topologies, this section scrutinizes the strengths and limitations of three proposed cross-spectrum formulations on both linear and logarithmic scales. Additionally, we assess each method at three selected reference points. The logarithmic scale indicates that each formulation is presented in the form of SPSL, yielding a sound spectrum in dB as commonly used in the field [67]. Figure 5.4 displays the contours using these three distinct cross-spectrum formulations on both scales at reference points P1 ($x/c = 0.99$, $y/c = 0.002$), P2 ($x/c = 0.15$, $y/c = 0.06$), and P3 ($x/c = 0.99$, $y/c = 0.5$) for the stair-strip case.

It is observed that the formulations $S_{xx}\exp(\mathrm{i}\phi_{xy})$ and S_{xy} do not visualize phase topologies on a logarithmic scale, regardless of the selection of reference point. The formulation $S_{xx}\exp(\mathrm{i}\phi_{xy})$ demonstrates an identical pressure spectrum on the logarithmic scale, highlighted by black-dashed boxes, when the reference points change. This is because the absolute value of the complex exponential is mathematically unity. In other words, the reference position does not affect the results. Conversely, S_{xy} shows sensitivity to the choice of reference point on both scales. When the reference point is positioned near the trailing edge (P1), the noise emanating from the trailing edge is prominently featured on both linear and logarithmic scales. When the reference point is near the leading edge (P2), the leading-edge noise emanation is more evident, as denoted in black-dashed circles in Fig. 5.4(b), while providing thicker hydrodynamic coherent structures compared to positions P1 or P3. When the reference point is situated within the acoustic propagation domain (P3), the dominant

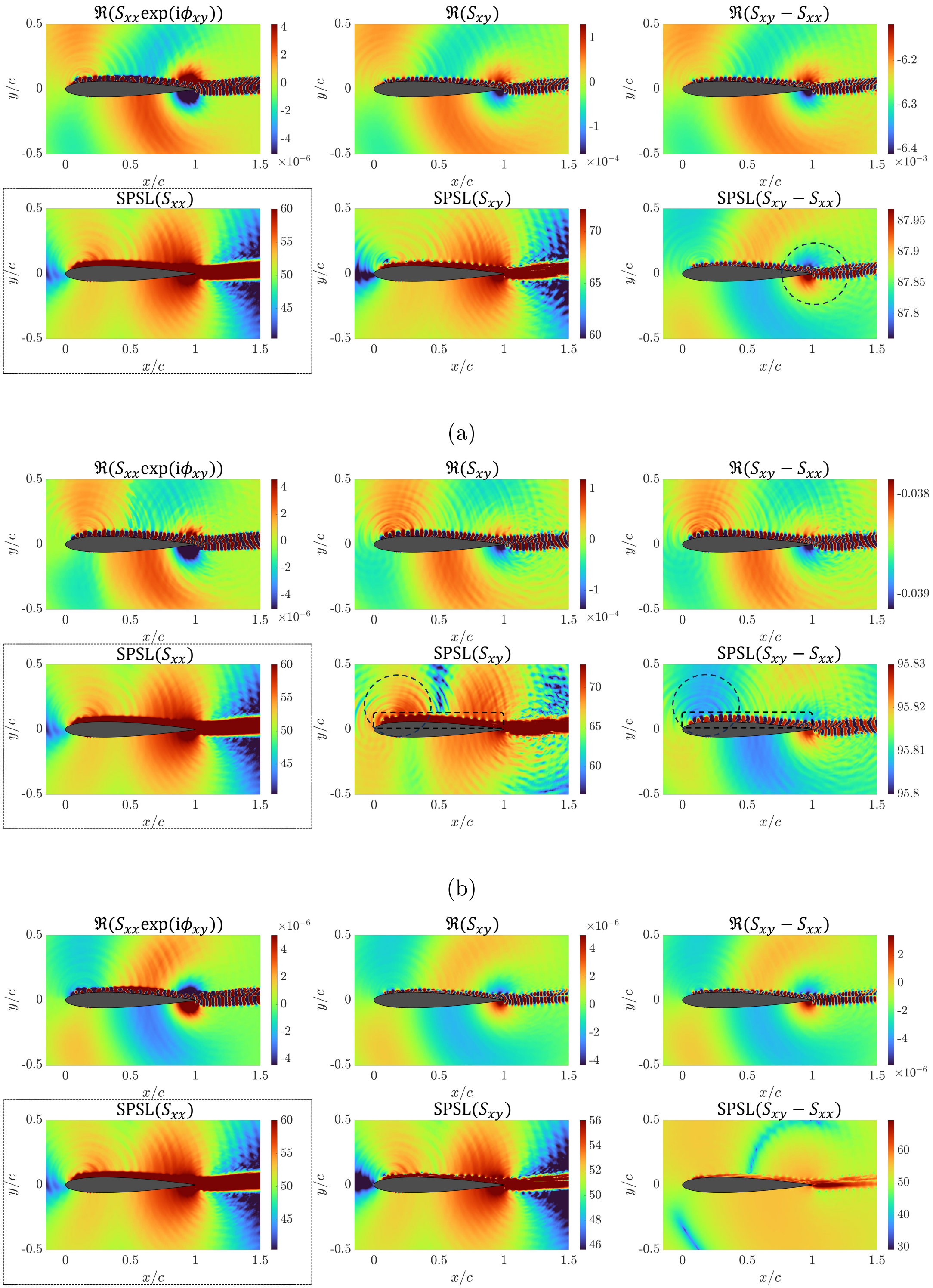

(a)

(b)

(c)

Figure 5.4: Snapshots of three different cross-spectrum formulations plotted on linear and logarithmic scales at 1 kHz for the stair-strip case using the reference point of (a) P1, (b) P2, and (c) P3.

noise source impacting that position, predominantly the trailing-edge noise, is accentuated. Therefore, the reference position can be effectively utilized to pinpoint the primary noise source at a specific location for a given frequency using the second formulation. However, the near-wall coherent acoustic source is not captured in the logarithmic scale using the second formulation as outlined by black-dashed boxes in Fig. 5.4(b). For the third formulation, $S_{xy} - S_{xx}$, the near-wall coherent structure and sound propagation are vividly illustrated even on the logarithmic scale, as marked by the black-dashed circle in Fig. 5.4(a). The placement of the reference point assists in determining the dominant noise source, particularly for P1 and P2 on both linear and logarithmic scales, and for P3 on the linear scale. Similar to S_{xy}, the development of coherent turbulent structures and leading-edge sound radiation are more pronounced using P2. However, at P3, $S_{xy} - S_{xx}$ offers a faint resolution of the pressure field on the logarithmic scale, lacking phase topology. This indicates that a high-resolution pressure field and relevant physical interpretations are more easily achievable when the reference point is strategically located in regions dominated by high-amplitude hydrodynamic turbulent flows (P1 and P2) rather than in low-amplitude acoustic pressure areas (P3). In the legend scale of $S_{xy} - S_{xx}$, the threshold band is notably narrow and centered around the specified pressure spectrum at the reference points for P1 and P2, particularly on the logarithmic scale, enabling the evaluation of sound magnitude at the point of interest at specific frequencies with high-resolution spatiotemporal coherent hydrodynamic and acoustic patterns. Overall, all cross-spectrum method formulations (the second and third formulations) provide enhanced physical insights into turbulent acoustic sources and sound generation mechanisms compared to solely using the APSD [100]. The relative phase-angle difference in the cross-spectrum formulations elucidates the acoustic sources and propagation patterns. Among the formulations, $S_{xy} - S_{xx}$ excels in visualizing explicit waveforms and turbulent wavy structures across both scales, especially when the reference point is situated near the surface, an ability not matched by the other two formulations on the logarithmic scale. Therefore, $S_{xy} - S_{xx}$ or $\mathrm{SPSL}_{\mathrm{xy-yy}}$ is selected as the representative formulation for the cross-spectrum method in the subsequent comparison with DMD and SPOD modes, using P1 as the reference point.

5.3 Comparison of the Cross-spectrum Method to DMD and SPOD Modes

The spatial domain utilized for the cross-spectrum method is also applied to the calculations for DMD and SPOD in the same manner. Figure 5.5 showcases the discrete-time DMD eigenvalues plotted against their corresponding frequencies on a unit circle. It also shows 22 SPOD eigen spectra, with the leading eigen spectra highlighted by a red line. The stair-strip case is selected for a comparative analysis of the representative pressure field. In Fig. 5.5(a), the DMD eigenvalue corresponding to a zero imaginary part, denoting $f = 0$, indicates a stationary mode where the flow is neither growing nor decaying over time, as elucidated in the study by Mohan et al. [162]. Figure 5.5(b) reveals that the leading eigen spectra are significantly more prominent, being two orders of magnitude greater than the secondary spectra, indicating a low-rank dynamic behavior. This underscores that the leading mode is the most energetic within the studied area. Additionally, the leading eigen spectra display three prominent peaks around 0.5 kHz, 3 kHz, and 5 kHz, which are denoted as vertical dashed lines in Fig. 5.5(b). These peaks correspond with the far-field acoustic spectra shown in Fig. 4.17(a), indicating that the leading eigen spectra effectively encapsulate the key acoustic dynamics.

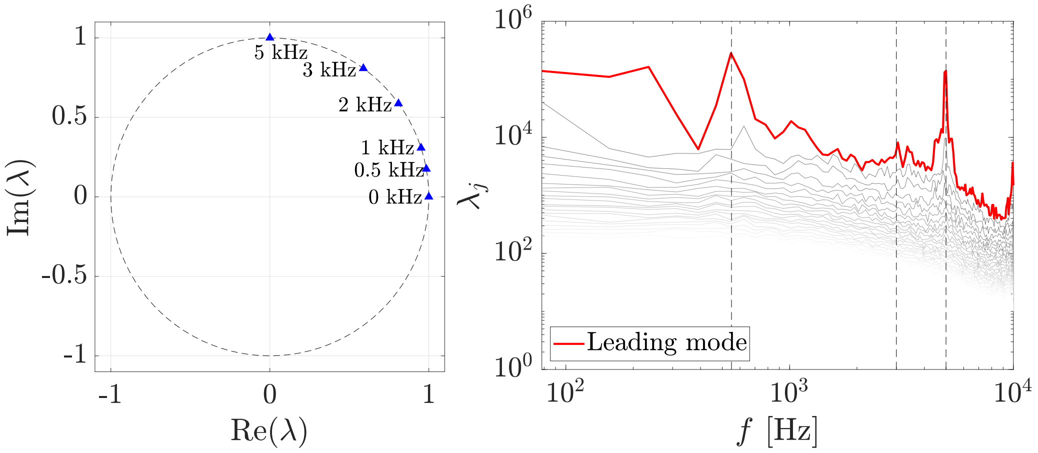

(a) (b)

Figure 5.5: Eignevalues of (a) DMD modes on a unit circle and (b) SPOD modes for the stair-strip case.

Figure 5.6 presents snapshots of the cross-spectrum formulation $S_{xy} - S_{xx}$ at 1 kHz using P1, depicted on both linear and logarithmic scales, alongside the corresponding DMD mode and leading SPOD mode. The color scale thresholds for the DMD and SPOD modes are determined in a similar manner to the cross-spectrum method. However, the mean value μ is excluded in the case of DMD and SPOD modes when computing the upper and lower limits of the color bar since their real parts typically oscillate around zero, as reported in studies by [109] and [193]. Note that even a minimal mean value, such as 10^{-6}, could introduce a bias in the color scale. Therefore, the threshold is set within a range of $\pm 2\sigma$. This approach ensures that each method's color scale is statistically determined based on its sampled values, obviating the need for manual adjustments to saturate the field of interest. At 1 kHz, the formulation $S_{xy} - S_{xx}$ exhibits resolutions comparable to those of DMD and SPOD leading mode. It adeptly identifies the chordwise anti-phase pattern of near-wall coherent wavy

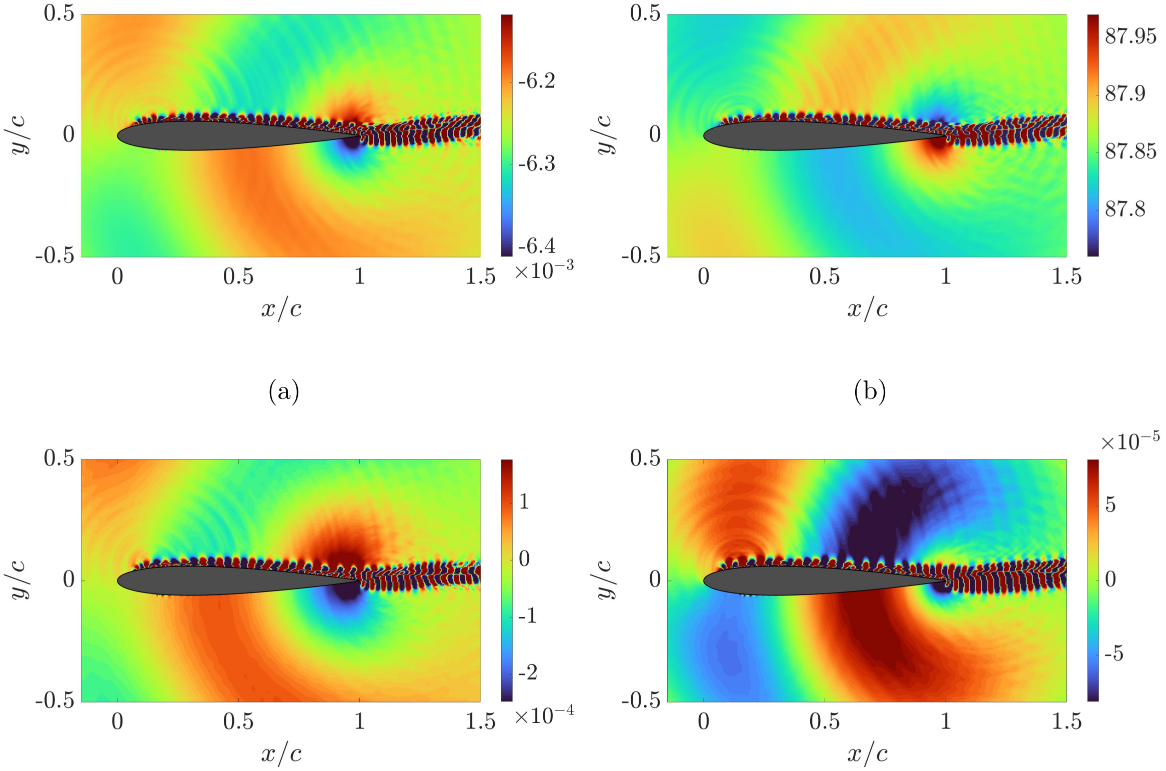

(a) (b)

(c) (d)

Figure 5.6: Snapshots of $S_{xy} - S_{xx}$ on (a) linear scale and (b) logarithmic scale, (c) DMD mode, and (d) leading SPOD mode at 1 kHz for the stair-strip case.

structures on the suction side, as well as the asymmetrical sound emission at the trailing edge, on both linear and logarithmic scales. A distinctive attribute of the cross-spectrum method, evident on the logarithmic scale, is its ability to evaluate near-field sound magnitude relative to the reference point, a feature not present in DMD and SPOD modes.

At 3 kHz, the acoustic waves emanating from the leading edge due to the interaction between the LSB and tripping, as discussed in [194], are consistently detected by all three methods — the cross-spectrum method, DMD, and SPOD. However, the cross-spectrum method stands out with its superior resolution in capturing wave propagation and the intricate interaction dynamics between the leading and trailing edges. A caution should be

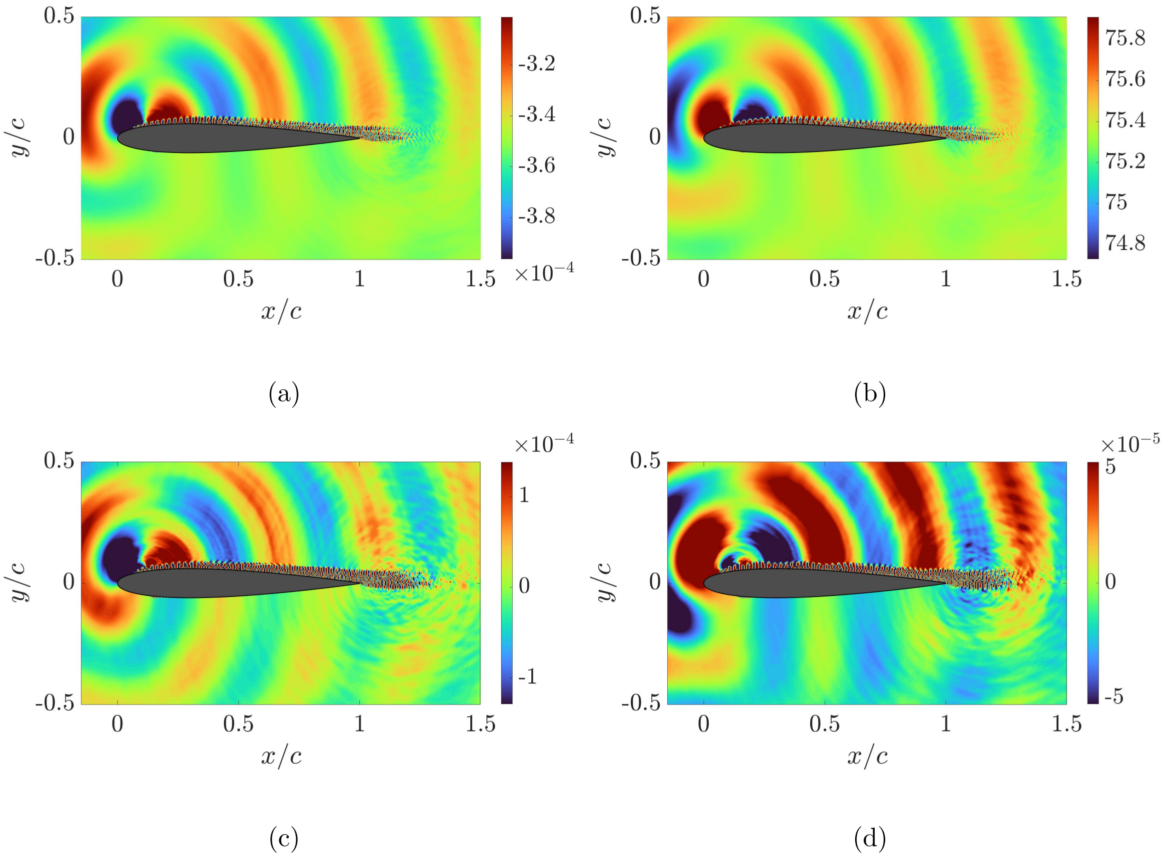

(a)

(b)

(c)

(d)

Figure 5.7: Snapshots of $S_{xy} - S_{xx}$ on (a) linear scale and (b) logarithmic scale, (c) DMD mode, and (d) leading SPOD mode at 3 kHz for the stair-strip case.

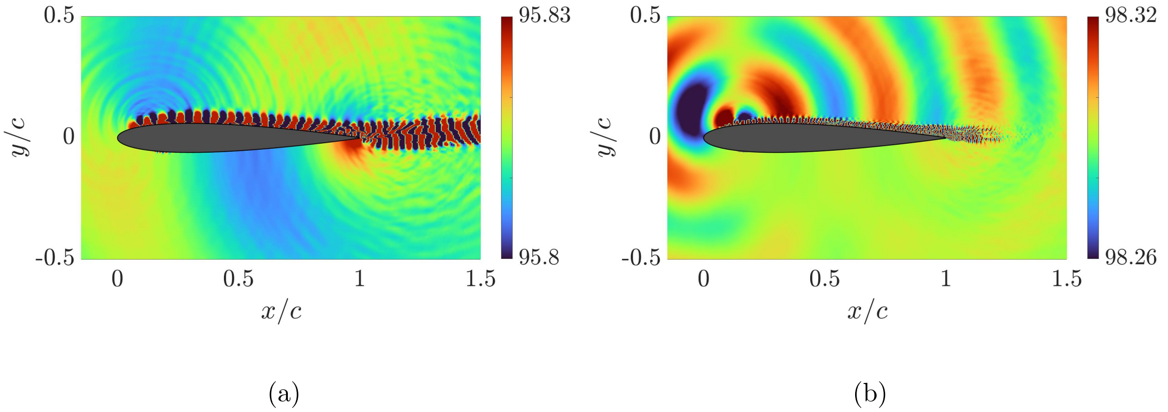

(a)

(b)

Figure 5.8: Snapshots of $S_{xy} - S_{xx}$ on a logarithmic scale at (a) 1 kHz and (b) 3 kHz at the reference point of P2 for the stair-strip case.

exercised when analyzing the magnitude of the cross-spectrum output on a logarithmic scale. To illustrate, consider the sound spectra at 3 kHz, which exhibit greater strength compared to those around 1 kHz as shown in Fig. 4.17(b). This indicates that tripping-induced noise surpasses trailing-edge noise in magnitude. However, the cross-spectrum field establishes a higher threshold range of approximately 88 dB at 1 kHz (see Fig. 5.6(b)), in contrast to the approximately 75 dB threshold at 3 kHz (see Fig. 5.7(b)). This difference arises because the reference point is positioned in proximity to the near-wall trailing edge (P1) for both cases. This indicates that trailing-edge scattering predominates as a noise source at 1 kHz. If the reference point is placed at the near-wall leading edge (P2), as presented in Fig. 5.8, the magnitude of the cross-spectrum output at 3 kHz exceeds that at 1 kHz, owing to the significant presence of tripping-induced noise at this frequency. This example illustrates the capability to accurately diagnose intense noise generation at each frequency by simply adjusting the reference point, especially when users are aware of potential multiple noise source locations. For instance, users can initially utilize P1 at 3 kHz and confirm that the primary noise source originates from the leading edge. At this stage, the magnitude of the cross-spectrum should not be considered accurate. Instead, users should employ P2 or a point near the leading edge to ascertain the true magnitude of the sound pressure level through the CPSD. This approach enables identification of both the noise source location and the magnitude of the sound pressure spectrum using the cross-spectrum method. This feature significantly enhances the method's effectiveness in conducting a thorough analysis and in gaining a deeper understanding of the mechanisms behind sound generation and propagation.

This study highlights the strengths of the cross-spectrum method, which effectively leverages both magnitude and phase information. By subtracting the spectral magnitude of the pressure field or S_{xx}, this method accentuates phase differences while still preserving the influence of sound magnitude in the pressure field. On the other hand, DMD and SPOD modes rely solely on the real part of eigenvectors for their representation. As mentioned earlier, it is important to carefully select the reference point in the cross-spectrum method to ensure accurate physical interpretations and analyses or to align with the specific noise source being investigated. Another notable advantage of the cross-spectrum method is its lower demand for extensive data manipulation and memory usage with regard to the CPSD calculation at the single point, which are requirements for matrix-size-dependent computations often associated with DMD or SPOD. This aspect renders the cross-spectrum method more efficient and accessible, especially beneficial for handling larger datasets or analyzing more complex systems. The simplicity of its implementation and computational efficiency, combined with its proven capability in effectively visualizing and analyzing flow-generated noise, positions the cross-spectrum method as a valuable and promising tool in the realms of flow and acoustic visualization.

5.4 Application of Cross-spectrum Method to Different Tripping Techniques

As part of the application of the developed method, we employ the cross-spectrum formulation $S_{xy} - S_{xx}$ on a logarithmic scale, denoted as $\mathrm{SPSL_{xy-xx}}$, using the reference point P1 for an in-depth analysis of different transition mechanisms resulting from boundary-layer tripping, compared to natural transition scenario. Figure 5.9 displays flow snapshots for the stair strip, suction and blowing, and natural transition at frequencies of 1 kHz and 3 kHz. At 1 kHz, the cross-spectrum method effectively identifies turbulent convection originating from the leading edge, which scatters as acoustic waves forming antisymmetric patterns typical of trailing-edge noise, as described in Ref. [173], across all transition scenarios. Notably, in the suction and blowing case, the trailing-edge acoustic sources and waveforms are intense enough to overshadow coherent wavy structures, unlike in the other scenarios. A distinct capability of the cross-spectrum method, which integrates both spectral magnitude and phase field, is evident in the threshold settings of the color scale. It highlights the significantly more intense noise source in suction and blowing compared to the stair strip and natural transition. This observation of near-field sound corresponds with a higher far-field sound pressure level for the suction and blowing, as shown in Fig. 4.17. In Fig. 5.9(a), the cross-spectrum method successfully captures subtle waveforms near the leading edge,

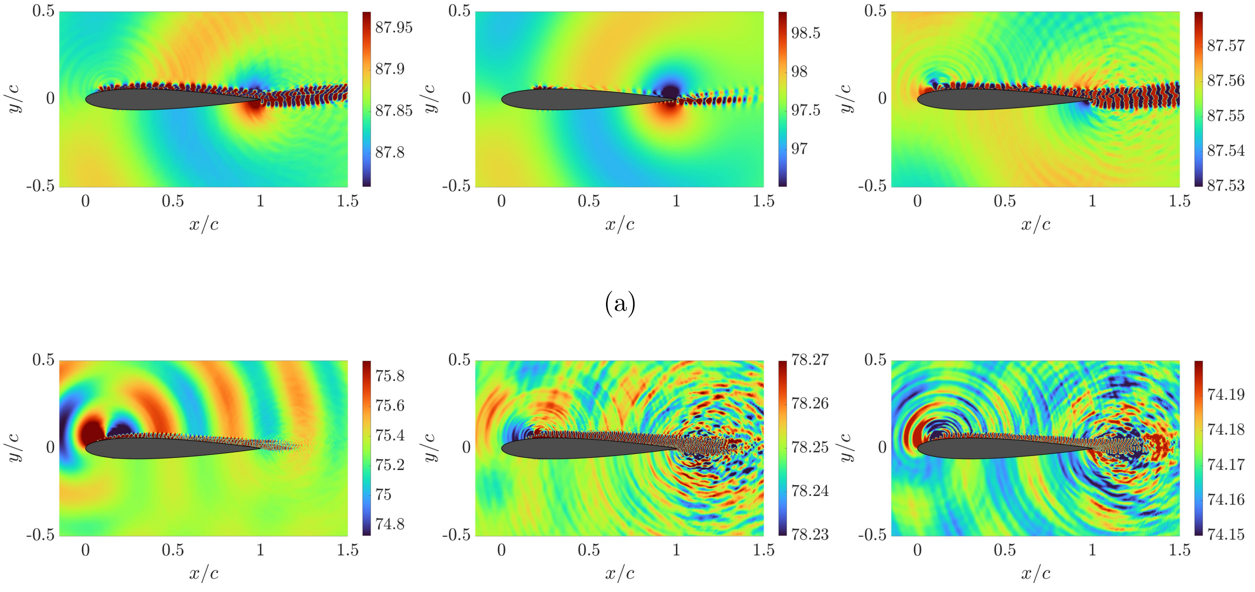

(a)

(b)

Figure 5.9: Snapshots of $\mathrm{SPSL}_{\mathrm{xy-xx}}$ for the stair strip (left), suction and blowing (mid), and natural transition (right) using the reference position of P1 at (a) 1kHz and (b) 3 kHz.

attributable to the LSB-tripping interaction in the stair-strip case and the self-excited LSB mechanism in the natural transition. However, the leading-edge noise is not seen in the suction and blowing. This underscores the method's sensitivity and accuracy in identifying nuanced acoustic phenomena. It is important to recognize that multiple wavelengths originating from both the leading and trailing edges can coexist at a specific frequency within the pressure field. These wavelengths, influenced by their respective phase speeds, conform to the dispersion relation, as elaborated in Ref. [195]. At 3 kHz, as shown in Fig. 5.9(b), the leading-edge noise, particularly prominent due to the LSB-tripping interaction, serves as a distinct acoustic mechanism in the stair-strip scenario. This phenomenon effectively masks the trailing-edge scattering noise. In contrast, for the other two scenarios, the dominant acoustic phenomena are the non-linear interactions between the leading-edge and trailing-edge sound waves. Overall, the cross-spectrum method effectively delineates key flow and acoustic dynamics at specific frequencies. It adeptly pinpoints and differentiates near-wall coherent sound sources and their propagation paths across various transition mechanisms. This capability aligns well with the objectives of widely used modal analysis approaches, enhancing our understanding of the intricate dynamics in these flow scenarios.

5.5 Summary

Analyzing and visualizing flow and acoustic fields is crucial for accurately identifying the true origin of noise sources and comprehending the processes of sound generation and propagation. To accomplish this, this chapter introduced a novel approach using cross power spectral density, comprising three distinct formulations, to analyze sound generation and propagation influenced by flow dynamics over a NACA 0012 airfoil. This novel method was evaluated against widely recognized modal analysis methods such as DMD and SPOD. This provided a robust framework for assessing the efficacy and insights offered by the cross-spectrum method in comparison to established modal analysis techniques.

The cross-spectrum method, particularly the formulation $S_{xy} - S_{xx}$ or $\mathrm{SPSL}_{\mathrm{xy-xx}}$, has been found to be highly effective in concurrently extracting sound magnitude and phase characteristics. It provides detailed insights into coherent turbulent convection near the wall and the propagation of acoustic waves originating from both leading and trailing edges. The primary advantage of $S_{xy} - S_{xx}$ over S_{xy} and $S_{xx}\exp(\mathrm{i}\phi_{xy})$ formulations lies in its robust capability to visualize high-resolution hydrodynamic coherent flow structures and sound propagation, while preserving sound magnitudes across both linear and logarithmic scales. This approach ensures that the near-field sound propagation from acoustic sources is consistent with the observed far-field acoustic spectra.

A crucial aspect to consider when using this method is its reliance on the chosen reference point. This reliance underscores the importance of conducting a preliminary assessment of flow characteristics at each potential reference point to ensure the accuracy of physical interpretations. For instance, arbitrarily placing the reference point—especially when users are unaware of potential noise sources—can lead to discrepancies in near-field sound magnitude variations (as derived from the cross-spectrum method) across frequencies, compared to the far-field sound spectrum obtained from the FW-H formulation. However, the flexibility to position the reference point anywhere, such as near the leading edge or trailing edge, enables the identification of the dominant acoustic source at specific frequencies. This strategic placement can be instrumental in isolating and analyzing specific aerodynamic noises.

Chapter 6

Airfoil Noise Mitigation

This chapter focuses on attenuating airfoil noise achieved through a sweep angle effect accounting for misaligned flow and trailing-edge morphing. Each comprises an independent section.

In Sec. 6.1, misaligned flow is implemented over a NACA 0012 airfoil configuration, specified at a chord-based Reynolds number, $Re = 4 \times 10^5$, Mach number, $M = 0.058$, and a zero incidence angle. The 30° and 45° swept airfoils are considered through the freestream rotation to simulate the effect of sweep angle, as shown in Fig. 2.1. Additionally, a straight airfoil with a reduced Mach number equal to the chordwise velocity component of the swept airfoil without spanwise flows is simulated. This chapter provides fundamental mechanisms governing noise reduction derived from the LES and Amiet's swept trailing-edge noise theory.

In Sec. 6.2, the trailing-edge morphing using the boat-tail angle is imposed to flow around a NACA 0018 airfoil configuration, specified at a chord-based Reynolds number, $Re = 6 \times 10^5$, Mach number, $M = 0.088$, and angle of attack, $\alpha = 0°$ and $4°$, respectively. Aerodynamic and aeroacoustic performances of morphed airfoils are described in this section.

6.1 Sweep Angle Effect with Misaligned Flow

6.1.1 Aerodynamic Flow Quantities and Radiated Sound Spectra

This section explores the impact of misaligned flow on aerodynamic flow quantities with regard to values of time-averaged and temporal fluctuations. The experimental data [91] under specific flows measured at a chord-based Reynolds number of 4×10^5 and a Mach number of 0.058 for the straight airfoil are compared with the straight flow. The zero angle of attack is only considered, and we plot all the predicted flow quantities on the upper side of the airfoil. Figure 6.1 plots negative pressure coefficients $-C_p$ and friction coefficients C_f on the surface of the straight, 30° misaligned, and 45° misaligned flows, along with experimental values obtained at the straight airfoil [91]. The two aerodynamic coefficients are defined as

$$-C_p = -\frac{p - p_\infty}{q_\infty} \tag{6.1}$$

$$C_f = \frac{\tau_w}{q_\infty}, \tag{6.2}$$

where q_∞ is the dynamic pressure defined as $1/2\rho_\infty U_\infty^2$. The predicted level of local peak around the tripping installation and spatial variation of pressure loading display an excellent agreement with the experiment. We observe that misaligned flow reduces aerodynamic pressure loading while simultaneously decreasing pressure gradient, which leads to flows being more attached at the trailing edge. When the gauged pressure is normalized by $q_\infty \cos^2(\psi)$, the pressure coefficient can be denoted as

$$-C_{p,x} = -\frac{p - p_\infty}{q_\infty \cos^2(\psi)}. \tag{6.3}$$

In Fig. 6.1(b), the pressure curves of the 30° misaligned and 45° misaligned flows are found to overlap with the straight flow. This suggests the flow similarity in the chordwise direction such that the chordwise pressure distribution is independent of the spanwise crossflow effect. The variation of friction coefficient, which normalizes the resultant wall shear stress from the chordwise, wall-normal, and spanwise directions, depicts a similar trend between the three predicted cases. The prediction of straight airfoil shows a strong match with the experiment. Note that the friction coefficients with misaligned flow remain lower in magnitude than the straight flow right beyond the tripping region, $x/c \approx 0.2$, which means that flow misalignment into tripping might cause lower levels of mixing and momentum transfer in turbulence than straight flow. However, their difference in magnitude is within 10% at $x/c \approx 0.4$, showing a similar flow evolution downstream. In the vicinity of the trailing edge, however, the baseline flow undergoes lower friction than two swept cases, which is attributed to higher nonequilibrium flows than misaligned flow scenarios driven by a higher adverse pressure gradient, as shown in Fig. 6.1(a). Figure 6.2 presents the time-averaged boundary-layer profiles at $x/c = 0.76$. Although two misaligned flow configurations display the thinner profiles around the log-law region and outer layer, approximately $y^+ > 60$, overall velocity profiles developed under fully turbulent flows are found to be analogous among three cases.

Additional inspection of near-wall boundary-layer profiles under crossflows can be made through the normal Reynolds stress tensors (chordwise $< uu >^+$, wall-normal $< vv >^+$, and spanwise $< ww >^+$) along with shear stress ($- < uv >^+$) predicted at $x/c = 0.76$, which are provided in Fig. 6.3. The reduction in chordwise Reynolds stress is markedly evident in the misaligned flow cases, particularly at $y^+ \approx 13$ ($y/c \approx 0.0008$), while turbulent crossflow fluctuations are energized, as indicated by the spanwise Reynolds stress. This shift of turbulent fluctuations from chordwise to spanwise direction is notably observed when flows are 45° misaligned where chordwise and spanwise velocity magnitudes are equivalent. Si-

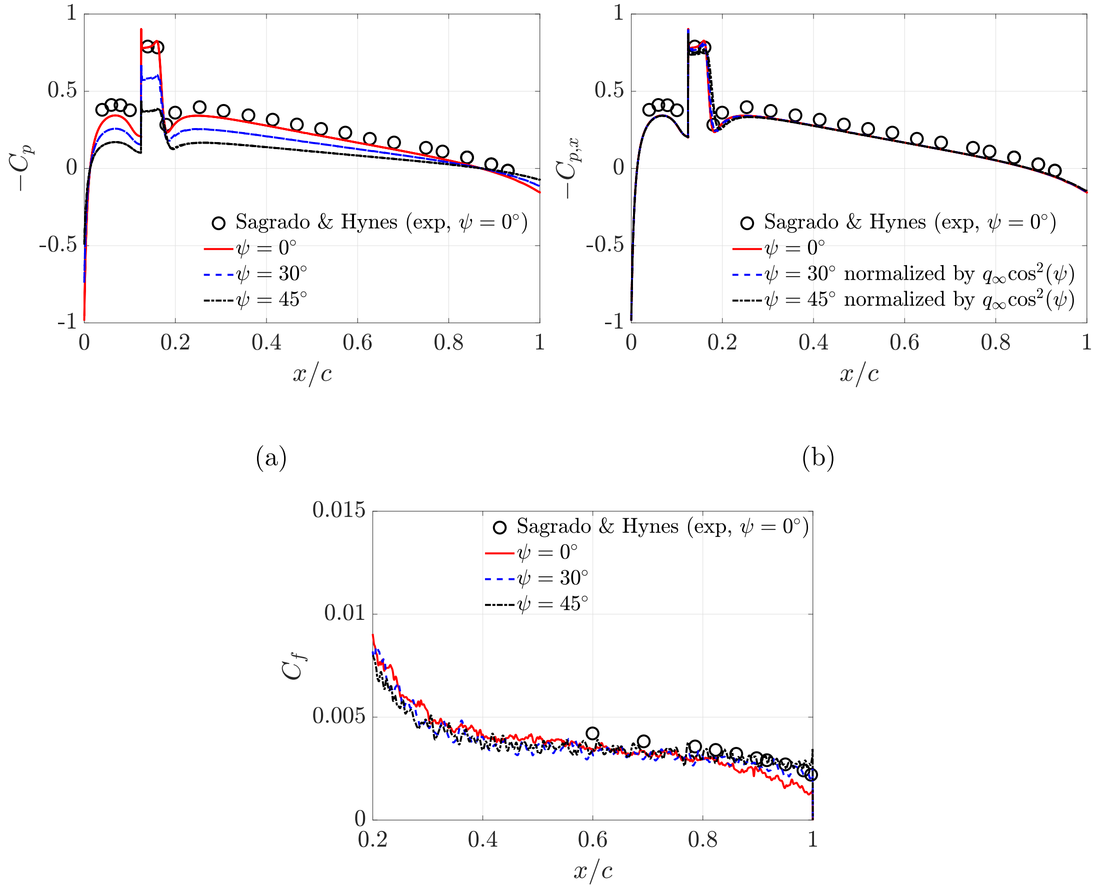

(a)

(b)

(c)

Figure 6.1: Time-averaged flow characteristics: (a) the surface pressure coefficients, (b) surface pressure coefficients normalized by $q_\infty \cos^2(\psi)$, and (c) friction coefficients on the airfoil compared with the available tripped experiment [91].

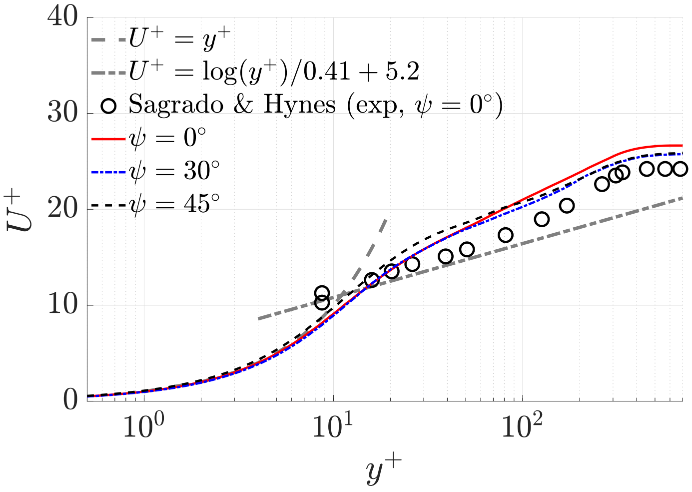

Figure 6.2: Time-averaged velocity profiles normalized by friction velocity along the wall units against the available tripped experiment [91] at $x/c = 0.76$.

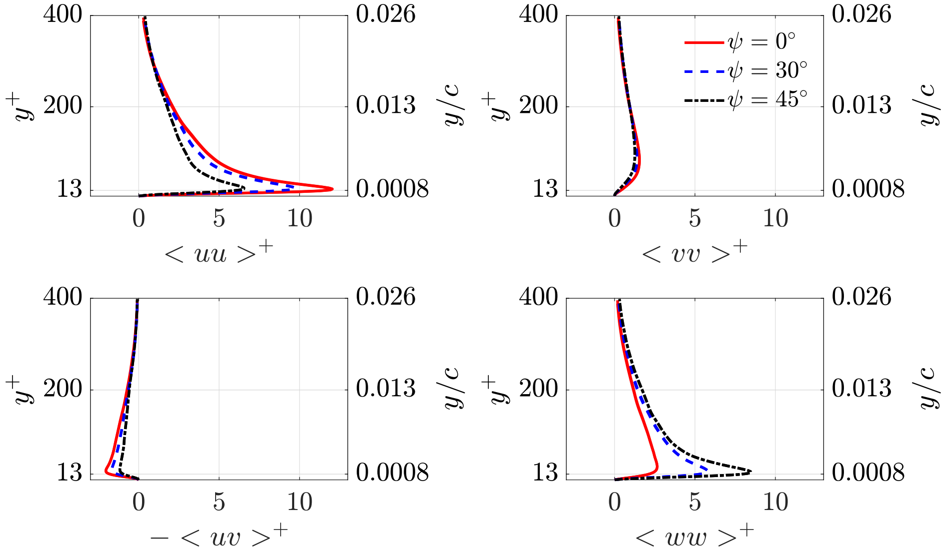

Figure 6.3: Reynolds stress components on the suction side of airfoil at $x/c = 0.76$.

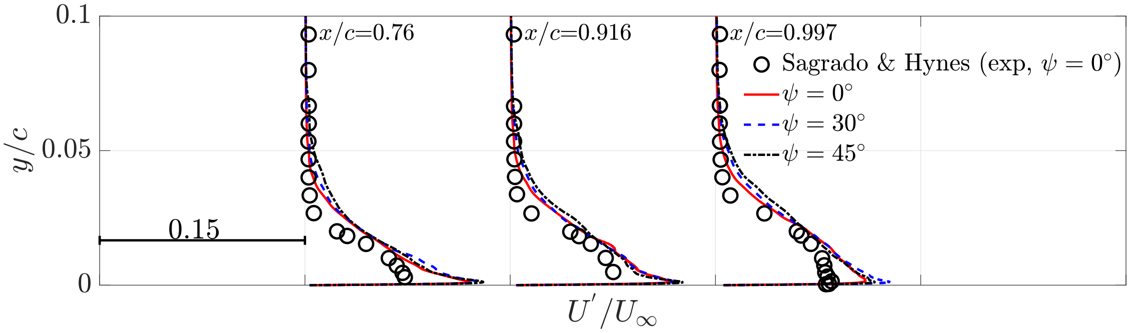

Figure 6.4: Turbulence intensity profiles against the available tripped experiment [91] on the suction side of airfoil.

multaneously, turbulent diffusion taking place in the wall-normal direction and shear stress tensor are weakly influenced by the cross-flow fluctuations, leading to a reduction in magnitude. Turbulence intensity (TI) proportional to the square root of the summation of normal Reynolds stress tensors is subsequently illustrated for three scenarios in Fig. 6.4. It is crucial to highlight that TI profiles and magnitudes are comparable for straight and misaligned flow scenarios, suggesting that near-wall turbulent boundary-layer flow fluctuations are consistent despite the presence of crossflow effect. The thicker TI profiles evolving in the chordwise direction are in good agreement with the experiment.

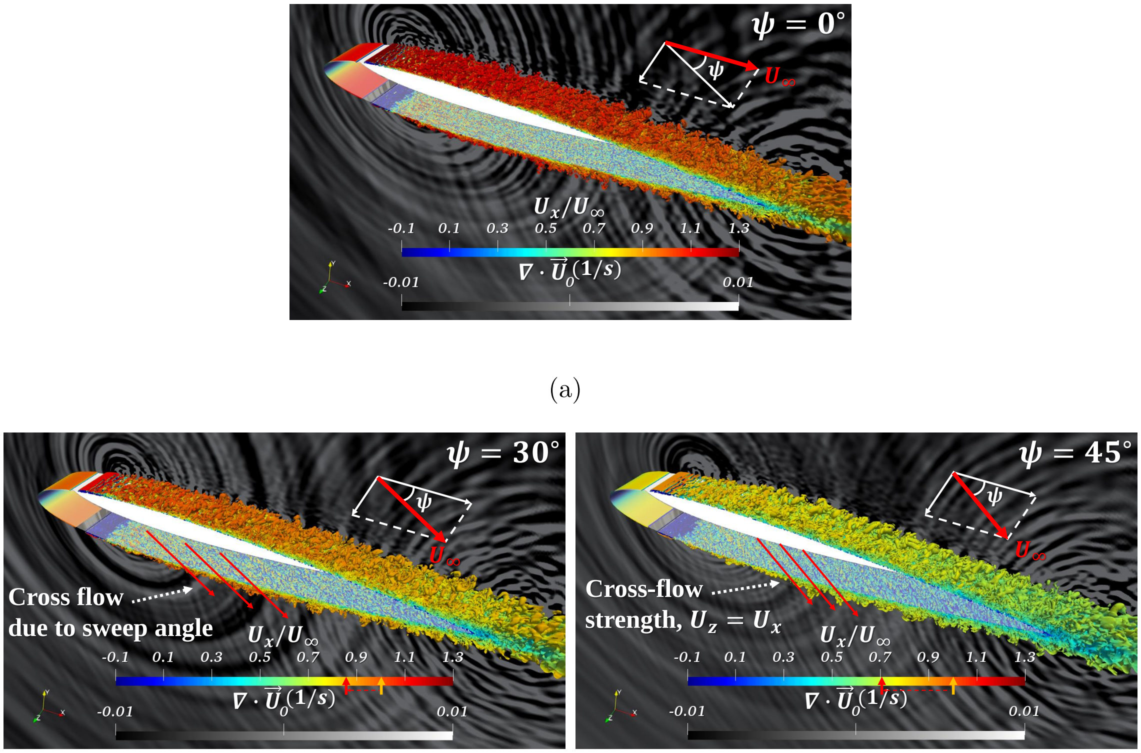

(a)

(b)

(c)

Figure 6.5: Normalized Q-criterion ($Qc^2/U_\infty^2 = 10$) colored with the streamwise velocity component (U_x/U_∞) with the dilatation field ($\nabla \cdot \vec{U}$) in the background at (a) $\psi = 0°$, (b) $\psi = 30°$, and (c) $\psi = 45°$.

Figure 6.5 illustrates an iso-surface of Q-criterion [152] normalized by the chord length and freestream velocity, along with the dilatation field [99] as a backdrop for $\psi = 0°, 30°$, and 45°. We select the value of the normalized Q-criterion to be 10, which clearly visualizes the distinct turbulence convection along the wall. It can be noticed that three cases are successfully tripped by the squared wire placed at $x/c = 0.125$, evolving from the spanwise-coherent T-S waves [39] to three-dimensional vortical structures downstream. The crossflow direction is denoted with red arrows on the lower side for the misaligned flow configurations to clarify the spanwise convection due to the sweep angle. The notable spanwise flow structures are corroborated by the higher contribution of the spanwise Reynolds stress tensor with

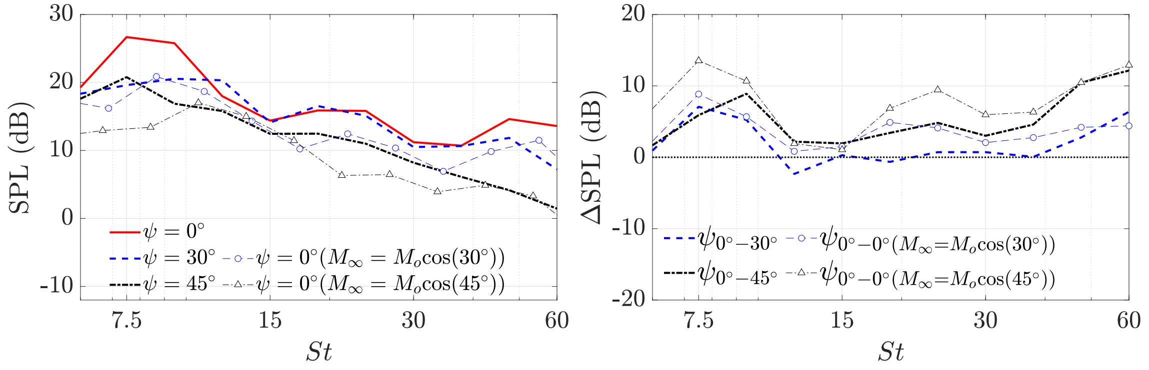

(a) (b)

Figure 6.6: One-third octave band SPL at a microphone positioned at $x/c = 1.0$, $y/c = 10.0$, and $z/c = 0.05$ for $\psi = 0°, 30°$, and $45°$ with two additional cases of reduced Mach number equivalent to 30° swept and 45° swept cases without the spanwise velocity component. (a) SPL and (b) Δ SPL.

increasing the sweep angle, as described in Fig. 6.3. It is important to note that flows with 30° and 45° misalignments decrease the chordwise velocity component by 14% and 30%, as denoted by the shift of arrow in the velocity colorbar, while increasing the spanwise velocity component by 50% and 70% of the freestream speed, respectively. As described earlier, the 45° swept scenario equalizes the magnitude of the chordwise and spanwise velocity components. The high-frequency wavefronts resulting from the diffraction of flow impinged on boundary-layer tripping are inevitable sound sources, typically observed for the similar numerical study [18]. Another observation is that sound scattering phenomena originating from trailing edge manifest for the three cases, playing a dominant factor in airfoil-self noise [10, 17, 173], a main interest of this current study.

We further examine radiated sound spectra from these noise sources through the computation of FW-H acoustic analogy [136], as described in Sec. 2.2.1, which are provided in Fig. 6.6. The sound receiver is positioned at $x/c = 1.0$, $y/c = 10.0$, and $z/c = 0.05$, where the wavelength of the lowest frequency in resolution is longer than the acoustic source length.

Table 6.1: OASPL and ΔOASPL in dB and A-weighted dB for the five computational cases. ΔOASPL is the difference between case.1 and the other four cases.

No.	Computational case	OASPL (dB)	ΔOASPL (dB)	OASPL (dBA)	ΔOASPL (dBA)
1	$\psi = 0°$	31.2	-	29.2	-
2	$\psi = 30°$	28.1	3.1	26.2	3.0
3	$\psi = 45°$	26.5	4.7	23.6	5.5
4	$\psi = 0°$ $(M_\infty = M_o \cos(30°))$	26.4	4.8	24.0	5.2
5	$\psi = 0°$ $(M_\infty = M_o \cos(45°))$	22.7	8.5	19.6	9.5

Figure 6.6(a) presents five different sound spectra plotted as one-third octave band sound pressure level (SPL), which includes the three primary cases: $\psi = 0°, 30°$, and $45°$, along with two cases of reduced Mach number equivalent to 30° misaligned ($M_\infty = M_o\cos(30°)$) and 45° misaligned ($M_\infty = M_o\cos(45°)$) scenarios. The last two cases do not consider the spanwise velocity component. The Strouhal number St, which normalizes frequency with the freestream velocity and chord length, or fc/U_∞ is represented on the frequency axis since the two additional cases with reduced Mach number are different in Reynolds number and Mach number from the three primary cases. One can notice that the straight airfoil indicates a quasi-tonal peak around $St \approx 7.5$, while this peak is found to decrease in the two misaligned cases as well as straight flows with reduced Mach number. The subsequent section will examine the noise reduction due to sweep angle around $St \approx 7.5$. On the other hand, noise abatement due to reduced chordwise velocity is directly associated with reduced Mach number because the dipole source is proportional to between the fourth and fifth power of velocity [196]. One can observe that the difference in sound spectra between sweep angle and reduced chordwise velocity is pronounced with increasing Strouhal numbers as shown in Fig. 6.6(b). The reduced noise in the 45° swept configuration is comparable to the effect of reduced chordwise velocity with $M_\infty = M_o\cos(30°)$ for $St < 40$, but a significantly greater reduction is observed for $St > 40$, approximating the effect of the more reduced velocity ($M_\infty = M_o\cos(45°)$). These SPLs are integrated as overall sound pressure level (OASPL) for the five computed cases, which are tabulated in Table 6.1. The SPL difference highlights the noise variation by subtracting each case from the baseline flow denoted as case 1. Both dB and A-weighted are represented, the latter accounting for the human's perception of sound. As predicted in the sound spectra, the presence of sweep angle or misaligned flow effectively reduces noise but not as much as the effect of reduced velocity. For example, the level of OASPL for the 45° misaligned flow is similar to that for the reduced Mach number of $M_\infty = M_o\cos(30°)$, as observed in SPL (Fig. 6.6). It can be inferred that the noise mitigation by the presence of crossflow is more complex than simply following the velocity power [196], which will be thoroughly investigated in the subsequent sections to reveal the physical insight.

6.1.2 Near-wall Turbulence Statistics, Flow Structures, and Phase Interference

In this section, we explore the influence of misaligned flow in near-wall turbulent flows, particularly in relation to noise sources. The spatiotemporal behavior of turbulent flows is statistically examined, and the spanwise correlation length, phase interference effects, and modal structures in the frequency of interest are thoroughly investigated in parallel. The two cases with reduced Mach number are cross-examined to highlight and differentiate the effects of misaligned flow on the flow and acoustic dynamics near the wall.

We first examine the two-point spatial correlations when the temporal lag is equal to zero, $R_{pp,\tau=0}$, which is a special case of the general definition of cross correlation [29, 160, 171] as follows:

$$R_{pp}(\mathbf{x_1}, \mathbf{x_2}, \tau) = \frac{E\left[p(\mathbf{x_1}, t)p(\mathbf{x_2}, t+\tau)\right]}{E\left[p^2(\mathbf{x_1}, t)\right]^{1/2} E\left[p^2(\mathbf{x_2}, t)\right]^{1/2}}, \tag{6.4}$$

where the operator $E[\cdot]$ denotes the expected value of the signal, and τ is the temporal lag between two signals at point $\mathbf{x_1}$ and point $\mathbf{x_2}$. Figure 6.7 showcases the normalized spatial correlations with centered at $x/c = 0.9$ on the chordwise and spanwise planes for $\psi = 0°$, $\psi = 30°$, and $\psi = 45°$. It is evident that the flow is highly correlated with the distinct elongation in the flow direction. This suggests that the crossflow effect could alter the decaying trend of spanwise coherence in turbulent flows. As the crossflow angle increases, the extent of the correlation also increases, especially in the spanwise direction. We further probe the spanwise correlation length in the frequency domain, which can be computed as follows [26, 98, 197]:

$$l_z(f) = \int_{-\infty}^{\infty} \sqrt{\gamma^2(\eta, f)} \mathrm{d}\eta, \tag{6.5}$$

where η is the spanwise separation distance equivalent to Δz, and γ^2 is the spanwise coherence function defined as

$$\gamma^2(\Delta z, f) = \frac{|\Phi_{pp}(\Delta z, f)|^2}{|\Phi_{pp}(z, 0, f)||\Phi_{pp}(z + \Delta z, 0, f)|}, \tag{6.6}$$

where the cross-spectrum Φ_{pp} is the Fourier transform of the space-time cross-correlation function:

$$\Phi_{pp}(z, \Delta z, f) = \int_{-\infty}^{\infty} \big\langle p(z, t) p(z + \Delta z, t + \tau) \big\rangle \, \mathrm{e}^{-\mathrm{i} f \tau} \, \mathrm{d}\tau, \tag{6.7}$$

where $\mathrm{i} = \sqrt{-1}$, and the operator $\langle \cdot \rangle$ denotes the ensemble average over the spanwise separation distance, Δz. It should be noted that spanwise coherence length numerically obtained is reported not to exponentially decay to zero, and, thus, the exponential curve fitting approach is practically adopted for the spanwise statistical modeling [168, 197–199]. We employ the Gaussian best-fit curve function [199–201] to determine the spanwise correlation length as follows:

$$\gamma(f, \eta) = \mathrm{e}^{-\eta^2 / l_z^2(f)}, \tag{6.8}$$

Figure 6.8 exhibits the spanwise correlation length normalized by the half span, l_z^*, along with the generalized Corcos' model in Eq. (2.23) for the three primary computed cases. As expected, the sweep angle increases the spanwise correlation across all scales of turbulence

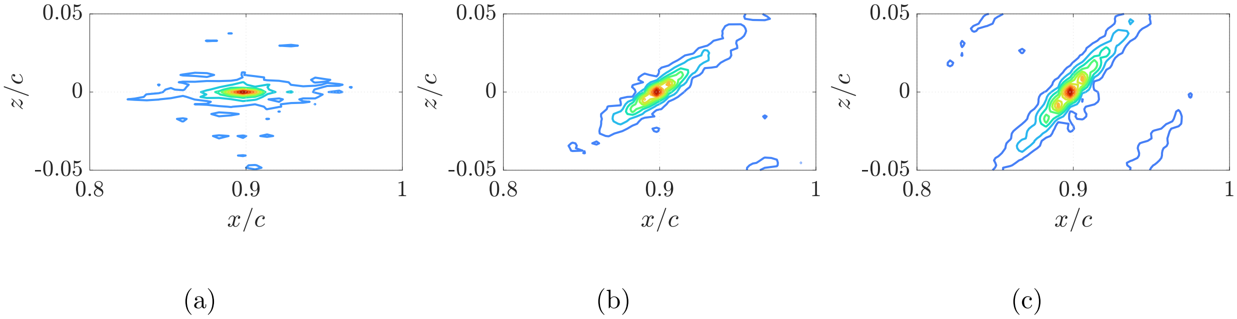

Figure 6.7: Contours of normalized spatial correlations with centered at $x/c = 0.9$ on the chordwise and spanwise planes for (a) $\psi = 0°$, (b) $\psi = 30°$, and (c) $\psi = 45°$. color levels range from 0 to 1 with an increment of 0.1.

when numerically obtained using LES data, as shown in Fig. 6.8(a). This means that misaligned flow yields an acoustic penalty, as the spanwise correlation length is one of the noise source terms formulated in Amiet's model [6, 34]. However, as shown in Fig. 6.8(b), the generalized Corcos' model decreases the spanwise correlation length with more misaligned flows. This opposite trend is pivotal in affecting the variation of the sound spectrum with misaligned flow between numerical simulations and analytical results, which will be comprehensively analyzed later. Despite the potential noise increase associated with the increased spanwise correlation in the numerical simulations, the misaligned flow cases lead to noise reduction compared to the straight flow case, as shown in Table 6.1. This suggests a need for further investigation into the dominant contributions of misaligned flows to noise reduction.

Now, we pivot to the spatiotemporal pattern in turbulence as a function of separation distance and time delay between two pressure signals. This correlation can be obtained through the general formulation of Eq. (6.4) when the time delay is not equal to zero. It should be noted that the streamwise or flow direction deviates from the chordwise axis for the misaligned flow configurations. Thus, we compute the correlations for all the flow statistics in the streamwise direction (ξ) as a reference axis, with the sweep angle ψ tilted relative to

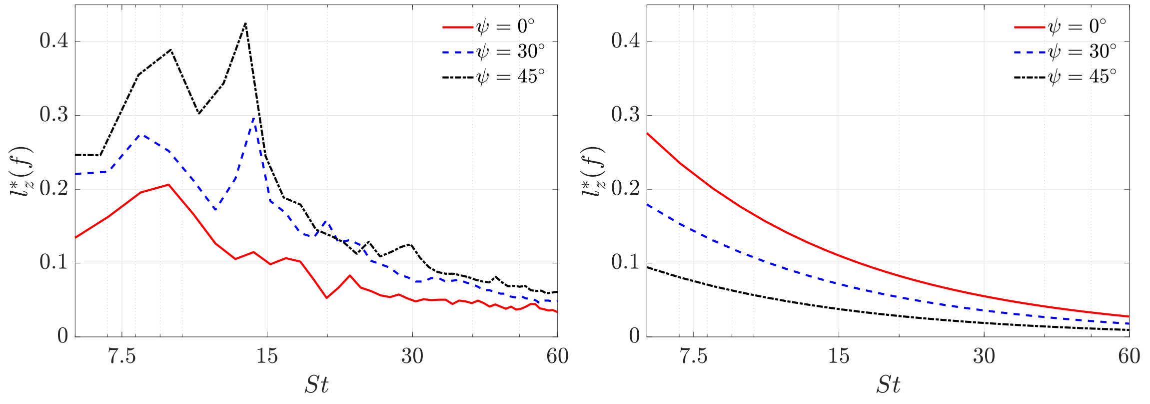

(a) (b)

Figure 6.8: Spanwise correlation length l_z^* normalized by the half-span length along the Strouhal number for $\psi = 0°, 30°$, and $45°$: (a) LES-based Gaussian best-fit curve function (Eq. (6.8)) and (b) generalized Corcos' model (Eq. (2.23)).

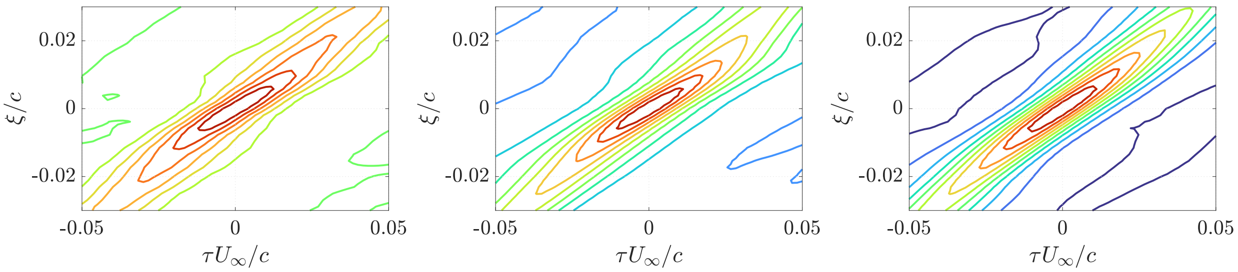

(a) (b) (c)

Figure 6.9: Contours of space-time correlation centered at $x/c = 0.9$ for (a) $\psi = 0°$, (b) $\psi = 30°$, and (c) $\psi = 45°$.

the airfoil chord. Figure 6.9 shows the normalized streamwise-temporal correlations [202–204] centered at $x/c = 0.9$ for $\psi = 0°$, $\psi = 30°$, and $\psi = 45°$. The correlations are averaged along the lines perpendicular to the streamwise direction. One can observe that the straight flow indicates a strong and coherent band, which decays with separation distance, a typical pattern of non-frozen turbulence [204, 205]. Furthermore, it represents a higher temporal correlation within and off the elliptical band than two misaligned flows. This is because the airfoil geometry on the axis perpendicular to the flow direction is homogeneous for the straight airfoil. Conversely, for the swept airfoil with misaligned flow, the spatiotemporal

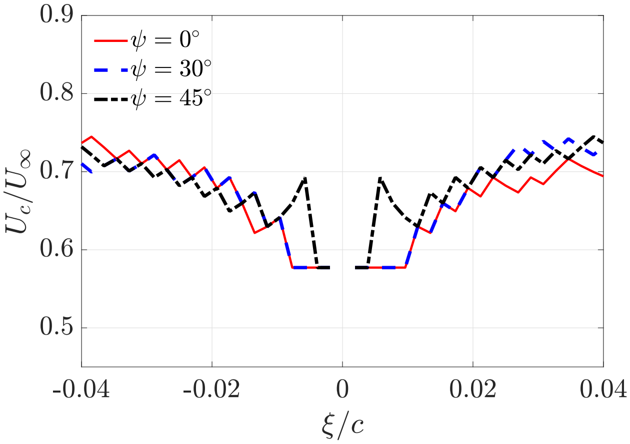

Figure 6.10: The ratio of convective speed of freestream U_c/U_∞ in the streamwise direction centered at $x/c = 0.9$ for $\psi = 0°, 30°$, and $45°$.

band is in the weaker and shorter form, indicating the rapid decaying pattern or shorter length scale of coherent turbulence in the streamwise direction. This is likely to be influenced by the airfoil's asymmetric curvature along the line normal to the freestream. The gradient in the space-time correlation contour physically represents the ratio of turbulence convection to the freestream velocity in the streamwise direction where the convection velocity is defined as follows [204, 206]

$$U_c(\Delta\xi) = \Delta\xi/\tau_{\max}(\Delta\xi), \tag{6.9}$$

where $\Delta\xi$ is the streamwise separation distance, and $\tau_{\max}(\Delta\xi)$ is the time delay at which the cross-correlation has the maximum value at each $\Delta\xi$. Figure 6.10 illustrates the ratio of convective speed to freestream U_c/U_∞ centered at $x/c = 0.9$ for the straight and misaligned flow scenarios. All cases demonstrate similarities in the ratio. This result aligns with the hypothesis that turbulence convection remains constant regardless of the presence or absence of the sweep angle, as suggested in the analytical approach [45]. This indicates that the convection velocity is not the primary factor contributing to noise reduction in the flow misalignments. While the turbulence convection shows similar magnitudes, misaligned flow induced by the sweep angle shortens the elliptical band within the high correlation region. Consequently, this alteration could influence pressure variation affected by turbulent convection due to its relevance to decaying behavior [168, 205], impacting spanwise flow disturbances [109] and ultimately leading to variations in the propagation characteristics of trailing-edge broadband noise. This insight provides a prominent cue for investigating the variation of pressure fluctuations on the surface, including phase interference distributed in both chordwise and spanwise directions, which will be examined in subsequent paragraphs.

Data-driven approaches involving spectral proper orthogonal decomposition (SPOD) have been frequently utilized for distilling physically critical flow structures [101, 102]. We extract SPOD modes from the near-wall pressure fluctuations, aiming to identify behaviors of energetic flow patterns responsible for noise generation and reduction mechanisms associated with misaligned flow at selected frequencies of interest. Details of SPOD algorithms and data structures can be found in Refs. [103–105]. Figure 6.11 elucidates the leading SPOD modal structures for the three primary cases at Strouhal numbers of about 15, 30, and 60. The iso-surfaces of the SPOD mode with the dark green and gold colors align with the values of -0.0005 and 0.0005, respectively. The contour on the bottom left is a slice taken at $x/c = 0.99$, perpendicular to the chordwise direction. At Strouhal number of 15, as shown in Fig. 6.11, the chordwise antiphase modal structures are observed to advect downstream, which are apparently homogeneous in the spanwise direction or $k_z \approx 0$. This feature is crucial for airfoil trailing-edge noise [109, 167, 170]. One can further observe the discontinuity of the SPOD modes between the upper and lower sides in a sliced view of the straight airfoil, a typical pattern of edge scattering of dipole noise source [87, 173]. As the sweep angle

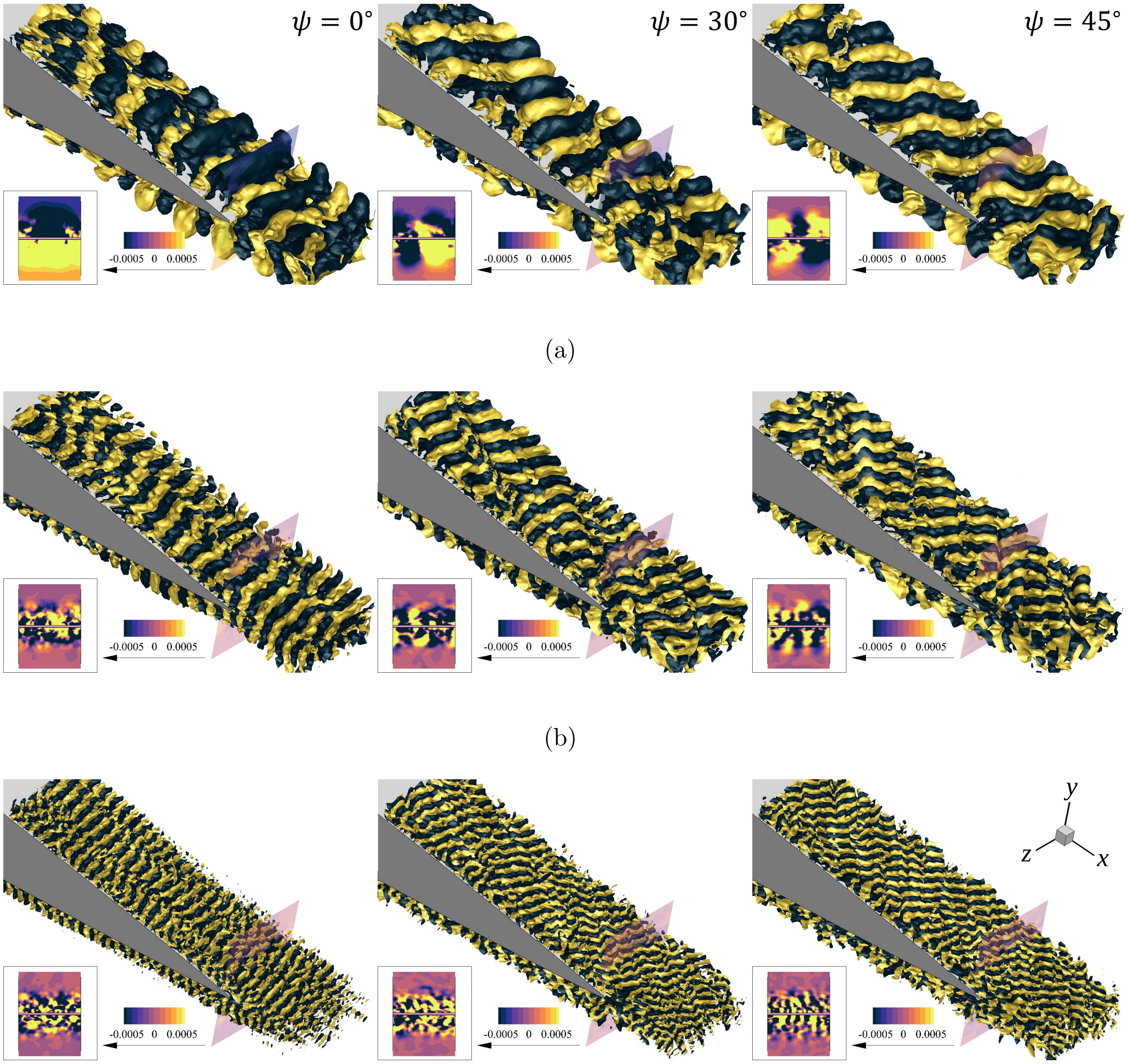

Figure 6.11: Pressure-based SPOD modal structures at (a) $St \approx 15$, (b) $St \approx 30$, and (c) $St \approx 60$. SPOD isosurfaces of -0.0005 and 0.0005 correspond to dark green and gold colors, respectively. The contour on the bottom left is a slice taken at $x/c = 0.99$, perpendicular to the chordwise direction, which spans from -0.0005 to 0.0005.

is imposed, the streamwise flow appears misaligned with the airfoil, resulting in anti-phase patterns or destructive interference among neighboring coherent structures in the spanwise direction. This is illustrated in the contours for the 30° and 45° sweep angles in Figs. 6.11(b) and 6.11(c), respectively. The convection of these misaligned coherent structures might also expedite the spanwise flow exchange, resulting in a strong spanwise correlation, as presented in Fig. 6.8(a). At the same time, these anti-phase flow topologies may likely be attributed to the reduction in noise magnitude or radiation inefficiency. As the Strouhal number increases, anti-phase patterns become more prominent, particularly at $St \approx 30$, leading to potentially greater noise reduction. However, too small turbulent length scales against the span length at $St \approx 60$ appear to eliminate the difference between flows with and without misalignment. It is important to note that concrete interpretation can be achieved when combined with pressure spectra as the source magnitude.

To quantify the effect of crossflow on phase interference in the spanwise direction, the phase angle between neighboring pressure fluctuations measured on the spanwise grid points

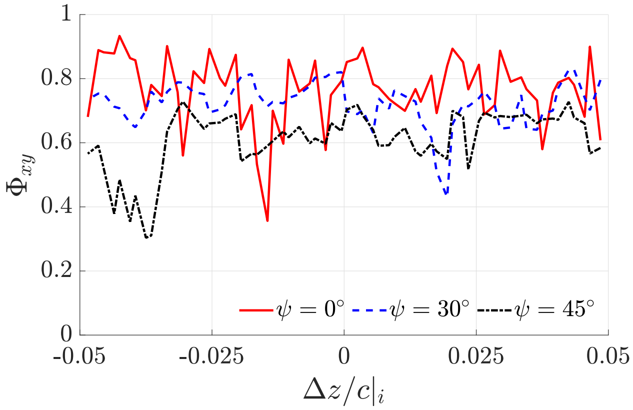

Figure 6.12: Spanwise phase interference levels defined in Eq. (6.10) for $\psi = 0°, 30°$, and 45° at $x/c \approx 0.99$.

(N_z), separated by a distance, $1/(N_z - 1)$, is averaged across the frequency [166]:

$$\Phi_{xy}(z/c) = \frac{1}{f_2 - f_1} \int_{f_1}^{f_2} \Re(\exp(\mathrm{i}\phi_{xy}(f, z/c)))\,\mathrm{d}f, \tag{6.10}$$

where ϕ_{xy} is the phase angle of cross-power spectral density, and z/c varies between -0.05 and 0.05. The variable Φ_{xy} ranges from -1 to +1, where -1 represents an out-of-phase relationship and +1 indicates an in-phase relationship. The three primary cases of the variable Φ_{xy} along the spanwise direction at $x/c \approx 0.99$ are plotted in Fig. 6.12. It is evident that the presence of crossflow alters the phase topology of spanwise neighboring pressures by decreasing the in-phase relation. To encompass the phase interference effects taking place in both chordwise and spanwise directions, the phase distributions from the span-averaged pressure are calculated along the chordwise direction. Figure 6.13(a) exemplifies the phase waves defined as $F(x/c, f) = \Re(\exp(\mathrm{i}\phi_{xy}(x/c, f)))$ for the straight ($\phi = 0°$) case at $St \approx 30$. Here, ϕ_{xy} is the phase angle between surface pressure fluctuations at an arbitrary point (x) and the one fixed at the trailing edge (y) as the reference pressure. This has the same

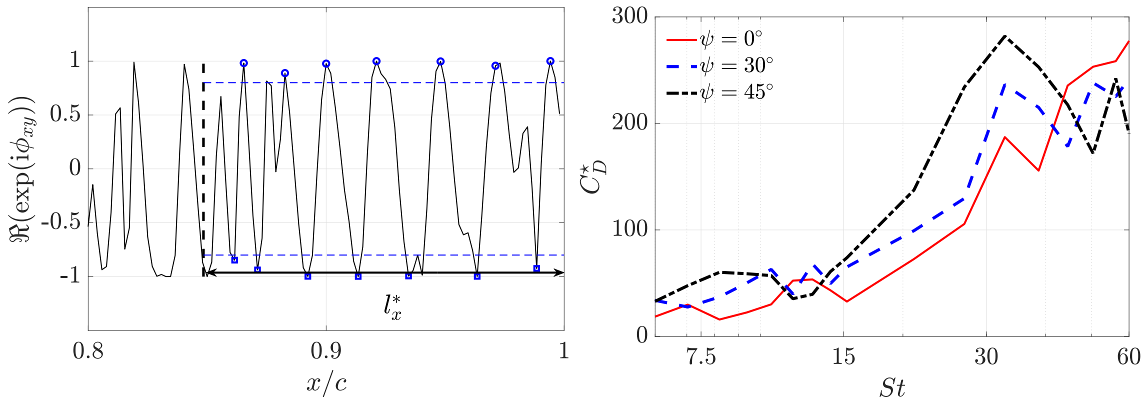

(a)

(b)

Figure 6.13: (a) Exemplary spanwise-averaged phase distributions along with the chordwise correlation length at the trailing edge for the straight flow ($\psi = 0°$) at $St \approx 30$ and (b) chordwise phase interference levels defined in Eq. (6.12) for the three computed cases.

physical meaning in phase relation as one defined in Eq. (6.10). Alternatively, it can be utilized to interpret the phase relation between spatially neighboring two signals at the same frequency because the reference position is identical. Thus, spatially varying phases with peak-to-peak fluctuations can be an indicator of how much destructive interference happens, which will be used as a key idea to quantify the destructive interference later. In addition, we calculate the chordwise correlation length to measure the phase interference occurring within the local coherent structure for non-frozen turbulence gust [168], which can be written with the following:

$$l_x^*(f) = \int_{\eta_{x,1}}^{\eta_{x,2}} \sqrt{\gamma^2(\eta_x, f)}\mathrm{d}\eta_x, \tag{6.11}$$

where γ^2 is a similar form as shown in Eq. (6.6) but a chordwise coherence function, η_x represents the chordwise separation distance normalized by the chord length, and the integration spans from $0.2c$ to x, where turbulent flows are established. Constructive or destructive wave interferences are only meaningful within this streamwise correlation length for the non-frozen gust case [168]. In this analysis, we place x at the trailing edge, which means that the correlation length is computed at the trailing edge. We further define a coefficient to quantify the level of destructive interference taking place in the unit correlation length, which can be written:

$$C_D^\star(f) = \frac{1}{l_x^*(f)} \sum_{x/c\in[1-l_x^*,1]} \mathcal{X}(|F(x/c,f)| > 0.8 \text{ and } |\nabla F(x/c,f)| \approx 0|)/2, \tag{6.12}$$

where $\mathcal{X}$ is the indicator function that returns 1.0 when the function value satisfies the conditions specified within the parenthesis. Dividing by factor 2 stands for the averaged phase fluctuations between positive and negative signs. We adopt the threshold value 0.8 as the marginal value of the out-of-phase behavior. As described above, the extent of spatial fluctuations of $F(x, f)$ is the key idea in defining the coefficient $C_D^\star$. An example of the resulting $\mathcal{X}$ is denoted as a blue-square (close to -1) or blue-circle (close to 1) symbol at $St \approx 30$ in Fig. 6.13(a). Note that it selectively includes fluctuations with a wave period falling within the threshold range while disregarding minor jitters. The coefficients $C_D^\star$ for the 30° and 45° misaligned flows exhibit higher destructive interferences than straight flows as shown in Fig. 6.13(b). This noticeably occurs around $15 < St < 40$, where misaligned flow structures act as out-of-phase behaviors across the span. This correlates with our observation of energetic leading SPOD modes for misaligned flows, as viewed earlier in Fig. 6.11. This substantiates the effectiveness of misaligned flows in generating destructive interference, leading to the potential mechanism of noise reduction. A similar conclusion can be drawn for serrated trailing edges where misaligned flows are dominant. The noise reduction mechanisms are likely to arise from the anti-phase behaviors of wall pressures resulting from misaligned flow convection [26, 197, 207].

6.1.3 Acoustic Sources and Propagative Characteristics

In this section, we delve into wall-pressure spectra (WPS) and scattering efficiency. To account for the flow misalignment, wavenumber-frequency spectra are calculated by taking the spatial Fourier transform of the cross-power spectral density, S_{qq}, as

$$\Phi_{qq}(k_x, k_z, \omega) = \frac{1}{(2\pi)^2} \iint_{-\infty}^{\infty} S_{qq}(\eta_x, \eta_z, \omega) \mathrm{e}^{\mathrm{i}(k_x \eta_x + k_z \eta_z)} \mathrm{d}\eta_x \mathrm{d}\eta_z, \tag{6.13}$$

where η_x and η_z are the chordwise and spanwise separation distances normalized by the chord length, respectively. S_{qq} is obtained in the space domain, $x/c \in [0.8, 1.0]$ in the entire spanwise direction, where trailing-edge scattering is dominant [30]. The reference point for

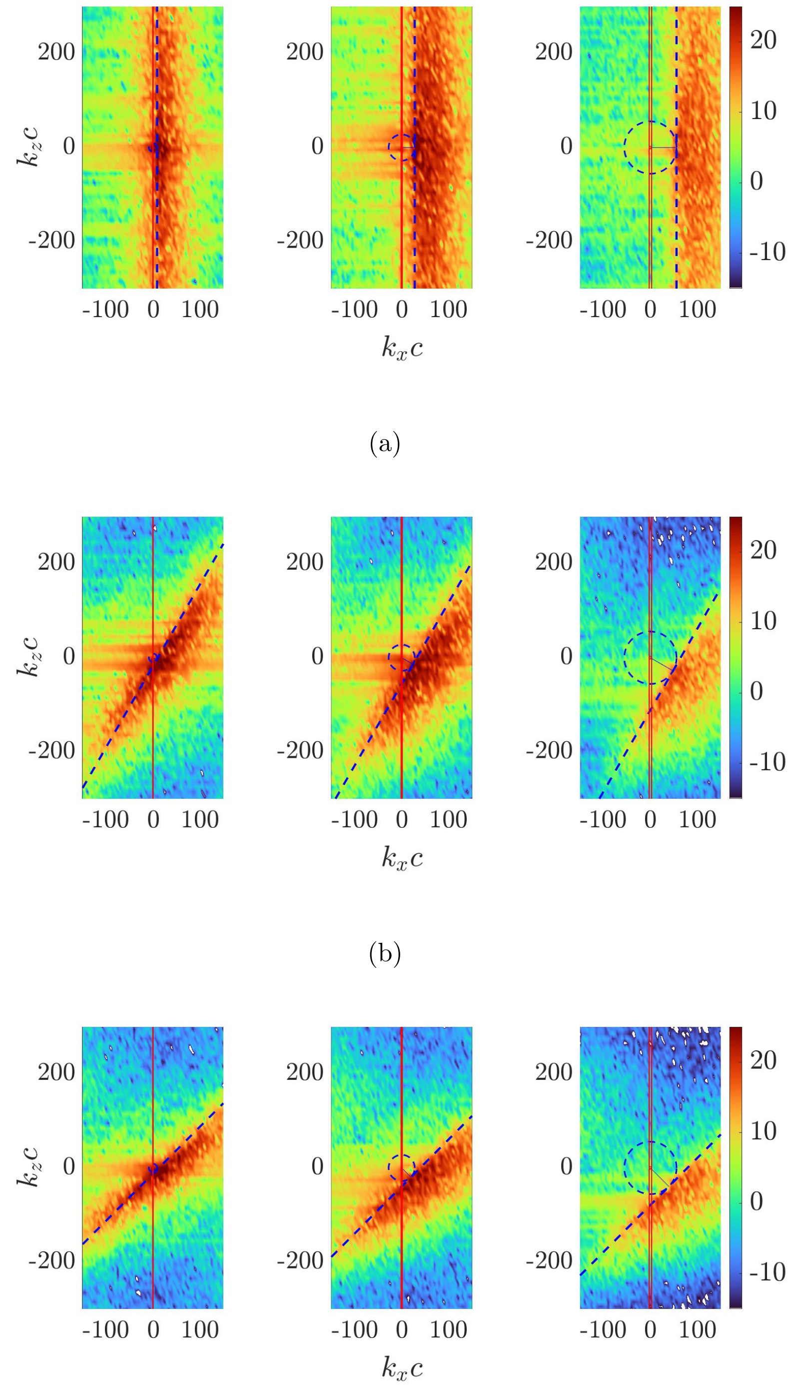

(a)

(b)

(c)

Figure 6.14: Contours of wavenumber-frequency spectra $\Phi_{qq}(k_x, k_z, f)$ at $St \approx 7.5$ (left), $St \approx 22.5$ (mid), and $St \approx 45$ (right): (a) $\psi = 0°$, and (b) $\psi = 30°$, and (c) $\psi = 45°$.

the cross-power spectral density is placed at the trailing edge in midspan. Figure 6.14 depicts the wavenumber-frequency spectra in logarithmic scale referenced to $P_{\text{ref}} = 20 \times 10^{-6}$ Pa over the domain of chordwise wavenumber k_x and spanwise wavenumber k_z at three different Strouhal numbers for the three primary cases. In the figure, the blue-dashed circle signifies a radius of ω/U_c originated from the dispersion relation at each frequency. This circle is the basis for defining a blue-dashed tangent line to designate the boundary beyond which the intense spectrum is observed. The red line is tangent to the red circle with a radius of ω/c_o, representing the acoustic spectrum, although it is minuscule compared to the blue circle. One can observe the shift of the area of the energetic spectrum to the higher chordwise wavenumber with higher frequencies. It can be found that the intense spectrum region is inclined with the misaligned flow, as shown in Figs. 6.14(b) and 6.14(c), respectively. Based on these observations, we derive a general form of a tangential line from (1) a point tangent to the circle defined as $P(\omega/U_c\cos(\psi), \omega/U_c\sin(\psi))$ and (2) slope of the tangent line, denoted as $-\tan^{-1}(\psi)$, both of which are plotted in Fig. 6.15. The complete line equation can be written as:

$$\left(k_z - \frac{\omega}{U_c}\sin(\psi)\right) = -\tan^{-1}(\psi)\left(k_x - \frac{\omega}{U_c}\cos(\psi)\right). \tag{6.14}$$

After rearranging equation (6.14), it can be expressed as,

$$\omega = k_x U_c \cos(\psi) + k_z U_c \sin(\psi). \tag{6.15}$$

It is noteworthy that Eq. (6.15) reverts to the dispersion relation of $\omega = \vec{k} \cdot \vec{U}_c$ accounting for the sweep angle, which yields the same form of equation 36 in the analytical derivation in Ref. [45]. Since the intense spectrum region corresponds to the convective ridge in the wavenumber-frequency spectrum [37, 206], we designate this region as the hydrodynamic

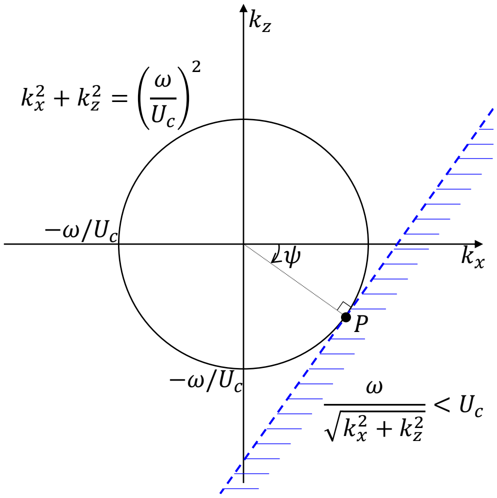

Figure 6.15: A circle with the radius determined by the ratio of convective phase speed (U_c) and arbitrary angular frequency (ω) in the domain of chordwise wavenumber (k_x) and spanwise wavenumber (k_z). A convective hydrodynamic area is demarcated by the blue dashed line (- - -) tangent to the point P and it is rotated by the sweep angle magnitude (ψ) on the circle.

area, visually delineated by the blue border (Fig. 6.15), which can formally be expressed as

$$\frac{\omega}{\sqrt{k_x^2 + k_z^2}} < U_c. \tag{6.16}$$

To investigate the effect of misaligned flow on the hydrodynamic wall pressure, which is the source of trailing-edge noise [6, 17, 34, 79], we utilize the relationship defined by the inequality in Eq. (6.16) to extract the convective hydrodynamic spectrum. This is achieved through the integration of wavenumber-frequency spectra:

$$\Phi_{qq,hy}(\omega) = \iint_{\frac{\omega}{\sqrt{k_x^2+k_z^2}}<U_c} \Phi_{qq}(k_x, k_z, \omega) \mathrm{d}k_x \mathrm{d}k_z. \tag{6.17}$$

Figure 6.16 presents the resulting hydrodynamic wavenumber-frequency spectra for the three primary flow scenarios along with the two reduced Mach number cases. The relative quantity between the baseline and the other four cases is provided in Fig. 6.16(b). The spectral magnitude is notably reduced at higher Strouhal numbers with increasing flow misalignment, although this reduction is not as pronounced as in the reduced Mach number

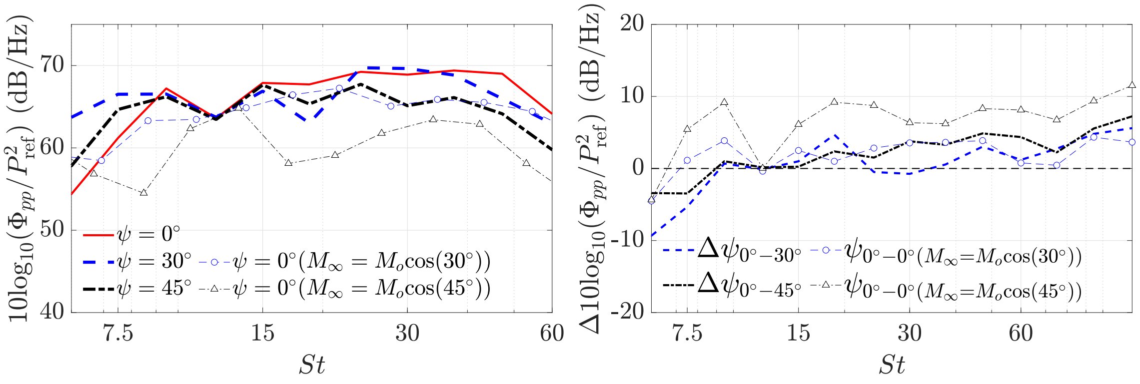

(a) (b)

Figure 6.16: Wall-pressure spectra filtered for the hydrodynamic region in the wavenumber domain: (a) spectral magnitude for the five computed cases and (b) spectral difference referenced to the baseline case.

cases. This is consistent with the far-field noise trends observed for the misaligned flow and reduced Mach number cases, as shown in Fig. 6.6. Note that the low Strouhal range, $St < 10$, shows a slight increase in pressure spectra, an opposite trend to the far-field sound levels viewed earlier in Fig. 6.6(b). This is likely due to the cumulative reduction of low-frequency compact dipole noise along the entire airfoil chord, not just limited to the trailing-edge region. Nevertheless, the reduced WPS is dominant across the entire frequency range, contributing to noise reduction via the misaligned flow. This is significant because the WPS is one of the important noise source terms in Amiet's model [6, 34, 35].

The subsequent analysis encompasses subdividing the airfoil into strips to emphasize the radiation efficiency. The schematic, resolution of wavelength, relevant descriptions can be found in Chapter 3. Figure 6.17 provides the sectional SPLs radiated from each strip of an airfoil. Three ranges of Strouhal numbers represent the low, mid, and high-frequency regions. At low-to-mid frequencies, sectional noise levels for the straight and misaligned flow scenarios are observed to be similar. However, at the high-frequency region, the sectional noise for the 45° misaligned flow is slightly lower than for the other two cases along the airfoil. A relatively lower peak noise observed near the tripping region for the 45° misaligned flow suggests a potential method to mitigate high-frequency noise when the flow is misaligned to the tripping. This further contributes to the reduction of noise levels from the fully developed flows behind the tripping region. Notably, the increasing trend in sectional noise magnitude with frequency is consistent with that observed in the hydrodynamic wall-pressure spectrum, as shown in Fig. 6.16, underlining that sectional noise is associated with a hydrodynamic noise source. Figure 6.18 depicts the cumulative pressure integrated from the sectional noise across the chord from the trailing edge. The increasing slope represents the in-phase or constructive behavior, while the decreasing slope denotes the out-of-phase or destructive behavior. At low frequencies, the noise levels for the misaligned flows are significantly lower than those of the straight flow. This corroborates the significant role of phase interference in attenuating the radiated pressure waves. At mid frequencies, noise levels between the straight and 30° misaligned flow start to deviate around $x/c = 0.7$, implying that noise mitigation is taking place from this region. Yet, trailing-edge scattering is most efficient across the 20% chord length from the trailing edge with the highest slope, consistent with previous observations [30, 110]. At $25 < St < 60$, the reduced noise from the 30° misaligned airfoil compared to the baseline case demonstrates considerable destructive interactions among neighboring noise sources across the airfoil. The much-reduced noise observed at the 45° misaligned airfoil is the combined effect arising from destructive interference and alleviated hydrodynamic noise sources due to the misaligned flow. From these analyses, the fundamental mechanisms of noise mitigation rooted in the misaligned flow are essentially out-of-phase behaviors between neighboring sources, resulting in lower radiation efficiency.

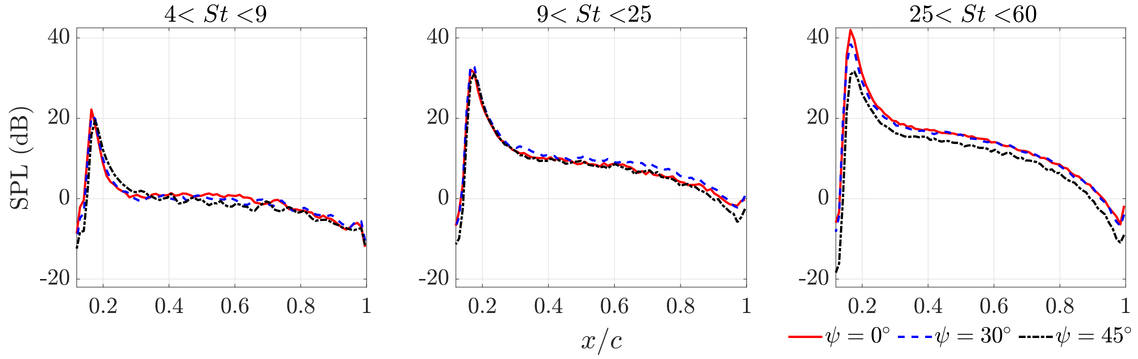

Figure 6.17: One-third octave band SPLs radiated from each strip from the leading-edge region to the trailing edge at $4 < St < 9$, $9 < St < 25$, and $25 < St < 60$.

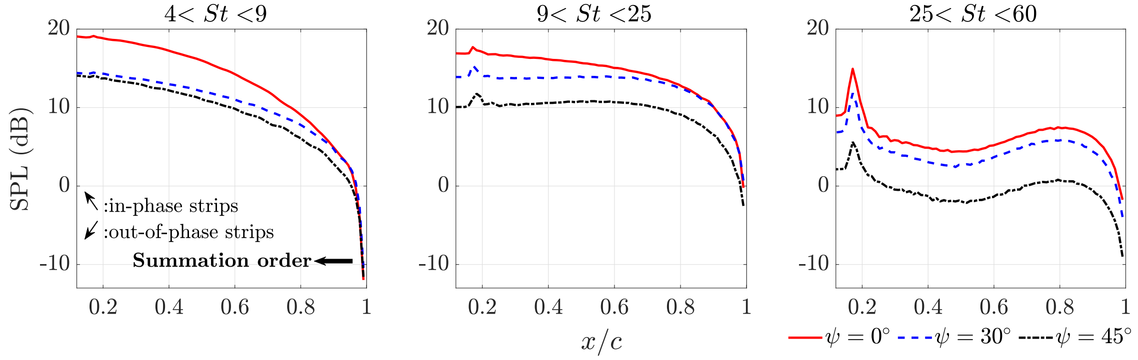

Figure 6.18: Cumulative one-third octave band SPLs radiated from each strip from the leading-edge region to the trailing edge at $4 < St < 9$, $9 < St < 25$, and $25 < St < 60$.

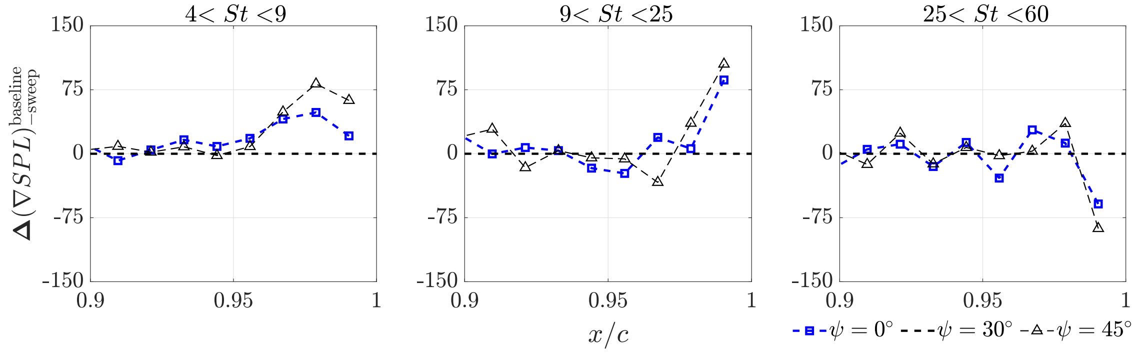

Figure 6.19: Difference of gradient of cumulative noise curve between the baseline and misaligned flow scenarios at $4 < St < 9$, $9 < St < 25$, and $25 < St < 60$.

To quantify the radiation efficiency, we compute the difference in the gradient of cumulative noise between the baseline and misaligned flow scenarios, as shown in Fig. 6.19. Higher radiation efficiency corresponds to a steeper gradient of the cumulative pressure curve. Therefore, a positive difference between the two gradients indicates decreased radiation efficiency in the misaligned flow case. At low-to-mid frequencies, misaligned flow clearly decreases radiation efficiency, where trailing-edge scattering predominantly occurs. Although the radiation efficiency is relatively high for the misaligned flows at high frequencies, the lower efficiencies at low-to-mid frequencies contribute to the overall reduction in noise levels due to the significant magnitude of SPLs in these ranges.

6.1.4 Cross-examination With Amiet's Swept Trailing-edge Noise Theory

The previous section comprehensively examined the noise mitigation mechanism and turbulent flow structures in the presence of misaligned flow within the numerical framework. In this section, we cross-examine these findings with an analytical approach using Amiet's swept trailing-edge noise theory [45]. Specifically, we investigate the influence of sweep angle on the variation of incident and scattered wall pressures in both magnitude and phase. Next, we explore the impact of WPS with and without sweep angle on the far-field acoustic spectra. Subsequently, the outcomes of Amiet's swept trailing-edge theory are compared with the FW-H results. Lastly, we discuss the spherical directivity to understand the effect of sweep angle on sound propagation. For brevity, we will focus on comparing the 45° misaligned flow with the straight flow.

Figure 6.20 presents the incident (g_0) and scattered (g_s) wall pressures, along with the combined quantity, in the chordwise direction at three selected Strouhal numbers. These wall functions are computed from Eqs. (2.15) and (2.17), respectively. Both straight and misaligned flow cases exhibit an exponential decay controlled by the factor ϵ in Eq. (2.15). However, in the case of misaligned flow, the incident wall pressures are higher than those

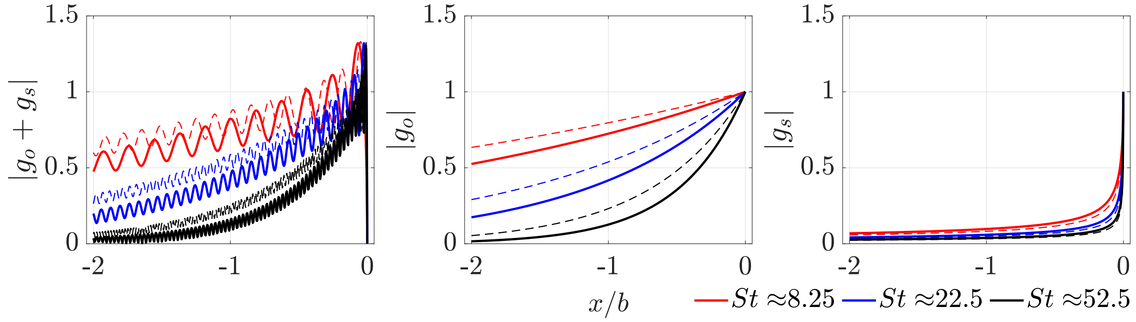

Figure 6.20: Magnitude of summation of incident (g_o) and scattered (g_s) wall pressures as well as individual magnitude for three Strouhal numbers. The solid and dashed lines are the cases for $\psi = 0°$ and $\psi = 45°$, respectively.

for the straight airfoil, which contrasts with the lower WPS observed for misaligned flows, especially for $St > 15$, in the numerical framework, as shown in Fig. 6.16. Meanwhile, the misaligned flow scenario shows lower scattered wall pressures than the straight flow scenario. It is seen that the integrated component from both wall pressures presents a higher magnitude for the flow with misalignment compared to the straight case, but the topology of the oscillatory wave appears different. This will be further analyzed through the phase function.

The phase function for the incident and scattered wall pressures is defined as $\Re(g)/|g|$, respectively, and is plotted in Fig. 6.21. It is noteworthy to observe the chordwise oscillatory waves, which become more pronounced with increasing frequency. This trend is particularly pronounced in the flow with misalignment, suggesting that the presence of a sweep angle expedites phase interference, thereby alleviating the scattering efficiency in Amiet's swept trailing-edge noise theory. These analytical observations are analogous to the main driver of noise reduction observed in the numerical framework. However, it is crucial to point out that the analytical approach does not account for the spanwise phase interference, which might also play a role in noise mitigation in the numerical approach, as visualized in Fig. 6.11.

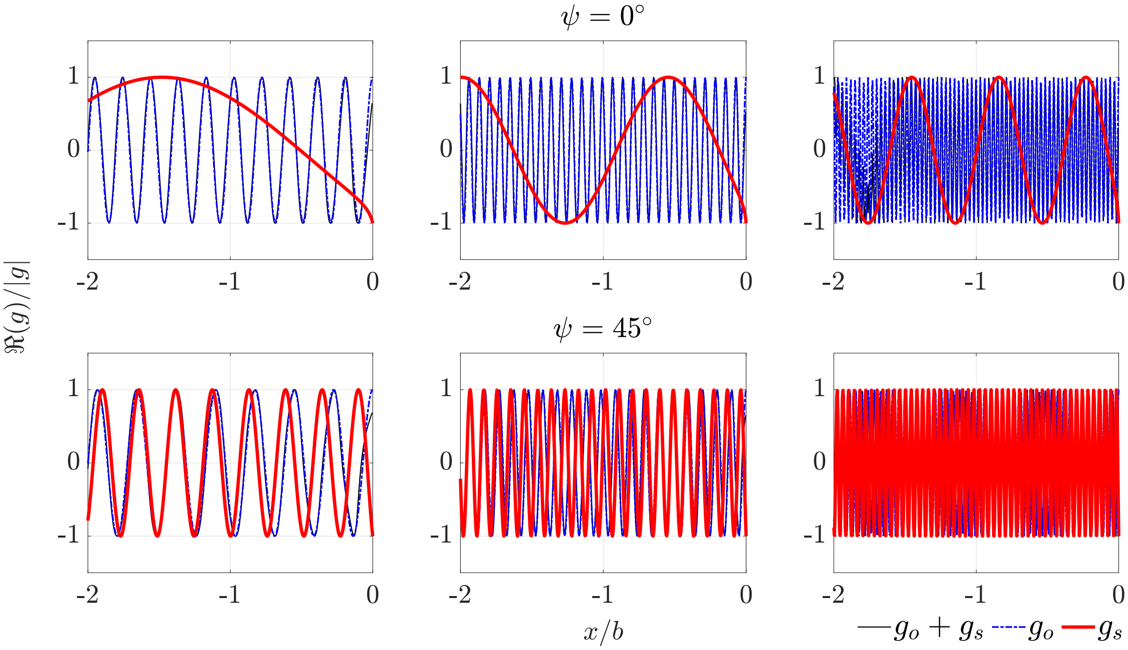

Figure 6.21: Phase of summation of incident (g_o) and scattered (g_s) wall pressures as well as their individual components for three Strouhal numbers: 8.25 (left), 22.5 (middle), and 52.5 (right).

Figure 6.22 presents SPLs predicted from Amiet's swept trailing-edge noise model, as outlined in Section 2.2.2. We analyze four distinct predictions. The first, referred to as the baseline, uses the WPS from the straight airfoil ($\psi = 0°$) as input to Amiet's model (Eq. (2.22)) with $\psi = 0°$. The second and third predictions consider the sweep angle either in the WPS or in Amiet's model, respectively. The fourth prediction incorporates the sweep angle into both the WPS and Amiet's model. Additionally, the SPL difference referenced to the baseline case, ΔSPL, is provided in Fig. 6.23(b). It is noted that the WPS is obtained from LES for each case, rather than from empirical formulations as in Ref. [45]. It is seen that there is a consistent noise benefit across the entire Strouhal range when the sweep angle is only included in Amiet's model. This is exactly the same result as in Ref. [45]. Conversely, when the sweep angle is considered only in the WPS, noise reduction increases with frequency. However, noise benefit is seldom observed in the low

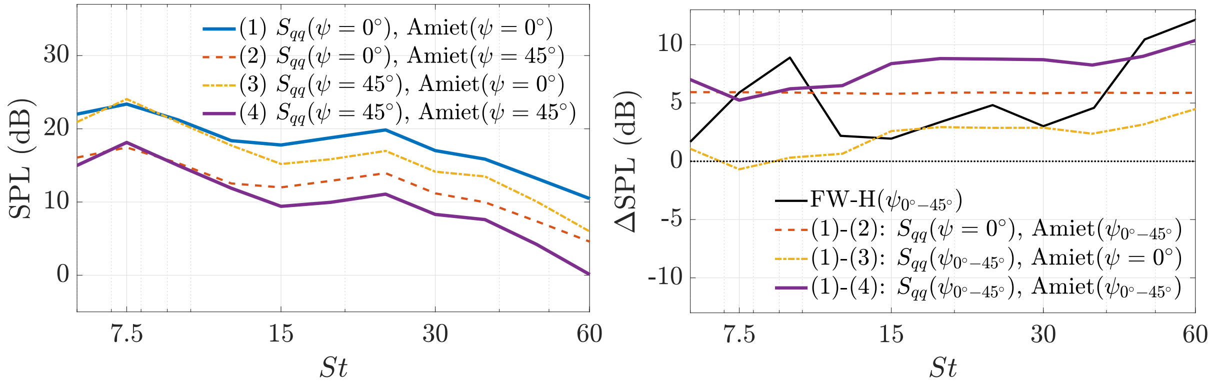

(a) (b)

Figure 6.22: Comparison of four different noise predictions from the WPS (S_{qq}) and Amiet's swept trailing-edge noise theory at an observer position, $x/c = 1.0$, $y/c = 10.0$, and $z/c = 0.05$: (a) SPL and ΔSPL.

Strouhal region below $St \approx 15$, which results from the higher pressure spectral magnitude, as demonstrated in Fig. 6.16. When both the WPS and Amiet's model incorporate the sweep angle, the reduced sound spectrum appears to be a linear superposition of the effects from the WPS and Amiet's model. Thus, the maximum noise reduction is achieved across the entire frequency range, with greater noise benefits at high frequencies. When compared with the FW-H prediction, considering the sweep angle in both the WPS and Amiet's model shows good agreement at $7 < St < 10$ and $St > 45$, while overestimating at $10 < St < 45$. In this Strouhal range, accounting for the sweep angle in the WPS provides a better match with the FW-H approach. This frequency-dependent predictive accuracy of the analytical approach necessitates the improvement of analytical modeling since it is physically correct to include the sweep angle in both the WPS and acoustic radiation like numerical simulations.

Figure 6.23 rearranges the previous SPL results to compare the spectrum shape and magnitude between the FW-H acoustic analogy and Amiet's swept trailing edge noise theory with the spanwise correlation length calculated from the generalized Corcos' model, as shown

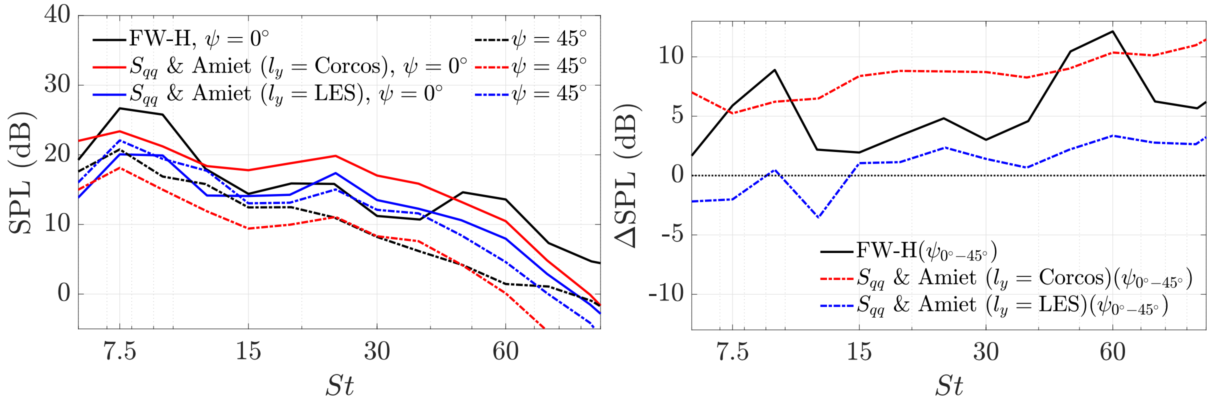

(a) (b)

Figure 6.23: FW-H acoustic analogy and Amiet's swept trailing-edge noise theory at an observer position, $x/c = 1.0$, $y/c = 10.0$, and $z/c = 0.05$: (a) SPL and (B) ΔSPL.

in Eq. (2.23) [45, 114]. To examine the effect of the spanwise correlation length on the radiated noise, we add an additional SPL predicted by Amiet's model with the spanwise correlation length obtained from the LES-based Gaussian fitting function, as viewed in Eq. (6.8) [198, 199]. The sweep angle is considered in both WPS and Amiet's model for the analytical approach. In Fig. 6.23(a), both FW-H and Amiet's predictions provide similar trends with and without the sweep angle, indicating the noise benefit of the sweep angle. The largest noise reduction is observed when the generalized Corcos' model is used in Amiet's model. In Fig. 6.23(b), one can observe the significant effect of spanwise correlation length on the noise level in Amiet's model. When the spanwise correlation length is obtained from the LES, the noise efficiency of the sweep angle notably drops. The extent of noise benefit is quite similar to when the sweep angle is only considered in the WPS, as shown in Fig. 6.22(b). The decreasing trend of the spanwise correlation length with sweep angle predicted when calculated from the generalized Corcos' model (Fig. 6.8(b)) is the contributing factor for the drastic noise reduction. On the other hand, the increasing trend of the spanwise

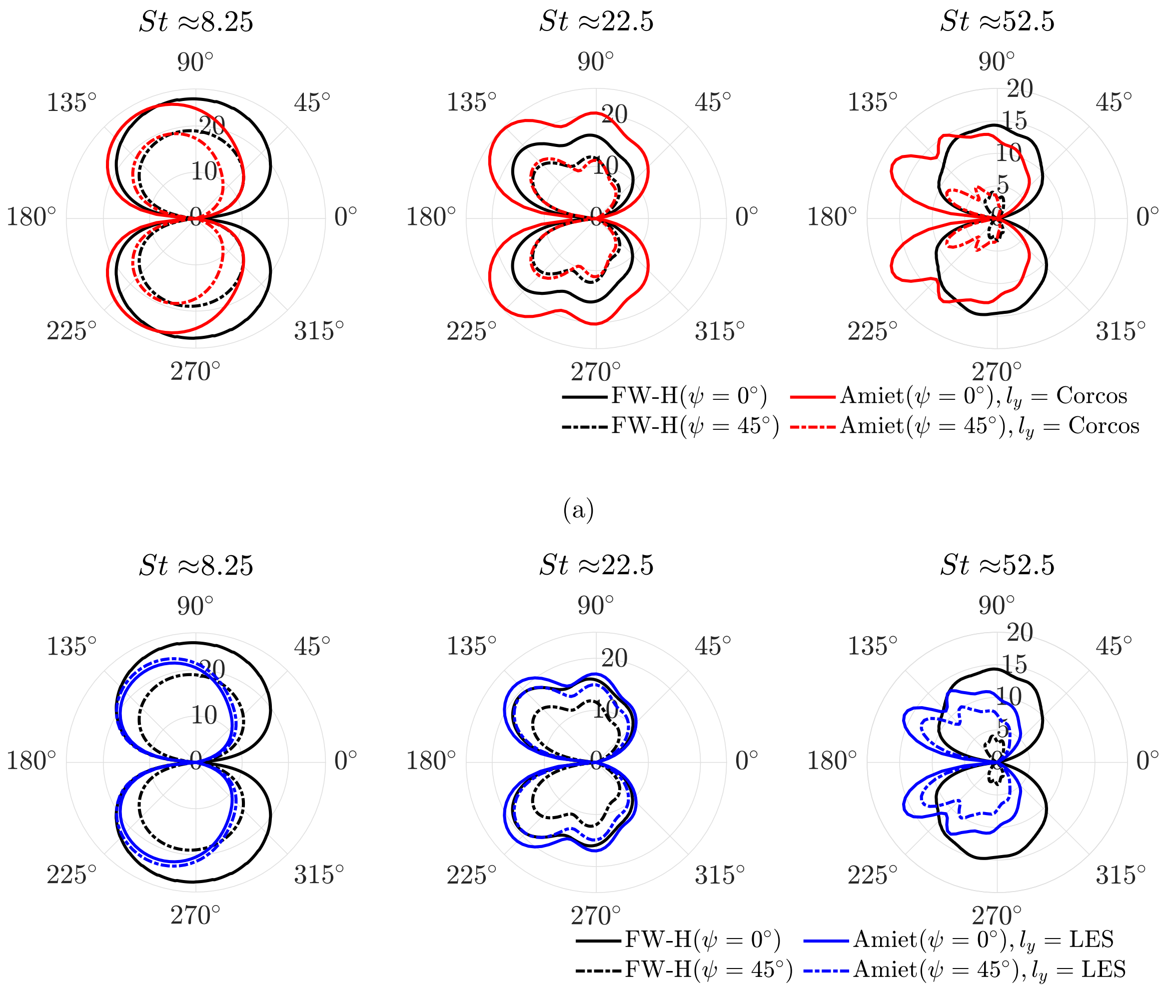

(a)

(b)

Figure 6.24: Directivity of FW-H and Amiet's swept trailing-edge noise theory at three selected Strouhal numbers recorded at the radius of $10.0c$ originated from the trailing edge with the spanwise correlation length using: (a) the generalized Corcos' model (Eq. (2.23)) and (b) LES-based Gaussian best-fit curve function (Eq. (6.8)).

correlation length obtained from the LES (Fig. 6.8(a)) calibrates the overestimation of noise reduction, which shows a better match with FW-H at $15 < St < 30$. At $St < 15$, the little noise benefit below $St < 15$ might be due to the absence of the spanwise phase interference effect in the extended Amiet's model.

The directivity patterns predicted by Amiet's theory with two approaches for the spanwise correlation length are depicted in polar plots and compared against the FW-H prediction at three Strouhal numbers in Fig. 6.24. The directivity shapes cover a range from compact dipolar sources at low frequencies to non-compact sources at mid to high frequencies of trailing-edge noise [10, 190]. One notable observation is that the directivity pattern differs between Amiet's model and the LES at $St \approx 52.5$. This difference might be due to other noise sources captured in the LES, such as tripping-induced high-frequency sound propagation [195]. For Amiet's theory with the generalized Corcos' model, as shown in Fig. 6.24(a), noise reduction is observed in all directions, closely matching the FW-H prediction, except at $St \approx 22.5$, where the noise is overly reduced. For Amiet's theory combined with the LES-based spanwise correlation length, a slight noise penalty occurs as the compact dipole source. At mid-to-high Strouhal numbers ($St \approx 22.5$ and 52.5), the noise benefit is lower in all directions compared to the FW-H prediction. The inclusion of spanwise phase interference in the analytical approach is believed to improve the accuracy in predicting the noise benefit of the sweep angle.

Lastly, the spherical directivity at $St \approx 15$ is illustrated in Fig. 6.25. We utilize Amiet's model with the generalized Corcos' model. The 3-D isometric and two-plane views are showcased. The first plane view is aligned with the chordwise and wall-normal directions, referred to as a polar plot with a polar angle (θ), as shown in Fig. 6.24, where $\theta = 0$ points

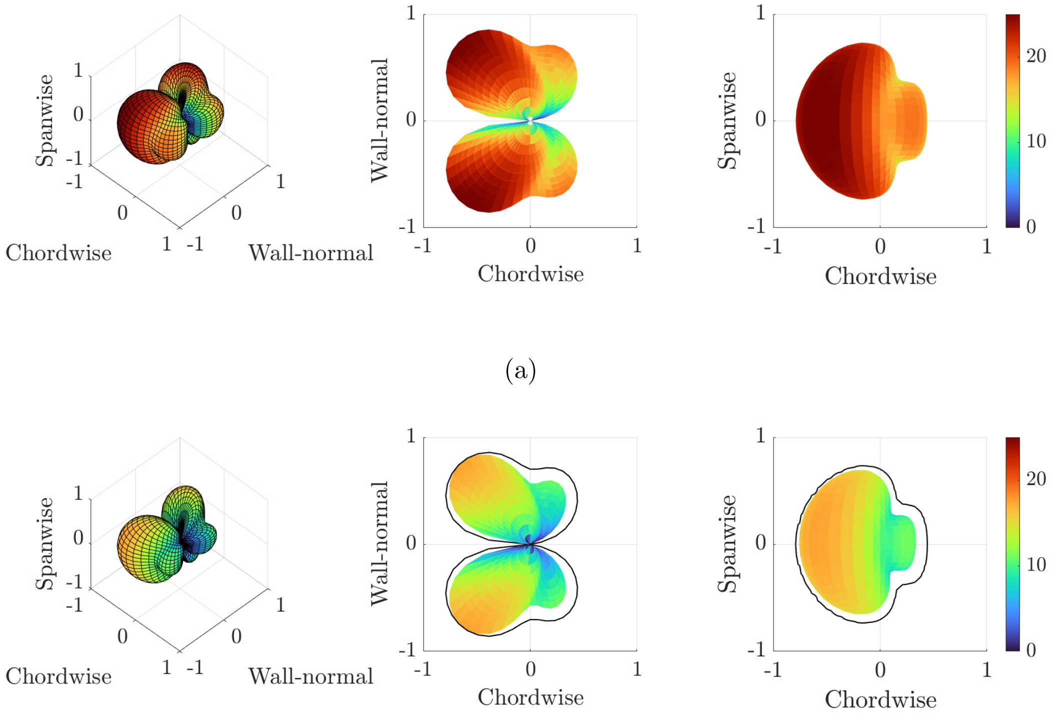

(a)

(b)

Figure 6.25: Spherical directivity with the isometric and two plane views at $St \approx$15 for (a) $\psi = 0°$ and (b) $\psi = 45°$, the latter being overlaid with the directivity shapes for $\psi = 0°$ with black solid lines in the plane views.

toward the trailing edge. The second plane view is aligned with the chordwise and spanwise directions, controlled by an azimuthal angle (ϕ) where $\phi = 0$ indicates the upstream location. The 3-D directivity shape is obtained by normalizing each axis by the spherical radius ($R = 10.0c$) and multiplying by the $\mathrm{SPL}_{\mathrm{max}}$. The contour scale represents the SPL strength for each case. The highest noise is observed around $\theta \approx 130°$ for both scenarios, making the two directivity plots resemble each other. However, the noise strength significantly drops for the misaligned flow. Relatively, the noise reduction is pronounced in the downstream area. In another view, spanwise asymmetry is observed, which is distinct in the downstream region beyond $\phi \approx \pm 130°$, although noise is reduced in all directions.

6.1.5 Summary

This section presented an in-depth examination of misaligned flow physics to reveal noise mitigation mechanisms, providing insights into the complexities of acoustic sources and propagation, specifically targeting trailing-edge noise. Additionally, the influence of misaligned flow on physics-informed analytical formulations was analyzed. We found that the extent of noise reduction across the broadband range did not correlate with simply reducing the Mach number in the absence of spanwise crossflow. Our findings showed that misaligned flow effectively reduces radiation efficiency through destructive phase interference. The novelty of this section lies in uncovering these noise reduction mechanisms driven by misaligned flow through detailed analyses and exploring the acoustic source terms in the analytical and numerical approaches.

The inclusion of misaligned flow to the straight airfoil caused asymmetric flow evolution in the spanwise direction due to the surface curvature of the airfoil. This shortened the spatiotemporal elliptical band characterizing non-frozen turbulence and caused incoherence off the band or normal to the flow direction, potentially influencing the mixing and distribution of pressure and velocities in turbulence and spanwise flow disturbances critical for acoustic scattering. For example, the spanwise flow convection resulted in a longer spanwise correlation in both spatial and frequency domains, which was the opposite trend to the model-based correlation length. When the SPOD modes were observed, the flow misalignment generated spanwise anti-phase coherent flow convection. This, in turn, played a crucial role in increasing destructive interference in both chordwise and spanwise directions, which were quantitatively demonstrated by defining the phase interference.

Misaligned flow influenced the topology of the area of intensive WPS when plotted in the wavenumber-frequency domain. We identified the strong hydrodynamic WPS region by using the dispersion relation. We demonstrated the drastically reduced hydrodynamic WPS, which is a main source of trailing-edge noise, due to flow misalignment, notably at $St > 15$. In the sectional noise analysis, we revealed that flow misalignment significantly reduces radiation efficiency as the sectional noise is gradually integrated. This clearly demonstrated the presence of destructive interference caused by flow misalignment. This provided solid evidence for the low-frequency noise reduction in the presence of misaligned flow despite a higher WPS magnitude compared to the straight flow. Thus, the combined effect of noise source and radiation efficiency is key to understanding the impact of misaligned flow on trailing-edge noise.

When the extended Amiet's model was used, the scattered wall pressure was found to experience intense oscillation in phase with the misaligned flow, suggesting that destructive interference alleviates scattering efficiency, ultimately reducing noise for the swept airfoil. However, the spanwise phase interference observed in the LES is not considered in the analytical approach. Furthermore, the opposite trend in the variation of spanwise correlation length between the LES and the generalized Corcos' model influenced the level of noise reduction across the frequency spectrum. For example, the generalized Corcos' model resulted in overly reducing noise with sweep angle in all directions, highlighting the asymmetric pattern in the spanwise direction. When the LES-based spanwise correlation length was utilized in Amiet's model, the level of reduced noise was found to be similar to the FW-H acoustic analogy, particularly at higher frequencies. Hence, the inclusion of these flow physics found in the LES could be a potential area for improvement in analytical modeling.

6.2 Trailing-edge Morphing

6.2.1 NACA 0018 Baseline and Morphed Airfoil Configurations

A NACA 0018 airfoil along with two morphed versions, M1 and M2, are illustrated in Fig. 6.26. The morphing of these airfoils primarily occurs from $x/c = 0.6$ to the trailing edge. Both morphed airfoils are designed using the PARFOIL airfoil design code [121, 122]. The M1 airfoil features a boat-tail angle factor (Δb) of -15, whereas the M2 airfoil has $\Delta b = 15$, compared to the baseline airfoil ($\Delta b = 0$). Despite these differences, both morphed airfoils share identical values for other design parameters, with the boat-tail angle measurement (X_B) at $x/c = 0.9$ and the predefined point for trailing-edge region (X_R) at $x/c = 0.3$. Based on the three PARFOIL design parameters, the thickness of morphed airfoils $t_{\text{morphed}}(X)$ are updated from the thickness of baseline airfoil $t_{\text{baseline}}(X)$ with the following [121, 122]:

$$t_{\text{morphed}}(X) = t_{\text{baseline}}(X) + \frac{\Delta b}{1000}\frac{(X - X_R)^4}{(X_B - X_R)^4}\frac{(X-1)}{(X_B - 1)}, \tag{6.18}$$

where X is the non-dimensional airfoil horizontal coordinate varying between 0 and 1. This results in the M1 and M2 airfoils exhibiting concave and convex shapes, respectively, compared to the baseline airfoil as shown in Fig. 6.26. It is important to note that the trailing-edge region of the M1 airfoil is almost flattened that it nearly resembles a flat plate. The infographic to estimate the boat-tail angles for the M1 and M2 airfoils is illustrated in Fig. 6.27. Since the boat-tail angle measurement point is set to $x/c = 0.9$, each solid line is connected between $x/c = 0.9$ and the trailing edge. The angles of each line projected onto the horizontal axis, defined as the boat-tail angles, for the baseline, M1, and M2 airfoils are denoted as ϕ_0, ϕ_1, and ϕ_2, which are 11.21°, 3.25°, and 19.18°, respectively. The variations of boat-tail angle are determined based on these lines, denoted as $\Delta\phi_1$ and $\Delta\phi_2$ for the M1 and M2 airfoils relative to the baseline, respectively. One can notice a slight deviation of the trailing edge for the M1 airfoil from the other two types of airfoils, resulting from the flattened effect. The resulting values of $\Delta\phi_1$ and $\Delta\phi_2$ are approximately 7.96°. Considering the presence of a finite gap between both sides of the airfoil that causes a slight increase in the total variation of the boat-tail angle, $2\Delta\phi$ is estimated to be roughly 16°. It should be noted that both morphed airfoils are configured to have a symmetric shape, which is different from the asymmetric designs typically explored in previous research [50–52].

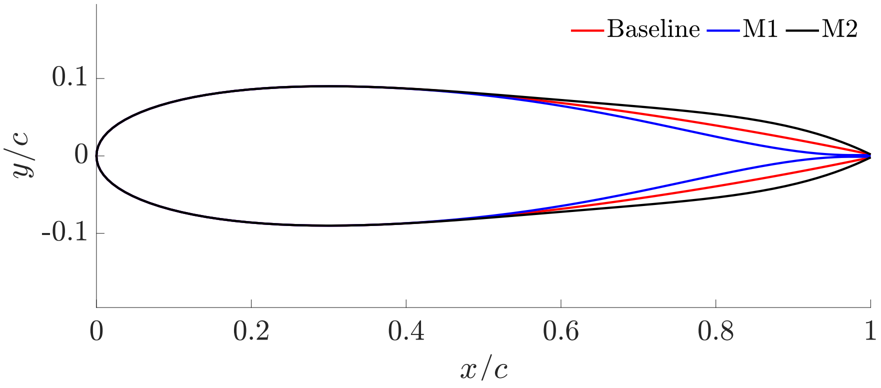

Figure 6.26: NACA 0018 airfoil and two morphed airfoil (M1 and M2) configurations.

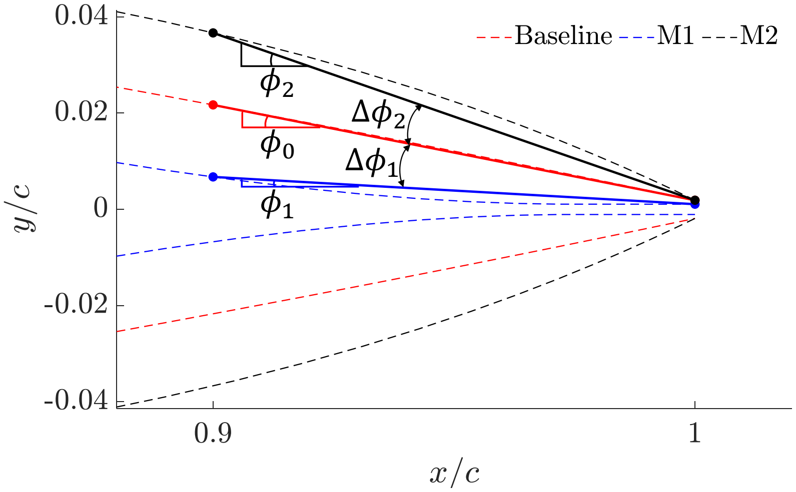

Figure 6.27: Boat-tail angle for three airfoils and the difference in the boat-tail angle for morphed airfoils.

6.2.2 Flow Evolution and Aerodynamic Forces

Figure 6.28 illustrates the surface pressure coefficients from LES and XFOIL for the NACA 0018 baseline and two morphed airfoils at angles of attack of 0° and 4°. A favorable correlation is observed between LES and XFOIL in terms of the impact of surface morphing on these coefficients. In Fig. 6.28(a), a notable local suction peak appears at the tripping region, followed by an adverse pressure gradient (APG) evolving downstream across all LES cases. It is crucial to highlight that both morphed airfoils exhibit distinct patterns of negative pressure coefficient ($-C_p$) near the trailing edge. Specifically, the M1 airfoil shows a lower intensity in $-C_p$ with either a zero or favorable pressure gradient, whereas the M2 airfoil displays a higher intensity in $-C_p$ with a more pronounced APG near the trailing edge. These observations suggest that the modifications in curvature significantly influence the distribution of aerodynamic loading on the airfoils, especially near the trailing edge. As the angle of attack increases, as depicted in Fig. 6.28(b), the pressure distributions on the suction side are profoundly affected by the local morphing at the aft of the airfoil. The

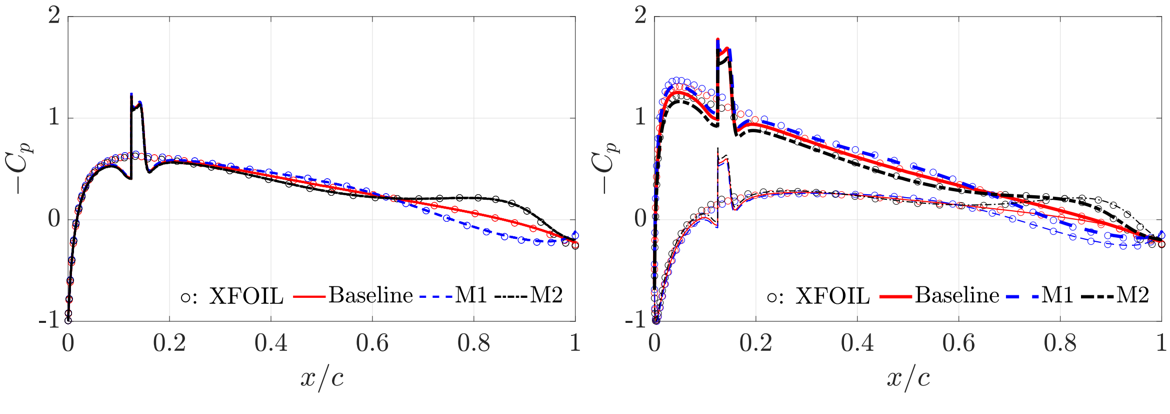

(a) (b)

Figure 6.28: Streamwise distributions of surface pressure coefficient $-C_p$ for the three airfoil configurations compared with XFOIL predictions at (a) $\alpha = 0°$ and (b) $\alpha = 4°$. At $\alpha = 4°$, the thicker and thinner lines denote the suction and pressure sides, respectively.

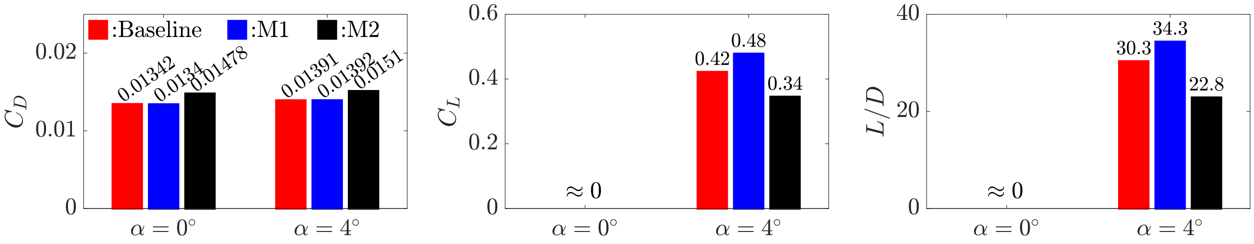

Figure 6.29: Drag coefficient C_D, lift coefficient C_L, and lift-to-drag ratio L/D for the baseline and morphed NACA 0018 airfoils at angles of attack of 0° and 4°.

M1 airfoil demonstrates a larger closed loop in $-C_p$, indicative of a potential increase in lift force. Furthermore, an additional lift gain is expected beyond $x/c \approx 0.7$ due to a more pronounced closed loop. Conversely, in the same streamwise range, the $-C_p$ curve of the M2 airfoil appears inverted, suggesting a higher suction on the pressure side near the trailing edge compared to the suction side, which likely contributes to a reduction in lift performance. Additionally, it is observed that the $-C_p$ values on the suction side of the M2 airfoil before $x/c \approx 0.7$ are even lower than those of the baseline airfoil, which could potentially result in a further loss of lift force. This detailed analysis underscores the critical role of airfoil trailing-edge morphing in shaping aerodynamic characteristics and performance.

To evaluate the effects of morphing on aerodynamic performance, the lift and drag coefficients, along with the lift-to-drag ratios, are presented in Fig. 6.29 for angles of attack at 0° and 4°. The drag force of the M1 airfoil shows little deviation from that of the baseline airfoil, despite the distinct $-C_p$ curve observed in Fig. 6.28. In contrast, it is noteworthy that the drag for the M2 airfoil increases by 10.13% and 8.55% compared to the baseline at 0° and 4°, respectively. This increase in drag for the M2 airfoil is mainly attributed to an increase in pressure drag due to the reduced pressure in the aft region, indicating that increased airfoil thickness in morphing could negatively impact drag performance. Conversely, the M1 airfoil exhibits a significant lift enhancement of 14.3% relative to the NACA 0018

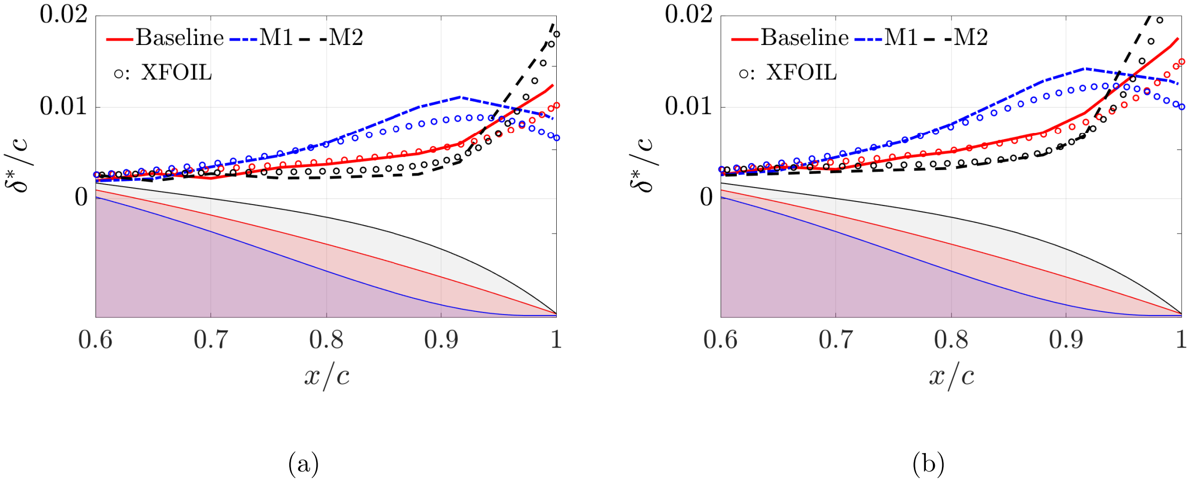

Figure 6.30: Streamwise distributions of displacement thickness δ^* divided by the airfoil chord c on the suction side compared with XFOIL predictions at (a) $\alpha = 0°$ and (b) $\alpha = 4°$.

baseline airfoil, unlike the M2 airfoil, which suffers a lift reduction of 19%. As suggested by the earlier discussion of the surface pressure curve in Fig. 6.28, the flattened shape of the M1 airfoil has a positive impact on lift performance. This improvement is driven by higher suction loading across the upstream suction side, supplemented by additional lift gain near the trailing edge. Analyzing these variations in lift and drag forces, the lift-to-drag ratio of the M1 airfoil demonstrates superior aerodynamic performance, being 13% higher than that of the NACA 0018 baseline airfoil. Meanwhile, the M2 airfoil's lift-to-drag ratio shows a significant decrease of 24.8% compared to the baseline at a 4° angle of attack.

Figure 6.30 displays the streamwise variations in displacement thickness downstream of the airfoil, where the effects of morphing are evident at both zero and four-degree incidence angles. To calculate the displacement thickness, a boundary-layer thickness δ is estimated using the local-reconstruction method proposed by Griffin et al. [175]. Notably, the two distinct morphed shapes induce significant variations in displacement thickness, which are found to be consistent with predictions from both LES and XFOIL. The M1 airfoil shows a notable development in displacement thickness higher than the other two airfoils between $x/c \approx 0.7$ to 0.9, but it sharply decreases near the trailing edge. This reduction is attributed to the favorable pressure gradient (FPG) effect, as observed in Fig. 6.28. The reduced displacement thickness near the trailing edge of the M1 airfoil is advantageous for noise attenuation, as displacement thickness is a critical parameter used to empirically predict the wall-pressure spectrum [78]. Conversely, the M2 airfoil exhibits a substantial increase in displacement thickness near the trailing edge, although it maintains a much lower thickness upstream near $x/c \approx 0.7$ to 0.9. This increase near the trailing edge could potentially result in a noise penalty when compared to the baseline airfoil. These variations in displacement thickness also become more pronounced at higher incidence angles, as illustrated in Fig. 6.30(b). The degree of variation observed at these higher angles is more significant in the morphed airfoils than at the zero incidence angle.

Turbulence intensities (TI) developed along boundary-layer profiles are depicted in Fig. 6.31 at three selected positions along the chord of the NACA 0018 baseline and two morphed airfoils at an angle of attack of $\alpha = 0°$. While the TI profiles of all three airfoils are similar at $x/c = 0.76$, marked differences emerge at $x/c = 0.916$ and $x/c = 0.997$ due to the distinct

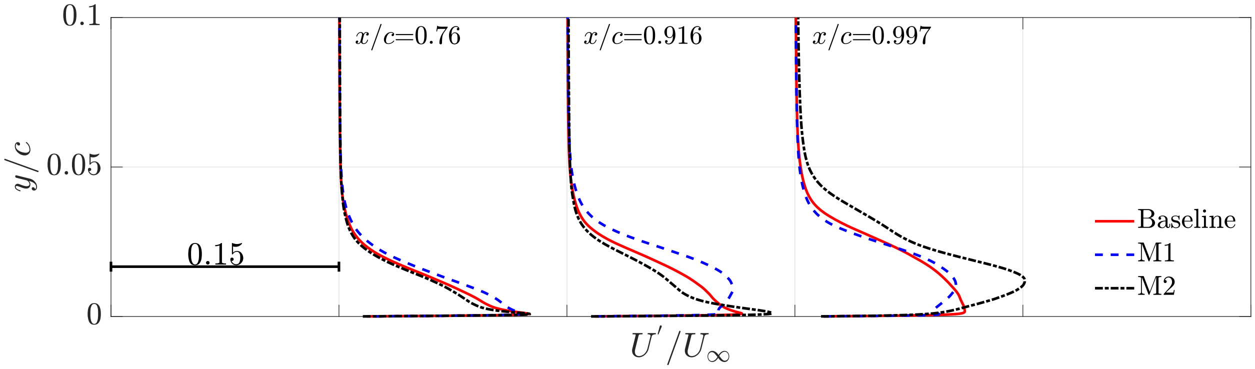

Figure 6.31: TI profiles at three streamwise locations for the baseline and morphed NACA 0018 airfoils at $\alpha = 0°$.

curvature morphing. At $x/c = 0.916$, where the M1 airfoil exhibits the greatest displacement thickness among the three airfoils, as illustrated in Fig. 6.30, its TI profiles are significantly thicker than those of the other two airfoils. Notably, near the wall, the M2 airfoil's TI profiles peak higher than those of the baseline. At $x/c = 0.997$, a location critical for trailing-edge scattering [195], the M2 airfoil's TI profiles are both thicker and reach a higher peak compared to the other two cases. This pronounced increase in TI is closely associated with the strong APG affecting the M2 airfoil at this location, as demonstrated in Fig. 6.28. The intense turbulent flows noted in the M2 airfoil are expected to interact significantly with the wall, potentially leading to a high wall-pressure spectrum and the resultant radiation of high-amplitude noise. Additionally, TI profiles have been similarily developed at a 4° angle of attack for both morphed airfoils, though these are not included here for brevity.

6.2.3 Near-Wall Flow and Acoustics

This section explores the near-wall flow and acoustic fields for both the baseline and morphed airfoils, assessing the noise levels radiated at various observer positions. Figure 6.32 illustrates the near-wall flow and acoustic perturbations at a zero incidence angle, visualized using the Q-criterion colored by the normalized streamwise velocity component, with the dilatation field displayed in the background. Initially, one can observe the fully developed three-dimensional turbulent structures, which are triggered by the quadrilateral trip wire placed at the leading edge on both sides of the airfoil. While the flow structures and acoustic waveforms of the M1 airfoil appear similar to those of the NACA 0018 baseline airfoil, a notable distinction arises near the trailing edge region. Here, the M1 airfoil maintains a

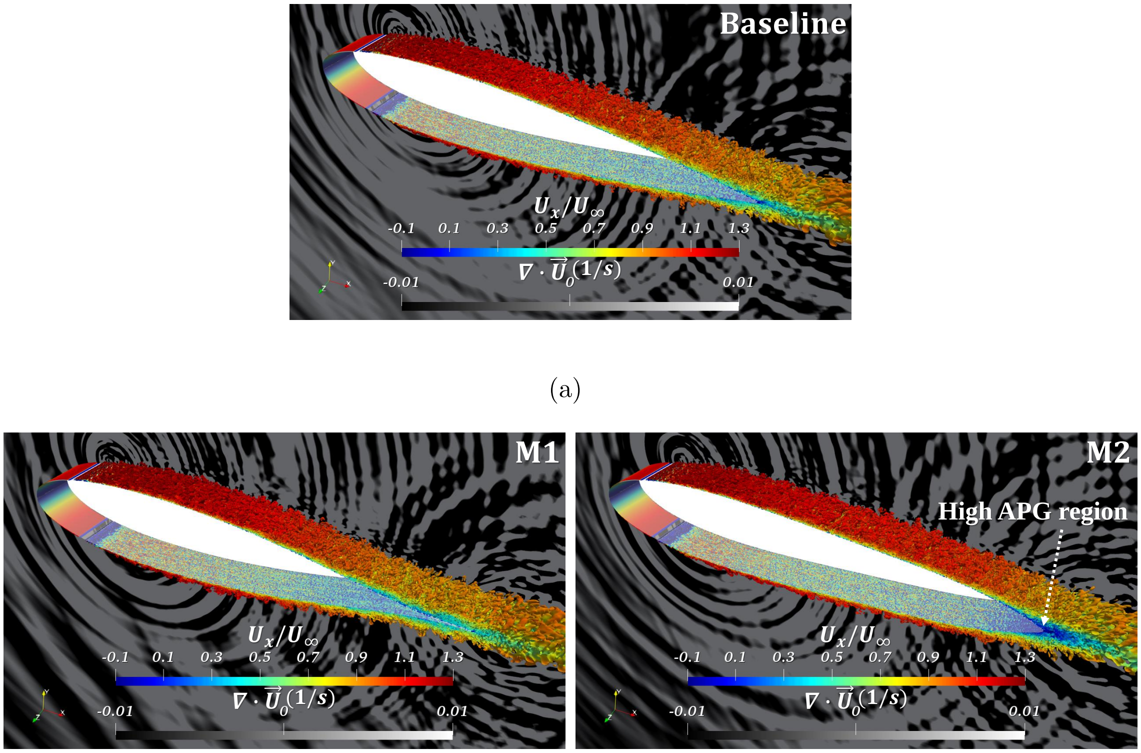

(a)

(b) (c)

Figure 6.32: Normalized Q-criterion ($Qc^2/U_\infty^2 = 10$) colored with the normalized streamwise velocity component (U_x/U_∞) with the dilatation field ($\nabla \cdot \vec{U}$) in the background at $\alpha = 0°$ for the (a) baseline, (b) M1, and (c) M2 airfoils.

higher streamwise velocity, induced by FPG flows, which helps to limit potential flow separation. Conversely, the flow structures near the trailing edge of the M2 airfoil reveal an extended region of APG, leading to flow separations as highlighted by the blue-colored zone. This emphasizes the detrimental effects of thicker morphing on both the aerodynamic force and the mechanisms of noise generation and propagation.

The radiated noise from each airfoil is evaluated using the FW-H acoustic analogy, focusing on an observer positioned 10 chords away from the trailing edge at midspan, as illustrated in Fig. 6.33. The sound spectra are depicted using A-weighted one-third octave band sound pressure levels (SPLs) to approximate the human ear's filtering process for sound perception. For the M1 airfoil, noise levels are effectively reduced up to $St \approx 25$ compared to the baseline airfoil. However, beyond this frequency, a high-frequency broadband hump emerges, suggesting that a flattened shape may increase high-frequency scattering efficiency. For the M2 airfoil, on the other hand, remarkably reduced noise levels at Strouhal range between 10 and 40, are observed compared to the baseline. However, those noise benefits are masked by low-frequency noise amplification seen below $St \approx 7$, approximately 10 dBA up, compared to the baseline airfoil. These phenomena are directly linked to the distinctive aerodynamic characteristics of the M2 airfoil, including the presence of high APG, increased displacement thickness, and separated flow regions affecting low-frequency noise, which are detailed in Figs. 6.28, 6.30, and 6.32, respectively.

The integration of SPLs across the frequency range, defined as OASPL, is conducted for the three airfoils at zero and four-degree incidence angles, as depicted in Fig. 6.34. It is observed that the OASPLs for all airfoils rise with an increase in angle of attack, attributable to more intense noise sources developing in higher non-equilibrium flows on the suction side. At both angles of attack, the two morphed airfoils exhibit a consistent trend: a noise benefit

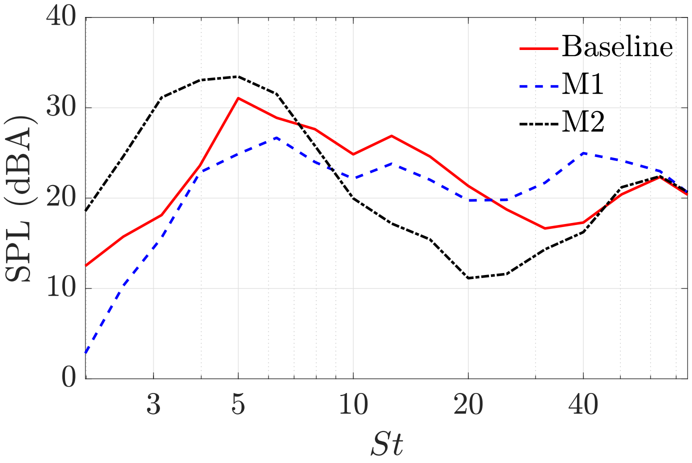

Figure 6.33: A-weighted one-third octave band SPLs predicted by the FW-H acoustic analogy at an observer position, $x/c = 1.0$, $y/c = 10.0$, and $z/c = 0.05$.

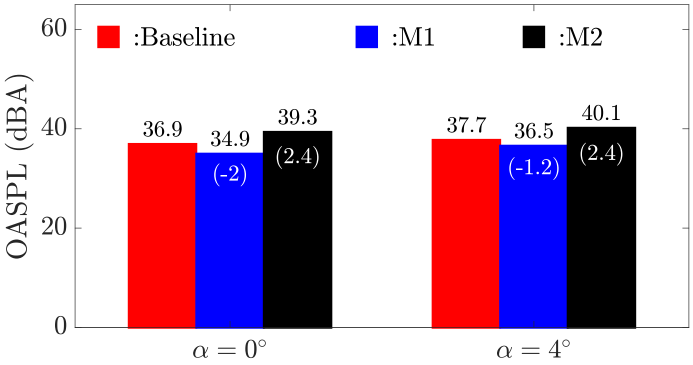

Figure 6.34: A-weighted OASPLs for the NACA 0018 baseline and morphed airfoils at $\alpha = 0°$ and 4°. The difference in OASPL between the baseline and each morphed airfoil is provided in the parenthesis.

for the M1 airfoil and a noise penalty for the M2 airfoil. A key factor in the acoustic performance of the M1 airfoil is its ability to revert to attached stable flows, which helps mitigate some of the increases in high-frequency noise, as detailed in Fig. 6.33. It is also noteworthy that the noise reduction achieved by the M1 airfoil is more pronounced at 0° than 4°. Conversely, the noise increment observed in the M2 airfoil is consistent despite an increase in the angle of attack.

The analysis of far-field noise is extended from a single observer to multiple locations by examining the directivity pattern of each airfoil scenario at a zero angle of attack, as illustrated in Fig. 6.35. Given that the directivity pattern at an angle of attack of 4° is similar to that at 0°, it has been omitted for conciseness. The measurements are taken using a circular microphone array with a radius of $10.0c$, centered at the trailing edge in midspan. Across both the baseline and the morphed airfoils, a similar directional shape is observed, transitioning from a low-frequency compact dipolar source to a cardiovascular shape embedded with multi-lobes, predominantly influenced by trailing-edge scattering up to $St \approx 20$. At $St \approx 30$, irregular directivity patterns emerge, which could be attributed to non-linear interactions between leading-edge tripping noise and trailing-edge noise [165,

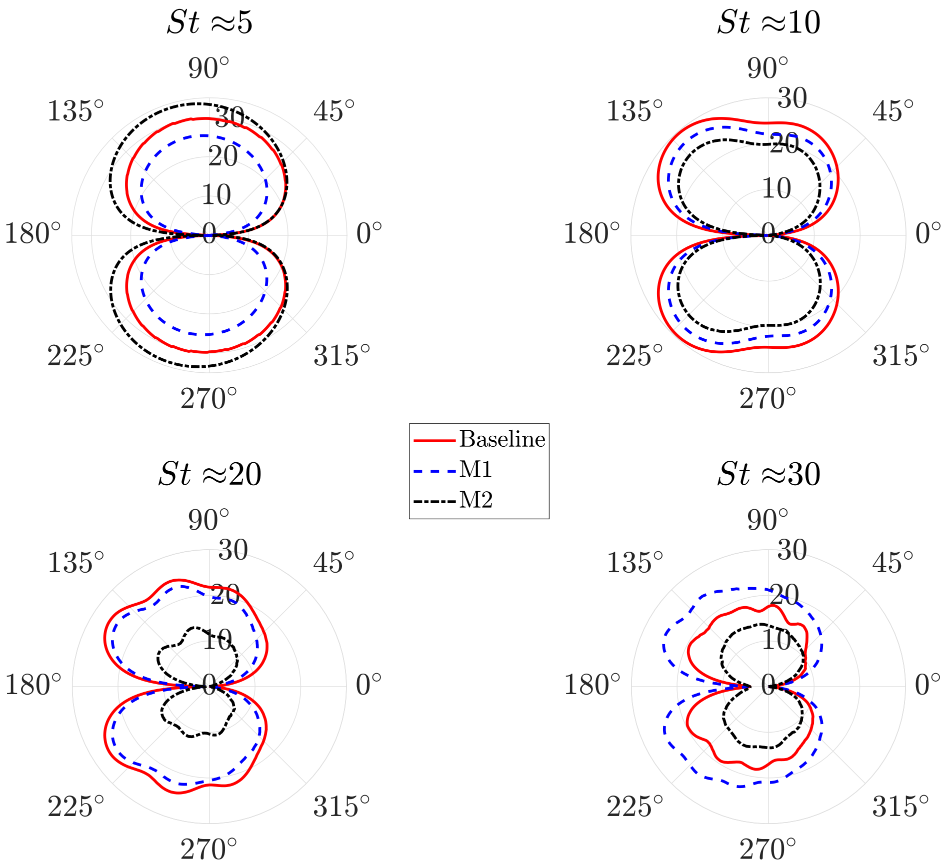

Figure 6.35: Directivity of A-weighted one-third octave band SPLs at four frequencies with the radius of 10.0c originated from the trailing edge of each airfoil at a zero angle of attack.

195]. When compared to the NACA 0018 baseline airfoil, the M1 airfoil demonstrates noise reduction in all directions up to $St \approx 20$, yet an omnidirectional increase in noise is noted at $St \approx 30$. This suggests that high-frequency noise increase occurs uniformly across all directions. For the M2 airfoil, significant low-frequency noise primarily manifests in the upstream direction. However, as the frequency increases, a notable reduction in noise is observed.

6.2.4 Low-fidelity Noise Predictions and Evaluation of Airfoil Performance at Trimmed Flight Condition

This section explores the predictive capability of different noise computation methods. The first and second approaches employ Amiet's model [6, 34, 35], but the WPS is obtained differently. The first approach takes the WPS directly obtained from the LES, while the second method determines the WPS using the empirical model. In this study, Lee's model [78] is employed where the model input is taken from XFOIL [123]. The third approach comes from the Brooks, Pope, and Marcolini (BPM) empirical model [5], which is formulated from the NACA 0012 wind tunnel database. The BPM model fundamentally consists of five different noise sources: turbulent boundary-layer trailing-edge noise (TBL-TEN), laminar-boundary layer vortex shedding noise (LBS-VS), trailing-edge bluntness noise, separation-stall noise, trailing-edge bluntness vortex shedding noise, and tip vortex noise, as described in Fig. 1.1. Here, the TBL-TEN and separation noise are only considered. These model-based approaches are compared with the FW-H acoustic analogy.

Figure 6.36 provides SPL plots of the baseline, M1, and M2 airfoils at a zero angle of attack, which are predicted from four different methods. Additionally, the SPL difference referenced to the FW-H is provided in Fig. 6.36(b). For the baseline airfoil, all the approaches show a similar spectral broadband shape. For the M1 airfoil, two Amiet's model-based approaches are able to predict both the occurrence of noise benefit below $St \approx 25$ and the noise penalty above that Strouhal range. However, the BPM model little presents M1's noise benefit. It is probably caused by the inconsistency of the highest peak frequency. For the M2 airfoil, all the model-based approaches deviate from the FW-H acoustic analogy. However, Amiet's model & WPS (LES) effectively captures M2's relative acoustic performance to the baseline, as shown in Fig. 6.36(b). The discrepancy in SPL between the FW-H and the model-based predictions might be attributed to the absence of non-frozen noise sources present upstream of the trailing edge. Although the noise source at the trailing edge is crucial, the morphed surface might induce nonlinear flow patterns, influencing WPS strengths and phase interference among acoustic sources. These behaviors are not considered in Amiet's theory, where the simplified flat plate is assumed, harmonically varying the noise source from the trailing edge to the leading edge. The BPM model also does not account for this localized morphing effect. Furthermore, the spanwise correlation length between the baseline and morphed airfoils is the same since Corcos' model is a function of convective phase speed. However, the surface curvature effect, particularly when the trailing edge is blunt, nonlinear

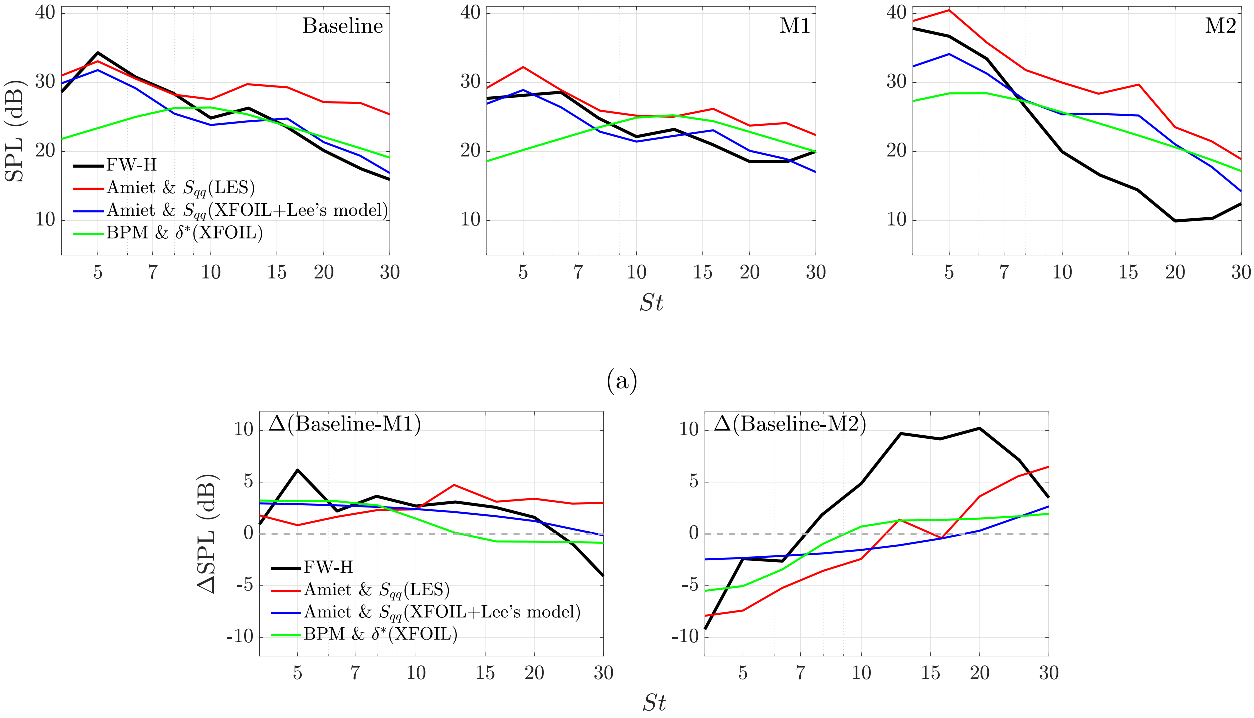

(a)

(b)

Figure 6.36: One-third octave band SPL for the baseline, M1, and M2 airfoils at $\alpha = 0°$ predicted through four different approaches at a microphone positioned at $x/c = 1.0$, $y/c = 10.0$, and $z/c = 0.05$: (a) SPL and (b) ΔSPL.

flow behaviors could affect the spanwise correlation length, a critical noise source term in Amiet's model, resulting in the accuracy of the radiated noise level.

Figure 6.37 provides SPL and ΔSPL plots similar to Fig. 6.36, while being measured at $\alpha = 4^\circ$. A notable difference, when compared to the zero angle of attack, is discrepancies in both SPL and ΔSPL between model-based approaches and FW-H acoustic analogy. Since flows are more driven by APG with the possible separation near the trailing edge at a higher incidence angle, the model uncertainty arising from unsteady flows and underlying assumptions in acoustic models could lead to more discrepancy to the FW-H acoustic analogy than what was observed at $\alpha = 0^\circ$.

Figure 6.38 shows the OASPLs from four prediction methods for the baseline and mor-

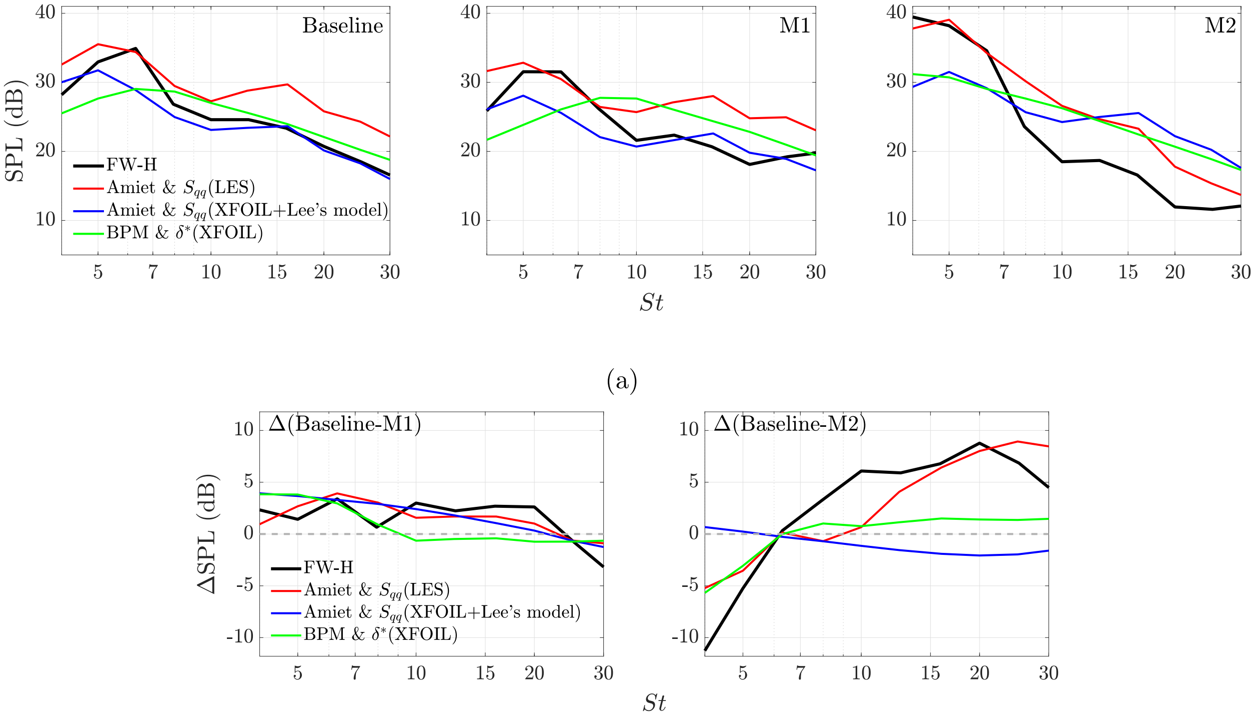

(a)

(b)

Figure 6.37: One-third octave band SPL for the baseline, M1, and M2 airfoils at $\alpha = 4^\circ$ predicted through four different approaches at a microphone positioned at $x/c = 1.0$, $y/c = 10.0$, and $z/c = 0.05$: (a) SPL and (b) ΔSPL.

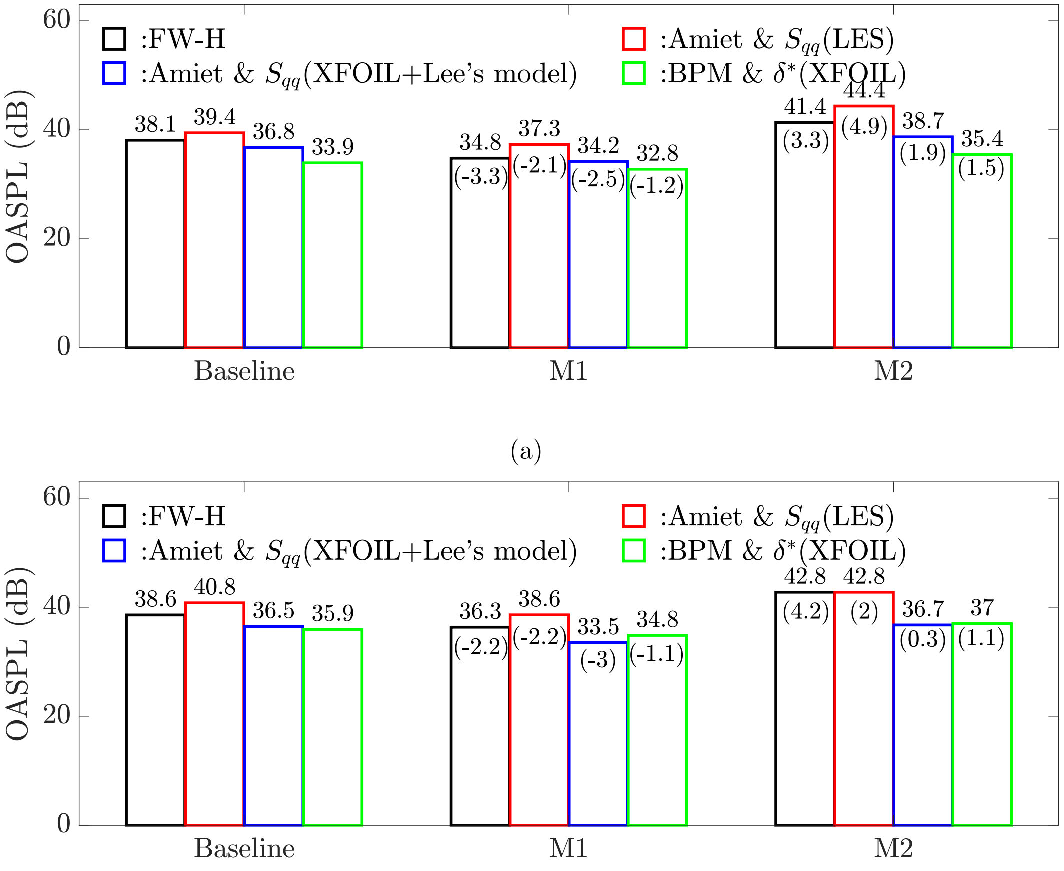

(a)

(b)

Figure 6.38: OASPL for the baseline, M1, and M2 airfoils predicted through four different approaches: at (a) $\alpha = 0°$ and (b) $\alpha = 4°$. The difference in OASPL between the baseline and each morphed airfoil is provided in the parenthesis.

phed airfoils at $\alpha = 0°$ and 4°. OASPL is integrated over the Strouhal range between 4 and 30. At both angles of attack, the model-based approaches effectively predict the noise benefit and penalty observed in M1 and M2 airfoils, respectively. However, the trend of increased noise with higher angles of attack is not observed in Amiet & S_{qq}(XFOIL+Lee's model) and BPM model, while Amiet & S_{qq}(LES) does not capture this trend only at M2's airfoil.

Lastly, the baseline and morphed airfoils' aerodynamic and aeroacoustic performances are evaluated at the trimmed flight condition for practical applications. XFOIL-based aerodynamic maps are first constructed to find the trimmed flight condition. Here, the trimmed

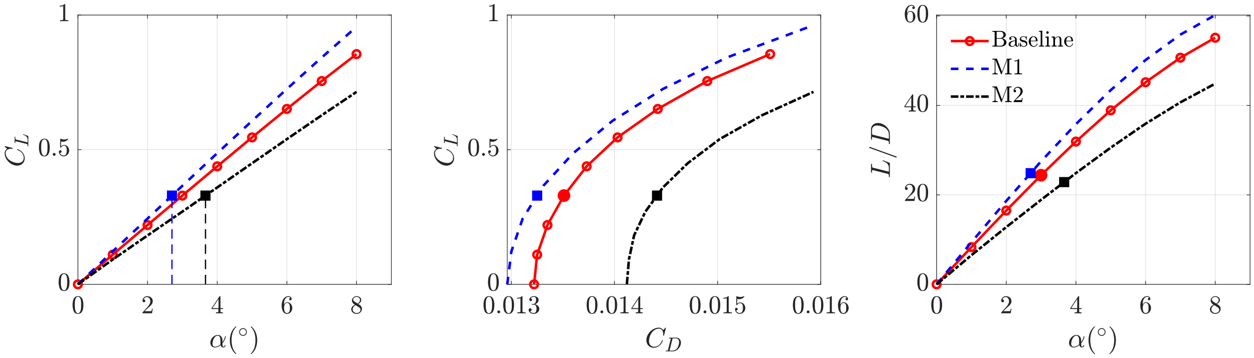

Figure 6.39: XFOIL-based aerodynamic forces including lift coefficient, drag coefficient, and lift-to-drag ratio for the baseline, M1, and M2 airfoils. The filled circle (baseline airfoil) and filled square (morphed airfoils) indicate the points at the trimmed angle of attack.

Table 6.2: Angles of attack for the baseline, M1, and M2 airfoils at the trimmed flight condition.

Targeted trimmed condition	C_L=0.3926
Baseline Airfoil	α_{trim}=3.0°
M1 Airfoil	α_{trim}=2.701°
M2 Airfoil	α_{trim}=3.663°

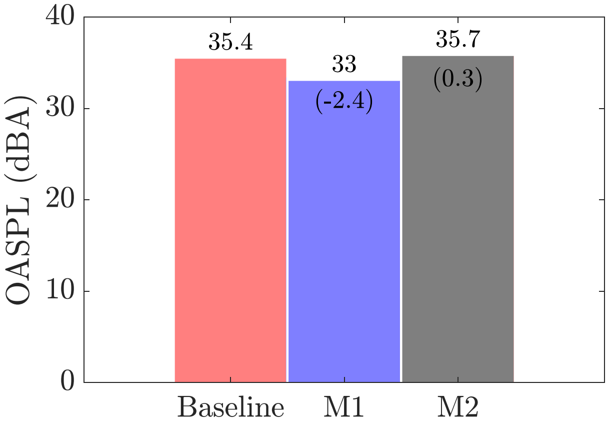

Figure 6.40: A-weighted OASPLs for the NACA 0018 baseline and morphed airfoils at the trimmed flight condition. The difference in OASPL between the baseline and each morphed airfoil is provided in the parenthesis.

angle is defined when all the airfoils' lift forces are set to hold the same value of 0.3926. Thus, a trimmed angle of attack can be calculated on the C_L-α curve, as shown in Fig. 6.39. The resulting trimmed angle of attack on each airfoil is tabulated in Table 6.2. At this trimmed flight condition, M1's airfoil is much more performant than the other two airfoils, indicating lower drag force and higher lift-to-drag ratio. When the OASPL is calculated using Amiet & WPS (XFOIL + Lee's model), M1's OASPL is 2.4 dBA lower than the baseline while M2's OASPL shows a slight increase than the baseline airfoil. This highlights the advantages of concave geometry in enhancing both aerodynamic and aeroacoustic performances, as well as the ease of airfoil design due to its simplified configuration.

6.2.5 Summary

This section explored the effects of curvature trailing-edge morphing of a NACA 0018 airfoil on the aerodynamics and aeroacoustics, specified at a Reynolds number of 6×10^5, a Mach number of 0.088, and angles of attack of 0° and 4°. The airfoils were morphed symmetrically into two distinct shapes: a concave shape (M1) and a convex shape (M2), each parameterized by the boat-tail angle with minor adjustments to other design parameters.

The M1 airfoil demonstrated enhanced performance in both aerodynamics and aeroacoustics. It exhibited a notable 14.3% increase in lift force with minimal changes in drag force, leading to an improvement in the lift-to-drag ratio by 13.2% compared to the baseline airfoil. This superior performance is attributed to the concave morphing of the airfoil, which promotes stable attached flows driven by FPG. Additionally, this morphing led to enlarged suction forces across the entire suction side of the airfoil, especially at a non-zero angle of attack. These aerodynamic benefits were accompanied by a reduction in noise levels, with the M1 airfoil achieving up to a 2 dBA decrease compared to the baseline, according to the findings from the FW-H approach. This noise reduction occurred despite the presence of high-frequency humps, indicating that the concave morphing not only enhances lift but also contributes to more effective noise management. This combination of improved lift and reduced noise underscores the dual benefits of the M1 airfoil's design, making it a compelling option for applications where both aerodynamic efficiency and noise mitigation are critical.

In contrast, the performance of the M2 airfoil deteriorated in both aerodynamics and aeroacoustics compared to the baseline airfoil. The primary cause of this degradation was the development of APG flows, which led to localized flow separations. This aerodynamic feature was pivotal in amplifying the low-frequency noise, which is a significant characteristic of the M2 airfoil's noise profile. Although there was a notable reduction in high-frequency noise levels, OASPL increased by up to 2.4 dBA. Additionally, the aerodynamic performance of the M2 airfoil suffered, as evidenced by a 24.8% decrease in the lift-to-drag ratio. This reduction highlights the negative impact of APG-induced flow separations, which compromise the airfoil's efficiency and noise characteristics.

Chapter 7

Concluding Remarks

This thesis has explored the fundamental mechanisms governing airfoil noise generation and reduction within turbulent boundary layer flows using large-eddy simulations. This chapter provides a summary of the research findings. It also highlights key contributions, recommendations for future work, and a list of publications.

7.1 Summary of Research Findings

- *Wavelet-based Pressure Decomposition*

To keep track of the true physics of noise source and propagation in the numerical simulations, coherent or denoised pressure was isolated by filtering out the incoherent pressure or background noise using a wavelet filtering based on the recursive denoising algorithm. The denoised pressure had a few but high wavelet coefficients and represented physical phenomena such as hydrodynamic wavy structures advecting along the wall and sound scattering mechanisms near the tripping region and trailing edge. On the other hand, the contribution of the background noise to the original pressure was found to be primarily dominant at high frequencies, with lower wavelet coefficients or sound spectrum levels. The effect of denoising was found to be noticeable near the tripping and trailing-edge regions where background noise was mostly produced. The underlying reasons for this effect were deduced as the diffusive, homogeneous, and random motion characteristics of turbulence filtered from turbulent flows, or insufficient grid resolution. It was shown at the far-field acoustic spectra that the background noise is dominant at high frequencies despite having a negligible sound amplitude. The PDF shape of denoised pressure was off the Gaussian distribution in the positive tail, demonstrating that the acoustic pressure on wall-bounded flows at a low Mach number could not be solely filtered with the Gaussian assumption. Overall, the wavelet-based pressure decomposition method has potential benefits for airfoil noise simulations. Firstly, it can effectively filter out background noise, revealing only the physically significant noise sources and sound propagation. Secondly, the threshold level or topology of the background noise may provide insight into the adequacy of grid resolution in the presence of small-length scales of turbulent flows.

- *Fourier-based Pressure Decomposition*

To elucidate the complexity of trailing-edge noise generation and propagation within turbulent boundary layer flows, wall pressure was decomposed into hydrodynamic and acoustic pressures through Fourier-based filtering. In parallel, incident and scattered pressures were analyzed based on Amiet's theory and analytical formulations. The hydrodynamic pressure source was found to arise from streamwise turbulent streaks along the wall, with phase velocities close to the convective speed. These turbulent structures exhibit incoherence between adjacent turbulent eddies, resulting in highly oscillatory phase variations, which give rise to non-propagating or evanescent waves. Consequently, the far-field noise radiated from the hydrodynamic pressure remained significantly lower than that of the decomposed acoustic component. Despite acting as inherently pseudo-sound sources, hydrodynamic pressure played a crucial role in generating acoustic pressure, primarily through interactions with spanwise-coherent turbulent structures near the trailing edge. On the other hand, the acoustic pressure revealed efficient propagation at nearly the speed of sound, with its spectral characteristics primarily associated with the effects of spanwise turbulent coherent structures. Despite the significantly lower magnitude, it played a predominant role in shaping far-field sound spectra. This predominance could be attributed to the in-phase behavior of the acoustic pressure, which was particularly pronounced in the case of compact dipolar sources at lower Strouhal numbers. Even at higher Strouhal numbers, the in-phase tendencies persisted within the streamwise correlation length, facilitating efficient sound propagation across the entire frequency range. In contrast, when comparing Amiet's theory with acoustic pressure, subtle disparities in their physical properties emerged. Amiet's theory relied solely on the wall-pressure spectrum in close proximity to the trailing edge, incorporating phase information from the integration of turbulent flows governed by the frozen turbulent gust assumption. This work, which delineates the distinct roles of hydrodynamic incident pressure and acoustic scattered pressure, is anticipated to make a substantial contribution to our understanding of scattering phenomena related to broadband trailing-edge noise in wall-bounded flows.

- *Effect of Boundary-layer Tripping on Airfoil Noise*

In-depth investigations were performed to understand the sound generation and propagation mechanisms of airfoil noise under two different numerical tripping models: (1) stair strip and (2) suction and blowing. The natural transition was scrutinized as a comparative baseline, and all the cases were simulated at a Reynolds number of 4×10^5, a Mach number of 0.058, and an angle of attack of 6.25°. As turbulent boundary layers developed on the suction side following the flow transition, the primary acoustic source in all cases was the scattering of hydrodynamic coherent structures by the trailing edge. This noise was detected as an antisymmetric wave and multi-lobe pattern at frequencies between $St = 15$ and 30, particularly intense within 10% of the airfoil chord near the trailing edge. However, the installation of tripping mechanisms introduced additional acoustic source phenomena. A common feature of tripping installations was the tonal peak around $St = 7.5$ due to vortex shedding. This far-field noise correlated with the spanwise coherent phase on the wall, meeting the necessary condition for tonal noise emission. Moreover, distinct noise mechanisms were discovered in the stair strip and the suction and blowing scenarios. In the stair strip scenario, the interaction between LSB and tripping amplified LSB broadband noise, with a high-frequency quasi-tonal peak. This noise amplification occurred in all azimuthal directions and peaked at $St = 45$, with a distinct additional oval shape in the downstream direction. In contrast, in the suction and blowing scenario, the spanwise coherent T-S waves and the presence of a separation bubble disrupted both velocity and pressure fields near the trailing edge on the airfoil pressure side. The acoustic radiation was characterized by a dipolar directivity pattern and an overall increase in SPL in a harmonic manner, being called laminar boundary layer vortex shedding noise. Comprehensive descriptions of flow phenomena, which draw connections from aerodynamic flow quantities as near-wall acoustic sources to far-field noise, are believed to be essential. This work will be useful for accurate predictions of airfoil noise, the development of innovative tripping mechanisms, and the analysis of flow-induced noise sources in comparable flow regimes.

- *Cross-spectrum Method for Acoustic Source Identification and Visualization*

To identify the origin of noise sources and understand sound production mechanisms, a cross-spectrum method with three distinct formulations – $S_{xx}\exp(\mathrm{i}\phi_{xy})$, S_{xy}, and $S_{xy} - S_{xx}$ – was proposed. The formulation $S_{xy} - S_{xx}$ in both linear and logarithmic scales has been found to be highly effective in extracting sound magnitude and phase characteristics, providing detailed coherent turbulent convection near the wall and the propagation of acoustic waves originating from both the leading and trailing edges. The cross-spectrum method has shown its potential by detecting the acoustic source and propagation that are on par with or surpass those of DMD and SPOD modes. A crucial aspect to consider when using this method is its reliance on the chosen reference point. This reliance underscores the importance of conducting a preliminary assessment of flow characteristics at each potential reference point to ensure the accuracy of physical interpretations. For instance, arbitrarily placing the reference point—especially when users are unaware of potential noise sources—can lead to discrepancies in near-field sound magnitude variations (as derived from the cross-spectrum method) across frequencies, compared to the far-field sound spectrum obtained from the FW-H formulation. However, the flexibility to position the reference point anywhere, such as near the leading edge or trailing edge, enables the identification of the dominant acoustic source at specific frequencies. This strategic placement can be instrumental in isolating and analyzing specific aerodynamic noises. The cross-spectrum method is free of matrix-size-dependent calculation because of its simple algorithm for calculating the power spectrum at a single point. This aspect renders the cross-spectrum method more efficient and practical, especially for practitioners dealing with large-scale datasets or complex systems.

- *Airfoil Noise Mitigation With a Sweep Angle*

The flow and acoustic fields were analyzed to examine governing mechanisms of noise mitigation when the flow was misaligned, equal to the flow physics in the swept airfoil. Amiet's swept trailing-edge noise theory was additionally employed to cross-examine it with numerical results. The flow misalignment was found to reduce noise compared to the straight airfoil, but the extent of noise reduction magnitude across the broadband range did not correlate with simply reducing the Mach number in the absence of spanwise crossflow. The flow misalignment generated the spanwise anti-phase coherent flow convection. This was the main driver for increasing the destructive interference in both chordwise and spanwise directions, ultimately reducing radiation efficiency across the entire frequency range. The generation dispersion relation between convective phase speed, wavenumber, and angular frequency accounting for the sweep angle was derived, which was utilized to show the reduced hydrodynamic WPS with misaligned flow. When misaligned flow was considered in Amiet's model, the destructive interference was found to be a distinct pattern related to the reduced noise with increasing flow misalignment. However, the spanwise phase interference observed in the LES was absent in the analytical approach. This work, which scrutinizes the noise reduction mechanism achieved through misaligned flow, is anticipated to make a significant contribution to designing a novel device to attenuate airfoil broadband noise. As misaligned flow is a simplified flow pattern observed in serrated geometries and the straight but rotating blade undergoing the Coriolis effect, this work is anticipated to be utilized to understand more complex flow and acoustic fields. Additionally, discovered flow physics, such as the behavior of spanwise coherent flows and phase topologies with the generalized dispersion relation, is anticipated to advance the physics-based analytical modeling.

- *Airfoil Noise Mitigation With Trailing-edge Morphing*

The effects of trailing-edge morphing on the aerodynamic and aeroacoustic performances were studied at a Reynolds number of 6×10^5, a Mach number of 0.088, and angles of attack of 0° and 4°, respectively. The baseline configuration was a NACA 0018 airfoil, which was morphed symmetrically into two distinct shapes: a concave shape (M1) and a convex shape (M2), each parameterized by the boat-tail angle. The M1 airfoil demonstrated enhanced performance in both aerodynamics and aeroacoustics. Its superior performance is attributed to the concave morphing of the airfoil, which promotes stable attached flows driven by FPG, reducing OASPL by up to 2 dBA compared to the baseline. The concave morphing not only reduced noise but also improved lift performance, making it a compelling option for applications. On the other hand, the M2 airfoil showed deteriorated performance in both aerodynamics and aeroacoustics compared to the baseline airfoil. The primary cause of the degradation was the development of APG flows and subsequent localized flow separations developed under a convex shape near the trailing edge. The flow feature influenced the amplification of the low-frequency noise, which is a significant characteristic of the M2 airfoil's noise profile. Consequently, OASPL was found to increase up to 2.6 dBA although noise reduced at high frequencies. Aerodynamically, the M2 airfoil showed a 24.8% decrease in the lift-to-drag ratio. This emphasizes that the convex shape induces APG-induced flow separations, negatively impacting aerodynamic efficiency and noise characteristics. The localized morphed effect affected the accuracy of the low-fidelity noise predictions compared to the FW-H acoustic analogy. In the trimmed flight condition, M1's airfoil performance in aerodynamics and aeroacoustics was much more performant than the baseline and M2 airfoils.

7.2 Contributions

This thesis advances our understanding of flow physics governing airfoil noise production and mitigation under turbulent boundary layer flows. The key contributions from each research work are summarized as follows:

- Unveiled purely physical aspects of airfoil noise generation and propagation in numerical simulations by identifying and eliminating numerical or background noise using the wavelet denoising algorithm.
- Uncovered distinct characteristics of hydrodynamic (incident) and acoustic (scattered) pressures on the wall, near the wall, and at the far field using the wavenumber-frequency decomposition.
- Clarified complex aerodynamic and aeroacoustic phenomena on different transition mechanisms characterized by boundary-layer tripping under APG flows.
- Presented cross-spectrum method capable of visualizing acoustic source and propagation while simultaneously providing the spectral magnitude and phase topologies.
- Revealed the noise reduction mechanisms when the flow is misaligned by discovering critical flow physics and suggested the possible improvements of model-based prediction accuracy.
- Studied morphed airfoils and attenuated noise levels while improving lift force by clarifying the flow features impacting aerodynamic and aeroacoustic performances.

7.3 Recommendations for Future Work

- Leverage the wavelet technique to isolate acoustic pressure in airfoil noise

If statistical or spectral characteristics of acoustic pressure are identified, the wavelet technique can be utilized to isolate acoustic pressure from the wall-bounded turbulent flows. This idea has never been approached, so it has significant research potential. It is expected to enhance the understanding of near-wall acoustic physics involving propagation within turbulent flows.

- Consider spanwise wavenumber in wavenumber-frequency decomposition

This thesis applied the wavenumber-frequency decomposition in the streamwise direction only. If the spanwise wavenumber is incorporated in the decomposition, it is expected to enhance our understanding of the noise reduction mechanisms by directly quantifying hydrodynamic and acoustic pressures under both streamwise and spanwise varying flows. This can be utilized in more complex airfoil geometry, such as serrated airfoils.

- Apply the sweep angle and morphed effect to the blade with rotational motion.

The sweep angle can be applied to the rotating blade. It was verified that radiation efficiency is alleviated across the misaligned flow in the swept airfoil, which can be utilized to mitigate various noise sources, including blade-wake interaction, blade-vortex interaction, and so on. When the blade is designed with the addition of a sweep angle and morphed (concave) shape, significant noise reduction is expected in all aerodynamic vehicles with lifting body configurations.

7.4 A List of Publications

- A list of journal manuscripts

1. **D. Kang**, S. Lee, D. Brouzet, and S. K. Lele, "Wavelet-based Pressure Decomposition for Airfoil Noise in low Mach Number Flows," *Physics of Fluids*, Vol. 35, pp. 075112, 2023 [191]. (Chapter 3)
2. **D. Kang** and S. Lee, "On the Role of Hydrodynamic and Acoustic Pressures in Trailing-edge Noise Using Numerical and Analytical Approaches," Under Review [208]. (Chapter 3)
3. **D. Kang** and S. Lee, "Aerodynamic and Aeroacoustic Effects of Different Transition Mechanisms on an Airfoil," *AIAA Journal*, Vol. 62, No. 4, pp. 1517–1535, 2024 [195]. (Chapter 4)
4. **D. Kang** and S. Lee, "Cross-Spectrum Method for Acoustic Source Identification and Visualization of Airfoil Noise," *Aerospace Science Technology*, pp. 109278, 2024 [209]. (Chapter 5)
5. **D. Kang** and S. Lee, "Effect of Misaligned Flow on Trailing-edge Noise," Under Review [210]. (Chapter 6)
6. **D. Kang** and S. Lee, "Effect of Trailing-edge Curvature on Noise Source and Radiation Characteristics of an Airfoil," In Preparation [211]. (Chapter 6)

- A list of conference papers

1. **D. Kang** and S. Lee, "Application of Wavelet Analysis to Trailing-edge Noise," 28th AIAA/CEAS Aeroacoustics Conference, Southampton, UK, June 14-17, 2022 [156]. (Chapter 3)

2. **D. Kang** and S. Lee, “Assessment of Wavelet-based Separation Algorithms on Turbulent Boundary Layer Trailing-edge Noise Prediction,” 11th International Conference on Computational Fluid Dynamics, Maui, Hawaii, July 11-15, 2022 [212]. (Chapter 3)
3. S. Lee, **D. Kang**, D. Brouzet, and S. K. Lele, “Airfoil Trailing-Edge Noise Source Identification Using Large-Eddy Simulation and Wavelet Transform,” Proceedings of the 2022 Center for Turbulence Research Summer Program, 2022 [213]. (Chapter 3)
4. **D. Kang** and S. Lee, “On the Effect of Boundary-layer Tripping for Trailing-edge Noise Predictions,” AIAA SciTech Forum, National Harbor, MD, Jan 23-27, 2023 [194]. (Chapter 4)
5. **D. Kang** and S. Lee, “A Revisit of Amiet’s Trailing-edge Noise Theory through Large-Eddy Simulations,” AIAA Aviation Forum, San Diego, CA, June 12-16, 2023 [140]. (Chapter 3)
6. **D. Kang** and S. Lee, “A New Acoustic Source Identification and Visualization Method for Airfoil Noise Using Large-Eddy Simulations,” AIAA SciTech Forum, Orlando, FL, Jan 8-12, 2024 [214]. (Chapter 5)
7. **D. Kang** and S. Lee, “Numerical and Analytical Investigations on Airfoil Noise Reduction with a Sweep Angle,” 30th AIAA/CEAS Aeroacoustics Conference, Rome, Italy, June 4-7, 2024 [215]. (Chapter 6)
8. **D. Kang** and S. Lee, “Aeroacoustic Study of Morphed Trailing-Edge Airfoils Using Large-Eddy Simulations,” 12th International Conference on Computational Fluid Dynamics, Kobe, Japan, July 14-19, 2024 [216]. (Chapter 6)
9. **D. Kang** and S. Lee, “Aerodynamic and Aeroacoustic Investigations of a NACA 0018 Airfoil with Morphed Trailing Edges,” Extended Abstract submitted [217]. (Chapter 6)

Appendix A

Amiet's Trailing-edge Noise Theory with Straight Flows

Amiet [6, 34, 35] developed a model for trailing-edge noise in uniform flow, considering a flat plate or a thin airfoil within a source coordinate system (X, Y, Z). Each axis coordinate is normalized by half the chord length, denoted as b, oriented in the streamwise, spanwise, and wall-normal directions. The airfoil streamwise extends from -2 to 0, and the origin of the source coordinate is at the trailing edge. The incident pressure field upstream of the trailing edge in the frequency domain is represented as follows:

$$g_o(X, Y, \omega) = \mathrm{e}^{-\mathrm{i}(\alpha\bar{K}X + \bar{K}_2 Y) + \epsilon\alpha\bar{K}X}, \tag{A.1}$$

where $\alpha = U_\infty/U_c$, $\bar{K} = Kb$ with $K = \omega/U_\infty$, $\bar{K}_2 = K_2 b$ with $K_2 = \omega y/(c_o S_o)$. Here, S_0 is $\sqrt{x_1^2 + \beta^2(x_2^2 + x_3^2)}$ for the observer located at (x_1, x_2, x_3), $\beta^2 = 1 - M^2$, $M = U_\infty/c_o$, c_o is the speed of sound, and ω is the angular frequency. The parameters U_∞ and U_c are the freestream velocity and turbulence convection velocity, the latter approximately being $0.8U_\infty$, consistent with the wavenumber-frequency decomposition (Sec. 2.3.2). In this paper, $K_2 = 0$. The parameter ϵ is used as an exponential convergence factor, designed to maintain the incident pressure at the trailing edge while causing it to exponentially diminish towards the leading edge [35, 139]. In this context, the value of the exponential convergence factor ϵ is set to 0.01. Importantly, the ultimate solution produced by Amiet's model is not significantly affected by the specific choice of this value. The scattered pressure is determined using Schwarzschild's solution, which satisfies the Kutta condition, and it is expressed as follows:

$$g_s(X, Y, \omega) = \mathrm{e}^{-\mathrm{i}\alpha\bar{K}X}[(1+\mathrm{i})E^*(-[\alpha\bar{K} + \bar{\kappa} + M\bar{\mu}]X) - 1], \tag{A.2}$$

where E^* is the complex error function defined as:

$$E^*(x) = \int_0^x \frac{\mathrm{e}^{-\mathrm{i}t}}{\sqrt{2\pi t}}\mathrm{d}t = C_2(x) - \mathrm{i}S_2(x). \tag{A.3}$$

In this equation, C_2 and S_2 are Fresnel integrals [141]. Here, $\bar{\kappa}^2 = \bar{\mu}^2 - \frac{\bar{K}_2^2}{\beta^2}$ with $\bar{\mu} = \bar{K}M/\beta^2$.

A.1 Aeroacoustic Transfer Functions

The aeroacoustic transfer function is derived by integrating the incident pressure and the scattered pressure from the leading edge to the trailing edge, utilizing the following equation:

$$\mathcal{L}(\vec{x}, \omega) = \int_{-2}^{0} g(X, Y, \omega)\mathrm{e}^{-\mathrm{i}\bar{\mu}\left(M - \frac{x_1}{S_0}\right)X}\,\mathrm{d}X, \tag{A.4}$$

where $\vec{x}$ denotes the vector of the observer coordinate system.

The aeroacoustic transfer function for the incident pressure is given by

$$\mathcal{L}_o(\vec{x}, \omega) = -\frac{1}{4\mathrm{i}C}, \tag{A.5}$$

where $C = \bar{K}_1 - \bar{\mu}\left(\frac{x_1}{S_0} - M\right)$.

The exact solution of the aeroacoustic transfer function for the scattered pressure can be obtained as

$$\mathcal{L}_s(\vec{x},\omega) = -\frac{\mathrm{e}^{2\mathrm{i}C}}{\mathrm{i}C}\left((1+\mathrm{i})\mathrm{e}^{-2\mathrm{i}C}\sqrt{\frac{B}{B-C}}E^*[2(B-C)] - (1+\mathrm{i})E^*[2B] + 1 - \mathrm{e}^{-2\mathrm{i}C}\right), \tag{A.6}$$

where $B = \bar{K}_1 + M\bar{\mu} + \bar{\kappa}$ with $\bar{K}_1 = \alpha\bar{K}$.

A.2 Far-field Acoustic Spectrum

The computation of the far-field acoustic spectrum radiated by the sound source is accomplished through the cross spectrum of Curle's acoustic analogy [87], which relates it to the surface pressure fields. The far-field spectrum at the observer location is expressed as follows:

$$S_{pp}(\vec{x},\omega) = 4\left(\frac{KMx_3b}{2\pi S_0^2}\right)^2 \frac{S}{2}|\mathcal{L}_o + \mathcal{L}_s|^2 l_y(\omega,k_y)S_{qq}(\omega), \tag{A.7}$$

where S stands for the airfoil span and S_{qq} is the wall pressure spectrum near the trailing edge. The parameter l_y is the spanwise correlation length near the trailing edge, which is calculated by Corcos' model [218] as follows:

$$l_y(\omega,k_y) = \frac{\omega/(b_cU_c)}{k_y^2 + \omega^2/(b_cU_c)^2}, \tag{A.8}$$

where $b_c = 1.0$ in this paper. It is worth noting that Eq. (A.7) yields a magnitude that is four times that of Amiet's original model [34]. This is because the scattering taking place on one side of an airfoil affects both sides [81, 142]. However, it is important to recognize that the incident field should not be influenced by the trailing-edge boundary condition or the Kutta condition. To address this, Li and Lee [11] introduced a correction to Eq. (A.5), dividing it by a factor of four. This modified equation is utilized in our analysis.

Appendix B

Sensitivity of Different Wavelet Kernels

In order to demonstrate that the results presented in the paper are independent of the choice of wavelet kernels, three different wavelet kernels are tested on the suction side of the airfoil at $x/c = 0.99$: Daubechies-12, Coiflets-5, and Symlets-8. Figure B.1 shows that different levels of iterations are observed in the convergence rate depending on the choice of wavelet kernels. However, all the kernels ultimately converge to the same order of the ratio of the number of incoherent wavelet coefficients to the total number of wavelet coefficients and threshold level. The number of iterations, converged ratio, and threshold level are tabulated in Table B.1 for the three different wavelet kernels.

Table B.1: The number of iterations, converged ratio, and threshold level for different wavelet kernels.

Wavelet kernel	Iterations	$N_{w,i}/N_{w,tot}$	Threshold level
Daubechies-12	14	0.969754	0.148615
Coiflets-5	11	0.969336	0.148018
Symlets-8	11	0.968839	0.148216

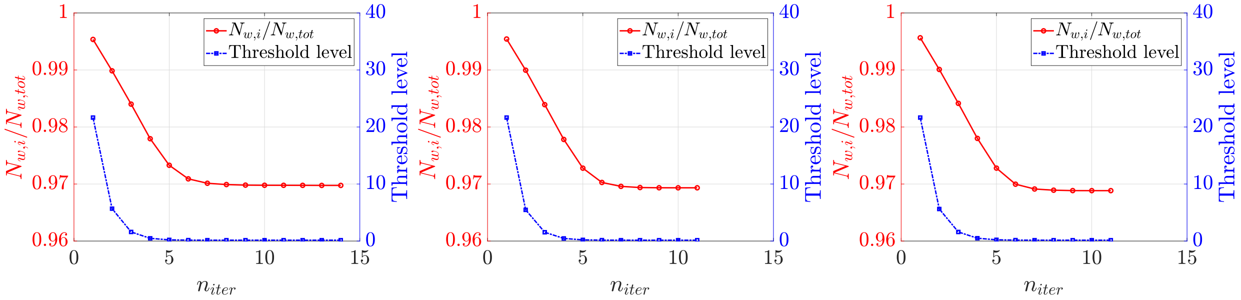

(a) (b) (c)

Figure B.1: Convergence of the ratio of the number of incoherent wavelet coefficients to the total number of the wavelet coefficients and the threshold level measured on the suction side of the airfoil at $x/c = 0.99$ for different wavelet kernels: (a) Daubechies-12, (b) Coiflets-5, and (c) Symlets-8.

The polar evolution of PDFs for the different wavelet kernels at $x/c = 0.99$ is plotted in Fig. B.2. It is shown that the statistical characteristics previously presented for decomposed pressures remain independent of the wavelet kernel chosen. Figure B.3 displays the wall pressure spectra using the different wavelet kernels at $x/c = 0.99$. It is shown that both the magnitude of the decomposed pressures and the transition of energy spectral contribution between coherent and incoherent pressures are independent of the choice of wavelet kernel.

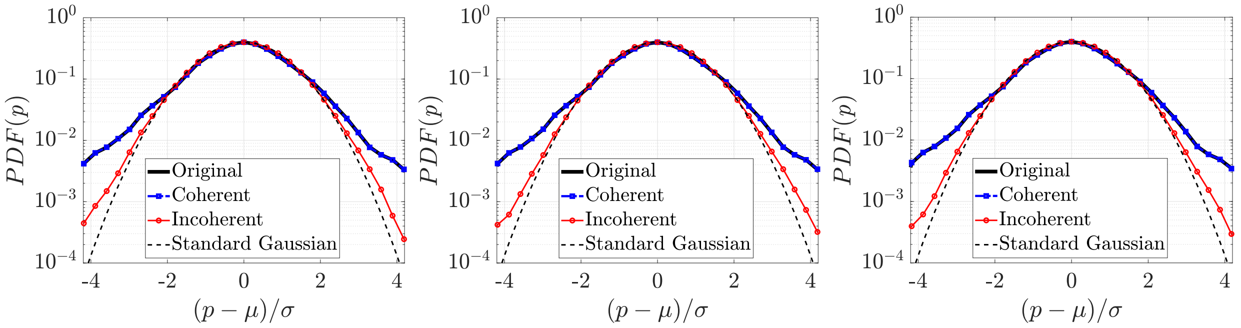

(a) (b) (c)

Figure B.2: Polar evolution of PDFs for the original, coherent, and incoherent pressures with standard distribution at $x/c = 0.99$ for different wavelet kernels: (a) Daubechies-12, (b) Coiflets-5, and (c) Symlets-8.

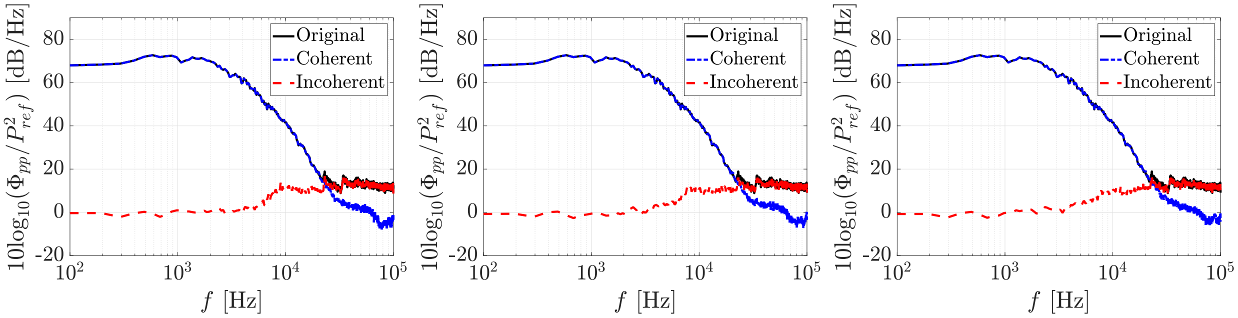

(a)

(b)

(c)

Figure B.3: Wall pressure spectra of the original, coherent, and incoherent pressures calculated from the wavelet-based decomposition at $x/c = 0.99$ using different wavelet kernels: (a) Daubechies-12, (b) Coiflets-5, and (c) Symlets-8.

Appendix C

Empirical Correlation Model

The Smol'yakov model [169] is formulated under as

$$l_x(\omega) = \frac{U_c}{\alpha_x \omega} A^{-1}, \tag{C.1}$$

with

$$A = \left[1 - \frac{\beta U_c}{\omega \delta^*} + \left(\frac{\beta U_c}{\omega \delta^*} \right)^2 \right]^{1/2}. \tag{C.2}$$

Here, α_x=0.124 and β=0.25. The convection velocity is defined as

$$\frac{U_c(\omega)}{U_0} = \frac{1.6\omega\delta^*/U_0}{1 + 16(\omega\delta^*/U_0)^2} + 0.6. \tag{C.3}$$

The displacement thickness, δ^*, is calculated from the LES at $x/c = 0.996$.

Figure C.1 illustrates the streamwise correlation lengths for integration along the resolved flow field, as expressed in Eq. (3.7), and the Smol'yakove model. The agreement between these two models validates the current integral approach for calculating the correction length under non-homogeneous turbulent flows over the finite chord.

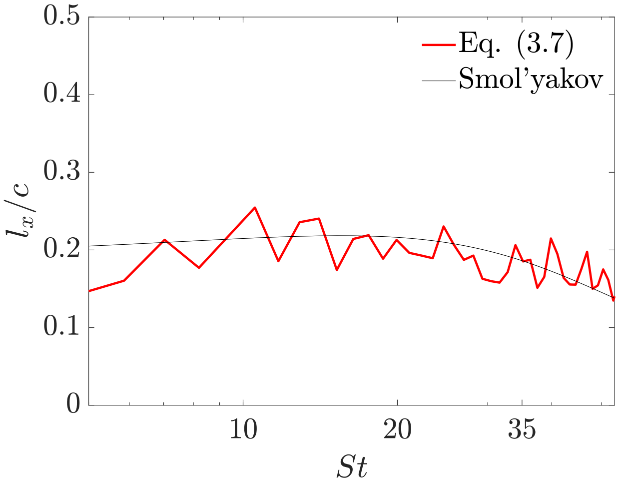

Figure C.1: Streamwise correlation lengths for Eq. (3.7) and Smol'yakov model.

Appendix D

Statistical Equilibrium of Flow Snapshots for DMD Analysis

The discrete-time eigenvalues associated with frequencies of interest are depicted on a unit circle in Fig. D.1. A zero real part of the eigenvalue, namely $St \approx 0$, represents the stationary mode, indicating that the flow field is neither growing nor decaying over time [162]. The stationary DMD mode is contrasted with the time-averaged pressure field for three cases to confirm that the sampled flow snapshots are in a state of statistical equilibrium, as demonstrated in Fig. D.2. The pressure field of the stationary mode, represented by the eigenvector, is a different quantity from the time-averaged pressure profile, so color scales are excluded for a qualitative comparison. The time-averaged pressure field demonstrates strong suction over the leading-edge curvature on the suction side, while the stagnation point is positioned near the leading edge on the pressure side. This is quite similar to the stationary DMD mode for the three cases, thus verifying that the number of flow snapshots is adequate for calculating eigenvalues and DMD modes [162].

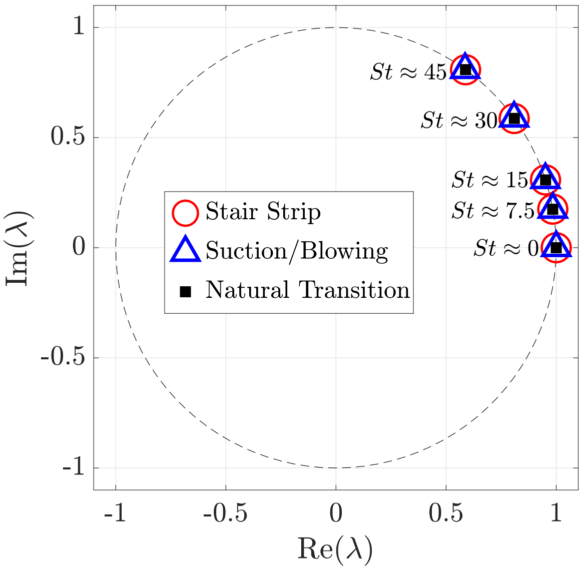

Figure D.1: Eigenvalues of DMD modes for three cases.

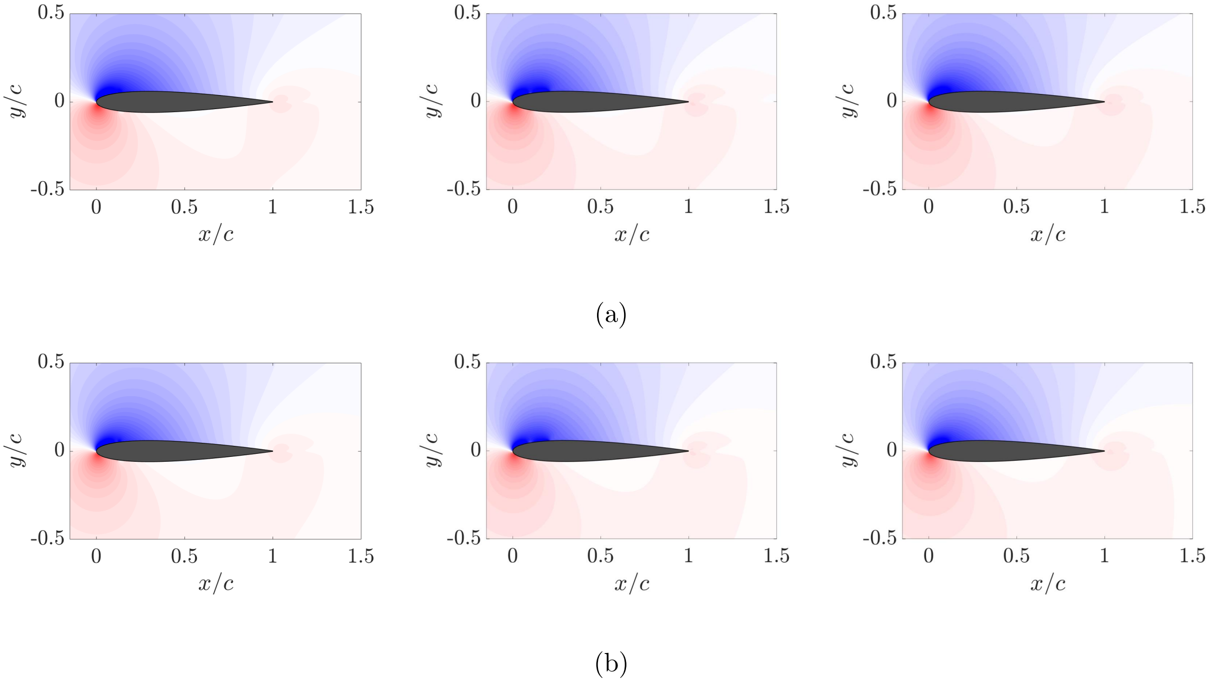

(a)

(b)

Figure D.2: (a): Time-averaged pressure field and (b): stationary DMD mode, $St \approx 0$. The blue and red colors denote the lower and higher values, respectively. The left, mid, and right columns denote the stair strip, suction and blowing, and natural transition, respectively.

References

[1] Johnson, W., and Silva, C., "NASA Concept Vehicles and the Engineering of Advanced Air Mobility Aircraft," *CEAS Aeronautical Journal*, Vol. 126, No. 1295, 2021, pp. 59–91.

[2] Jia, Z., and Lee, S., "Computational Study on Noise of Urban Air Mobility Quadrotor Aircraft," *Journal of the American Helicopter Society*, Vol. 67, 2022, p. 012009.

[3] Jia, Z., and Lee, S., "High-Fidelity Computational Analysis on the Noise of a Side-by-Side Hybrid VTOL Aircraft," *Journal of the American Helicopter Society*, Vol. 67, 2022, p. 022005.

[4] Holden, J., and Goel, N., "Fast-Forwarding to a Future of On-Demand Urban Air Transportation," *Uber Elevate*, 2016.

[5] Brooks, T. F., Pope, D. S., and Marcolini, M. A., "Airfoil Self-Noise and Prediction," NASA RP 1218, 1989.

[6] Amiet, R. K., "Noise Due to Turbulent Flow Past a Trailing Edge," *Journal of Sound and Vibration*, Vol. 47, 1976, pp. 387–393.

[7] Sandberg, R. D., Sandham, N. D., and Joseph, P. F., "Direct Numerical Simulations of Trailing-edge Noise Generated by Boundary-Layer Instabilities," *Journal of Sound and Vibration*, Vol. 304, 2007, pp. 677–690.

[8] Sandberg, R. D., and Jones, L. E., "Direct Numerical Simulations of Low Reynolds Number Flow Over Airfoils With Trailing-edge Serrations," *Journal of Sound and Vibration*, Vol. 330, 2011, pp. 3818–3831.

[9] Sandberg, R. D., and Sandham, N. D., "Direct Numerical Simulation of Turbulent Flow Past a Trailing Edge and the Associated Noise Generation," *Journal of Fluid Mechanics*, Vol. 596, 2008, pp. 353–385.

[10] Lee, S., Ayton, L., Bertagnolio, F., Moreau, S., Chong, T., and Joseph, P., "Turbulent Boundary Layer Trailing-edge Noise: Theory, Computation, Experiment, and Application," *Progress in Aerospace Sciences*, Vol. 126, 2021, p. 100737.

[11] Li, S., and Lee, S., "Prediction of Urban Air Mobility Multi-Rotor VTOL Broadband Noise Using UCD-QuietFly," *Journal of the American Helicopter Society*, Vol. 66, 2021, p. 032004.

[12] Li, S., and Lee, S., "Acoustic Analysis and Sound Quality Assessment of a Quiet Helicopter for Air Taxi Operations," *Journal of the American Helicopter Society*, Vol. 67, 2022, p. 032001.

[13] Pröbsting, S., and Yarusevych, S., "Laminar Separation Bubble Development on an Airfoil Emitting Tonal Noise," *Journal of Fluid Mechanics*, Vol. 780, 2015, pp. 167–191.

[14] Tam, C. K., *Computational Aeroacoustics: A Wave Number Approach*, Vol. 33, Cambridge University Press, Cambridge, U.K., 2012.

[15] Wang, M., and Moin, P., "Computation of Trailing-edge Flow and Noise Using Large-eddy Simulation," *AIAA Journal*, Vol. 38, No. 12, 2000, pp. 2201–2209.

[16] Wagner, C., Hüttl, T., and Sagaut, P., *Large-Eddy Simulation for Acoustics*, Vol. 20, Cambridge University Press, Cambridge, U.K., 2007.

[17] Wolf, W. R., Azevedo, J. L., and Lele, S. K., "Convective Effects and the Role of Quadrupole Sources for Aerofoil Aeroacoustics," *Journal of Fluid Mechanics*, Vol. 708, 2012, pp. 502–538.

[18] Bodling, A., and Sharma, A., "Numerical Investigation of Noise Reduction Mechanisms In a Bio-Inspired Airfoil," *Journal of Sound and Vibration*, Vol. 453, 2019, pp. 314–327.

[19] Turner, J. M., and Kim, J. W., "Quadrupole Noise Generated from a Low-Speed Aerofoil in Near-and Full-Stall Conditions," *Journal of Fluid Mechanics*, Vol. 936, 2022, pp. 1–27.

[20] Moreau, S., "The Third Golden Age of Aeroacoustics," *Physics of Fluids*, Vol. 34, 2022, p. 031301.

[21] Sandberg, R. D., Jones, L. E., Sandham, N. D., and Joseph, P. F., "Direct Numerical Simulations of Tonal Noise Generated by Laminar Flow Past Airfoils," *Journal of Sound and Vibration*, Vol. 320, 2009, pp. 838–858.

[22] Jones, L. E., Sandberg, R. D., and Sandham, N. D., "Direct Numerical Simulations of Forced and Unforced Separation Bubbles on an Airfoil at Incidence," *Journal of Fluid Mechanics*, Vol. 602, 2008, pp. 175–207.

[23] Ffowcs-Williams, J. E., and Hall, L. H., "Aerodynamic Sound Generation by Turbulent Flow in the Vicinity of a Scattering Half Plane," *Journal of Fluid Mechanics*, Vol. 40, 1970, pp. 657–670.

[24] Cesar, L. M., Jawahar, H. K., and Azarpeyvand, M., "Airfoil Trailing-edge Noise Reduction Using Flow Suction," *2018 AIAA/CEAS Aeroacoustics Conference*, Atlanta, GA, 2018, p. 2814. Jun. 25–29, AIAA Paper No. 2018–2814.

[25] Shi, Y., and Lee, S., "Airfoil Trailing Edge Noise Reduction Using a Boundary-Layer Bump," *Acta Acustica united with Acustica*, Vol. 105, No. 5, 2019, pp. 814–826.

[26] Avallone, F., Van Der Velden, W. C. P., Ragni, D., and Casalino, D., "Noise Reduction Mechanisms of Sawtooth and Combed-Sawtooth Trailing-Edge Serrations," *Journal of Fluid Mechanics*, Vol. 848, 2018, pp. 560–591.

[27] Shi, Y., and Lee, S., "Numerical Study of 3-D Finlets Using RANS CFD for Trailing Edge Noise Reduction," *International Journal of Aeroacoustics*, Vol. 19, No. 1–2, 2020, pp. 95–118.

[28] Wei, Z., Wang, S., Farris, S., Chennuri, N., Wang, N., Shinsato, S., and Gu, G. X., “Towards Silent and Efficient Flight by Combining Bioinspired Owl Feather Serrations with Cicada Wing Geometry,” *Nature Communications*, Vol. 15, No. 1, 2024, p. 4337.

[29] Jiang, C., Moreau, D., de Silva, C., and Doolan, C., “Noise Generation Mechanisms of a Micro-Tube Porous Trailing Edge,” *Journal of Sound and Vibration*, Vol. 571, 2024, p. 118085.

[30] Teruna, C., Avallone, F., Ragni, D., Rubio-Carpio, A., and Casalino, D., “Numerical Analysis of a 3-D Printed Porous Trailing Edge for Broadband Noise Reduction,” *Journal of Fluid Mechanics*, Vol. 926, 2021, p. A17.

[31] Chapman, D. R., “Computational Aerodynamics Development and Outlook,” *AIAA Journal*, Vol. 17, 1979, pp. 1293–1313.

[32] Chapman, D. R., “Large Eddy Simulations: How to Evaluate Resolution,” *International Journal of Heat and Fluid Flow*, Vol. 30, 2009, pp. 1016–1025.

[33] Brouzet, D., “Investigation of Direct Combustion Noise in Turbulent Premixed Jet Flames Using Direct Numerical Simulations,” *The University of Melbourne*, 2020.

[34] Amiet, R. K., “Acoustic Radiation from an Airfoil in a Turbulent Stream,” *Journal of Sound and Vibration*, Vol. 41, No. 4, 1975, pp. 407–420.

[35] Amiet, R. K., “Effect of the Incident Surface Pressure Field on Noise due to Turbulent Flow past a Trailing Edge,” *Journal of Sound and Vibration*, Vol. 57, No. 2, 1978, pp. 305–306.

[36] Howe, M. S., “A Review of the Theory of Trailing-edge Noise,” *Journal of Sound and Vibration*, Vol. 61, No. 3, 1978, pp. 437–465.

[37] Terracol, M., Manoha, E., Herrero, C., Labourasse, E., and Redonnet, S., “Hybrid Methods for Airframe Noise Numerical Prediction,” *Theoretical and Computational Fluid Dynamics*, Vol. 19, 2005, pp. 197–227.

[38] Tinney, C. E., and Jordan, P., “The Near Pressure Field of Co-Axial Subsonic Jets,” *Journal of Fluid Mechanics*, Vol. 611, 2008, pp. 175–204.

[39] White, F. M., and Majdalani, J., *Viscous Fluid Flow*, third ed., McGraw-Hill, New York, 2006, Chap. 5.

[40] Dos Santos, F., Even, N. A., Botero-Bolvar, L., Venner, C. H., and Santana, L., “Influence of Surface Roughness Geometry on Trailing Edge Wall Pressure Fluctuations and Noise,” *AIAA Aviation Forum*, Virtual Event, 2021, p. 2294. Aug 2–6, AIAA Paper No. 2021–2294.

[41] Carolus, T., and Beiler, M., “Skewed Blades in Low Pressure Fans-A Survey of Noise Reduction Mechanisms,” *3rd AIAA/CEAS Aeroacoustics Conference*, Atlanta, GA, 1997, p. 1591. May. 12–14, AIAA Paper No. 1997–1591.

[42] Envia, E., and Nallasamy, M., "Design Selection and Analysis of a Swept and Leaned Stator Concept," *Journal of Sound and Vibration*, Vol. 228, No. 4, 1999, pp. 793–836.

[43] Casalino, D., Diozzi, F., Sannino, R., and Paonessa, A., "Aircraft Noise Reduction Technologies: A Bibliographic Review," *Aerospace Science and Technology*, Vol. 12, No. 1, 2008, pp. 1–17.

[44] Krömer, F. J., "Sound Emission of Low-Pressure Axial Fans Under Distorted Inflow Conditions," *FAU University Press*, 2018.

[45] Grasso, G., Roger, M., and Moreau, S., "Analytical Model of the Source and Radiation of Sound from the Trailing Edge of a Swept Airfoil," *Journal of Sound and Vibration*, Vol. 493, 2021, p. 115838.

[46] Ghodake, D., Sanjosé, M., Moreau, S., and Henner, M., "Effect of Sweep on Axial Fan Noise Sources Using the Lattice Boltzmann Method," *International Journal of Turbomachinery, Propulsion and Power*, Vol. 7, No. 4, 2022, p. 34.

[47] Grasso, G., Roger, M., and Moreau, S., "Effect of Sweep Angle and of Wall-Pressure Statistics on the Free-Field Directivity of Airfoil Trailing-Edge Noise," *25th AIAA/CEAS Aeroacoustics Conference*, Delft, The Netherlands, 2019, p. 2612. May. 20–23, AIAA Paper No. 2019–2612.

[48] Crighton, D. G., and Leppington, F. G., "On the Scattering of Aerodynamic Noise," *Journal of Fluid Mechanics*, Vol. 46, No. 3, 1971, pp. 577–597.

[49] Spiropoulos, M. I., Margnat, F., Valeau, V., and Jordan, P., "Acoustics of Turbulent Eddies Impinging on a Semi-Infinite Rigid Wedge," *AIAA Aviation Forum*, San Diego, CA, 2023, p. 3509. Jun. 12–16, AIAA Paper No. 2023–3509.

[50] Jawahar, H. K., Vemuri, S. S., and Azarpeyvand, M., "Aerodynamic Noise Characteristics of Airfoils with Morphed Trailing Edges," *International Journal of Heat and Fluid Flow*, Vol. 93, 2022, p. 108892.

[51] Watkins, J., and Bouferrouk, A., "The Effects of a Morphed Trailing-Edge Flap on the Aeroacoustic and Aerodynamic Performance of a 30P30N Aerofoil," *Acoustics*, Vol. 4, No. 1, 2022, pp. 248–267.

[52] Casari, N., Fadiga, E., Oliani, S., Piovan, M., Pinelli, M., and Suman, A., "Low-Noise Airfoils for Turbomachinery Applications: Two Examples of Optimization," *International Journal of Turbomachinery, Propulsion and Power*, Vol. 9, No. 1, 2024.

[53] Jawahar, H. K., Ai, Q., and Azarpeyvand, M., "Experimental and Numerical Investigation of Aerodynamic Performance for Airfoils with Morphed Trailing Edges," *Renewable Energy*, Vol. 127, 2018, pp. 355–367.

[54] Bashir, M., Zonzini, N., Martel, S. L., Botez, R. M., Ceruti, A., and Wong, T., "Numerical Investigation of the Dynamic Stall Reduction on the UAS-S45 Aerofoil Using

the Optimised Aerofoil Method," *The Aeronautical Journal*, Vol. 128, No. 1321, 2024, pp. 441–468.

[55] Bashir, M., Negahban, M. H., Botez, R. M., and Wong, T., "Numerical Simulation of the Transient Flow around the Combined Morphing Leading-Edge and Trailing-Edge Airfoil," *Biomimetics*, Vol. 9, No. 2, 2024, p. 109.

[56] Schneider, K., Farge, M., Pellegrino, G., and Rogers, M. M., "Coherent Vortex Simulation of Three-Dimensional Turbulent Mixing Layers Using Orthogonal Wavelets," *Journal of Fluid Mechanics*, Vol. 534, 2005, pp. 39–66.

[57] Schneider, K., Ziuber, J., Farge, M., and Azzalini, A., "Coherent Vortex Extraction and Simulation of 2D Isotropic Turbulence," *Journal of Turbulence*, Vol. 7, 2006, p. N44.

[58] Okamoto, N., Yoshimatsu, K., Schneider, K., Farge, M., and Kaneda, Y., "Coherent Vortices in High Resolution Direct Numerical Simulation of Homogeneous Isotropic Turbulence: A Wavelet Viewpoint," *Physics of Fluids*, Vol. 19, 2007, p. 115109.

[59] Ruppert-Felsot, J., Farge, M., and Petitjeans, P., "Wavelet Tools to Study Intermittency: Application to Vortex Bursting," *Journal of Fluid Mechanics*, Vol. 636, 2009, pp. 427–453.

[60] Bassenne, M., Urzay, J., Schneider, K., and Moin, P., "Extraction of Coherent Clusters and Grid Adaptation in Particle-Laden Turbulence Using Wavelet Filters," *Physical Review Fluids*, Vol. 2, 2017, p. 054301.

[61] Schneider, K., and Vasilyev, O. V., "Wavelet Methods in Computational Fluid Dynamics," *Annual Review of Fluid Mechanics*, Vol. 42, No. 1, 2010, pp. 473–503.

[62] Farge, M., Schneider, K., and Kevlahan, N., "Non-Gaussianity and Coherent Vortex Simulation for Two-Dimensional Turbulence Using an Adaptive Orthogonal Wavelet Basis," *Physics of Fluids*, Vol. 11, 1999, pp. 2187–2201.

[63] Farge, M., Pellegrino, G., and Schneider, K., "Coherent Vortex Extraction in 3D Turbulent Flows Using Orthogonal Wavelets," *Physical Review Letters*, Vol. 87, 2001, p. 054501.

[64] Farge, M., Schneider, K., Pellegrino, G., Wray, A. A., and Rogallo, R. S., "Coherent Vortex Extraction in Three-Dimensional Homogeneous Turbulence: Comparison Between CVS-wavelet and POD-Fourier Decompositions," *Physics of Fluids*, Vol. 15, 2003, pp. 2886–2896.

[65] Schlegel, M., Noack, B. R., Comte, P., Kolomenskiy, D., Schneider, K., Farge, M., Luchtenburg, D. B., Scouten, J. E., and Tadmor, G., "Reduced-order Modelling of Turbulent Jets for Noise Control," *Numerical Simulation of Turbulent Flows and Noise Generation*, 2009, pp. 3–27.

[66] Nguyen van Yen, R., Farge, M., and Schneider, K., "Scale-Wise Coherent Vorticity Extraction for Conditional Statistical Modeling of Homogeneous Isotropic Two-Dimensional Turbulence," *Physica D: Nonlinear Phenomena*, Vol. 241, 2012, pp. 186–201.

[67] Mancinelli, M., Pagliaroli, T., Di Marco, A., Camussi, R., and Castelain, T., "Wavelet Decomposition of Hydrodynamic and Acoustic Pressures in the Near Field of the Jet," *Journal of Fluid Mechanics*, Vol. 813, 2017, pp. 716–749.

[68] Hajczak, A., Sanders, L., Vuillot, F., and Druault, P., "Wavelet-based Separation Methods Assessment on the Near Pressure Field of a Landing Gear Subcomponent," *25th AIAA/CEAS Aeroacoustics Conference*, Delft, The Netherlands, 2019, p. 2482. May. 20–23, AIAA Paper No. 2019–2482.

[69] Camussi, R., and Meloni, S., "On the Application of Wavelet Transform in Jet Aeroacoustics," *Fluids*, Vol. 6, 2021, p. 299.

[70] Camussi, R., Meloni, S., and Bogey, C., "On the Influence of the Nozzle Exhaust Initial Conditions on the Near Field Acoustic Pressure," *Acta Acustica*, Vol. 6, 2022, p. 57.

[71] Arndt, R. E., Long, D. F., and Glauser, M. N., "The Proper Orthogonal Decomposition of Pressure Fluctuations Surrounding a Turbulent Jet," *Journal of Fluid Mechanics*, Vol. 340, 1997, pp. 1–33.

[72] Manoha, E., Bulté, J., and Caruelle, B., "LAGOON: An Experimental Database for the Validation of CFD/CAA Methods for Landing Gear Noise Prediction," *14th AIAA/CEAS Aeroacoustics Conference*, Vancouver, British Columbia, Canada, 2008, p. 2816.

[73] Lighthill, M. J., "On Sound Generated Aerodynamically I. General Theory," *Proceedings of the Royal Society of London. Series A, Mathematical and Physical Sciences*, Vol. 211, No. 1107, 1952, pp. 564–587.

[74] Wang, M., Moreau, S., Iaccarino, G., and Roger, M., "LES Prediction of Wall-Pressure Fluctuations and Noise of a Low-Speed Airfoil," *International Journal of Aeroacoustics*, Vol. 8, No. 3, 2009, pp. 177–197.

[75] Howe, M. S., "Edge-source Acoustic Green's Function for an Airfoil of Arbitrary Chord, with Application to Trailing-edge Noise," *Quarterly Journal of Mechanics and Applied Mathematics*, Vol. 54, No. 1, 2001, pp. 139–155.

[76] Howe, M. S., "Trailing Edge Noise at Low Mach Numbers," *Journal of Sound and Vibration*, Vol. 225, No. 2, 1999, pp. 211–238.

[77] Taylor, G. I., "The Spectrum of Turbulence," *Proceedings of the Royal Society of London. Series A-Mathematical and Physical Sciences*, Vol. 164, No. 919, 1938, pp. 476–490.

[78] Lee, S., "Empirical Wall-Pressure Spectral Modeling for Zero and Adverse Pressure Gradient Flows," *AIAA Journal*, Vol. 56, No. 5, 2018, pp. 1818–1829.

[79] Lee, S., and Shum, J. G., "Prediction of Airfoil Trailing Edge Noise Using Empirical Wall Pressure Spectrum Models," *AIAA Journal*, Vol. 57, No. 3, 2019, pp. 888–897.

[80] Li, S., and Lee, S., "Prediction of Rotorcraft Broadband Trailing-edge Noise and Parameter Sensitivity Study," *Journal of the American Helicopter Society*, Vol. 65, No. 4, 2020, pp. 1–14.

[81] Roger, M., and Moreau, S., "Back-Scattering Correction and Further Extensions of Amiet's Trailing-Edge Noise Model. Part I: Theory," *Journal of Sound and Vibration*, Vol. 286, No. 3, 2005, pp. 477–506.

[82] Moreau, S., Roger, M., and Jurdic, V., "Effect of Angle of Attack and Airfoil Shape on Turbulence-Interaction Noise," *11th AIAA/CEAS Aeroacoustics Conference*, Monterey, CA, 2005, p. 3509. May. 23–25, AIAA Paper No. 2005–2973.

[83] Oberai, A. A., Roknaldin, F., and Hughes, T., "Computation of Trailing-Edge Noise Due to Turbulent Flow over an Airfoil," *AIAA Journal*, Vol. 40, No. 11, 2002, pp. 2206–2216.

[84] Khalighi, Y., Mani, A., Ham, F., and Moin, P., "Prediction of Sound Generated by Complex Flows at Low Mach Numbers," *AIAA Journal*, Vol. 48, No. 12, 2010, pp. 306–316.

[85] Martínez-Lera, P., Schram, C., Bériot, H., and Hallez, R., "An Approach to Aerodynamic Sound Prediction Based on Incompressible-Flow Pressure," *Journal of Sound and Vibration*, Vol. 333, No. 1, 2014, pp. 132–143.

[86] Martínez-Lera, P., Christophe, J., and Schram, C., "Computation of the Self-Noise of a Controlled-Diffusion Airfoil Based on the Acoustic Analogy," *International Journal of Aeroacoustics*, Vol. 16, No. 1–2, 2017, pp. 44–64.

[87] Curle, N., "The Influence of Solid Boundaries upon Aerodynamic Sound," *Proceedings of the Royal Society of London. Series A. Mathematical and Physical Sciences*, Vol. 231, No. 1187, 1955, pp. 505–514.

[88] Braslow, A. L., Harris Jr, R. V., and Hicks, R. M., "Use of Grit-Type Boundary-Layer Transition Trips on Wind-Tunnel Models," NASA RP 3579, 1966.

[89] Mabey, D. G., "A Review of Scale Effects in Unsteady Aerodynamics," *Progress in Aerospace Sciences*, Vol. 28, No. 4, 1991, pp. 273–321.

[90] Tabatabaei, N., Vinuesa, R., Rolu, R., and Schlatter, P., "Techniques for Turbulence Tripping of Boundary Layers in RANS Simulations," *Flow, Turbulence and Combustion*, Vol. 108, No. 3, 2022, pp. 661–682.

[91] Garcia-Sagrado, A., and Hynes, T., "Wall Pressure Sources Near an Airfoil Trailing

Edge Under Turbulent Boundary Layers," *Journal of Fluids and Structures*, Vol. 30, 2012, pp. 3–34.

[92] Ye, Q., Avallone, F., Ragni, D., Choudhari, M., and Casalino, D., "Effect of Surface Roughness Geometry on Boundary-Layer Transition and Far-Field Noise," *AIAA Journal*, Vol. 59, No. 7, 2021, pp. 2396–2408.

[93] Dos Santos, F. L., Sanders, M. P., Dantas de Santana, L., and H. Venner, C., "Influence of Tripping Devices in Hastening Transition in a Flat Plate Submitted to Zero and Favorable Pressure Gradients," *AIAA SciTech Forum*, Orlando, FL, 2020, p. 0046. Jan. 6–10, AIAA Paper No. 2020–0046.

[94] Dos Santos, F. L., Botero-Bolívar, L., Venner, C., and de Santana, L. D., "Influence of Roughness Trips on Near- and Far-Field Trailing-Edge Noise," *AIAA Journal*, Vol. 60, No. 10, 2022, pp. 5880–5889.

[95] Ribeiro, A. F. P., Fares, E., and Choudhari, M., "DNS of Laminar to Turbulent Transition on NACA 0012 Airfoil with Sand Grain Roughness," *10th International Conference on Computational Fluid Dynamics*, Barcelona, Spain, July 9–15, 2018.

[96] Wolf, W. R., and Lele, S. K., "Trailing-Edge Noise Predictions Using Compressible Large-Eddy Simulation and Acoustic Analogy," *AIAA Journal*, Vol. 50, No. 11, 2012, pp. 2423–2434.

[97] Bodling, A., and Sharma, A., "Implementation of the Ffowcs Williams-Hawkings Equation: Predicting the Far Field Noise From Airfoils While Using Boundary Layer Tripping Mechanisms," *Proceedings of the ASME 2018*, Montreal, Quebec, Canada, 2018.

[98] Winkler, J., Wu, H., Moreau, S., Carolus, T., and Sandberg, R. D., "Trailing-edge Broadband Noise Prediction of an Airfoil With Boundary-Layer Tripping," *Journal of Sound and Vibration*, Vol. 482, 2020, p. 115450.

[99] Powell, A., "On Aerodynamic Sound from Dilatation and Momentum Fluctuations," *Journal of the Acoustical Society of America*, Vol. 33, No. 12, 1961, pp. 1798–1799.

[100] Jones, L. E., Sandham, N. D., and Sandberg, R. D., "Acoustic Source Identification for Transitional Airfoil Flows Using Cross Correlations," *AIAA Journal*, Vol. 48, No. 10, 2010, pp. 2299–2312.

[101] Brunton, S. L., Noack, B. R., and Koumoutsakos, P., "Machine Learning for Fluid Mechanics," *Annual Review of Fluid Mechanics*, Vol. 52, No. 1, 2020, pp. 477–508.

[102] Taira, K., Brunton, S. L., Dawson, S. T., Rowley, C. W., Colonius, T., McKeon, B. J., Schmidt, O. T., Gordeyev, S., Theofilis, V., and Ukeiley, L. S., "Modal Analysis of Fluid Flows: An Overview," *AIAA Journal*, Vol. 55, No. 12, 2020, pp. 4013–4041.

[103] Towne, A., Schmidt, O. T., and Colonius, T., "Spectral Proper Orthogonal Decomposition and its Relationship to Dynamic Mode Decomposition and Resolvent Analysis,"

Journal of Fluid Mechanics, Vol. 847, 2018, pp. 821–867.

[104] Schmidt, O. T., Towne, A., Rigas, G., Colonius, T., and Brès, G. A., "Spectral Analysis of Jet Turbulence," *Journal of Fluid Mechanics*, Vol. 855, 2018, pp. 953–982.

[105] Schmidt, O. T., and Colonius, T., "Guide to Spectral Proper Orthogonal Decomposition," *AIAA Journal*, Vol. 58, No. 3, 2020, pp. 1023–1033.

[106] Schmid, P. J., "Dynamic Mode Decomposition of Numerical and Experimental Data," *Journal of Fluid Mechanics*, Vol. 656, 2010, pp. 5–28.

[107] Tu, J. H., Rowley, C. W., Luchtenburg, D. M., Brunton, S. L., and Kutz, J. N., "On Dynamic Mode Decomposition: Theory and Applications," *Journal of Computational Dynamics*, Vol. 1, 2014, pp. 391–421.

[108] Kutz, J. N., Brunton, S. L., Brunton, B. W., and Proctor, J. L., *Dynamic Mode Decomposition: Data-Driven Modeling of Complex Systems*, Society for Industrial and Applied Mathematics, Philadelphia, PA, 2016, Chaps. 1,2,8.

[109] Sano, A., Abreu, L. I., Cavalieri, A. V. G., and Wolf, W. R., "Trailing-Edge Noise from the Scattering of Spanwise-Coherent Structures," *Physical Review Fluids*, Vol. 4, 2019, p. 094602.

[110] Hu, Y. S., Wan, Z. H., Ye, C. C., Sun, D. J., and Lu, X. Y., "Noise Reduction Mechanisms for Insert-Type Serrations of the NACA-0012 Airfoil," *Journal of Fluid Mechanics*, Vol. 941, 2022, p. A57.

[111] Asada, H., and Kawai, S., "POD and DMD of Three-Dimensional Transonic Aircraft Buffet Using Large-Scale LES Data," *AIAA SciTech Forum*, Orlando, FL, 2024, p. 0494. Jan. 8–12, AIAA Paper No. 2024–0494.

[112] Schmid, P. J., "Dynamic Mode Decomposition and Its Variants," *Annual Review of Fluid Mechanics*, Vol. 54, No. 1, 2022, pp. 225–254.

[113] Giez, J., Vion, L., Roger, M., and Moreau, S., "Effect of the Edge-and-Tip Vortex on Airfoil Selfnoise and Turbulence Impingement Noise," *22nd AIAA/CEAS Aeroacoustics Conference*, Lyon, France, 2016, p. 2996. May 30–June 1, AIAA Paper No. 2019–2996.

[114] Caiazzo, A., and Desmet, W., "A Generalized Corcos Model for Modelling Turbulent Boundary Layer Wall Pressure Fluctuations," *Journal of Sound and Vibration*, Vol. 372, 2016, pp. 192–210.

[115] Zarri, A., Christophe, J., Moreau, S., and Schram, C., "Influence of Swept Blades on Low-Order Acoustic Prediction for Axial Fans," *Acoustics*, Vol. 2, No. 4, 2020, pp. 812–832.

[116] Chen, H., Chen, S., and Matthaeus, W. H., "Recovery of the Navier-Stokes Equations Using a Lattice-Gas Boltzmann Method," *Physical Review A*, Vol. 45, No. 8, 1992, p.

R5339.

[117] Krömer, F. J., Moreau, S., and Becker, S., "Experimental Investigation of the Interplay Between the Sound Field and the Flow Field in Skewed Low-Pressure Axial Fans," *Journal of Sound and Vibration*, Vol. 442, 2019, pp. 220–236.

[118] Sofla, A. Y. N., Meguid, S. A., Tan, K. T., and Yeo, W. K., "Shape Morphing of Aircraft Wing: Status and Challenges," *Materials & Design*, Vol. 31, No. 3, 2010, pp. 1284–1292.

[119] Barbarino, S., Bilgen, O., Ajaj, R. M., Friswell, M. I., and Inman, D. J., "A Review of Morphing Aircraft," *Journal of Intelligent Material Systems and Structures*, Vol. 22, No. 9, 2011, pp. 823–877.

[120] Howe, M. S., *Sound Generation in a Fluid with Rigid Boundaries*, Cambridge University Press, Cambridge, U.K., 1998.

[121] Lim, J. W., "Application of Parametric Airfoil Design for Rotor Performance Improvement," *44th European Rotorcraft Forum*, Netherlands, Sept, 2018.

[122] Liu, C., and Lee, S., "Parametric Airfoil Design and Sensitivity Analysis for Turbulent Boundary-Layer Trailing-Edge Noise Reduction," *AIAA Journal*, Vol. 60, No. 4, 2022, pp. 2324–2341.

[123] Drela, M., "XFOIL: An Analysis and Design System for Low Reynolds Number Airfoils," *Low Reynolds Number Aerodynamics: Proceedings of the Conference Notre Dame, Indiana, USA*, Springer, Berlin, Heidelberg, June 5–7, 1989, pp. 1–12.

[124] Howe, M., *Acoustics of Fluid-Structure Interactions*, Cambridge University Press, Cambridge, U.K., 1998, Chap. 3.

[125] Moin, P., Squires, K., Cabot, W., and Lee, S., "A Dynamic Subgrid-Scale Model for Compressible Turbulence and Scalar Transport," *Physics of Fluids*, Vol. 3, 1991, pp. 2746–2757.

[126] Piomelli, U., "Large-Eddy Simulation-Present State and Future Perspectives," *36th AIAA Aerospace Sciences Meeting and Exhibit*, Reno, NV, 1998, p. 534. Jan. 12–15, AIAA Paper No. 1998–534.

[127] Blazek, J., *Computational Fluid Dynamics: Principles and Applications*, Butterworth-Heinemann, 2015.

[128] Favre, A., "Equations des Gaz Turbulents Compressibles," *Journal de mécanique*, Vol. 4, No. 3, 1965.

[129] Nicoud, F., and Ducros, F., "Subgrid-Scale Stress Modelling Based on the Square of the Velocity Gradient Tensor," *Flow, Turbulence and Combustion*, Vol. 62, 1999, pp. 183–200.

[130] Weller, H. G., Tabor, G., Jasak, H., and Fureby, C., "A Tensorial Approach to Computational Continuum Mechanics Using Object-Oriented Techniques," *Computers in Physics*, Vol. 12, No. 6, 1998, pp. 620–631.

[131] Menter, F. R., "Two-equation eddy-viscosity turbulence models for engineering applications," *AIAA Journal*, Vol. 32, No. 8, 1994, pp. 1598–1605.

[132] Garmann, D. J., and Visbal, M. R., "Micro-Cavity Actuation for Control of Dynamic Stall on Swept Wing Sections," *AIAA SciTech Forum*, National Harbor, MD & Online, 2023, p. 0861. Jan 23–27, AIAA Paper No. 2023–0861.

[133] Mankbadi, R. R., Afari, S. O., and Golubev, V. V., "High-Fidelity Simulations of Noise Generation in a Propeller-Driven Unmanned Aerial Vehicle," *AIAA Journal*, Vol. 59, No. 3, 2021, pp. 1020–1039.

[134] Georgiadis, N. J., Rizzetta, D. P., and Fureby, C., "Large-Eddy Simulation: Current Capabilities, Recommended Practices, and Future Research," *AIAA Journal*, Vol. 48, No. 8, 2010, pp. 1772–1784.

[135] Brentner, K. S., and Farassat, F., "Modeling Aerodynamically Generated Sound of Helicopter Rotors," *Progress in Aerospace Sciences*, Vol. 39, No. 2–3, 2003, pp. 83–120.

[136] Ffowcs Williams, J. E., and Hawkings, D. L., "Sound Generated by Turbulence and Surface in Arbitrary Motion," *Journal of Philosophical Transaction of the Royal Society of London*, Vol. 264, No. 1151, 1969, pp. 321–342.

[137] Brentner, K. S., Bres, G. A., Perez, G., and Jones, H. E., "Maneuvering Rotorcraft Noise Prediction: A New Code for a New Problem," *American Helicopter Society Aerodynamics, Acoustics, and Test and Evaluation Technical Specialist Meeting*, San Francisco, CA, Jan 23–25, 2002.

[138] Lee, S., Brentner, K., Farassat, F., and Morris, P., "Analytic Formulation and Numerical Implementation of an Acoustic Pressure Gradient Prediction," *Journal of Sound and Vibration*, Vol. 319, No. 3–5, 2009, pp. 1200–1221.

[139] Schlinker, R., and Amiet, R., "Helicopter Rotor Trailing Edge Noise," *7th Aeroacoustics Conference*, Palo Alto, CA, 1981, p. 2001. Oct. 5–7, AIAA Paper No. 1981–2001.

[140] Kang, D., and Lee, S., "A Revisit of Amiet's Trailing-edge Noise Theory through Large-Eddy Simulations," *AIAA Aviation Forum*, San Diego, CA, 2023, p. 3629. Jun. 12–16, AIAA Paper No. 2023–3629.

[141] Abramowitz, M., *Handbook of Mathematical Functions*, Dover Publications, New York, 1970.

[142] Moreau, S., and Roger, M., "Back-Scattering Correction and Further Extensions of Amiet's Trailing-Edge Noise Model. Part II: Application," *Journal of Sound and Vi-*

bration, Vol. 323, No. 1–2, 2009, pp. 397–425.

[143] Li, S., and Lee, S., "Analytic Prediction of Rotor Broadband Noise with Serrated Trailing Edges," *Proceedings of the 78th VFS International Annual Forum*, Fort Worth, Texas, May 10–12, 2022.

[144] Grossmann, A., and Morlet, J., "Decomposition of Hardy Functions into Square Integrable Wavelets of Constant Shape," *SIAM Journal on Mathematical Analysis*, Vol. 15, No. 4, 1984, pp. 723–736.

[145] Meneveau, C., "Analysis of Turbulence in the Orthonormal Wavelet Representation," *Journal of Fluid Mechanics*, Vol. 232, 1991, pp. 469–520.

[146] Camussi, R., and Guj, G., "Orthonormal Wavelet Decomposition of Turbulent Flows: Intermittency and Coherent Structures," *Journal of Fluid Mechanics*, Vol. 348, 1997, pp. 177–199.

[147] Grizzi, S., and Camussi, R., "Wavelet Analysis of Near-Field Pressure Fluctuations Generated by a Subsonic Jet," *Journal of Fluid Mechanics*, Vol. 698, 2012, pp. 93–124.

[148] Azzalini, A., Farge, M., and Schneider, K., "Nonlinear Wavelet Thresholding: A Recursive Method to Determine The Optimal Denoising Threshold," *Applied and Computational Harmonic Analysis*, Vol. 18, No. 2, 2005, pp. 177–185.

[149] Donoho, D. L., and Johnstone, J. M., "Ideal Spatial Adaptation by Wavelet Shrinkage," *Biometrika*, Vol. 81, No. 3, 1994, pp. 425–455.

[150] Shubham, S., Sandberg, R. D., Moreau, S., and Wu, H., "Surface Pressure Spectrum Variation With Mach Number on a CD Airfoil," *Journal of Sound and Vibration*, Vol. 526, 2022, p. 116762.

[151] Hatman, A., and Wang, T., "A Prediction Model for Separated-Flow Transition," *International Gas Turbine & Aeroengine Congress & Exhibition*, 1998.

[152] Hunt, J., Wray, A., and Moin, P., "Eddies, Streams, and Convergence Zones in Turbulent Flows," *In Studying turbulence using numerical simulation databases, 2. Proceedings of the 1988 summer program*, 1998.

[153] Kato, C., Iida, A., Takano, Y., Fujita, H., and Ikegawa, M., "Numerical Prediction of Aerodynamic Noise Radiated from Low Mach Number Turbulent Wake," *31st Aerospace Sciences Meeting*, Reno, NV, 1993, p. 145. Jan. 11–14, AIAA Paper No. 1993–145.

[154] Arias Ramírez, W., and Wolf, W. R., "Effects of Trailing Edge Bluntness on Airfoil Tonal Noise at Low Reynolds Numbers," *Journal of the Brazilian Society of Mechanical Sciences and Engineering*, Vol. 38, 2016, pp. 2369–2380.

[155] Le, A., Roytershteyn, V., Karimabadi, H., Stanier, A., Chacon, L., and Schneider, K., "Wavelet Methods for Studying the Onset of Strong Plasma Turbulence," *Physics of*

Plasmas, Vol. 25, No. 12, 2018, p. 122310.

[156] Kang, D., and Lee, S., "Application of Wavelet Analysis to Trailing-edge Noise," *28th AIAA/CEAS Aeroacoustics Conference*, Southampton, United Kingdom, 2022, p. 2891. Jun. 14–17, AIAA Paper No. 2022–2891.

[157] Lilly, J. M., and Olhede, S. C., "Higher-Order Properties of Analytic Wavelets," *IEEE Transactions on Signal Processing*, Vol. 57, No. 1, 2008, pp. 146–160.

[158] Lilly, J. M., and Olhede, S. C., "On the Analytic Wavelet Transform," *IEEE Transactions on Information Theory*, Vol. 56, No. 8, 2010, pp. 4135–4156.

[159] Lilly, J. M., and Olhede, S. C., "Generalized Morse Wavelets as a Superfamily of Analytic Wavelets," *IEEE Transactions on Signal Processing*, Vol. 60, No. 11, 2012, pp. 6036–6041.

[160] Shin, K., and Hammond, J., *Fundamentals of Signal Processing for Sound and Vibration Engineers*, John Wiley & Sons, 2008.

[161] Szoke, M., Fiscaletti, D., and Azarpeyvand, M., "Influence of Boundary Layer Flow Suction on Trailing Edge Noise Generation," *Journal of Sound Vibration*, Vol. 475, 2020, p. 115276.

[162] Mohan, A. T., Gaitonde, D. V., and Visbal, M. R., "Model Reduction and Analysis of Deep Dynamic Stall on a Plunging Airfoil," *Computers & Fluids*, Vol. 129, 2016, pp. 1–19.

[163] Jiménez, J., "Near-Wall Turbulence," *Physics of Fluids*, Vol. 25, No. 10, 2013, p. 101302.

[164] Abreu, L. I., Cavalieri, A. V., Schlatter, P., Vinuesa, R., and Henningson, D. S., "Spectral Proper Orthogonal Decomposition and Resolvent Analysis of Near-Wall Coherent Structures in Turbulent Pipe Flows," *Journal of Fluid Mechanics*, Vol. 900, 2020, p. A11.

[165] Colonius, T., and Lele, S. K., "Computational Aeroacoustics: Progress on Nonlinear Problems of Sound Generation," *Progress in Aerospace Sciences*, Vol. 40, No. 6, 2004, pp. 345–416.

[166] Kim, J., Haeri, S., and Joseph, P., "On the Reduction of Airfoil–Turbulence Interaction Noise Associated With Wavy Leading Edges," *Journal of Fluid Mechanics*, Vol. 792, 2016, pp. 526–552.

[167] Abreu, L. I., Tanarro, A., Cavalieri, A. V., Schlatter, P., Vinuesa, R., Hanifi, A., and Henningson, D. S., "Spanwise-Coherent Hydrodynamic Waves Around Flat Plates and Airfoils," *Journal of Fluid Mechanics*, Vol. 927, 2021, p. A1.

[168] Tian, H., and Lyu, B., "The Impact of Non-Frozen Turbulence on the Noise Prediction For Serrated Trailing Edges," *AIAA Aviation Forum*, San Diego, CA, 2023, p. 3824.

June. 12–16, AIAA Paper No. 2023–3824.

[169] Smol'yakov, A. V., "A New Model for the Cross Spectrum and Wavenumber-Frequency Spectrum of Turbulent Pressure Fluctuations in a Boundary Layer," *Acoustical Physics*, Vol. 52, 2006, pp. 331–337.

[170] Nogueira, P. A., Cavalieri, A. V., and Jordan, P., "A Model Problem for Sound Radiation by an Installed Jet," *Journal of Sound and Vibration*, Vol. 391, 2017, pp. 95–115.

[171] Bogey, C., and Bailly, C., "An Analysis of the Correlations Between the Turbulent Flow and the Sound Pressure Fields of Subsonic Jets," *Journal of Fluid Mechanics*, Vol. 583, 2007, pp. 71–97.

[172] Tiomkin, S., and Jaworski, J. W., "Revisiting the Frozen Gust Assumption Through the Aeroacoustic Scattering of Wavepackets by a Semi-Infinite Plate," *Journal of Sound and Vibration*, Vol. 571, 2024, p. 117989.

[173] Desquesnes, G., Terracol, M., and Sagaut, P., "Numerical Investigation of the Tone Noise Mechanisms over Laminar Airfoils," *Journal of Fluid Mechanics*, Vol. 591, 2007, pp. 155–182.

[174] Roberts, W. B., "Calculation of Laminar Separation Bubbles and their Effect on Airfoil Performance," *AIAA Journal*, Vol. 18, No. 1, 1980, pp. 25–31.

[175] Griffin, K. P., Fu, L., and Moin, P., "General Method for Determining the Boundary Layer Thickness in Nonequilibrium Flows," *Physical Review Fluids*, Vol. 6, No. 2, 2021, p. 024608.

[176] Schlichting, H., and Gersten, K., *Boundary Layer Theory*, ninth ed., Springer, Berlin, 2016, Chap. 15.

[177] Kingan, M. J., and Pearse, J. R., "Laminar Boundary Layer Instability Noise Produced by an Aerofoil," *Journal of Sound and Vibration*, Vol. 322, No. 4–5, 2009, pp. 808–828.

[178] Lowson, M., Fiddes, S., and Nash, E., "Laminar Boundary Layer Aeroacoustic Instabilities," *32nd Aerospace Sciences Meeting and Exhibit*, Reno, NV, 1994, p. 0358. Jan 10–13, AIAA Paper No. 1994–0358.

[179] McAlpine, A., Nash, E. C., and Lowson, M. V., "On the Generation of Discrete Frequency Tones by the Flow Around an Aerofoil," *Journal of Sound and Vibration*, Vol. 222, No. 5, 1999, pp. 753–779.

[180] Nash, E. C., Lowson, M. V., and McAlpine, A., "Boundary-Layer Instability Noise on Aerofoils," *Journal of Fluid Mechanics*, Vol. 382, 1999, pp. 27–61.

[181] Tam, C. K., and Ju, H., "Aerofoil Tones at Moderate Reynolds Number," *Journal of Fluid Mechanics*, Vol. 690, 2012, pp. 536–570.

[182] Deuse, M., and Sandberg, R. D., "Different Noise Generation Mechanisms of a Con-

trolled Diffusion Aerofoil and Their Dependence on Mach Number," *Journal of Sound and Vibration*, Vol. 476, 2020, p. 115317.

[183] Wu, H., Sandberg, R. D., and Moreau, S., "Stability Characteristics of Different Aerofoil Flows at Re_c= 150,000 and the Implications for Aerofoil Self-Noise," *Journal of Sound and Vibration*, Vol. 506, 2021, p. 116152.

[184] Longhouse, R. E., "Vortex Shedding Noise of Low Tip Speed, Axial Flow Fans," *Journal of Sound and Vibration*, Vol. 53, No. 1, 1977, pp. 25–46.

[185] Ricciardi, T. R., Wolf, W. R., and Taira, K., "Transition, intermittency and phase interference effects in airfoil secondary tones and acoustic feedback loop," *Journal of Fluid Mechanics*, Vol. 937, 2022, p. A23.

[186] Ricciardi, T. R., and Wolf, W. R., "Switch of Tonal Noise Generation Mechanisms in Airfoil Transitional Flows," *Physical Review Fluids*, Vol. 7, No. 8, 2022, p. 084701.

[187] Arbey, H., and Bataille, J., "Noise Generated by Airfoil Profiles Placed in a Uniform Laminar Flow," *Journal of Fluid Mechanics*, Vol. 134, 1983, pp. 33–47.

[188] Jaiswal, P., Pasco, Y., Yakhina, G., and Moreau, S., "Experimental Investigation of Aerofoil Tonal Noise at Low Mach Number," *Journal of Fluid Mechanics*, Vol. 932, 2022, p. A37.

[189] Christophe, J., "Application of Hybrid Methods to High Frequency Aeroacoustics," *Université Libre de Bruxelles*, 2011.

[190] Wang, M., Freund, J. B., and Lele, S. K., "Computational Prediction of Flow-Generated Sound," *Annual Review of Fluid Mechanics*, Vol. 38, No. 1, 2006, pp. 483–512.

[191] Kang, D., Lee, S., Brouzet, D., and Lele, S. K., "Wavelet-based Pressure Decomposition for Airfoil Noise in Low Mach Number Flows," *Physics of Fluids*, Vol. 35, No. 7, 2023, p. 075112.

[192] Arcondoulis, E. J. G., Doolan, C. J., Zander, A. C., and Brooks, L. A., "A Review of Trailing Edge Noise Generated by Airfoils at Low to Moderate Reynolds Number," *Acoustics Australia*, Vol. 38, No. 3, 2010, pp. 129–133.

[193] Jeun, J., Karnam, A., Jun Wu, G., Lele, S. K., Baier, F., and Gutmark, E. J., "Aeroacoustics of Twin Rectangular Jets Including Screech: Large-Eddy Simulations with Experimental Validation," *AIAA Journal*, Vol. 60, No. 11, 2022, pp. 6340–6360.

[194] Kang, D., and Lee, S., "On the Effect of Boundary-layer Tripping for Trailing-Edge Noise Predictions," *AIAA SciTech Forum*, National Harbor, MD, 2023, p. 0972. Jan. 23–27, AIAA Paper No. 2023–0972.

[195] Kang, D., and Lee, S., "Aerodynamic and Aeroacoustic Effects of Different Transition Mechanisms on an Airfoil," *AIAA Journal*, Vol. 62, No. 4, 2024, pp. 1517–1535.

[196] Powell, A., "On the aerodynamic noise of a rigid flat plate moving at zero incidence," *Journal of the Acoustical Society of America*, Vol. 31, No. 12, 1959, pp. 1649–1653.

[197] Romani, G., Casalino, D., and Velden, W. V. D., "Numerical analysis of airfoil trailing-edge noise for straight and serrated edges at incidence," *AIAA Journal*, Vol. 59, No. 7, 2021, pp. 2558–2577.

[198] Casalino, D., and Jacob, M., "Prediction of Aerodynamic Sound from Circular Rods via Spanwise Statistical Modelling," *Journal of Sound and Vibration*, Vol. 262, No. 4, 2003, pp. 815–844.

[199] Jacob, M. C., Boudet, J., Casalino, D., and Michard, M., "A Rod-Airfoil Experiment as a Benchmark for Broadband Noise Modeling," *Theoretical and Computational Fluid Dynamics*, Vol. 19, 2005, pp. 171–196.

[200] Seo, J. H., and Moon, Y. J., "Aerodynamic Noise Prediction for Long-Span Bodies," *Journal of Sound and Vibration*, Vol. 306, No. 3–5, 2007, pp. 564–579.

[201] Orselli, R., Meneghini, J., and Saltara, F., "Two and Three-Dimensional Simulation of Sound Generated by Flow Around a Circular Cylinder," *15th AIAA/CEAS Aeroacoustics Conference*, Miami, FL, 2009, p. 3270. May 11–13, AIAA Paper No. 2009–3270.

[202] He, G. W., and Zhang, J. B., "Elliptic Model for Space-Time Correlations in Turbulent Shear Flows," *Physical Review E*, Vol. 73, No. 5, 2006, p. 055303.

[203] Park, G. I., and Moin, P., "Space-Time Characteristics of Wall-Pressure and Wall Shear-Stress Fluctuations in Wall-Modeled Large Eddy Simulation," *Physical Review Fluids*, Vol. 1, No. 2, 2016, p. 024404.

[204] He, G., Jin, G., and Yang, Y., "Space-Time Correlations and Dynamic Coupling in Turbulent Flows," *Annual Review of Fluid Mechanics*, Vol. 49, No. 1, 2017, pp. 51–70.

[205] Fisher, M. J., and Davies, P. O. A. L., "Correlation Measurements in a Non-Frozen Pattern of Turbulence," *Journal of Fluid Mechanics*, Vol. 18, No. 1, 1964, pp. 97–116.

[206] Hu, N., Reiche, N., and Ewert, R., "Simulation of Turbulent Boundary Layer Wall Pressure Fluctuations via Poisson Equation and Synthetic Turbulence," *Journal of Fluid Mechanics*, Vol. 826, 2017, pp. 421–454.

[207] Lyu, B., Azarpeyvand, M., and Sinayoko, S., "Prediction of noise from serrated trailing edges," *Journal of Fluid Mechanics*, Vol. 793, 2016, pp. 556–588.

[208] Kang, D., and Lee, S., "On the Role of Hydrodynamic and Acoustic Pressures in Trailing-edge Noise Using Numerical and Analytical Approaches," *Under Review*, 2024.

[209] Kang, D., and Lee, S., "Cross-Spectrum Method for Acoustic Source Identification and Visualization of Airfoil Noise," *Aerospace Science and Technology*, 2024, p. 109278.

[210] Kang, D., and Lee, S., "Effect of Misaligned Flow on Trailing-edge Noise," *Under*

Review, 2024.

[211] Kang, D., and Lee, S., "Effect of Trailing-edge Curvature on Noise Source and Radiation Characteristics of an Airfoil," *In Preparation*, 2024.

[212] Kang, D., and Lee, S., "Assessment of Wavelet-based Separation Algorithms on Turbulent Boundary Layer Trailing-Edge Noise Prediction," *11th International Conference on Computational Fluid Dynamics*, Maui, Hawaii, July 11–15, 2022.

[213] Lee, S., Kang, D., Brouzet, D., and Lele, S. K., "Airfoil Trailing-Edge Noise Source Identification Using Large-Eddy Simulation and Wavelet Transform," *Proceedings of the Summer Program*, 2022.

[214] Kang, D., and Lee, S., "A New Acoustic Source Identification and Visualization Method for Airfoil Noise Using Large-Eddy Simulations," *AIAA SciTech Forum*, Orlando, FL, 2024, p. 1906. Jan. 8–12, AIAA Paper No. 2024–1906.

[215] Kang, D., and Lee, S., "Numerical and Analytical Investigations on Airfoil Noise Reduction with a Sweep Angle," *30th AIAA/CEAS Aeroacoustics Conference*, Rome, Italy, 2024, p. 3285. Jun. 4–7, AIAA Paper No. 2024–3285.

[216] Kang, D., and Lee, S., "Aeroacoustic Study of Morphed Trailing-Edge Airfoils Using Large-Eddy Simulations," *12th International Conference on Computational Fluid Dynamics*, Kobe, Japan, 2024. July 14–19.

[217] Kang, D., and Lee, S., "Aerodynamic and Aeroacoustic Investigations of a NACA 0018 Airfoil with Morphed Trailing Edges," *AIAA SciTech Forum*, Orlando, FL, 2025. Jan. 6–10.

[218] Corcos, G. M., "The Structure of the Turbulent Pressure Field in Boundary-layer Flows," *Journal of Fluid Mechanics*, Vol. 18, No. 3, 1964, pp. 353–378.